

Trygve K. Løvli

# Nonlinear Analysis of Reinforced Concrete Beams without Shear Reinforcement

Master's thesis in Civil and Environmental Engineering

Supervisor: Max A. N. Hendriks

June 2022



Trygve K. Løvli

# **Nonlinear Analysis of Reinforced Concrete Beams without Shear Reinforcement**

Master's thesis in Civil and Environmental Engineering  
Supervisor: Max A. N. Hendriks  
June 2022

Norwegian University of Science and Technology  
Faculty of Engineering  
Department of Structural Engineering





## MASTER THESIS 2022

SUBJECT AREA: Design of Concrete Structures	DATE: 10.06.2022	NO. OF PAGES: 189
--	---------------------	----------------------

TITLE:

### **Nonlinear Analysis of Reinforced Concrete Beams without Shear Reinforcement**

IKKELINEÆRE ANALYSER AV ARMERTE BETONGBJELKER UTEN SKJÆRARMERING

BY:

Trygve K. Løvli



SUMMARY:

This thesis utilized nonlinear finite element analysis (NLFEA) as a tool to numerically reflect the behavior of reinforced concrete beams of different geometries. The finite element program utilized was DIANA with version 10.4, as this program supports a large number of numerical models for the different properties of reinforced concrete. The overall goal of this thesis was to investigate the stability and accuracy of fixed numerical models through a specter of varying beam geometries.

In 2018, an experimental study was performed on longitudinal reinforced concrete beams of varying height and length subjected to a four-point bending load (Suchorzewski et al., 2018). The beams in the experiment had a total of five different geometries. Due to the geometrical deviation in the beams, different failure mechanisms were obtained. Thus, the experiment offered the possibility to see how numerical models were able to perform as they were set to reflect RC beams with different geometries and failure modes.

The numerical modelling procedures were limited to local, smeared, total-strain based crack approaches. Also, the numerical models were simplified by using 2D plane stress elements, and symmetry boundary conditions. The fixed modelling choices, that were common for all analyses, were affected by varying research papers and guidelines for nonlinear analyses of reinforced concrete. The varying modelling parameters were concerning the influence of different shear retention models, crack models and tension stiffening.

None of the numerical models were concluded to be superior considering the summarized performance. It was rather found that the applicability of the models varied between beam geometries and failure modes. Thereby, it was concluded that none of the numerical models within the scope of this thesis were able to properly simulate all variations of geometries and failure modes.

RESPONSIBLE TEACHER: Jan A. Øverli

SUPERVISOR(S): Max A. N. Hendriks

CARRIED OUT AT: Department of Structural Engineering, NTNU, Trondheim



## MASTEROPPGAVE 2022

FAGOMRÅDE: Prosjektering av Betongkonstruksjoner	DATO: 10.06.2022	ANTALL SIDER: 189
---	---------------------	----------------------

TITTEL:

### IKKELINEÆRE ANALYSER AV ARMERTE BETONGBJELKER UTEN SKJÆRARMERING

Nonlinear Analysis of Reinforced Concrete Beams without Shear Reinforcement

UTFØRT AV:

Trygve K. Løvli



SAMMENDRAG:

I denne oppgaven ble ikkelineær elementmetode brukt som et verktøy til å numerisk reflektere oppførselen til armerte betongbjelker med ulik geometri. Elementmetodeprogrammet som ble brukt var DIANA med versjon 10.4, da dette programmet har mange numeriske modeller som representerer ulike egenskaper i armert betong. Hovedmålet med denne oppgaven var å undersøke stabiliteten og nøyaktigheten til numeriske modeller for flere ulike bjelkegeometrier, uten å endre modellene mellom bjelkegeometriene.

I 2018 ble et eksperiment på strekkarmerte betongbjelker med varierende høyde og lengde utsatt for firepunkts bøyetest gjennomført (Suchorzewski et al., 2018). Bjelkene i eksperimentet hadde totalt fem ulike geometrier. Som følge av de varierende bjelkegeometriene ble forskjellige bruddmekanismer observert. Dermed ga eksperimentet gode muligheter til å undersøke hvordan ulike numeriske modeller klarte å representere armerte betongbjelker med varierende geometrier og bruddmekanismer.

De numeriske modellene var begrenset til å være lokale, "smeared", totaltøynings-baserte rissmodeller. I tillegg var de numeriske modellene forenklet ved at kun elementer med 2D plan spenning ble brukt, samt symmetri-randbetingelser. De konstante modelleringsvalgene, altså de som var felles i alle analysene, ble i stor grad preget av forskningsartikler og retningslinjer for ikkelineære analyser av armert betong. De varierende modelleringsvalgene omhandlet innflytelsen av ulike modeller for den resterende skjærstivheten i riss, ulike rissmodeller og "tension stiffening".

Summert sett var ingen av de numeriske modellene overlegne. Resultatene viste heller at brukbarheten til de ulike numeriske modellene varierte for ulike geometrier og bruddmekanismer. Dermed ble også konklusjonen at ingen av de numeriske modellene som ble brukt i denne oppgaven klarte å gi gode nok estimater for alle variasjonene av geometrier og bruddmekanismer vist i eksperimentet.

FAGLÆRER: Jan A. Øverli

VEILEDER(E): Max A.N. Hendriks

UTFØRT VED: Institutt for konstruksjonsteknikk, NTNU, Trondheim

# Abstract

This thesis utilized nonlinear finite element analysis (NLFEA) as a tool to numerically reflect the behavior of reinforced concrete beams of different geometries. The finite element program utilized was DIANA with version 10.4, as this program supports a large number of numerical models for the different properties of reinforced concrete. The overall goal of this thesis was to investigate the stability and accuracy of fixed numerical models through a specter of varying beam geometries.

In 2018, an experimental study was performed on longitudinal reinforced concrete beams of varying height and length subjected to a four-point bending load (Suchorzewski et al., 2018). The tests were performed in two series, where the first series scaled the beams in the height direction and the second scaled the beams in the length direction. There were three different geometries in each series, however, the two series had one common geometry, resulting in a total of five different geometries to be numerically simulated. Due to the geometrical deviation in the beams, different failure mechanisms were obtained, namely, flexural bending, tension shear and compression shear failure. Thus, the experiment offered the possibility to investigate how different numerical models were able to perform as they were set to reflect RC beams with different geometries and failure modes.

The numerical modelling procedures were limited to local, smeared, total-strain based crack approaches. Also, the numerical models were simplified by using 2D plane stress elements, and symmetry boundary conditions. Furthermore, the modelling choices in this thesis can be separated into the categories of fixed and varying modelling choices. The fixed modelling choices, that were common for all analyses, were affected by varying research papers and guidelines for nonlinear analyses of reinforced concrete. The varying modelling parameters were concerning the influence of different shear retention models, crack models and tension stiffening. Thus, this thesis contains three sub-investigations which analyze the influence of each varying modelling parameter.

The shear retention models consisted of the damage based, Al-Mahaidi and aggregate based shear retention model. The numerical behavior varied greatly for the different shear retention models, and they possessed different strengths and weaknesses. In the second investigation, the rotating crack model, the fixed crack model and three variations of the threshold value in the rotating to fixed crack model were investigated. It showed that the rotating to fixed crack models were acting between the fully rotating and fully fixed crack model. Hence, as neither the rotating or fixed crack model were able to give consistent and accurate simulations of all beams, neither did the rotating to fixed crack models. In the third and final investigation, the influence of tension stiffening was analyzed. The inclusion of this effect improved the estimations for some of the beams, but not for all.

None of the numerical models were concluded to be superior considering the summarized performance. It was rather found that the applicability of the models varied between beam geometries and failure modes. Thereby, it was concluded that none of the numerical models within the scope of this thesis were able to properly simulate all variations of geometries and failure modes.



# Sammendrag

I denne oppgaven ble ikkelineær elementmetode brukt som et verktøy til å reflektere oppførselen til armerte betongbjelker med ulik geometri numerisk. Elementmetodeprogrammet som ble brukt var DIANA med versjon 10.4, da dette programmet har mange numeriske modeller som representerer ulike egenskaper i armert betong. Hovedmålet med denne oppgaven var å undersøke stabiliteten og nøyaktigheten til numeriske modeller for flere ulike bjelkegeometrier, uten å endre modellene mellom bjelkegeometriene.

I 2018 ble et eksperiment på strekkarmerte betongbjelker av varierende høyde og lengde gjennomført (Suchorzewski et al., 2018). Bjelkene var fritt opplagt med to punktlaster, som dermed resulterte i en firepunkts lastpåkjenning. Testene ble gjennomført i to serier, hvor bjelkehøyden ble skalert i den første serien, og bjelkelengden ble skalert i den andre serien. Det var tre forskjellige geometrier i hver serie, men seriene hadde én felles geometri, som resulterte i at totalt fem forskjellige geometrier skulle bli simulert numerisk. Som følge av de varierende bjelkegeometriene ble tre ulike bruddmekanismer observert, nemlig momentbrudd, skjærstrekk og skjærtrykk. Dermed ga eksperimentet gode muligheter til å undersøke hvordan ulike numeriske modeller klarte å representere armerte betongbjelker med varierende geometrier og bruddmekanismer.

De numeriske modellene var begrenset til å være lokale, "smeared", totaltøynings-baserte rissmodeller. I tillegg var de numeriske modellene forenklet ved at kun elementer med 2D plan spenning ble brukt, samt symmetri-randbetingelser. Modelleringsvalgene i denne oppgaven kan deles inn i to kategorier, de konstante og de varierende. De konstante modelleringsvalgene, altså de som var felles i alle analysene, ble i stor grad preget av forskningsartikler og retningslinjer for ikkelineære analyser av armert betong. De varierende modelleringsvalgene omhandlet innflytelsen av ulike modeller for den resterende skjærstivheten i riss, ulike rissmodeller og "tension stiffening". Derved inneholder denne masteroppgaven tre delundersøkelser som analyserer effekten av de varierende modelleringsvalgene.

De ulike modellene for skjærstivhet i riss besto av den skadebaserte, Al-Mahaidi og den tilslagsbaserte modellen. Den numeriske oppførselen varierte stort mellom modellene, og de viste ulike styrker og svakheter. I den andre analysen ble den roterende rissmodellen, den ikke-roterende rissmodellen og tre variasjoner av terskelverdien til den roterende til ikke-roterende rissmodellen. Det viste seg at den roterende til ikke-roterende rissmodellen hadde en oppførsel og kapasitetsestimering som kan sies å være i mellom den roterende og ikke-roterende modellen. Dermed, ettersom verken den roterende eller ikke-roterende modellen klarte å gi konsistente og presise simuleringer av alle bjelkene, klarte heller ikke den roterende til ikke-roterende modellen dette. I den tredje og siste analysen ble påvirkningen av tension stiffening analysert. Inkluderingen av denne effekten forbedret de numeriske estimeringene for noen av bjelkene, men ikke alle.

Summert sett var ingen av de numeriske modellene overlegne. Resultatene viste heller at brukbarheten til de ulike numeriske modellene varierte for ulike geometrier og bruddmekanismer. Dermed ble også konklusjonen at ingen av de numeriske modellene som ble brukt i denne oppgaven klarte å gi gode nok estimater for alle variasjonene av geometrier og bruddmekanismer vist i eksperimentet.

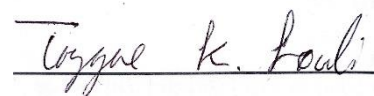


# Preface

This master's thesis is the final work of a two-year master's degree at NTNU in Civil and Environmental Engineering at the department of Structural Engineering. The thesis was completed during a period of 20 weeks which took place in the spring semester 2022. The work in this thesis corresponds to 30 credits.

The large amount of time given to complete this thesis offered a great opportunity to learn about the theory of nonlinearity, which prior to this work was an untouched subject for this author. In particular, the complex nonlinear behavior of reinforced concrete, and how this is implemented into a numerical finite element program was considered to be valuable and interesting knowledge and was a motivating factor through the work on this thesis. The numerical program used in this thesis is called DIANA, with version 10.4. A lot of research had to be done in order to comprehend the variety of opportunities the program had to offer, and to understand how the program worked in general.

The author would like to express his gratitude to his supervisor Professor Max A.N Hendriks from NTNU and Delft University of Technology and also Professor Jan A. Øverli from NTNU for the motivation, guidance, and interesting discussions they provided throughout the realization of this thesis. Furthermore, I would like to thank the DIANA support center, in particular Jesus Mediavilla, for the thorough and extensive responses they gave in order to help me understand different features in the program. Finally, I would like to thank the author of the experiment, Dr. Jan Suchorzewski from Gdansk University of Technology, for responding to the questions I had regarding the experiment itself.



Trygve Kristoffer Løvli

Trondheim, 10.06.2022



# Contents

Abstract .....	V
Sammendrag .....	VII
Preface.....	IX
1 Introduction .....	1
2 Theory and Methods for Nonlinear Finite Element Analysis of Reinforced Concrete Structures .....	3
2.1 Finite Element Analysis .....	3
2.1.1 Elements .....	3
2.2 Nonlinear Finite Element Analysis.....	5
2.2.1 Incremental-Iterative Solution Procedure.....	6
2.2.2 Incremental Procedure .....	6
2.2.3 Iterative Method .....	7
2.2.4 Arc Length Method with Indirect Displacement Control .....	8
2.2.5 Line Search.....	9
2.2.6 Convergence Criteria.....	10
2.3 Plain Concrete Characteristics.....	10
2.3.1 Tension Behavior .....	10
2.3.2 Compression Behavior.....	13
2.3.3 Poisson's Ratio Reduction .....	18
2.3.4 Unloading and Reloading .....	19
2.4 Reinforced Concrete .....	19
2.4.1 Reinforcement Model.....	19
2.4.2 Bond-slip .....	20
2.4.3 Tension Stiffening .....	22
2.5 Crack Modelling .....	24
2.5.1 Fixed Crack Model.....	26
2.5.2 Rotating Crack Model .....	27
2.5.3 Rotating to Fixed Crack Model .....	28
2.5.4 Shear Retention .....	29
2.6 Modes of Failure .....	31
2.6.1 Flexural Failure.....	31
2.6.2 Tension Shear Failure.....	31
2.6.3 Compression Shear Failure .....	31
2.7 Size Effect.....	31
2.7.1 Stochastic Size Effect .....	32
2.7.2 Energetic Size Effect .....	32

3	Finite Element Modelling of Five Beams Tested by Suchorzewski et al.....	33
3.1	Experimental Setup.....	34
3.2	Non-variable Modelling Parameters.....	36
3.3	Variable Modelling Parameters.....	42
3.3.1	Shear Retention Models.....	42
3.3.2	Crack Models.....	42
3.3.3	Tension Stiffening.....	43
4	Finite Element Results and Discussion.....	47
4.1	The Influence of Shear Retention Models.....	48
4.1.1	Beam S1D18a108.....	48
4.1.2	Beam S1&2D36a108.....	50
4.1.3	Beam S1D72a108.....	53
4.1.4	Beam S2D36a72.....	57
4.1.5	Beam S2D36a36.....	59
4.1.6	Comparisons and Remarks.....	60
4.2	The Influence of Crack Models.....	64
4.2.1	Beam S1D18a108.....	64
4.2.2	Beam S1&2D36a108.....	67
4.2.3	Beam S1D72a108.....	69
4.2.4	Beam S2D36a72.....	70
4.2.5	Beam S2D36a36.....	72
4.2.6	Comparisons and Remarks.....	73
4.3	The Influence of Tension Stiffening.....	77
4.3.1	Beam S1D18a108.....	80
4.3.2	Beam S1&2D36a108.....	81
4.3.3	Beam S1D72a108.....	83
4.3.4	Beam S2D36a72.....	85
4.3.5	Beam S2D36a36.....	86
4.3.6	Comparisons and Remarks.....	88
5	Conclusion.....	92
6	Suggestions for Further Research.....	95
	Bibliography.....	96
	Appendix A.....	100
A.1	Compression and Tensile Behavior.....	100
A.2	Compressive Reduction due to Lateral Cracking.....	103
A.3	Shear Retention.....	105
A.4	Confinement.....	107

Appendix B .....	109
B.1 Calculation of Threshold Strain Value in the Rotating to Fixed Crack Model .....	109
B.2 Calculation of Tension Stiffening Zone .....	110
B.3 Calculation of Analytical Initial Stiffness and Crack Initiation Values .....	111
Appendix C .....	116
C.1 Crack Strain Patterns of the Shear Retention Analyses .....	118
C.1.1 Crack Strain Patterns of Beam S1D18a108 .....	118
C.1.2 Crack Strain Patterns of Beam S1&2D36a108 .....	120
C.1.3 Crack Strain Patterns of Beam S1D72a108 .....	124
C.1.4 Crack Strain Patterns of Beam S2D36a72 .....	128
C.1.5 Crack Strain Patterns of Beam S2D36a36 .....	131
C.2 Crack Strain Patterns of the Crack Model Analyses .....	134
C.2.1 Crack Strain Patterns of Beam S1D18a108 .....	135
C.2.2 Crack Strain Patterns of Beam S1&2D36a108 .....	138
C.2.3 Crack Strain Patterns of Beam S1D72a108 .....	144
C.2.4 Crack Strain Patterns of Beam S2D36a72 .....	150
C.2.5 Crack Strain Patterns of Beam S2D36a36 .....	153
C.3 Crack Strain Patterns of the Tension Stiffening Analyses .....	159
C.3.1 Crack Strain Patterns of Beam S1D18a108 .....	159
C.3.2 Crack Strain Patterns of Beam S1&2D36a108 .....	160
C.3.3 Crack Strain Patterns of Beam S1D72a108 .....	163
C.3.4 Crack Strain Patterns of Beam S2D36a72 .....	166
C.3.5 Crack Strain Patterns of Beam S2D36a36 .....	167

# List of Figures

Figure 2.1 – 8-noded quadrilateral isoparametric plane stress element (DIANA TNO,2020)	4
Figure 2.2 – 3+3-noded 2D line element (DIANA TNO, 2020)	4
Figure 2.3 – 3-noded 2D class-III beam element (DIANA TNO, 2020)	5
Figure 2.4 – 11-noded 2D line element (DIANA TNO, 2012)	5
Figure 2.5 – Displacement controlled incremental procedure (DIANA TNO, 2020)	6
Figure 2.6 – Regular Newton-Raphson iteration method (DIANA TNO, 2020)	7
Figure 2.7 – Snap-through and snap-back behavior (DIANA TNO,2020)	8
Figure 2.8 – Line search iteration (DIANA TNO, 2020)	9
Figure 2.9 – Hordijk tension softening (DIANA TNO, 2020)	12
Figure 2.10 – Parabolic compression curve (DIANA TNO, 2020)	14
Figure 2.11 – Influence of lateral confinement on the compressive stress-strain curve (DIANA TNO, 2020)	17
Figure 2.12 – Reduction factor due to lateral cracking (DIANA TNO, 2020)	18
Figure 2.13 – Loading-unloading-reloading (DIANA TNO, 2020)	19
Figure 2.14 – Bond-slip back-bone curve of fib Model Code 2010 (DIANA TNO, 2020)	21
Figure 2.15 – JSCE stiffening (DIANA TNO, 2020)	22
Figure 2.16 - Relative crack coordinate system	26
Figure 2.17 – Reduced shear stiffness (DIANA TNO, 2020)	29
Figure 3.1 – Beam S1D18a108	34
Figure 3.2 – Beam S1&2D36a108	34
Figure 3.3 – Beam S1D72a108	35
Figure 3.4 – Beam S2D36a72	35
Figure 3.5 – Beam S2D36a36	35
Figure 3.6 – Mesh layout for beam S1D18a108	40
Figure 3.7 – Mesh layout for beam S1&2D36a108	41
Figure 3.8 – Mesh layout for beam S1D72a108	41
Figure 3.9 – Mesh layout for beam S2D36a72	41
Figure 3.10 – Mesh layout for beam S2D36a36	41
Figure 3.11 – Beam S1D18a108 with tension stiffening zone	44
Figure 3.12 – Beam S1&2D36a108 with tension stiffening zone	45
Figure 3.13 – Beam S1D72a108 with tension stiffening zone	45
Figure 3.14 – Beam S2D36a72 with tension stiffening zone	45
Figure 3.15 – Beam S2D36a36 with tension stiffening zone	46
Figure 4.1 – Force-deflection plot for the experiment and varying shear retention models for beam S1D18a108	48
Figure 4.2 – Force-deflection plot for the experiment and varying shear retention models for beam S1&2D36a108	50
Figure 4.3 – Crack strain plot of S1&2D36a108 with the Al-Mahaidi shear retention model, establishment of an alternative crack formation	52
Figure 4.4 – Force-deflection plot for the experiment and varying shear retention models for beam S1D72a108	53
Figure 4.5 – Crack strain (left) and principal stress (right) before and after the emergence of a crack in the top part of the beam for the Al-Mahaidi shear retention model	54
Figure 4.6 – Crack strain plots with short anchorage (left) and an isotropic linear elastic corner (right)	55

Figure 4.7 – Force-deflection plot using the Al-Mahaidi shear retention model for beam S1D72a108 with and without a linear elastic corner .....	56
Figure 4.8 – Force-deflection plot for the experiment and varying shear retention models for beam S2D36a72.....	57
Figure 4.9 – Force-deflection plot for the experiment and varying shear retention models for beam S2D36a36.....	59
Figure 4.10 – Capacity comparison (left) and a capacity deviation diagram (right) between numerical and experimental results for the shear retention analysis .....	61
Figure 4.11 – Initial slope of the numerical and experimental force-deflection curves for beam S1D18a108, S1&2D36a108, S1D72a108, S2D36a72 and S2D36a36 .....	62
Figure 4.12 – Experimental and numerical shear strength $\tau = P/2td$ ( $P = 2V$ ) for varying a/d-ratios for different shear retention models .....	63
Figure 4.13 – Force-deflection plot for the experiment and varying crack models for beam S1D18a108.....	64
Figure 4.14 – Crack width formation after failure for the fully rotating crack model for beam S1D18a108.....	65
Figure 4.15 – Force-deflection plot for the experiment and varying crack models for beam S1&2D36a108.....	67
Figure 4.16 – Reestablishment of crack pattern reflected in the force-deflection curve ..	68
Figure 4.17 – Force-deflection plot for the experiment and varying crack models for beam S1D72a108.....	69
Figure 4.18 – Force-deflection plot for the experiment and varying crack models for beam S2D36a72 .....	70
Figure 4.19 – Crack strain plots for A) fully fixed damage based model and B) fully rotating crack model just before failure for beam S2D36a72 .....	71
Figure 4.20 – Force-deflection plot for the experiment and varying crack models for beam S2D36a36 .....	72
Figure 4.21 – Capacity comparison (left) and a capacity deviation diagram (right) between numerical and experimental results for the crack model analysis .....	74
Figure 4.22 – Experimental and numerical shear strength $\tau = P/2td$ ( $P = 2V$ ) for varying a/d-ratios for different crack models .....	75
Figure 4.23 – Non-converged load steps presented as percentage (bar) and in numbers (numbers above bar) for each analysis for each beam.....	76
Figure 4.24 – The concrete stress (SXX) in the longitudinal direction plotted along the dashed line just above the reinforcement. This is plotted on top of the crack strain for the beam S1D18a108 with the aggregate shear retention model analyzed in chapter 4.1.1. The left scale holds the unit of measurement N/mm <sup>2</sup> . The horizontal and vertical beam aspect ratio is not correct. ....	77
Figure 4.25 – The concrete stress (SXX) in the longitudinal direction plotted along the beam cut-off. This is plotted on top of the crack strain for the beam S1D18a108 with the aggregate shear retention model analyzed in chapter 4.1.1. The underneath scale holds the unit of measurement N/mm <sup>2</sup> . The horizontal and vertical beam aspect ratio is not correct. ....	77
Figure 4.26 – Crack strain plot before the crack localizes for the damage based shear retention model in beam S1D18a108 .....	78
Figure 4.27 – Output file logging for step 10 and 11 in the damage based shear retention model in beam S1D18a108.....	79
Figure 4.28 – Force-deflection plot for the experiment and numerical models with and without tension stiffening for beam S1D18a108.....	80
Figure 4.29 – The crack strain pattern A) without and B) with tension stiffening after failure for beam S1D18a108 .....	80
Figure 4.30 – Force-deflection plot for the experiment and numerical models with and without tension stiffening for beam S1&2D36a108.....	81

Figure 4.31 – The crack strain pattern A) without and B) with tension stiffening after failure for beam S1&2D36a108 .....	82
Figure 4.32 – Force-deflection plot for the experiment and numerical models with and without tension stiffening for beam S1D72a108.....	83
Figure 4.33 – The crack strain pattern for the A) experimental, B) without, and C) with tension stiffening after failure for beam S1D72a108.....	84
Figure 4.34 – Force-deflection plot for the experiment and numerical models with and without tension stiffening for beam S2D36a72 .....	85
Figure 4.35 – The crack strain pattern with tension stiffening after failure for beam S1D72a108, where large cracks develop in the tension stiffening zone .....	86
Figure 4.36 – Force-deflection plot for the experiment and numerical models with and without tension stiffening for beam S2D36a36 .....	86
Figure 4.37 – The reinforcement stress plot SXX with local yielding plotted alone (upper figure) and together with the respective crack strain plot (lower figure). The legend to the right only represents the reinforcement stress SXX. ....	87
Figure 4.38 – Poisson’s effect of compressive strut (left) where the arrows illustrate the strain directions and a free body diagram of the end support region cut out at an inclined crack (right) where the arrows illustrate the forces .....	88
Figure 4.39 – Capacity comparison (left) and a capacity deviation diagram (right) between the numerical and experimental results for the tension stiffening analysis.....	89
Figure 4.40 – Crack pattern comparison at failure of the fixed, damage based shear retention model without tension stiffening and the experiment .....	90
Figure 4.41 – Experimental and numerical shear strength $\tau = P/2td$ ( $P = 2V$ ) for varying a/d-ratios for the damage based model with and without tension stiffening .....	91
Figure A.1 – Four-noded isoparametric plane stress element (DIANA TNO, 2020) .....	100
Figure A.2 – Model setup for compression and tension validation test.....	100
Figure A.3 – Parabolic compression response with secant unloading and reloading.....	101
Figure A.4 – Hordijk tensile response with secant unloading and reloading.....	102
Figure A.5 – Model setup for validation of compressive reduction due to lateral cracking .....	103
Figure A.6 – Compressive behaviors for different lateral strain values .....	103
Figure A.7 – Analytical vs. numerical plots of the lateral reduction of compressive strength .....	104
Figure A.8 – Model setup for shear retention tests .....	105
Figure A.9 – A comparison of shear retention models for different tensile strain values for the damage based, Al-Mahaidi and aggregate based shear retention model .....	105
Figure A.10 – Reduction factor $\beta$ as a function of the total normal strain $\epsilon_{nn}$ for the damage based, Al-Mahaidi, and aggregate based shear retention model.....	106
Figure A.11 – Model setup for confinement test.....	107
Figure A.12 – Compressive behaviors for different ratios of confinements .....	108
Figure B.1 – Uncracked cross section (Øverli, 2016) .....	112
Figure B.2 – Moment diagrams of the unit load and the external loading .....	113
Figure C.1 – Crack pattern at failure for beam S1D18a108 (Suchorzewski et al., 2018) .....	116
Figure C.2 – Crack pattern at failure for beam S1&2D36a108 (Suchorzewski et al., 2018) (critical crack is marked in red) .....	116
Figure C.3 – Crack pattern at failure for beam S1D72a108 (Suchorzewski et al., 2018) (critical crack is marked in red) .....	117

Figure C.4 – Crack pattern at failure for beam S2D36a72 (Suchorzewski et al., 2018), where A) failed in tension shear and B) failed in compression shear. (critical crack is marked in red) .....	117
Figure C.5 – Crack pattern at failure for beam S2D36a36 (Suchorzewski et al., 2018) (critical crack is marked in red) .....	117
Figure C.6 – Crack plot specification for shear retention models for beam S1D18a108.	118
Figure C.7 – Crack strain plots beam S1D18a108, damage based .....	118
Figure C.8 – Crack strain plots beam S1D18a108, Al-Mahaidi.....	119
Figure C.9 – Crack strain plots beam S1D18a108, aggregate based .....	119
Figure C.10 – Crack plot specification for shear retention models for beam S1&2D36a108 .....	120
Figure C.11 – Crack strain plots beam S1&2D36a108, damage based .....	121
Figure C.12 – Crack strain plots beam S1&2D36a108, Al-Mahaidi .....	122
Figure C.13 – Crack strain plots beam S1&2D36a108, aggregate based .....	123
Figure C.14 – Crack strain plot specification for shear retention models for beam S1D72a108.....	124
Figure C.15 – Crack strain plots beam S1D72a108, damage based .....	125
Figure C.16 – Crack strain plots beam S1D72a108, Al-Mahaidi .....	126
Figure C.17 – Crack strain plots beam S1D72a108, aggregate based .....	127
Figure C.18 – Crack plot specification for shear retention models for beam S2D36a72	128
Figure C.19 – Crack strain plots beam S2D36a72, damage based .....	128
Figure C.20 – Crack strain plots beam S2D36a72, Al-Mahaidi.....	129
Figure C.21 – Crack strain plots beam S2D36a72, aggregate based .....	130
Figure C.22 – Crack plot specification for shear retention models for beam S2D36a36	131
Figure C.23 – Crack strain plots beam S2D36a36, damage based .....	132
Figure C.24 – Crack strain plots beam S2D36a36, Al-Mahaidi.....	133
Figure C.25 – Crack strain plots beam S2D36a36, aggregate based .....	134
Figure C.26 – Crack plot specification for crack models for beam S1D18a108 .....	135
Figure C.27 – Crack strain plots beam S1D18a108, fully fixed .....	135
Figure C.28 – Crack strain plots beam S1D18a108, rotating to fixed – threshold at half full crack .....	136
Figure C.29 – Crack strain plots beam S1D18a108, rotating to fixed – threshold at fully developed crack .....	136
Figure C.30 – Crack strain plots beam S1D18a108, rotating to fixed – threshold at 5*fully developed crack .....	137
Figure C.31 – Crack strain plots beam S1D18a108, fully rotating.....	137
Figure C.32 – Crack strain plot specification for crack models for beam S1&2D36a108	138
Figure C.33 – Crack strain plots beam S1&2D36a108, fully fixed .....	139
Figure C.34 – Crack strain plots beam S1&2D36a108, rotating to fixed – threshold at half full crack .....	140
Figure C.35 – Crack strain plots beam S1&2D36a108, rotating to fixed – threshold at fully developed crack .....	141
Figure C.36 – Crack strain plots beam S1&2D36a108, rotating to fixed – threshold at 5*fully developed crack.....	142
Figure C.37 – Crack strain plots beam S1&2D36a108, fully rotating .....	143
Figure C.38 – Crack strain plot specification for crack models for beam S1D72a108 (the crack plot extractions are marked as dots for better visibility) .....	144
Figure C.39 – Crack strain plots beam S1D72a108, fully fixed.....	145
Figure C. 40 – Crack strain plots beam S1D72a108, rotating to fixed – threshold at half full crack .....	146
Figure C.41 – Crack strain plots beam S1D72a108, rotating to fixed – threshold at fully developed crack .....	147

Figure C.42 – Crack strain plots beam S1D72a108, rotating to fixed – threshold at 5*fully developed crack .....	148
Figure C.43 – Crack strain plots beam S1D72a108, fully rotating.....	149
Figure C.44 – Crack plot specification for crack models for beam S2D36a72 .....	150
Figure C.45 – Crack strain plots beam S2D36a72, fully fixed.....	150
Figure C.46 – Crack strain plots beam S2D36a72, rotating to fixed – threshold at half full crack .....	151
Figure C.47 – Crack strain plots beam S2D36a72, rotating to fixed – threshold at fully developed crack .....	151
Figure C.48 – Crack plots strain beam S2D36a72, rotating to fixed – threshold at 5*fully developed crack .....	152
Figure C.49 – Crack strain plots beam S2D36a72, fully rotating .....	152
Figure C.50 – Crack strain plot specification for crack models for beam S2D36a36 (the crack plot extractions are marked as dots for better visibility) .....	153
Figure C.51 – Crack strain plots beam S2D36a36, fully fixed.....	154
Figure C.52 – Crack strain plots beam S2D36a36, rotating to fixed – threshold at half full crack .....	155
Figure C.53 – Crack strain plots beam S2D36a36, rotating to fixed – threshold at fully developed crack .....	156
Figure C.54 – Crack strain plots beam S2D36a36, rotating to fixed – threshold at 5*fully developed crack .....	157
Figure C.55 – Crack strain plots beam S2D36a36, fully rotating .....	158
Figure C.56 – Crack plot specification with and without tension stiffening for beam S1D18a108.....	159
Figure C.57 – Crack strain plots for beam S1D18a108, damage based without tension stiffening .....	159
Figure C.58 – Crack strain plots for beam S1D18a108, damage based with tension stiffening .....	160
Figure C.59 – Crack plot specification with and without tension stiffening for beam S1&2D36a108.....	160
Figure C.60 – Crack strain plots for beam S1&2D36a108, damage based without tension stiffening .....	161
Figure C.61 – Crack strain plots for beam S1&2D36a108, damage based with tension stiffening .....	162
Figure C.62 – Crack plot specification with and without tension stiffening for beam S1D72a108.....	163
Figure C.63 – Crack strain plots for beam S1D72a108, damage based without tension stiffening .....	164
Figure C.64 – Crack strain plots for beam S1D72a108, damage based with tension stiffening .....	165
Figure C.65 – Crack plot specification with and without tension stiffening for beam S2D36a72 .....	166
Figure C.66 – Crack strain plots for beam S2D36a72, damage based without tension stiffening .....	166
Figure C.67 – Crack strain plots for beam S2D36a72, damage based with tension stiffening (The figures are not the same, even though they are very similar) .....	167
Figure C.68 – Crack plot specification with and without tension stiffening for beam S2D36a36 .....	167
Figure C.69 – Crack strain plots for beam S2D36a36, damage based without tension stiffening .....	168
Figure C.70 – Crack strain plots for beam S2D36a36, damage based with tension stiffening .....	169

# List of Tables

Table 3.1 – Constitutive model for concrete .....36

Table 3.2 – Kinematic assumptions concrete .....36

Table 3.3 – Concrete material properties for each series.....36

Table 3.4 – Constitutive model for reinforcement steel .....38

Table 3.5 – Kinematic assumptions reinforcement .....38

Table 3.6 – Kinematic and constitutive assumptions for reinforcement bond interface elements .....38

Table 3.7 – Bond-slip conditions .....39

Table 3.8 – Kinematic and constitutive assumptions for support and loading plate interface elements .....39

Table 3.9 – Equilibrium control .....40

Table 3.10 – Threshold total normal strain values for different beams .....43

Table 3.11 – Tension stiffening zones, Maekawa compared to the Eurocode. ....44

Table 4.1 – Summary of chapter 4.1 – The influence of varying shear retention models 60

Table 4.2 – Summary of chapter 4.2 – The influence of varying crack models .....73

Table 4.3 – Summary of chapter 4.3 – The influence of tension stiffening .....88

Table B.1 – Calculation of threshold strain value in the rotating to fixed crack model ..109

Table B.2 – Calculation of tension stiffening zone .....111

Table B.3 – Analytical, numerical, and experimental initial stiffness .....114

Table B.4 – Deflection at crack initiation .....115



# 1 Introduction

A linear finite element analysis (LFEA) provides relatively fast and easy procedures with low-cost analyses, in addition to the possibility of super positioning several load cases. Hence, LFEA has appealing features in a design case. However, LFEA cannot realistically represent reinforced concrete, as the behavior of this composite material is dominated by nonlinear properties. Examples of such properties are concrete cracking, reinforcement yielding, bond-slip between the reinforcement and the concrete, and even internal bond failure between the concrete mortar and aggregate. Thereby, nonlinear finite element analysis (NLFEA) has the potential to give a more realistic representation of the structural behavior in reinforced concrete than what is possible with a LFEA. Note the formulation “has the potential”. This wording is used because the amount of expertise needed to perform an analysis drastically increases when switching from a linear to a nonlinear approach. It requires an understanding of the numerical nonlinear procedure itself, but also a deeper understanding of the material in use and how the material properties are converted into numerical formulations.

In the early 2000’s, Frank Vecchio addressed a number of uncertainties when performing NLFEA (Vecchio, 2001). Amongst these was the fact that any approach will be more suited to certain structure/loading situations and less so to others, and that no approach would perform well over the entire range of structural details and loading conditions encountered in practice. Since then, research papers and guidelines have been published which have addressed advantages and disadvantages of the modelling options one may encounter in the process of creating a nonlinear numerical model. This has made it easier, and possibly less dangerous for engineers (who are not experts in NLFEA) to perform these types of analyses. Ideally, there would have been a unified solution procedure which gave accurate results for all types of structures. This might be difficult to obtain, however, this idea sets the foundation for this thesis.

In 2018 an experimental study on reinforced concrete beams without shear reinforcement was performed (Suchorzewski et al., 2018). The beams were scaled independently along either height or length, leaving a total of five different beam geometries. Also, experimental tests on beams of similar geometry and concrete mixture were repeated, which increased the reliability of the experimental results. As the beam geometries varied, different failure mechanisms, such as flexural, tension shear and compression shear failure, were obtained. In addition, the scaling of the beams also introduced the size effect to the behavior and capacity of the beams. In this thesis, the main objective is to investigate if it is possible to obtain sufficient and good results with one nonlinear solution procedure for the five beam geometries in Suchorzewski’s experiment.

Numerical simulations of the experiment has in fact already been carried through by, amongst others, the authors of the experiment (Suchorzewski et al., 2018; Marzec et al., 2019). In these simulations an elasto-plastic damage model was used, enhanced by non-local softening, performed in Abaqus. In order to obtain the information needed to utilize the non-local softening, they used the UMAT subroutine. The numerical results were very good, however, the methods that were used exceeds the scope of this thesis, mainly because it was not completely performed with pre-existing options provided from the analyze software itself. Hence, the analyses in this thesis will not use non-local softening. Furthermore, a smeared, total-strain based crack model will be the basis in all analyses. With these limitations, the research question becomes:

*To which extent can a unified solution procedure simulate reinforced concrete beams without shear reinforcement with varying shear span to effective depth ratio with different sizes based on local material models?*

The analyses done in this thesis can be sub-divided into three categories. First, the investigation of an appropriate shear retention model was carried through. This implies that only the total-strain based fixed crack model was used. Within these analyses, three shear retention models were examined, namely the damage based model, the Al-Mahaidi model and the aggregate based model. Second, the effect of different crack models were examined. This included the fixed and rotating crack model, but also a relatively new hybrid model, namely, the rotating to fixed crack model. Finally, the effect of tension stiffening was analyzed. Hence, three sub-questions shall also be answered. These are formulated as follows:

*What is the influence of varying shear retention models?*

*What is the influence of varying crack models?*

*What is the influence of tension stiffening?*

DIANA FEA is the software program which is used to perform the analyses in this thesis. DIANA is a multi-purpose finite element software package that is dedicated to a wide range of applications in civil engineering and has a large number of options concerning reinforced concrete.

This thesis attempts to enable understanding of the modelling choices that were made, and why they were made. Thereby, a theory chapter, presenting the theoretical background for the modelling choices is first presented. Then, a modelling chapter, which has the purpose of giving the reader an overview of exactly which modelling choices that was made throughout the analyses. Results and discussion are then presented, before the conclusion and suggestions to further work. Finally, the information and calculations in the appendix is meant to work as additional support to the arguments and discussions in the thesis. In that case, the relevant chapter in the appendix will be referred to.

# 2 Theory and Methods for Nonlinear Finite Element Analysis of Reinforced Concrete Structures

This chapter explains the theory behind the modelling choices that were done in this thesis. The analyses were performed in DIANA, which is a finite element analysis program with a great number of opportunities for modelling reinforced concrete.

Chapter 2.1 and Chapter 2.2 contains information about finite element analysis in general, and information about the NLFEA. Chapter 2.3 and Chapter 2.4 describes the material behavior models of plain and reinforced concrete selected in DIANA, including comments on how these models may relate to physical reality. Chapter 2.5 describes the different crack models used, Chapter 2.6 discuss the different failure modes obtained in the experiment and analyses and Chapter 2.7 briefly discuss the size effect.

In this thesis, the total-strain based crack model was used. This includes that uniaxial material models are modelled with explicitly specified biaxial effects. Some of the uniaxial and biaxial effects were also tested in a simple validation test, presented in Appendix A.

## 2.1 Finite Element Analysis

Finite element analysis (FEA) is a method to solve field problems numerically (Cook et al., 2001). FEA is solved by discretizing a body into a finite number of elements. The behavior of these elements are described by a stiffness matrix. The elements are connected at the nodes by enforcing compatibility and equilibrium. Boundary conditions must also be applied. The resulting set of simultaneous algebraic equations are solved with respect to the displacements.

### 2.1.1 Elements

2D plane stress elements can be used to limit the calculation time. Due to problems such as parasitic shear, volumetric locking and incompatible strain concepts when using linearly interpolated isoparametric elements in nonlinear analyses, DIANA recommends using higher order elements. In this case, the eight-noded quadrilateral isoparametric plane stress element was used. It is based on quadratic interpolation and Gauss integration. By default, DIANA applies 2x2 integration which yields optimal stress points (DIANA TNO, 2020).

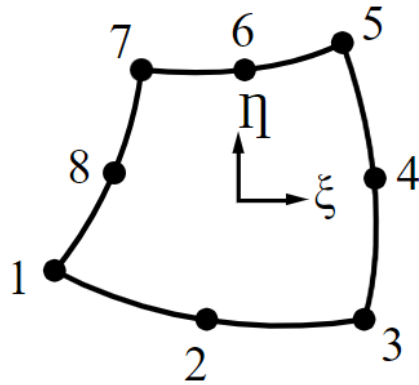


Figure 2.1 – 8-noded quadrilateral isoparametric plane stress element (DIANA TNO,2020)

The interface element between the load/support steel-plates and the concrete was the 3+3, 2D line element. This is an interface element between two lines in a 2D configuration. It uses quadratic interpolation and a 3-point Newton-Cotes integration scheme.

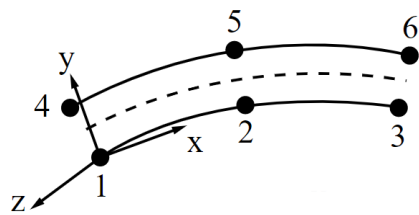


Figure 2.2 – 3+3-noded 2D line element (DIANA TNO, 2020)

If the user chooses a beam or truss element representation of reinforcement in DIANA, independent elements and corresponding interface elements are established to reflect the reinforcement and bond-slip between the steel and concrete. This is in contrast to an embedded element formulation of the reinforcement, where the reinforcement is added through increasing the stiffness in the mother element. Hence, the reinforcement strain will always be the same as strain in the surrounding elements and thereby this formulation assumes full interaction between the concrete and the reinforcement bars. In this thesis, beam elements were selected to represent the reinforcement. The element was a three-node, 2D class-III beam element, with quadratic interpolation and 2-point Gauss integration.

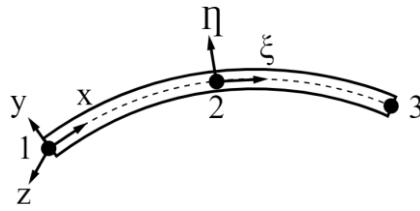


Figure 2.3 – 3-noded 2D class-III beam element (DIANA TNO, 2020)

The corresponding interface element is an 11-node 2D line element. The element is an interface element between quadratic line and quadratic quadrilateral plane element in a 2D configuration. The element is based on quadratic interpolation and uses a 3-point Newton-Cotes integration scheme in the longitudinal direction.

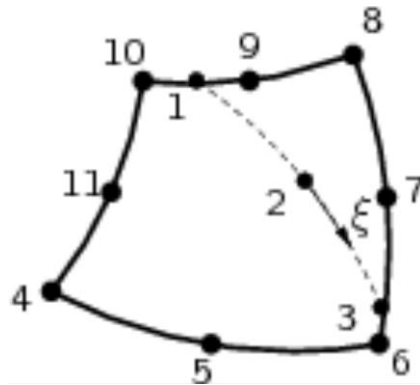


Figure 2.4 – 11-noded 2D line element (DIANA TNO, 2012)

## 2.2 Nonlinear Finite Element Analysis

Nonlinearities in structural mechanics can be:

- Material nonlinearity, as nonlinear elasticity, plasticity, and creep.
- Contact nonlinearity, which concerns the gaps of adjacent parts opening or closing.
- Geometrical nonlinearity, which regards how large deformations might change structural equilibrium equations and load directions.

The problems in these categories are nonlinear because stiffness, and perhaps loads become functions of the displacement or deformation. Thus, the linear stiffness, displacement and force relation can no longer be solved in a direct one-step procedure (Cook et al., 2001). The following chapters (Chapter 2.2.1 – Chapter 2.2.6) explain matters as the incremental procedure, iterative method, convergence criteria and additional solution-improving techniques. These are all important to obtain a nonlinear solution.

However, the options are many and only the methods and procedures used in the analyses of this thesis will be of focus.

### 2.2.1 Incremental-Iterative Solution Procedure

In a NLFEA, the relation between the force and displacement vector is no longer linear. As for the linear analysis, the goal in a nonlinear analysis is to find a displacement vector that obtains equilibrium between internal and external forces. However, in contrast to the LFEA, this is not a one-step procedure. The incremental-iterative solution procedure enables a numerical solution of nonlinear problems. This includes that the total external load is divided into a number of increments. To ensure equilibrium at the end of each increment, an iterative solution algorithm may be used. In principal, the equilibrium solution to a nonlinear problem could be solved with one total load increment, however, doing that has some important drawbacks. The first and most obvious drawback is that it is difficult to iterate through very large load steps when the solution consists of strong nonlinearities, and if the iteration process actually does find a solution, information of the structural behavior will be very limited. In addition to this, the internal force vector might also depend on the displacement in the history. This would be the case if the material is path-dependent, which means that different stress levels can be obtained for different strain paths. Hence, the incremental-iterative solution method has several advantages.

### 2.2.2 Incremental Procedure

In this thesis, a displacement controlled incremental procedure was used. This means that load was applied to the structure by prescribing certain displacements. The alternative is to use the load controlled incremental procedure, where a certain load intensity is applied at each load step. In the case of the displacement controlled increment procedure, the external force vector is not increased directly, but will be calculated through the stresses caused by the induced displacement (DIANA TNO, 2020).

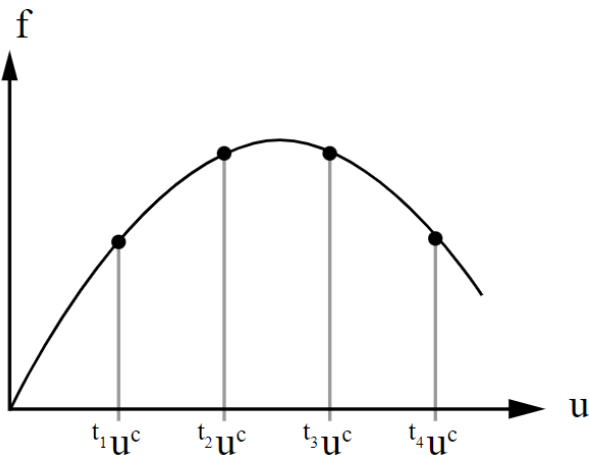


Figure 2.5 – Displacement controlled incremental procedure (DIANA TNO, 2020)

The use of a displacement controlled incremental procedure was motivated by the fact that the experiment that was analyzed also inflicted the load through displacement-controlled conditions (Suchorzewski et al., 2018). Furthermore, this method is often more stable than the load controlled procedure (Hendriks and Roosen, 2019). However, the displacement control restricts the displacement of a point to a prescribed value. This means that the dead weight and also asymmetric displacement in the case of multiple loads are restrained. Nevertheless, the influence of dead weight was assumed to be neglectable compared to the applied load. A quick check of this was done by multiplying the concrete volume of the experimental beam with the lowest capacity with a reinforced concrete density of  $2500 \text{ kg/m}^3$ , giving a dead weight of just below 4% of the applied load (in the most critical case of the five beams). Furthermore, the asymmetry was also not considered as the analyses were performed on half beams with symmetry boundary conditions.

### 2.2.3 Iterative Method

The regular Newton-Raphson iteration method was utilized. This method evaluates the stiffness matrix at every iteration and yields a quadratic convergence rate. This means that it in general finds convergence with only a few iterations. However, a new stiffness matrix is created at every iteration which makes each iteration relatively time consuming (DIANA TNO, 2020).

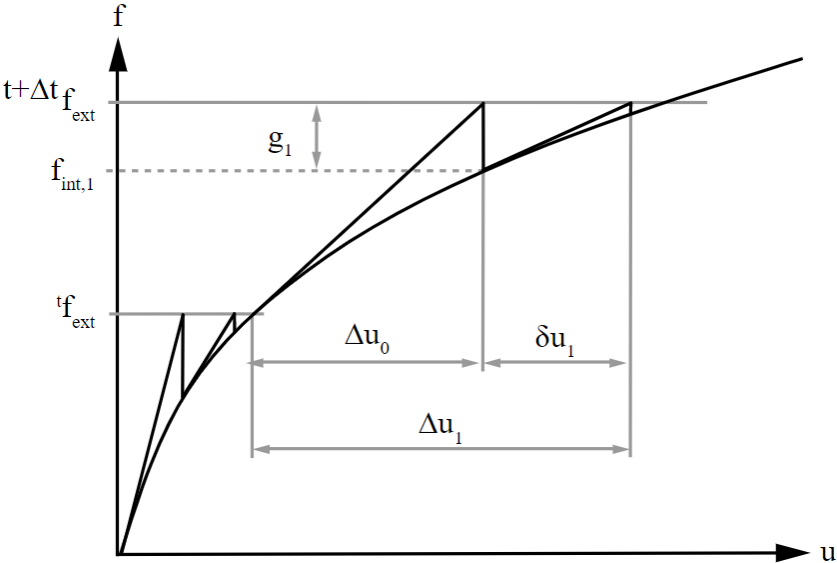


Figure 2.6 – Regular Newton-Raphson iteration method (DIANA TNO, 2020)

Figure 2.6 shows regular Newton-Raphson iterations for two load increments. The basic procedure can be described as following:

1. Start increment with increasing the external load,  $f_{ext}^{t+\Delta t}$ .
2. Calculate the tangent stiffness,  $K_t^{i+1} = K_t^i + \frac{dK}{du} \Delta u^i$
3. Estimate the new displacement,  $\Delta u^{i+1} = \Delta u^i + \frac{f_{ext}^{t+\Delta t} - f_{int}^i}{K_t^{i+1}}$
4. Estimate the secant stiffness using the estimated displacement,  $K^{i+1} = K(\Delta u^{i+1})$
5. Use the secant stiffness to estimate the internal force,  $f_{int}^{i+1} = K^{i+1} \Delta u^{i+1}$
6. Estimate the out-of-balance force,  $g^{i+1} = f_{ext}^{t+\Delta t} - f_{int}^{i+1}$
7.  $g^{i+1} > tolerance \rightarrow$ Back to step 2,  $g^{i+1} \leq tolerance \rightarrow$ End increment

In step 2 in the above procedure, a new tangent stiffness is evaluated, and this is done every time a new iteration is carried through, as seen in step 7. This is in contrast to the modified Newton-Raphson method which would go back to step 3, meaning that the recalculation of the tangent stiffness would only be done at every new increment.

## 2.2.4 Arc Length Method with Indirect Displacement Control

The arc length control was applied in the analyses. This method is especially important for a load controlled incremental procedure, as this would result in very large predictions for the displacement when the load-displacement curve exhibits a so-called snap-through behavior, which includes horizontal curves. As explained in Chapter 2.2.2, we use a displacement controlled incremental procedure. However, the arc-length method is also important when applying the load as a prescribed deformation because the method is able to capture snap-back behavior, where the displacement controlled incremental procedure alone fails.

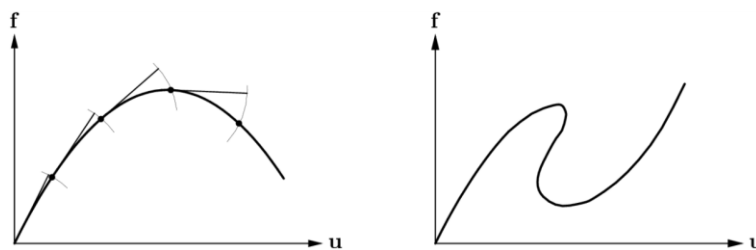


Figure 2.7 – Snap-through and snap-back behavior (DIANA TNO,2020)

The basic idea behind the arc length methods is that both load and displacement increments are modified during the iterations. Within the arc-length method, one must choose whether to use the spherical path or updated normal plane. In this case, the spherical path was selected, which means that the iterations are confined to the surface of a hypersphere.

Furthermore, indirect displacement control was utilized. By default, in DIANA, all displacements are included in the calculation of the arc length. Such strategy is adequate for analysis models with global failure behaviors, but for structures that fail locally, which are typical for concrete structures, the arc-length method can perform better if only a part

of the displacements are considered in the calculation. Hence, this constraint was applied to the node which showed most displacement in a linear-elastic analysis.

### 2.2.5 Line Search

Line search improves the convergence rate and is especially useful if the ordinary iteration process fails. The ordinary predictions might be far from equilibrium when strong nonlinearities as concrete cracking occurs (DIANA TNO, 2020).

The line search algorithm uses a prediction of the iterative displacement increment obtained by the ordinary iteration algorithm and scales this by a value to minimize the energy potential. To determine an optimal magnification factor, the incremental displacement vector,  $\Delta u_{i+1}$ , is calculated from a scaled iterative increment:

$$\Delta u_{i+1} = \Delta u_i + \eta \delta u_{i+1} \tag{2.1}$$

where  $\delta u_{i+1}$  is derived from the selected iteration method. A minimum value of the potential energy requires that the derivation of the potential energy with respect to the scaling factor,  $\eta$ , is equal to zero:

$$s(\eta) = \frac{\partial \Pi}{\partial \eta} = \frac{\partial \Pi}{\partial u} \frac{\partial u}{\partial \eta} = g(\eta)^T \delta u = 0 \tag{2.2}$$

Eq. (2.2) can be satisfied by calculating  $s$  at various values of  $\eta$ . The two first values are derived from the original iteration process. Once the search direction is calculated, the values  $s(0)$  and  $s(1)$  are calculated by the inner product of  $\delta u$  with the out-of-balance force at the start and the end of the iteration (DIANA TNO, 2020).

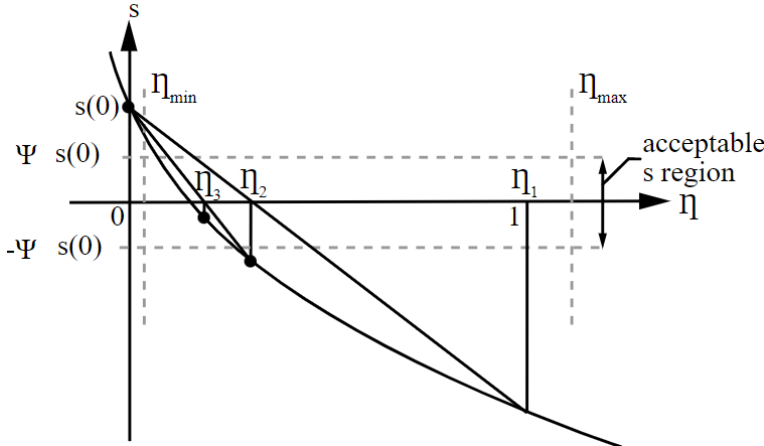


Figure 2.8 – Line search iteration (DIANA TNO, 2020)

## 2.2.6 Convergence Criteria

The convergence criteria is the selected criteria for which the iteration process stops. The stopping criteria consists of two parts. That is, if convergence, or if a maximum number of iterations is reached. Both of these must be specified by the user. In this thesis, the energy norm was used to detect convergence. This norm is composed of internal forces and the relative displacements, and can be denoted as follows:

$$\text{Energy norm ratio} = \left| \frac{\delta u_i^T (f_{int}^{i+1} + f_{int}^i)}{\Delta u_0^T (f_{int}^1 + f_{int}^0)} \right| \quad (2.3)$$

Note that the internal force is used and not the out-of-balance force. The reason for this is that use of the out-of-balance force would be improper as the line search procedure could then minimize the norm before the solution really converges to equilibrium.

## 2.3 Plain Concrete Characteristics

Concrete behavior can be modelled in a diverse number of ways, including models based on nonlinear elasticity, plasticity, fracture mechanics, damage continuum mechanics and others (Vecchio, 2001). A common way of selecting material models for concrete is to use a uniaxial material model as basis, extended with additional models that take other material effects into account, such as the effects of confinement and lateral cracking. (Engen, 2017). This is the case for the total-strain based crack model in DIANA. The total-strain based crack model describes the tensile and compressive behavior of a material with one stress-strain relationship and describe the cracking and crushing of concrete with a nonlinear elasticity relation. However, the model is not hypo-elastic, as the unloading and reloading follows the secant stiffness (DIANA TNO, 2020). Furthermore, the biaxial effects are explicitly added by the user.

In this chapter, concrete characteristics and how these are modelled through the total-strain based crack model in DIANA are investigated and elaborated. As DIANA provides several different models concerning the material behavior of concrete, only the models used in the numerical analyses in this thesis were in focus.

### 2.3.1 Tension Behavior

Initially, the stress-strain curve in tension acts almost linearly. In normal strength concrete the cracking process will start as debonding or expanding existing micro cracks in the cement paste at approximately 80% of the peak load. When the peak load is reached, a large amount of micro cracks will localize in a narrow zone and eventually split the specimen in two. Thus, a macro crack is formed. This zone (fracture process zone, FPZ) will probably develop in the weakest part of the specimen (Ulfkjær, 1992). This behavior is known as strain localization. The irreversible strain in the concrete, that takes place before the peak stress is reached, can be neglected when comparing it to the crack opening

displacement. Hence, the uncracked concrete material can be treated in a linear elastic manner (Reinhardt et al., 1986).

Experiments show a post-peak stress-strain relation which is not completely brittle, but rather exhibit a nonlinear decreasing behavior (Reinhardt et al., 1986; Chen and Su, 2013). This phenomenon is known as tension softening. In addition to fitting the experimental results, a softening behavior will also lead to numerical stability, in contrast to a fully brittle response. However, it is questioned whether the softening behavior is in fact a plain concrete property, or if it is a result of the experimental testing method (Kostovos and Pavlović, 1995).

In this thesis, the Hordijk tension softening model was used. This model is governed by the fracture energy and a crack bandwidth. The mode I fracture energy will be released in an element once the tensile strength is violated. The mode I fracture energy equals to the area under the normal stress-strain crack opening diagram. To accommodate the smeared cracking framework, which is described in Chapter 2.5, the stress-strain crack opening relation must be transformed into the average stress-average strain relation. This can be done by geometrically relating the crack opening to the average strain of the element over the specified reference length. Physically, this is equivalent to smearing the discrete fracture localization over a reference domain. This reference length can be conveniently assumed to be equal to the element dimension (Maekawa et al., 2003). With this approach, a mesh independent procedure is fulfilled. It can be useful to have a look on how this is implemented in DIANA, before considering the actual softening model. First, the relation between the crack stress  $\sigma_{nn}^{cr}$  and the crack strain  $\varepsilon_{nn}^{cr}$  in the normal direction can be written as:

$$\sigma_{nn}^{cr}(\varepsilon_{nn}^{cr}) = f_t \times y\left(\frac{\varepsilon_{nn}^{cr}}{\varepsilon_{nn.ult}^{cr}}\right) \quad (2.4)$$

where  $f_t$  is the tensile strength and  $\varepsilon_{nn.ult}^{cr}$  is the ultimate crack strain. The general function  $y(\dots)$  represents the actual softening diagram. If the softening behavior on the constitutive level is related to the mode I fracture energy  $G_f^I$  through an equivalent length or crack bandwidth denoted as  $h$ , it can be derived as:

$$G_f^I = h \int_{\varepsilon_{nn}^{cr}=0}^{\varepsilon_{nn}^{cr}=\infty} \sigma_{nn}^{cr}(\varepsilon_{nn}^{cr}) d\varepsilon_{nn}^{cr} \quad (2.5)$$

In short, the above equation is the area under the stress-strain curve multiplied with the crack bandwidth. If we combine eq. (2.4) and eq. (2.5) we get:

$$G_f^I = hf_t \int_{\varepsilon_{nn}^{cr}=0}^{\varepsilon_{nn}^{cr}=\infty} y\left(\frac{\varepsilon_{nn}^{cr}}{\varepsilon_{nn.ult}^{cr}}\right) d\varepsilon_{nn}^{cr} \quad (2.6)$$

with the assumption that  $f_t$  is constant. Change from the variable  $\varepsilon_{nn}^{cr}$  to:

$$x = \frac{\varepsilon_{nn}^{cr}}{\varepsilon_{nn.ult}^{cr}} \quad (2.7)$$

and consequently  $d\varepsilon_{nn}^{cr}$  to  $\varepsilon_{nn.ult}^{cr} dx$ , the obtained relation becomes:

$$G_f^I = hf_t \left( \int_{x=0}^{x=\infty} y(x) dx \right) \varepsilon_{nn.ult}^{cr} \quad (2.8)$$

If we set  $\int_{x=0}^{x=\infty} y(x) dx = \alpha$  the final expression is noted as:

$$\varepsilon_{nn.ult}^{cr} = \frac{1}{\alpha} \times \frac{G_f^I}{hf_t} \quad (2.9)$$

The ultimate strain  $\varepsilon_{nn.ult}^{cr}$  is assumed to be constant during the analysis and is a material property calculated from the tensile strength  $f_t$ , the fracture energy  $G_f^I$ , and the element area represented by the equivalent length  $h$ .

Hordijk, Cornelissen and Reinhardt (Cornelissen et al., 1986; Hordijk, 1991) proposed an expression for the softening behavior of concrete which results in a crack stress equal to zero at a crack strain  $\varepsilon_{nn.ult}^{cr}$ .

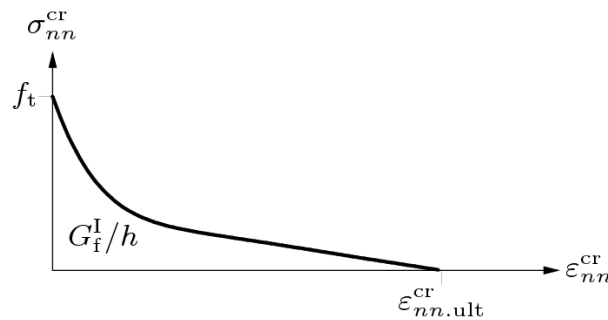


Figure 2.9 – Hordijk tension softening (DIANA TNO, 2020)

For  $0 < \varepsilon_{nn}^{cr} < \varepsilon_{nn.ult}^{cr}$  the relation of the crack stress in the Hordijk softening curve is given by:

$$\frac{\sigma_{nn}^{cr}(\varepsilon_{nn}^{cr})}{f_t} = \left(1 + \left(c_1 \frac{\varepsilon_{nn}^{cr}}{\varepsilon_{nn.ult}^{cr}}\right)^3\right) \exp\left(-c_2 \frac{\varepsilon_{nn}^{cr}}{\varepsilon_{nn.ult}^{cr}}\right) - \frac{\varepsilon_{nn}^{cr}}{\varepsilon_{nn.ult}^{cr}} (1 + c_1^3) \exp(-c_2) \quad (2.10)$$

and for  $\varepsilon_{nn.ult}^{cr} < \varepsilon_{nn}^{cr} < \infty$ :

$$\frac{\sigma_{nn}^{cr}(\varepsilon_{nn}^{cr})}{f_t} = 0 \quad (2.11)$$

The expression for the ultimate strain,  $\varepsilon_{nn.ult}^{cr}$ , can be calculated as:

$$\alpha = \int_{x=0}^{x=\infty} y(x) dx = 0.195 \quad (2.12)$$

which results in an ultimate crack strain of:

$$\varepsilon_{nn.ult}^{cr} = 5.136 \frac{G_f^I}{hf_t} \quad (2.13)$$

To obtain the specific numbers in eq. (2.12) and (2.13), the values  $c_1 = 3$  and  $c_2 = 6.93$  must be used. These constants are implicitly used in DIANA, as the user only specifies the tensile strength,  $f_t$ , and the mode I fracture energy,  $G_f^I$ . The empirical constants  $c_1$  and  $c_2$  were chosen by fitting eq. (2.10) to uniaxial tensile tests (Hordijk, 1991). A simple validation test of the Hordijk tensile curve is presented in Appendix A.1.

It is in fact the rapid decrease of the tensile softening curve that allows the cracks to localize in the smeared crack model. This happens because when a crack appears, the decreasing normal stiffness will release the tension stress in the surrounding elements, allowing for a larger opening in the present crack.

Furthermore, the pre-peak stress-strain behavior is not included here because it simply follows the Young's modulus  $E_c$ , which is assumed similar in tension and compression.

### 2.3.2 Compression Behavior

Due to the heterogeneity of concrete, a uniformly distributed external load can result in a nonuniform distribution of internal stresses and deformations. In addition to this, nonuniformly distributed internal strength and the presence of initial internal stress causes the progressive failure of internal bonds between the mortar and the aggregate as the external load increases. As progressive loading is taking place, a diminishing number of internal bonds are capable of resisting the externally applied load, which will lead to a

gradually weakened material. It can be advantageous to separate the compressive stress-strain curve in plain concrete into three parts. First, when the load stress is ranging from 0-30% of the peak stress, the increase of number and length of cracks in the concrete is negligible, and the concrete show a linear elastic behavior. Nevertheless, there are still preexisting bond cracks. These cracks can be the result of volume changes in the cement paste during hydration, bleeding, and drying shrinkage. Second, with further stress increase, up to about 70-90% of the peak stress, new bond cracks are formed and expand to mortar cracks. The mortar cracks connect the adjacent bond cracks. Third, by inflicting additional stress, more cracks coalesce, and the crack growth becomes unstable. This means that the load must decrease to avoid an uncontrolled crack growth. In contrast, the stable crack growth is taking place before the peak load, which means that they grow only when the load is increased. Softening can be defined as a gradual decrease of mechanical resistance due to a continuous increase of deformation forced upon a material specimen or structure. Hence, softening of the concrete takes place in the post-peak decrease of the mechanical resistance (Vonk, 1992).

DIANA provides several concrete compression models which reflects the physical description of the compression behavior in the above section. One of the many models accessible in DIANA is the parabolic compression curve.

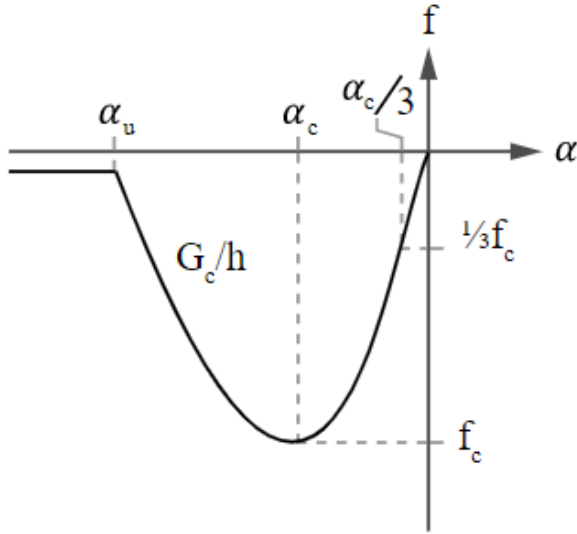


Figure 2.10 – Parabolic compression curve (DIANA TNO, 2020)

The parabolic compression curve consists of four functions depending on the strain level. The curve is linear and follows the elastic modulus  $E_c$ , until one-third of the strain at the maximum compressive strength,  $f_c$ , is reached. That is, for  $\alpha_c/3 < \alpha_j \leq 0$ :

$$f = -f_c \frac{1}{3} \left( \frac{\alpha_j}{\alpha_c/3} \right) \tag{2.14}$$

When  $\alpha_c < \alpha_j \leq \alpha_c/3$ , the function takes the form:

$$f = -f_c \frac{1}{3} \left( 1 + 4 \left( \frac{\alpha_j - \alpha_c/3}{\alpha_c - \alpha_c/3} \right) - 2 \left( \frac{\alpha_j - \alpha_c/3}{\alpha_c - \alpha_c/3} \right)^2 \right) \quad (2.15)$$

and for  $\alpha_u < \alpha_j \leq \alpha_c$ :

$$f = -f_c \frac{1}{3} \left( 1 + \left( \frac{\alpha_j - \alpha_c}{\alpha_u - \alpha_c} \right)^2 \right) \quad (2.16)$$

When  $\alpha_j \leq \alpha_u$  the function is zero or a small user specified residual strength, as illustrated in Figure 2.10. The strain values are calculated as:

$$\alpha_c/3 = -\frac{1}{3} \frac{f_c}{E}; \alpha_c = -\frac{5}{3} \frac{f_c}{E}; \alpha_u = \min \left( \alpha_c - \frac{3}{2} \frac{G_c}{h f_c}, 2.5 \alpha_c \right) \quad (2.17)$$

Hence, the softening part of the curve is governed by the fracture energy,  $G_c$ , and the characteristic element length,  $h$ . This is in contrast to the Thorenfeldt compression curve, which is not regularized with an element length, nor dependent on the fracture energy. This, in addition to not being unit-free, is the reason that it is not advised to use (Hendriks and Roosen, 2019), and is one of the reasons why the parabolic curve were chosen above the Thorenfeldt curve in this thesis. Note that a simple validation test of the parabolic compression curve is performed in Appendix A.1.

As the undamaged, uniaxial compression curve has been defined, further effects can now be included. Namely confinement effects, and reduction due to lateral damage. The confinement effect is related to the increase in both strength and ductility as a result of increasing isotropic stress (DIANA TNO, 2020). Isotropic stress is the result of multi-axial pressure from external loading, which might be denoted as active confinement, or it can be the result of passive confinement, such as stresses arising when the expansion in a specimen due to the Poisson effect is constrained (Deaton, 2013). The latter might be especially relevant for fully exploited structures, as the Poisson's ratio does not stay constant, but in fact increases rapidly as the stress levels approach the ultimate strength (Kostovos and Pavlović, 1995). The confinement effects are shown in experimental tests by, amongst others, van Mier (van Mier et al., 1997), where several tests were done with different concrete mixtures and rate of lateral confinements. The lateral confinement in this experiment was the result of the friction that occurred between the loading plates and the concrete, so-called passive confinement. The confined zones cover a larger part of the concrete specimen as the specimen height/diameter ratio decreases. The experiments showed that the increase of the confinement zones gave both higher ultimate stress and strains. The increase of strength due to increasing isotropic stress is in DIANA expressed

with the Hsieh-Ting-Chen failure surface, which is a four-parameter failure criterion as follows:

$$f = 2.0108 \frac{J_2}{f_{cc}^2} + 0.9714 \frac{\sqrt{J_2}}{f_{cc}} + 9.1412 \frac{f_{c1}}{f_{cc}} + 0.2312 \frac{I_1}{f_{cc}} - 1 = 0 \quad (2.18)$$

where:

$$J_2 = \frac{1}{6} ((\sigma_{c1} - \sigma_{c2})^2 + (\sigma_{c2} - \sigma_{c3})^2 + (\sigma_{c3} - \sigma_{c1})^2) \quad (2.19)$$

and:

$$I_1 = \sigma_{c1} + \sigma_{c2} + \sigma_{c3} \quad (2.20)$$

and finally:

$$f_{c1} = \max(\sigma_{c1}, \sigma_{c2}, \sigma_{c3}) \quad (2.21)$$

$f_{c1}$  is in this case the maximum principal stress. The four-parameter failure criterion was created in hopes of achieving a model which could easily be implemented in finite-element formulations. The parameters in this equation combines the uniaxial tensile and compressive strength, biaxial compressive strength, and experimental data of triaxial tests on concrete specimens. The resulting functional form appears to be a linear combination of three other criteria, namely, the von Mises, the Drucker-Prager and the Rankine's criterion (Hsieh et al., 1982). The stress failure is denoted as  $f_{c3}$  and is determined by scaling the linear elastic stress vector by a factor  $s$ ,  $\sigma_c = sE\varepsilon$  such that eq. (2.18) is satisfied. The compressive failure stress in a multi-axial stress situation is then given by:

$$f_{c3} = s * \min(\sigma_{c1}, \sigma_{c2}, \sigma_{c3}) \quad (2.22)$$

which gives the confined compressive failure strength:

$$f_{cf} = -f_{c3} \quad (2.23)$$

and can also be expressed as:

$$f_{cf} = K_{\sigma} f_{cc} \quad (2.24)$$

where  $K_\sigma$  is the peak stress factor and  $f_{cc}$  is the uniaxial compressive strength. The correspondence between the peak stress factor  $K_\sigma$  and the peak strain factor  $K_\varepsilon$  is discussed by Selby and Vecchio, which claims that the peak strain increases much more rapidly than the peak stress as confining pressure is increased, thus, different factors should be applied (Selby and Vecchio, 1997). However, in DIANA this is simplified, such that:

$$K_\sigma = K_\varepsilon \quad (2.25)$$

In the parabolic compression curve, one can see that the strain formulations are dependent on the compressive  $f_c$  such that the confinement effect will anyway affect the strain and the stress by the same factor. An illustration of the confinement effects are shown in Figure 2.11.

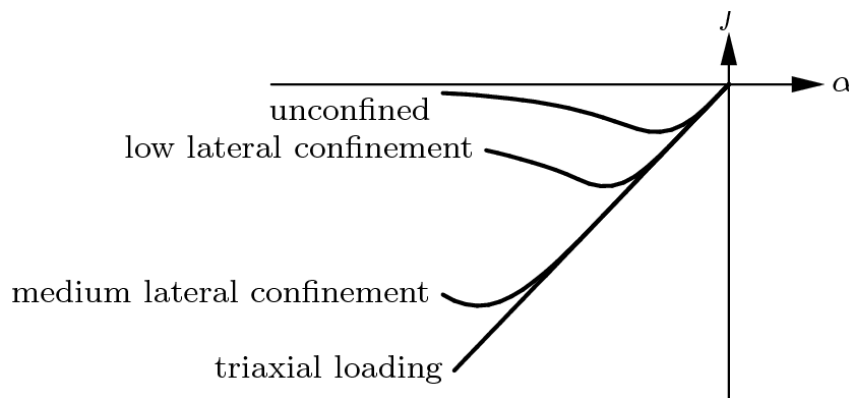


Figure 2.11 – Influence of lateral confinement on the compressive stress-strain curve (DIANA TNO, 2020)

The confinement effect was illustrated in Appendix A.4.

Furthermore, another factor affecting the compression behavior is the lateral cracking. Cracked concrete will have large tensile strains perpendicular to the principal compressive direction, which will reduce the compressive strength. If the material is cracked in the lateral direction, a factor,  $\beta_{\sigma_{cr}}$ , governs the reduction of the the peak stress. These values can be interpret by Vecchio and Collins, or JSCE, where the critical parameter  $\beta_{\sigma_{cr}}$  is dependendt on the lateral cracking. In this thesis, the reduction due to lateral cracking was modelled by the Vecchio and Collins 1993-model (Vecchio and Collins, 1993). The strain parameter  $\beta_{\varepsilon_{cr}}$  is set to 1 in the presented models, which means that the peak strain is not explicitly reduced do to lateral cracking. However, once again, as the strains in the parabolic compression curve formulation are diretly dependent on the compressive

strength, a compressive reduction (due to lateral cracking) will implicitly affect the strains. The reduction factor by Vecchio and Collins is denoted as follows:

$$\beta_{\sigma_{cr}} = \frac{1}{1 + K_c} \leq 1 \quad (2.26)$$

where

$$K_c = 0.27 \left( -\frac{\alpha_{lat}}{\varepsilon_0} - 0.37 \right) \quad (2.27)$$

where  $\alpha_{lat} = \sqrt{\alpha_{l,1}^2 + \alpha_{l,2}^2}$  which are the average lateral damage of the lateral damages in each lateral direction, and  $\varepsilon_0 = -\frac{f_c}{E} \cdot \beta_{\varepsilon_{cr}}$  plotted as a function of  $-\frac{\alpha_{lat}}{\varepsilon_0}$  gives Figure 2.12.

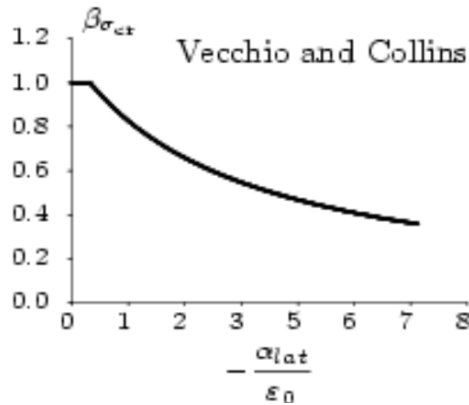


Figure 2.12 – Reduction factor due to lateral cracking (DIANA TNO, 2020)

To validate the effect of lateral damage, a simple element test was performed, and is presented in Appendix A.2.

### 2.3.3 Poisson's Ratio Reduction

In a cracked state, the Poisson effect ceases to exist. Stretching in a cracked direction does no longer lead to contraction in the perpendicular directions. Similar to a damage formulation where the secant stiffness reduces after cracking, the Poisson's ratio is reduced at the same pace (DIANA TNO, 2020).

## 2.3.4 Unloading and Reloading

Hypo-elasticity means that the loading and unloading follows the same stress-strain path. However, this approach would be an inaccurate description of the concrete model, given that the chosen compressive and tensile behavior models could exceed the elastic range. In DIANA, secant unloading, and reloading is used (DIANA TNO, 2020). This is also proven to reflect experimental results (Deaton, 2013). The importance of selecting the correct unloading/reloading path is particularly important for cyclic loading. However, this will also occur when proportional loading is inflicted to the concrete structure, as cracking will result in local stress releases of the surrounding elements, and thereby local unloading.

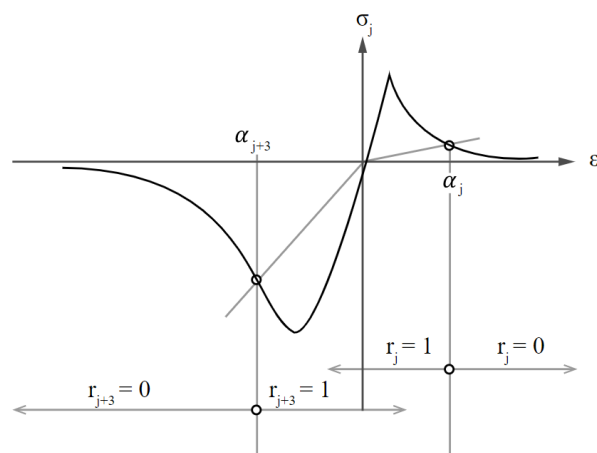


Figure 2.13 – Loading-unloading-reloading (DIANA TNO, 2020)

Figure 2.13 illustrates the procedure, where it is unloaded and reloaded in the compressive and tensile domain. Also, the secant unloading-reloading was illustrated in a simple validation test of the compressive and tensile behavior of concrete in Appendix A.1.

## 2.4 Reinforced Concrete

### 2.4.1 Reinforcement Model

DIANA offers embedded and bond-slip reinforcement modelling. The embedded reinforcement adds truss-like stiffness to the surrounding structural elements. These elements are referred to as mother elements. Weight is not added from the reinforcement, nor removed from the concrete in the space occupied of the reinforcement. The mother element also does not diminish in stiffness due to the space occupied by the reinforcement. Nevertheless, these inaccuracies would probably be of negligible influence in a normal sized structure. When the reinforcement is embedded in the mother elements it utilizes the strain computed from the displacement field, which means that the reinforcement holds the same

strain as the surrounding concrete. This implies perfect bond conditions between reinforcement and concrete (DIANA TNO, 2020). On the other hand, bond-slip modelling does not imply perfect bond conditions, but rather gives the bond between the reinforcement steel and the surrounding concrete a certain strength. The bond between concrete and steel bars is no longer perfect when concrete damage around bars takes place (Brisotto et al., 2012). Kostovos argue that the small tensile strength of concrete will be critical, and since tensile failure will most likely take place before bond failure, embedded modelling can be justified (Kostovos and Pavlović, 1995). However, this argument may be weakened when considering a nonlinear analysis, where it can be difficult to presume the structural behavior once damage and several cracks is affecting the structure. When choosing bond-slip reinforcement in DIANA, the user has the option to select truss or beam elements, which are connected to the mother elements by interface elements. If the reinforcement model uses an embedded or discrete truss formulation, the reinforcement bars have no bending stiffness. Thus, only the reinforcement modelled with beam elements can obtain dowel actions which allow the longitudinal reinforcement to contribute to the shear resistance in the beam. This is why beam elements were used in this thesis.

## 2.4.2 Bond-slip

As mentioned in the previous chapter, if not embedded, DIANA connects the reinforcement to the mother elements through interface elements. For these interface elements, the user can select a diversity of bond-slip models. However, all bond-slip models include a linear normal and shear stiffness which must first be applied. The normal stiffness modulus sets a relation between the relative displacements and the tractions normal to the bar. The shear stiffness modulus relates the shear traction to the relative shear displacement in the longitudinal direction of the reinforcement (DIANA TNO, 2020). These values should be very stiff, so that the elastic relative displacement is negligible. However, too high stiffness values may result in numerical difficulties. DIANA provides the following guidelines for normal and tangential stiffness for interface elements:

$$K_n = 100 E/l_e \sim 1000 E/l_e \quad (2.28)$$

with the  $E$  as Young's modulus of the surrounding interfaces, and  $l_e$  as the average mesh element size. The tangential stiffness is derived from the normal stiffness:

$$K_t = K_n/10 \sim K_n/100 \quad (2.29)$$

Furthermore, DIANA offers six curves for the relations between shear traction and slip, namely the Cubic, Power law, Multilinear, Shima bond-slip, Shima bond-slip-strain, and finally a bond-slip model of the fib Model Code for concrete structures 2010 (DIANA TNO, 2020). The influence of different bond-slip models were not investigated in this thesis, as only the bond-slip model of the fib Model Code was used.

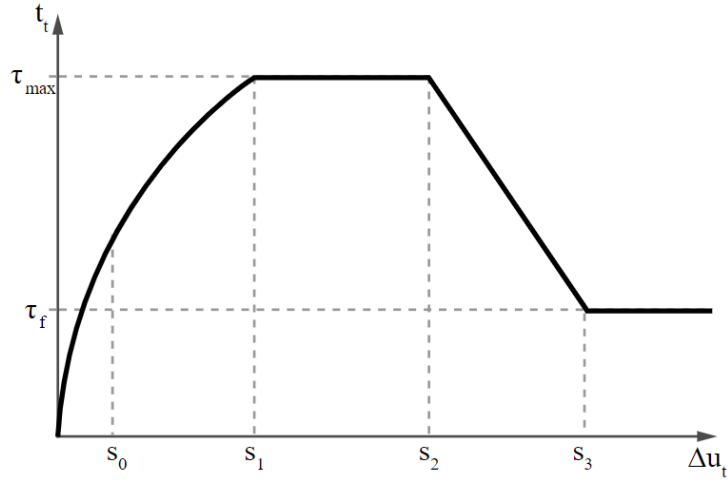


Figure 2.14 – Bond-slip back-bone curve of fib Model Code 2010 (DIANA TNO, 2020)

For  $0 \leq s \leq s_1$ :

$$\tau = \tau_{max}(s/s_1)^\alpha \quad (2.30)$$

and for  $s_1 \leq s \leq s_2$ :

$$\tau = \tau_{max} \quad (2.31)$$

and for  $s_2 \leq s \leq s_3$ :

$$\tau = \tau_{max} - (\tau_{max} - \tau_f)(s - s_2)/(s_3 - s_2) \quad (2.32)$$

and finally, for  $s_3 \leq s$ :

$$\tau = \tau_f \quad (2.33)$$

In the first section a power function for the bond-slip stress  $\tau$  develops from zero to the maximum bond-slip stress  $\tau_{max}$  at a relative slip displacement  $s_1$ . In the second section the bond-slip stress  $\tau$  remains constant at  $\tau_{max}$  until a relative slip displacement  $s_2$ . In the third section the bond-slip stress  $\tau$  reduces linearly to the ultimate bond-slip stress  $\tau_f$  at the relative slip displacement  $s_3$ . In the figure, an additional relative displacement  $s_0$  is marked. This is not included in the original model from fib but inserted by DIANA since an exponent value smaller than 1 would result in an undefined stiffness in the origin. This is

solved by using a linear development in the bond-slip stress between zero and  $s_0$  such that the stress value at  $s_0$  equals the bond-slip stress as defined by the power function (DIANA TNO, 2020).

### 2.4.3 Tension Stiffening

The tension stiffening effect arises when cracking orthogonal to the reinforcement initiates. Obviously, the concrete tensile strength in a fully developed crack is zero. However, the stiffening effect is a result of the stiffness contribution that the concrete provides in between cracks, as the tensile stresses are transferred from steel to concrete by bond action. This lets the reinforcement steel to have less strain between the cracks, and progressively larger towards the cracks (Kostovos and Pavlović, 1995). This local stress distribution can be considered by modelling the average post-cracking tensile behavior. Since concrete continues to bear a part of the applied tension after cracking, tensile stress of the concrete in reinforced concrete gradually decreases when the average strain exceeds the crack strain. This differs from the stress release behavior of plain concrete, which exhibits a sharp drop immediately after cracking and no recovery of the stress transfer mechanism. The fundamental difference in post-cracking tensile behavior of plain concrete and concrete in reinforced concrete is due to the difference in the tensile resistant mechanism. Plain concrete resists tension through bridging of aggregates at the crack surface only, whereas reinforced concrete resists tension mainly through the bond stress transfer from the reinforcement bar (Maekawa et al., 2003). DIANA provides a tension stiffening model from the Japan Society of Civil Engineers (JSCE).

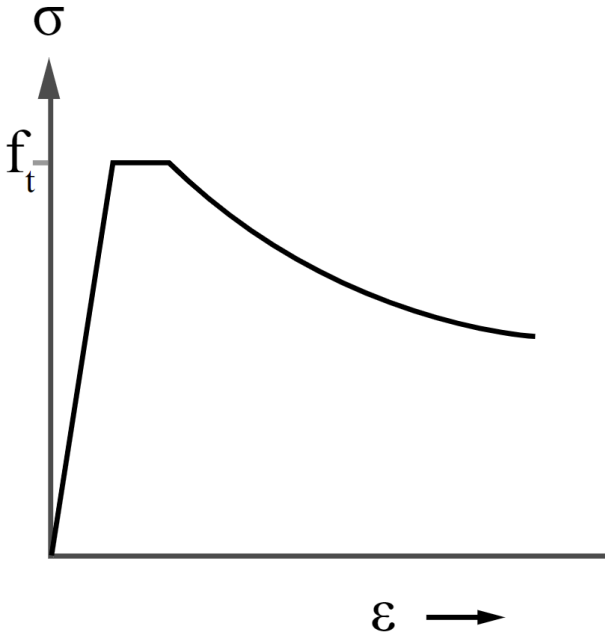


Figure 2.15 – JSCE stiffening (DIANA TNO, 2020)

The descending part in Figure 2.15 is mathematically described as:

$$\sigma = f_t(\varepsilon_{tu}/\varepsilon)^c \quad (2.34)$$

where  $\sigma$  is the average tensile stress,  $\varepsilon$  is the average tensile strain,  $f_t$  is uniaxial tensile strength,  $\varepsilon_{tu}$  is the cracking strain and  $c$  is the stiffening parameter. The stiffening parameter  $c$  is set to be 0.4 for deformed bars and 0.2 for welded wire mesh (Maekawa et al., 2003).

At this point, a concrete tensile softening (Chapter 2.3.1) and stiffening post-cracking behavior is established. Thus, the next step considers where to apply the different behaviors. As longitudinal reinforcements rarely covers the whole beam, a stiffening behavior that covers the whole beam would be unrealistic. Hence, the establishment of stiffening zones is needed. A formulation provided by Maekawa et al is as follows (Maekawa et al., 2003):

$$h_{max} = \frac{\sqrt{\pi}}{2} d_b \sqrt{\frac{f_y}{f_t}} \quad (2.35)$$

where  $h_{max}$  is the height of the stiffening zone,  $d_b$  is the diameter of the reinforcement bar and  $f_y$  and  $f_t$  is the yield strength of the reinforcement bar and the tensile strength of the concrete, respectively. However, eq. (2.35) applies for reinforcement bars that fully transfer the bond stress. Thus, an adjustment factor,  $K$ , takes the concrete cover,  $t_c$ , and diameter bar,  $d_b$ , into account:

$$K = \left( \frac{t_c - d_b}{5.5d_b} \right)^{0.5} \quad (2.36)$$

which is based on experimental data. Furthermore, to take into account that if bars in the same layer are placed far away from each other, the following equation is suggested:

$$h_e = \frac{nh_{max}^2}{b} \quad (2.37)$$

where  $h_e$  is equivalent height of the stiffening zone,  $n$  is the number of steel bars, and  $b$  is the width of the thickness of the RC member. By combining eq. (2.35), (2.36) and (2.37) we finally obtain the following equation for estimation of the tension stiffening zone:

$$h_{stiffening} = \frac{\left( \frac{\sqrt{\pi}}{2} d_b \sqrt{\frac{f_y}{f_t}} K \right)^2 n}{b} = \frac{\pi f_y d_b (t_c - d_b) n}{22 f_t b} \quad (2.38)$$

with the symbol descriptions described above. Note that this is the height of only one layer, meaning that if there are multiple layers, each layer is individually calculated. Overlapping and zones that fall out of the structural boundaries are disregarded.

Alternatively, the Eurocode suggests the effective height as (Eurocode 2):

$$h_{stiffening} = \min\{2.5(h - d); (h - x)/3; h/2\} \quad (2.39)$$

where  $h$  is the beam height,  $d$  is the effective height and  $x$  is the height of the compression zone. Also, the Norwegian national annex provides:

$$h_{stiffening} \geq h - d + 1.5d_b \quad (2.40)$$

Because of cracking and bond destruction continuously evolving as further loading is applied, Kostovos and Pavlović claims that the stiffness of the RC tie tends towards that of the bare bar, hence, tension stiffening effect is unlikely to affect the ultimate load predictions. However, the deflection might be more sensitive (Kostovos and Pavlović, 1995). Nevertheless, a sensitivity study including the tension stiffening effect is performed in Chapter 4.3.

## 2.5 Crack Modelling

As finite element modelling essentially is based on a continuum-mechanic technique, an incompatibility issue arises whenever cracks are developing in the model, as cracks physically separates the structure. In order to overcome this, two crack modelling approaches are suggested, namely the discrete and smeared crack model.

The discrete crack model introduces an actual gap in the finite element mesh at the location of a crack. This includes doubling and separating the nodal coordinates lying along individual crack paths, as well as automatically redefining of the mesh around the cracks to be able to represent various paths (Kostovos and Pavlović, 1995). Although this model allows for a precise prediction of the localized deformation at cracks, the discrete crack approach requires pre-defining of the tensile fracture zones, when the finite element is generated. However, the position of the cracks is not known beforehand for most structural analyses. DIANA offers two models the cracking modelled in a discrete manner, namely the discrete cracking model and the crack dilatancy model. Even though it could have been interesting to investigate the numerical behavior of the structures in a predefined crack path system, this is beyond the scope of this thesis, as it is of interest to carry out numerical simulations applicable in general engineering design cases, where the crack patterns are unknown. Thus, the discrete crack model is not further discussed in this thesis.

The smeared crack model, on the other hand, makes use of the drastic material changes caused by the cracking as a means of simulating discontinuity, which in our case would be the Hordijk softening curve. Such material changes include reducing or removing the stiffness properties orthogonal to the crack, without introducing any gap in the initial mesh, and leaving the mesh unchanged throughout the analysis. Since material properties are evaluated only at specific points in an element, such as integration points, the alteration of the material properties due to cracking consequently affects the contributing region from

which these properties are evaluated, hence smearing the effect of cracking over the whole of that region. Thereby, smeared modelling represents cracked areas by modifying stiffness properties and stresses at the relevant Gauss points. Thus, smeared models simply replace uncracked stiffness matrices by cracked ones. The fact that there is no need for redefining the mesh through this process constitutes a computational advantage compared to the discrete crack model (Kostovos and Pavlović, 1995). The smeared crack approach can be subdivided into the fully rotating crack model, fixed crack model, multiple non-orthogonal crack models and hybrid crack models (Vecchio, 2001). However, there is an essential difference between the multiple non-orthogonal crack model, or the multi-directional fixed crack model as it is denoted in DIANA, and the other models. The multi-directional fixed crack model allows for several non-orthogonal cracks to appear in the same integration point. This is in contrast to the other models, which only allows for maximum two orthogonal cracks. The latter can be described by the total-strain based crack model and has the characteristics of describing the stress as a function of the strain. These properties are evaluated in the directions given by the crack directions. Hence, the strain can be noted as:

$$\varepsilon = \varepsilon^{total} \quad (2.41)$$

with one stress-strain relation gives the stress:

$$\sigma = \sigma(\varepsilon) \quad (2.42)$$

This procedure is not possible for the multi-directional fixed crack model, due to several cracks in one integration point. Hence this model uses a decomposed strain model, consisting of the elastic strain and the crack strain:

$$\varepsilon = \varepsilon^e + \varepsilon^{cr} \quad (2.43)$$

giving the elastic stress-strain relation as:

$$\sigma = \sigma(\varepsilon - \varepsilon^{cr}) \quad (2.44)$$

and the crack stress-strain relation as a function of the crack strain:

$$\sigma^{cr} = \sigma(\varepsilon^{cr}) \quad (2.45)$$

The further sub-decomposition of the crack strain allows for the possibility of modelling a number of cracks that simultaneously occur. The initiation of cracks are governed by a tension cut-off criterion and a threshold angle between two consecutive cracks, which must be simultaneously satisfied (DIANA TNO, 2020). However, the effect of using multi-directional fixed crack models was not investigated. Thereby, this thesis includes an investigation of different total-strain based crack models, namely the fixed, fully rotating

and a hybrid crack model. The latter is, in DIANA, denoted as the rotating to fixed crack model.

## 2.5.1 Fixed Crack Model

Traditionally, the stress-strain law for smeared cracking has been set-up with a reference to fixed principal nst-axes of orthotropy (Rots and Blaauwendraad, 1989). In the nst-notation, the n represents the normal crack direction (mode I), while s and t in this case represents the in-plane tangential crack direction (mode II), and out-of-plane tangential crack direction (mode III) respectively. To simplify the notations, and because the analyses in this thesis operated in a 2D-plane stress formulation, mode III is neglected in the following notations. See Figure 2.16.

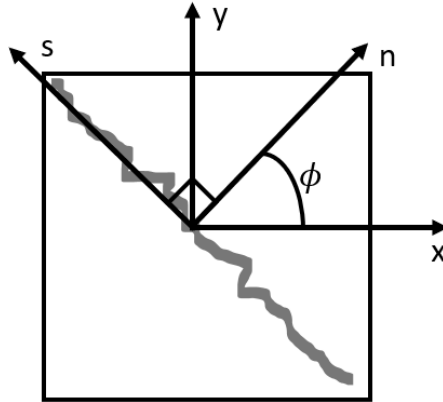


Figure 2.16 - Relative crack coordinate system

Initially, the concrete is treated as an isotropic material, meaning that the same material properties yields in all directions. However, once cracking is initiated, the isotropic properties are replaced with an orthotropic material law, and can be noted as follows:

$$\begin{bmatrix} \sigma_{nn} \\ \sigma_{ss} \\ \sigma_{ns} \end{bmatrix} = \begin{bmatrix} \frac{\mu E}{1 - \nu^2 \mu} & \frac{\nu \mu E}{1 - \nu^2 \mu} & 0 \\ \frac{\nu \mu E}{1 - \nu^2 \mu} & \frac{E}{1 - \nu^2 \mu} & 0 \\ 0 & 0 & \frac{\beta E}{2(1 + \nu)} \end{bmatrix} \begin{bmatrix} \varepsilon_{nn} \\ \varepsilon_{ss} \\ \gamma_{ns} \end{bmatrix} \quad (2.46)$$

where  $E$  is Young's modulus,  $\nu$  is Poisson's ratio, and  $\mu$  and  $\beta$  are the reduction factors for mode I and mode II stiffness (Rots and Blaauwendraad, 1989). The concept of the fixed crack model is that the crack is fixed upon initiation (DIANA TNO, 2020). This includes the need to specify a shear retention factor, as the principal stresses keeps rotating after crack

initiation, creating tangential crack stresses. The shear retention will be further elaborated in Chapter 2.5.4. DIANA relates the global (xy) and local crack (ns) strains as:

$${}^{t+\Delta t}_{i+1}\varepsilon_{ns} = \mathbf{T}{}^{t+\Delta t}_{i+1}\varepsilon_{xy} \quad (2.47)$$

where the transformation matrix,  $\mathbf{T}$ , can be denoted as:

$$\mathbf{T} = \mathbf{T}({}^{t+\Delta t}_{i+1}\varepsilon_{xy}) \quad (2.48)$$

meaning that the transformation matrix,  $\mathbf{T}$ , is a relative angle function dependent on the strain situation and whether the fixed or rotating crack model is applied. For the fixed crack model, the transformation matrix,  $\mathbf{T}$ , is fixed upon cracking, whereas for the rotating crack model,  $\mathbf{T}$ , is constantly changing. If  $\phi$  represent the angle between x and n in Figure 2.16, the transformation matrix,  $\mathbf{T}$ , is expressed as:

$$\mathbf{T} = \begin{bmatrix} \cos^2\phi & \sin^2\phi & \sin\phi\cos\phi \\ \sin^2\phi & \cos^2\phi & -\sin\phi\cos\phi \\ -2\sin\phi\cos\phi & 2\sin\phi\cos\phi & \cos^2\phi - \sin^2\phi \end{bmatrix} \quad (2.49)$$

## 2.5.2 Rotating Crack Model

The rotating crack model, or the coaxial stress-strain model, is appealing in the way that there is no need for a shear retention specification. The basic concept, which was touched upon in the previous chapter, is that the crack direction is constantly rotating according to the principle strain. In the step-by-step computation, only one crack is considered as active, and the previous cracks are erased from the memory (Maekawa et al., 2003). Even though the physical aspect of this model is not as easy to stand by as the fixed crack model, it has during a long period of time shown its suitability for modelling reinforced concrete structures (DIANA TNO, 2020). As mentioned in Chapter 2.5.1, in the rotating crack model equation the transformation matrix,  $\mathbf{T}$ , is constantly changing, and is dependent on the current strain situation.

An issue with the rotating crack model was the fact that material orthotropy generally implies the rotation of principal stress to deviate from the rotation of principle strain. Consequently, when the axes of material orthotropy co-rotate with the axes of principal strain, they will cease to coincide with the axes of principal stress. Hence, the direct use of the principal stress-strain curves then becomes inconsistent. However, to solve this, co-axiality between principal stresses and strains may be enforced in the following manner. By virtue of Mohr's strain circle, a small increment of shear strain causes the direction of principal strain to rotate by an angle  $\Delta\phi_\varepsilon$  according to:

$$\Delta\phi_\varepsilon = \frac{1}{2} \arctan \frac{\Delta\gamma_{12}}{2(\varepsilon_{11} - \varepsilon_{22})} \quad (2.50)$$

where  $\Delta\gamma_{12}$  is the shear strain increment in the 1,2 reference frame and  $\varepsilon_{11}$  and  $\varepsilon_{22}$  are the initial principal strains. In the same way, Mohr's stress circle indicates that a small increment of shear stress causes principal stress rotation by an angle of  $\Delta\phi_\sigma$  according to:

$$\Delta\phi_\sigma = \frac{1}{2} \arctan \frac{\Delta\tau_{12}}{(\sigma_{11} - \sigma_{22})} \quad (2.51)$$

Co-axiality between principal stresses and strains is enforced by  $\Delta\phi_\varepsilon = \Delta\phi_\sigma$ . Hence:

$$\Delta\tau_{12} = \frac{(\sigma_{11} - \sigma_{22})}{2(\varepsilon_{11} - \varepsilon_{22})} \Delta\gamma_{12} \quad (2.52)$$

With the statement in eq. (2.52), the formulation of the tangential stress-strain law for a consistent rotating crack concept then becomes:

$$\begin{bmatrix} \Delta\sigma_{11} \\ \Delta\sigma_{22} \\ \Delta\tau_{12} \end{bmatrix} = \begin{bmatrix} \frac{\partial\sigma_{11}}{\partial\varepsilon_{11}} & \frac{\partial\sigma_{11}}{\partial\varepsilon_{22}} & 0 \\ \frac{\partial\sigma_{22}}{\partial\varepsilon_{11}} & \frac{\partial\sigma_{22}}{\partial\varepsilon_{22}} & 0 \\ 0 & 0 & \frac{(\sigma_{11} - \sigma_{22})}{2(\varepsilon_{11} - \varepsilon_{22})} \end{bmatrix} \begin{bmatrix} \Delta\varepsilon_{11} \\ \Delta\varepsilon_{22} \\ \Delta\gamma_{12} \end{bmatrix} \quad (2.53)$$

In eq. (2.53) the derivatives can be inserted directly as the shear term guarantees coaxiality between principal stress and principal strain (Rots and Blaauwendraad, 1989).

### 2.5.3 Rotating to Fixed Crack Model

The rotating to fixed crack model is, as the name suggests, a hybrid crack model which consists of both rotating and fixed cracks depending on the total strain level. In DIANA the user specifies a critical strain value. Until this value is reached, the crack acts as a rotating crack and is aligned with the principal strains in the respective integration point. When the critical total strain,  $\varepsilon_f$ , is reached, the crack orientation is fixed and the model changes from the rotating to the fixed crack model (DIANA TNO, 2020). Note that the threshold strain value,  $\varepsilon_f$ , is compared with the total principal strain  $\varepsilon_1$ , and not the crack strain. This means that if a threshold value is specified to be smaller than a strain value initiating a crack, or put differently, smaller than  $f_t/E$ , it will result in a completely fixed crack model. DIANA provides no clear guidelines for defining the critical threshold strain, hence, an investigation of the influence of a varying threshold value will be carried out in Chapter 4.2.

### 2.5.4 Shear Retention

A consequence of using the fixed crack model is the presence of a tangential shear resistance in the crack, as the principle stresses keeps rotating after initiation. The reduced mode I normal stiffness in the crack forces the principal stresses to rotate to find a new equilibrium position, which includes an immediate shear stress along the crack surface. The physical interpretation of this tangential shear resistance can be assessed as aggregate interlock. This is the result of the crack pattern navigating in the cement paste between aggregates, causing an unsmooth crack surface to form in which aggregates pointing out in the crack will prevent the crack from tangential slipping. This resistance is denoted as shear retention, and is specified by reducing the shear stiffness in the crack by a retention factor,  $\beta$ , which relates the shear crack stiffness to the undamaged shear stiffness in the following manner:

$$G^{cr} = \beta G \tag{2.54}$$

with  $0 \leq \beta \leq 1$ .

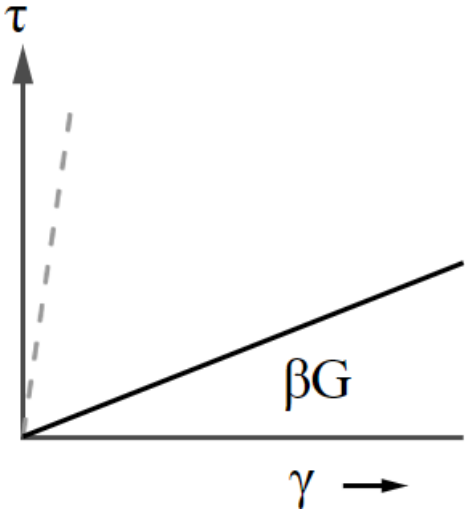


Figure 2.17 – Reduced shear stiffness (DIANA TNO, 2020)

Early versions attempted to set the shear retention factor equal to zero, meaning that there was no shear stiffness as cracks were formed. However, this was a rather crude approximation of reality as cracks in heterogeneous materials may be well capable of transmitting shear stresses due to aggregate interlock, as mentioned above. Moreover, the sudden switch from the initial isotropic linear-elastic law to an orthotropic law with zero stiffness implies a strong discontinuity which turned out to amplify numerical difficulties (Rots and Blaauwendraad, 1989).

DIANA provides a number of shear retention models. It is possible to use a constant shear retention value, full or reduced, however this might result in shear stress-locking on the

crack surfaces, as the size of the crack opening does not affect the shear stiffness reduction. Hence, only variable shear retention models were investigated in this thesis. This is also according to the recommendations in the guidelines for NLFEA of concrete structures (Hendriks and Roosen, 2019).

The damage based shear retention model decreases the shear stiffness proportional to the decrease of the normal stiffness as a crack evolves. In other words, the secant shear stiffness degrades at the same rate as the secant tensile stiffness due to cracking (Hendriks and Roosen, 2019). Hence, the reduced crack shear stiffness in DIANA is expressed as:

$$G^{cr} = \frac{E^{cr}}{2(1 + \nu^{cr})} \quad (2.55)$$

where  $E^{cr}$  is the tensile secant modulus after cracking, and  $\nu^{cr}$  is the reduced Poisson's ratio, according to Chapter 2.3.3. This also implies that there is no residual shear stiffness across macro-cracks (Rots and Blaauwendraad, 1989). The motivation for the use of this model is that it often provides conservative results, and that it is user-friendly, as no extra specifications are needed.

In contrast to the damage based shear retention model, when using the Al-Mahaidi shear retention model, DIANA demands a minimum shear retention specification. DIANA recommends this value to be no larger than 0.01. Hence, to avoid further numerical instabilities, this was the minimum shear retention value chosen in this thesis. The Al-Mahaidi shear retention factor evolves in the following manner:

$$\beta = 0.4 \frac{f_t}{E \varepsilon_{nn}} \quad (2.56)$$

where  $f_t$  is the tensile strength,  $E$  is the Young's modulus, and  $\varepsilon_{nn}$  is the total normal strain (DIANA TNO, 2020). By analyzing eq. (2.56) one can see that the shear retention factor immediately drops to 0.4 as the first crack is initiated, and then continues decreasing with increasing normal strain. Similarities can be drawn between the Al-Mahaidi and damage based shear retention models as they both decrease with increasing strain, however, the Al-Mahaidi is not directly governed by the tension softening model, as is the case for the damage based.

Finally, the aggregate based shear retention model was analyzed. As the other models, this model also reduces the shear capacity as the crack width increases. However, the aggregate based shear retention model assumes that all contact is lost and thereby zero shear resistance in the crack, when the crack is wider than half the mean aggregate size. The linear decay of the shear retention reads:

$$\beta = 1 - \left( \frac{2}{d_{agg}} \right) \varepsilon_{nn}^{cr} h_{cr} \quad (2.57)$$

where  $d_{agg}$  is the mean aggregate size,  $\varepsilon_{nn}^{cr}$  is the crack normal strain, and  $h_{cr}$  is the crack bandwidth (DIANA TNO, 2020). The crack strain multiplied with the crack bandwidth is the numerical interpretation of the crack width. Physically, this model makes sense. However,

this model implies that half of the mean aggregate size is pointing out between cracks along the whole crack length. In reality, we have little control of where the crack develops and neither where different aggregate sizes locate. Hence, to use the mean aggregate size might be interpret as non-conservative.

The three shear retention models presented in this chapter were compared in a simple one-element test and is presented in Appendix A.3.

## 2.6 Modes of Failure

This chapter will briefly discuss different failure modes in concrete beams, obtained as a result of varying geometrical aspects. However, failure modes including stirrup failure etc., will not be examined here, as this is not relevant for the present study. Furthermore, several and more detailed versions of the failure modes described below exist, however, the presented failure modes are the main failure modes seen in the experimental and numerical results in this thesis.

### 2.6.1 Flexural Failure

For a shear span to effective depth ratio,  $a/d$ , above 6, flexural failure displays either yielding of the longitudinal reinforcement and crushing of the concrete in the compression zone or just excessive yielding of the longitudinal reinforcement (de Putter et al., 2022). This will occur in at a section of maximum moment and will result in vertical cracks forming in from the bottom of the beam.

### 2.6.2 Tension Shear Failure

For a shear span to effective depth ratio,  $a/d$ , above 2.5 and to about 6, the diagonal crack starts from the last flexural crack and turns gradually into a crack more and more inclined under the shear loading. Such a crack does not proceed immediately to failure. The diagonal crack encounters resistance as it moves up into the compression zone, hence, flattens out, and stops at some point. Further loading will expand the crack until sudden failure occurs (Lafta and Ye, 2016).

### 2.6.3 Compression Shear Failure

For shear span to effective depth ratio,  $a/d$ , between approximately 1.0 and 2.5 , the shear failure is mainly caused by the crushing of concrete in the compression zone at the top of the critical diagonal crack, or in other words, in the top of the strut. This type of failure is known as shear compression failure (Zararis, 2003).

## 2.7 Size Effect

To capture the size effect, and no other influences, one must consider structures of different sizes but geometrically similar shapes. According to standard criteria, failure is

indicated when the nominal stress reaches the nominal strength of the concrete (Bažant, 1984). However, when taking the size effect into account, the nominal strength may deviate for the same material. Thus, the strength of structural materials is not constant – it decreases with increasing size of the specimen (Carpinteri, 1989). Two size effects are of major importance under loading, namely the stochastic and energetic size effect (Suchorzewski et al., 2018).

### 2.7.1 Stochastic Size Effect

This size effect concerns the heterogeneity of the concrete material and is referred to as the statistical (or stochastic) size effect. With this heterogeneity follows a strength variability throughout the concrete structure. This property is independent of the structure size. However, the stress gradient normally varies inversely with the structure size, which means that the region of nearly maximum stress becomes larger in a larger structure. Therefore, a coalition of low strength and peak stress is higher for larger structures. This results in declining strength with increasing structural size. Nevertheless, the decline stops when the region of nearly maximum stress becomes much larger than the region of low strength, which provides a horizontal asymptotic limit as the structure gets very large (Bažant, 1984).

### 2.7.2 Energetic Size Effect

This second size effect is called the energetic or deterministic size effect. In summary, the source of the energetic size effect is a mismatch between the size dependence of the energy release rate and the energy consumption rate by fracture (cracking). A significant part of the energy release increases with the square of the structure size, while the energy consumption increases in proportion to the structure size. Therefore, the nominal stress must decrease to reduce the energy release rate of the structure to achieve equilibrium between the energy consumption and the energy release (Bažant, 2000).

# 3 Finite Element Modelling of Five Beams Tested by Suchorzewski et al.

In this chapter, the modelling setup is established. To make optimal choices in a NLFEA, a certain amount of experience and expertise is needed, as the application is rarely straightforward (Vecchio, 2001). Thereby, many of the modelling choices in this thesis were influenced by guidelines and research papers made by experts in the field. Some papers were especially important through the realization of this thesis, and these are presented below:

- The experimental study of shear strength and failure mechanisms in RC beams scaled along height or length, done by Suchorzewski, Korol, Tejchman and Mróz (Suchorzewski et al., 2018). These experiments are the basis for comparison for the analyses done in this thesis. The different size adjustments and failure mechanisms obtained in the experiments creates a good foundation for analyzing the robustness and stability of different modelling procedures.
- The guidelines for nonlinear finite element analysis of concrete structures (Hendriks et al., 2017; Hendriks and Roosen, 2019). The guidelines are provided in a summarized and clear way, with reasons for why to use the different applications presented.
- The article by de Putter et al. (de Putter et al., 2022). In this research, 19 alternative 2D nonlinear finite element approaches were benchmarked against 101 experiments on RC beams. The large amount of analyses uses the total-strain based crack model with either fixed or rotating crack models, varying element sizes, reinforcement models, bond-slip models, and equilibrium conditions. Accuracy and deviations were documented, and certain issues with the different models were pointed out. Thus, the newly published article is highly relevant, and inspired several of the modelling choices for the analyses in this thesis.

It is worth mentioning that some of the authors in the experimental study presented above also ran numerical simulations of the experiment (Suchorzewski et al., 2018; Marzec et al., 2019), and good correlation between numerical and experimental results was obtained. In these analyses an elasto-plastic damage model was used, enhanced by non-local softening, and were performed in Abaqus. Some inspiration and ideas were also extracted from these analyses. In the analyses, they used a 2D plane stress format with symmetry boundary conditions – meaning they only modelled one half of the beam. Despite of these simplifications, good results were obtained. The motivation for modelling in a plane stress formulation with symmetry boundary conditions were that computational time decreases, and that the beam thickness was quite slender. Furthermore, the good results obtained in the non-local model, confirms that these simplifications can be made and good accuracy can still be preserved.

With a crack band model, as used in the analyses in this thesis, it lies within the mathematical formulation that the cracking strain is uniformly distributed over the width of the band, with a sudden jump at the band boundary. Nevertheless, a more realistic description would include a nonuniform variation of the cracking strain, as the density of cracks or microcracks will increase towards the center of the fracture process zone. The latter may be achieved by adopting the concept of a non-local continuum. Summarized, this concept assumes that the stress at a point is not a function of the smoothed stress at the same point but a function of the smoothed strain distribution over a certain

characteristic volume centered at that point. The mean strain is defined as a certain averaging integral over the characteristic volume with a suitable empirical weighting function (Bažant, 1986). Further elaboration or investigation of the non-local model will not be provided in this thesis. The main reason for this is that it is not a direct option in DIANA, and that the main scope was to investigate the capability of local procedures. The very short introduction of the non-local approach was merely meant to inform the reader of an alternative approach, which has proved to be successful in the numerical estimation of the experiment investigated in this thesis.

### 3.1 Experimental Setup

The experiments by Suchorzewski were done in two series (Suchorzewski et al., 2018). In series 1, the beams were scaled along the height, and in series 2, the beams were scaled along the length. In each series there were three variations of the respective variable (*d* or *l*), resulting in six different beams. However, the two series had a common geometry, resulting in a total of five different geometries. The experimental results showed that the behavior of the one common geometry was so similar that two separate numerical analyses was considered to be unnecessary. Thereby, throughout the analyses in this thesis, there are five variations of the geometry. The geometries are illustrated in Figure 3.1–Figure 3.5, where the measures are given in millimeters. The notations has the following meaning: S1/S2 refers to the relevant series, D18/D36/D72 refers to the effective height, and a36/a72/a108 refers to the shear span. Note that Figure 3.2 states S1&2, meaning that this geometry is applied in both series. The anchorage length was 130 mm for S1D18a108, 310 mm for S2D18a36, S2D18a72 and S1&2D18a108, and 670 mm for S1D72a108. Also, all the rebars had a diameter of 20 mm.

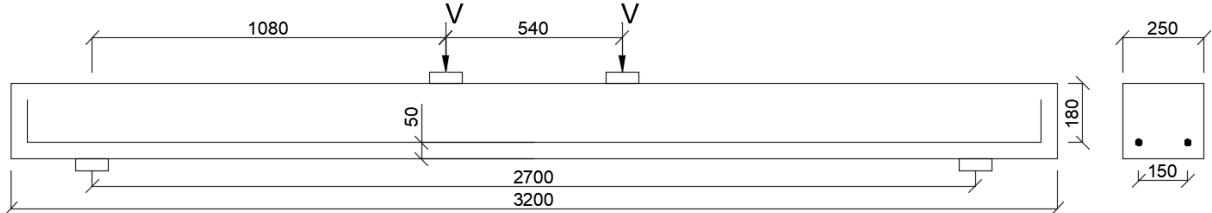


Figure 3.1 – Beam S1D18a108

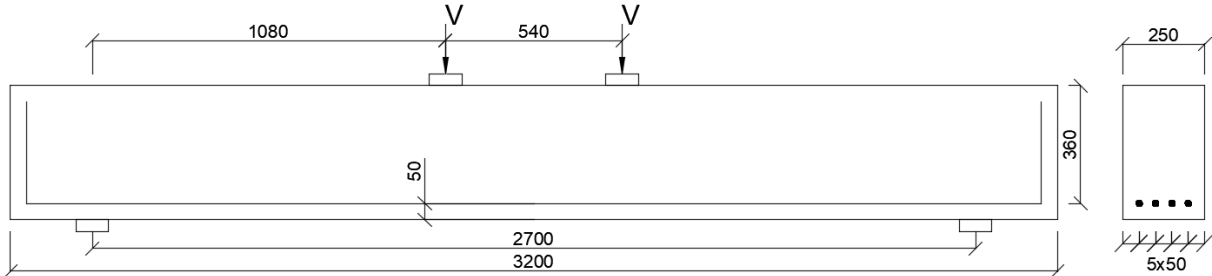


Figure 3.2 – Beam S1&2D36a108

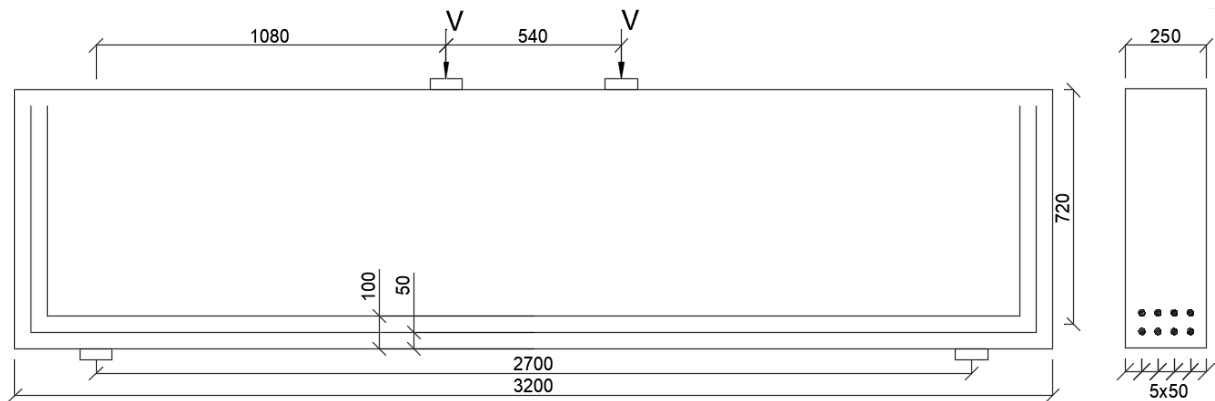


Figure 3.3 – Beam S1D72a108

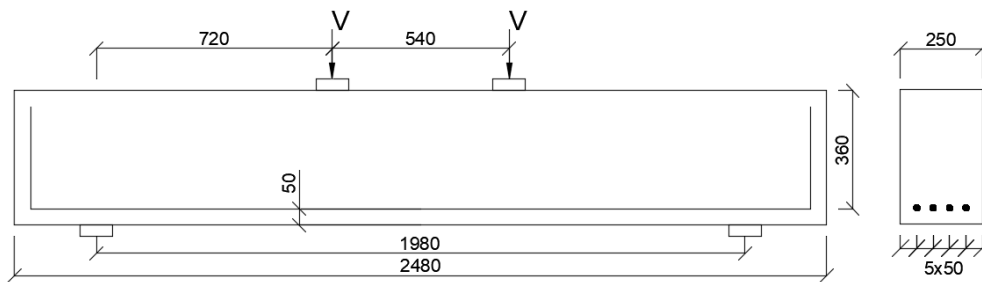


Figure 3.4 – Beam S2D36a72

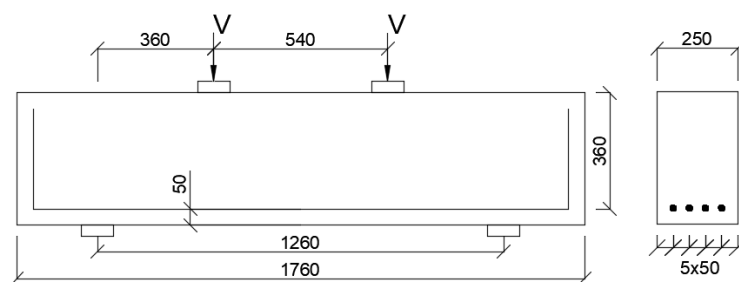


Figure 3.5 – Beam S2D36a36

As mentioned, only half of the beams were modelled. This was done by restraining all movement in the longitudinal direction at the midspan of the beams. An illustration of this can be seen in Figure 3.11 – Figure 3.15.

## 3.2 Non-variable Modelling Parameters

Table 3.1 – Constitutive model for concrete

<b>Constitutive model for concrete</b>	
Crack model	Total-strain based smeared crack model
Tensile softening curve	Hordijk
Crack bandwidth	Govindjee projection
Compressive curve	Parabolic
Compression strength reduction	Vecchio and Collins, 1993
Confinement effects	Hsieh-Ting-Chen
Poisson's ratio reduction	Damage based

Table 3.2 – Kinematic assumptions concrete

<b>Kinematic assumptions concrete</b>	
Element type	8-node quadrilateral plane stress element
Integration and interpolation	2x2 Gaussian, quadratic interpolation
Element size	$\approx h/20 \geq 1 * \text{Max aggregate size}$

Table 3.3 – Concrete material properties for each series

<b>Concrete material properties for each series</b>		
	Series 1	Series 2
Compressive cylinder strength, $f_c$	47.4 N/mm <sup>2</sup>	51.0 N/mm <sup>2</sup>
Tensile strength, $f_t$	2.81 N/mm <sup>2</sup>	3.61 N/mm <sup>2</sup>
Young's modulus, $E$	33100 N/mm <sup>2</sup>	35300 N/mm <sup>2</sup>
Poisson's ratio, $\nu$	0.2	0.2
Tensile fracture energy, $G_F$	0.093 N/mm	0.095 N/mm
Compressive fracture energy, $G_C$	23.25 N/mm	24.75 N/mm

The compressive strength, tensile strength, and Young's modulus in Table 3.3 are reported experimental values (Suchorzewski et al., 2018). The compressive strength was reported as cube strength. The relation between cube compressive strength and cylinder compressive strength may depend on several factors (Kumari, 2015), however, the cylinder strength was assumed to be 80% of the cube strength.

As can be seen in Table 3.3, some deviation is present between the series, even though the same concrete recipe mix was used. The Poisson's ratio was recommended to be 0.2 by the guidelines for NLFEA of concrete structures (Hendriks and Roosen, 2019). The tensile fracture energy was calculated according to Bažant and Becq-Giraudon (Bažant and Becq-Giraudon, 2002), where the area under the initial tangent of the of the softening stress was established as:

$$G_f = \alpha_0 \left( \frac{f_c}{0.051} \right)^{0.46} \left( 1 + \frac{d_{max}}{11.27} \right)^{0.22} \left( \frac{w}{c} \right)^{-0.30} \quad (3.1)$$

where the  $\alpha_0$  is a coefficient depending on the aggregate type and is 1 for round aggregates,  $f_c$  is the uniaxial cylinder strength,  $d_{max}$  is the maximum aggregate size and  $w/c$  is the water-cement ratio. The value determination, elaboration and understanding of eq. (3.1) were aided by Suchorzewski's article (Suchorzewski et al., 2018). Furthermore, the area under the complete stress-separation curve was determined as:

$$G_F = 2.5G_f \quad (3.2)$$

Finally, the compressive fracture energy can be related to the tensile fracture energy by (Nakamura and Higai, 2001):

$$G_C = 250G_F \quad (3.3)$$

For the S1&2D36a108 analyses, the material properties from series 1 were used.

Table 3.4 – Constitutive model for reinforcement steel

<b>Constitutive model for reinforcement steel</b>	
Yield strength, $f_y$	560 MPa
Young's Modulus, $E_s$	205 GPa
Plasticity model	Von Mises with linear hardening
Hardening modulus, $E_h$	$0.02E_s$
Hardening type	Isotropic
Ultimate strain, $\varepsilon_u$	25‰
Poisson's ratio, $\nu$	0.3

The material properties of the reinforcement steel was also reported by Suchorzewski (Suchorzewski et al., 2018). The hardening modulus,  $E_h$ , was modelled according to Hendriks et al. (Hendriks et al., 2017), and the ultimate strain was the same as in de Putter's research (de Putter et al., 2022).

Table 3.5 – Kinematic assumptions reinforcement

<b>Kinematic assumptions reinforcement</b>	
Element type	3-node plane stress beam element
Integration and interpolation	2-point Gaussian, quadratic interpolation

Table 3.6 – Kinematic and constitutive assumptions for reinforcement bond interface elements

<b>Kinematic and constitutive assumptions for reinforcement bond interface elements</b>	
Element type	11-node plane stress line element
Integration and interpolation	3-point Newton-Cotes, quadratic interpolation
Shear stiffness, plate/support plate interface	1000 N/mm <sup>2</sup> /mm
Normal stiffness, plate/support plate interface	100000 N/mm <sup>2</sup> /mm

The shear and normal stiffness values for the bond interface was calculated according to eq. (2.28) and eq. (2.29) in Chapter 2.4.2 based on fixed (for all analyses) approximate values, being Young's modulus equal to 30 000 N/mm<sup>2</sup>, an element length of 30 mm, and the factors 100 and 1/100 for  $K_n$  and  $K_t$ , respectively.

Table 3.7 – Bond-slip conditions

<b>Bond-slip conditions</b>	
Maximum bond-slip stress, $\tau_{max}$	17.4 N/mm <sup>2</sup>
$s_0$	0.06 mm
$s_1$	1 mm
$s_2$	2 mm
$s_3$	5 mm
$\alpha$	0.4
Ultimate bond-slip stress, $\tau_{bf}$	7.0 N/mm <sup>2</sup>

The bond-slip values were estimated according to fib Model Code 2010 (fib Model Code 2010) and were based on good bond conditions. The minor material deviations between series 1 and 2 were assumed to be negligible when calculating the bond-slip stress. Hence averaged bond-slip stress values were set as basis for all analyses. These values are presented in Table 3.7.

Table 3.8 – Kinematic and constitutive assumptions for support and loading plate interface elements

<b>Kinematic and constitutive assumptions for support and loading plate interface elements</b>	
Element type	3+3-noded plane stress line element
Integration and interpolation	3-point Newton-Cotes, quadratic interpolation
Shear stiffness, load/support plate interface	1MPa/mm, linear
Normal stiffness, plate/support plate interface	1000 MPa/mm, no-tension

The shear and normal stiffness values in Table 3.8 was taken to be the same as in de Putter’s research (de Putter et al., 2022). Note that the element selection of the interfaces, presented in Table 3.6 and Table 3.8, are not explicitly chosen. These elements are automatically adapted to fit the element selected in Table 3.2. This also applies for the reinforcement beam element presented in Table 3.5, which is either quadratic or linear, depending on the general element type selected in Table 3.2.

Table 3.9 – Equilibrium control

<b>Equilibrium control</b>	
Arc-length control	Spherical path, with indirect displacement control of the node which showed largest displacement in an elastic analysis
Load control	Applied as prescribed deformation with step length: $u_{peak}/50$ – but 20 steps up to the first step of $u_{peak}/50$
Iteration scheme	Full Newton-Raphson with line search, 100 iterations
Continuation	Continuation in case of nonconverged load steps
Norm	Energy with tolerance 0.0001

Also, several of the equilibrium control procedures were inspired by de Putter’s research (de Putter et al., 2022). The mesh layout are presented in Figure 3.6 – Figure 3.10.

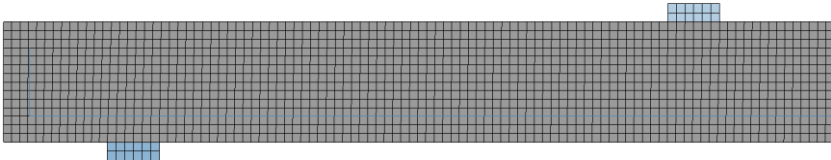


Figure 3.6 – Mesh layout for beam S1D18a108

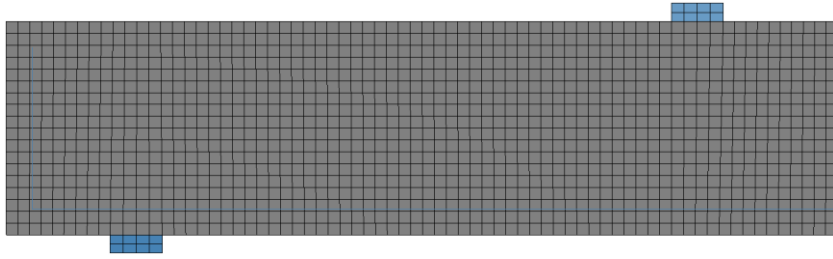


Figure 3.7 – Mesh layout for beam S1&2D36a108

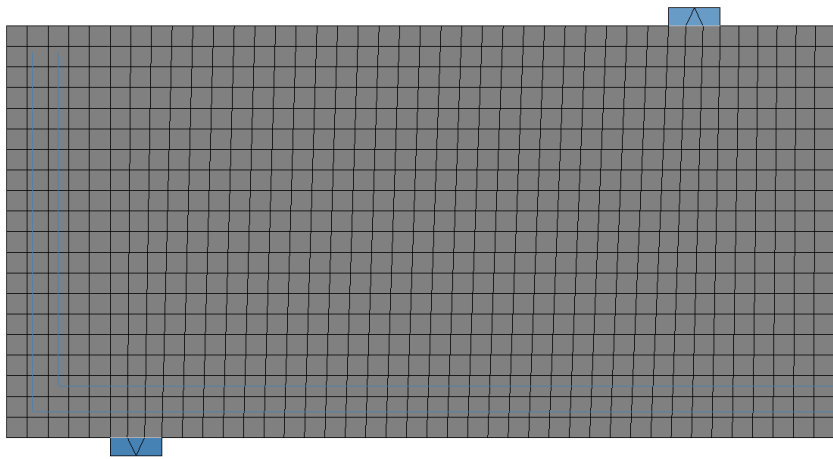


Figure 3.8 – Mesh layout for beam S1D72a108

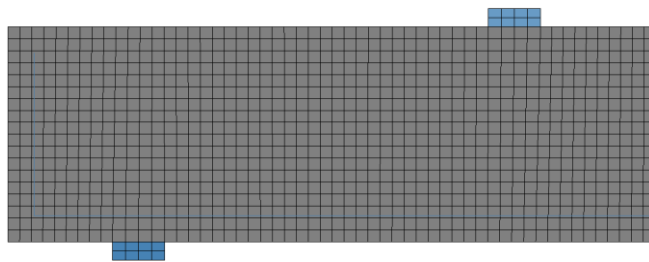


Figure 3.9 – Mesh layout for beam S2D36a72

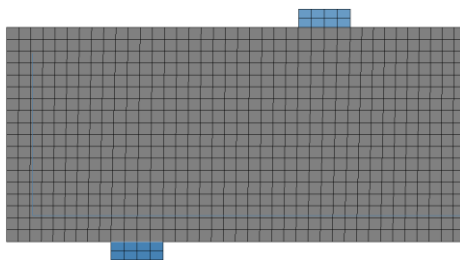


Figure 3.10 – Mesh layout for beam S2D36a36

## 3.3 Variable Modelling Parameters

The following chapters, Chapter 3.3.1 – Chapter 3.3.3, presents the varying modelling parameters. The influence of different shear retention models, total-strain based crack models and the tension stiffening effect were investigated. It is these variations that will be investigated in Chapter 4.

### 3.3.1 Shear Retention Models

The motivation for these analyses is the large deviations in the shear retention models given in DIANA (see Chapter 2.5.4 for theory and Appendix A.3 for visual illustrations of the different shear retention models). The damage based and aggregate based shear retention models are both recommended in the guidelines for NLFEA of concrete structures (Hendriks and Roosen, 2019). The damage based is recommended due to its conservative formulation, and its ease of use, as no extra value specifications is needed from the user. The aggregate based is physically easy to understand, as the retention depends on the crack width and the aggregates in the concrete. The Al-Mahaidi shear retention model was also investigated, with a lower bound value of 0.01 as recommended by the DIANA guidelines (DIANA TNO, 2020). This shear retention model was not recommended in the guidelines (Hendriks and Roosen, 2019), however, due to its instant decrease of retention as a crack occurs, it is interesting to see how it acts compared to the other two. In summary, the aggregate provides a relatively high amount of shear retention, the damage based provides a relatively low amount of shear retention and is reaching zero when a macro-crack is formed, and the Al-Mahaidi provides a relatively low amount of shear retention, but a small amount of shear retention still remains as the crack grows large.

### 3.3.2 Crack Models

Both the rotating and fixed crack models were analyzed in de Putters research, where the general conclusion was that rotating crack models works better for beams with shear reinforcement, while fixed crack models performed better for beams without shear reinforcement (de Putter et al., 2022). However, a relatively new feature in DIANA is to use the rotating to fixed crack model as explained in Chapter 2.5.3. This model can be explained as a hybrid model of rotating and fixed cracks, as it initially follows the rotating crack propagation until a certain normal strain value is reached, where it stops rotating, and turns into a fixed crack.

The first decision in this model is to choose appropriate threshold strain values, in which the crack changes from rotating to fixed. In every analysis, the fully rotating and fully fixed crack model will be plotted in order to see how the hybrid model works in comparison. As mentioned in Chapter 2.5.3, the threshold value is the total strain, meaning that a threshold value lower than  $f_t/E$  will give a crack model that act as fully fixed. Three hybrid models will be used for each beam, representing half-open, fully open, and finally a total strain value resulting in 5 times fully open crack. Because of different material values, geometries and element sizes, the threshold values will vary for each beam. See Table 3.10 for the applied values, and Appendix B.1 for the calculation procedure.

Table 3.10 – Threshold total normal strain values for different beams

<b>Threshold total normal strain values for different beams</b>			
	Half-open crack	Fully open crack	5xFully open crack
S1D18a108	0.0054	0.0107	0.0532
S1&2D36a108	0.0038	0.0075	0.0370
S1D72a108	0.0022	0.0043	0.0213
S2D36a72	0.0030	0.0060	0.0295
S2D36a36	0.0030	0.0060	0.0295

The second decision is which shear retention model to use in the fixed crack model. The crack model investigation was purposely done after the shear retention analyses in order to determine an appropriate shear retention model to use in these analyses. As can be seen in Chapter 4.1 the Al-Mahaidi shear retention model had the overall better performance. However, this model was sensitive in terms of creating an alternative crack path, giving the beam more capacity. Also, this model requires a lower bound shear retention value, which remains a bit arbitrary to determine. Therefore, the damage based will be used for beam S1D72a108, S2D36a72 and S2D36a36, while the aggregate based model will be used where the damage based heavily underestimated the capacity, that is for beam S1D18a108 and S1&2D36a108. Note that the overall goal of this thesis is to reach a unified solution procedure, which will not be a direct outcome of these analyses, as we change the shear retention model for some of the beams. The reason for this is that it would be difficult to estimate the quality of the rotating to fixed crack models if the fixed crack model include wrong failure modes or give either very underestimated or overestimated capacities. Hence, optimal shear retention models were chosen in order to see if the rotating to fixed crack model could further improve these results.

### 3.3.3 Tension Stiffening

Finally, the tension stiffening (TS) effect is analyzed. The theory is presented in Chapter 2.4.3 and the calculation of TS heights is carried through in Appendix B.2. Kostovos and Pavlović claims that the TS effect does not affect the ultimate capacity, due to the fact that continuously extensive cracking lets the stiffness of the RC tie to tend towards the one of the bare bar (Kostovos and Pavlović, 1995). However, since the capacity of the beams in the fixed crack model is sensitive regarding the shear retention model, as presented in Chapter 4.1, in combination with the shear retention models being dependent on the tension softening model, as presented in Chapter 2.5.4, an investigation of the TS effect may be interesting. Several reasons are presented in Chapter 4.3.

Table 3.11 – Tension stiffening zones, Maekawa compared to the Eurocode.

<b>Tension stiffening zones, Maekawa vs EC</b>		
	Maekawa mm	EC mm
S1D18a108	91	80
S1&2D36a108	141	96
S1D72a108	419	184
S2D36a72	121	97
S2D36a36	121	97

In Appendix B.2, a comparison of the Maekawa and Eurocode TS zones are investigated, and a summary of the results are presented in Table 3.11. As Table 3.11 presents, the Eurocode is in general more conservative, using a smaller height than the Maekawa model. For the S1D72a108, the Maekawa model resulted in a very large TS zone, being larger than half of the total beam height. This could result in a problem, because the 2D TS in the total-strain based crack model does not account for the direction of the bond effect on the concrete. Hence, finite elements which are found to be in the effective embedment zone of a reinforcing bar are designated isotropic TS (Hauke and Maekawa, 1999). If the TS zone is too large, an overly stiff post-cracking behavior could act in the inclined cracks in the shear zone, which in reality have the properties of plain concrete. DIANA does in fact offer anisotropic TS behavior, however, this is only applicable in the Maekawa-Fukuura Concrete Model, which is not used in this thesis (DIANA TNO, 2020). The resulting stiffening zones are presented in Figure 3.11 – Figure 3.15. The shaded area represents the TS zone, while the unshaded area represents the plain concrete with the Hordijk tension softening.

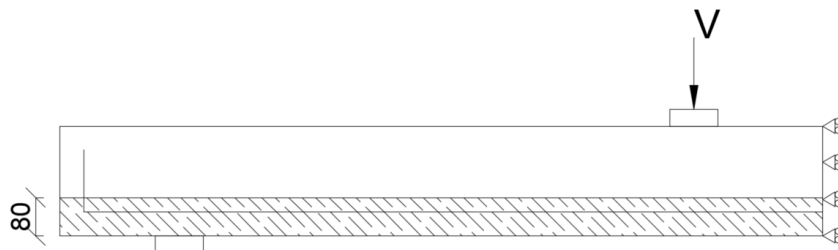


Figure 3.11 – Beam S1D18a108 with tension stiffening zone

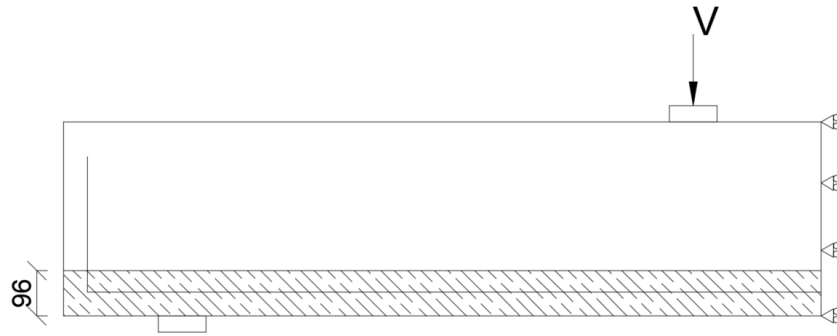


Figure 3.12 – Beam S1&2D36a108 with tension stiffening zone

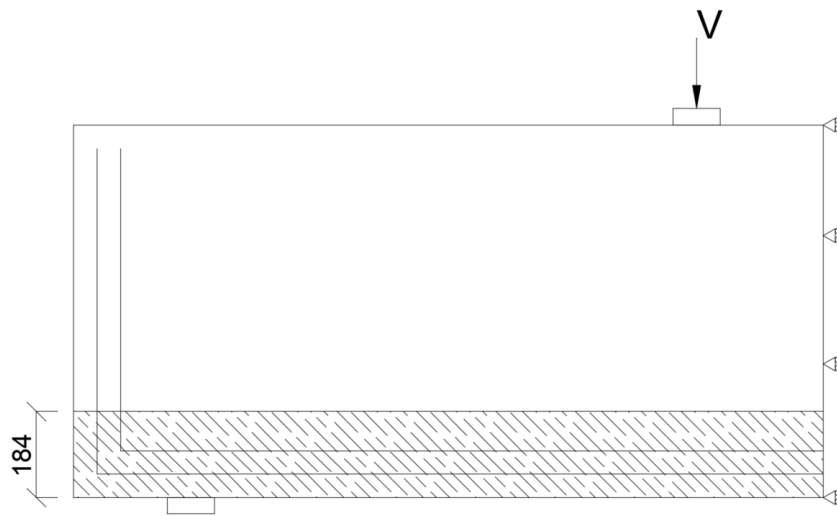


Figure 3.13 – Beam S1D72a108 with tension stiffening zone

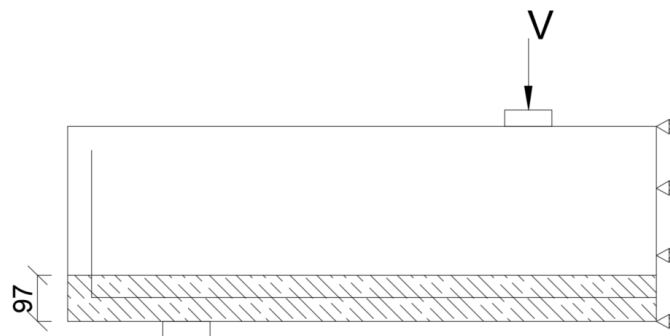


Figure 3.14 – Beam S2D36a72 with tension stiffening zone

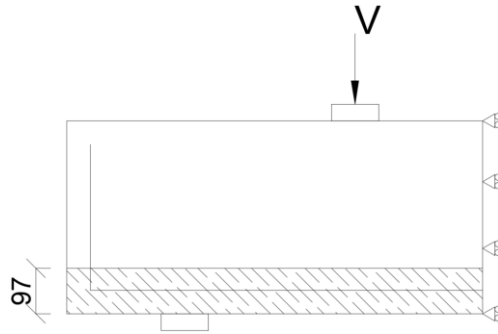


Figure 3.15 – Beam S2D36a36 with tension stiffening zone

Another question is which crack model and shear retention model to use. At this point, different types of both the former and the latter have been analyzed. In these analyses, only the fixed crack model with damage based shear retention shall be used despite the fact that we already know that the damage based model gives inaccurate results for the flexural (S1D18a108, S1&2D36a108) beams. This is done to investigate if the TS model may improve the damage based results on the more flexural beams as well. As can be seen in Chapter 2.5.4 and in Appendix A.3, the damage based shear retention model is conservative as the shear stiffness degrades at the same rate as the secant tensile stiffness due to cracking. Hence, with another softening model in the concrete surrounding the reinforcement, another result might be obtained with the damage based model.

## 4 Finite Element Results and Discussion

This chapter presents the obtained numerical results and the discussion of these. The result layout will follow the same order as presented in Chapter 3.3. There are, as mentioned, five different beam geometries to analyze. These geometries are presented in Figure 3.1 – Figure 3.5. Only half of the beam is modelled, with plane stress formulations. The results will contain comparisons between the numerical analyses and the experiment by Suchorzewski et al. (Suchorzewski et al., 2018).

Appendix C presents the experimental crack pattern, and also numerical crack strain plots with specifications of where on the force-deflection curve the crack plots were extracted. The reason for this is that the amount of different beams and analyses results in a very large number of crack plots, which would be cumbersome to include in Chapter 4. Hence, as this chapter merely discusses the most important crack observations with a limited amount of crack plot visualizations, the complete set of crack strain plots are presented in the appendix.

Furthermore, an important topic was how to determine the failure modes. In de Putters research, a schematic procedure was established in order to define the different failure mechanisms (de Putter et al., 2022). They separated between three different failure modes. Namely, the flexural failure, which implies yielding of the longitudinal reinforcement and crushing of the compression zone or just excessive yielding of the longitudinal reinforcement. Tension shear failure was identified as failure due to opening of the critical inclined crack without crushing of the compression zone, and finally the compression shear failure was marked by crushing of the diagonal strut. However, as the number of analyses in this thesis are fewer than in de Putters, it is possible to evaluate the failure modes more carefully in each analysis.

The consequence of having very clear and specific criteria is that it may fog the mechanisms that actually cause the beams to fail. This can be exemplified by explaining the failure mechanisms of a flexural failure and a compression shear failure. The general understanding of a flexural failure is that the beam bends so much that the reinforcement reaches yielding in the zone of maximum moment. Then, the reinforcement experience large strains, and the cross section gets a smaller, more localized compression zone, which eventually cause concrete crushing. This would let the concrete crush in the area of maximum moment, which will be caused by large stresses aligned with the longitudinal direction of the beam. On the other hand, a compression shear failure, which is described in Chapter 2.6.3, exhibits crushing of concrete underneath the loading plate due to large compressive forces in the beam strut. Furthermore, if the reinforcement yields, the failure of the beam can still be concrete crushing due to too large forces in the compressive diagonal strut, rather than concrete crushing in the area of maximum moment.

In this thesis, several factors played a role when deciding the failure mode. These are factors as global versus local reinforcement yielding (see Figure 4.37), stiffness change after yielding took place, the area of concrete crushing, crack pattern and relative numerical capacities. The main goal is always to locate the mechanism which causes the beam to fail. Obviously, this way of determining failure modes leaves more room for classification errors, as the failure mode does not depend on one single factor. However, the following chapters will attempt to explain the reasons behind each classification, especially where the failure modes are indistinct.

# 4.1 The Influence of Shear Retention Models

Chapter 4.1.1 – Chapter 4.1.5 compare the shear retention models within one beam analysis, while Chapter 4.1.6 compare how the numerical analyses perform overall.

The crack strain plots for the analyses performed in this chapter are visually presented in Appendix C.1.

## 4.1.1 Beam S1D18a108

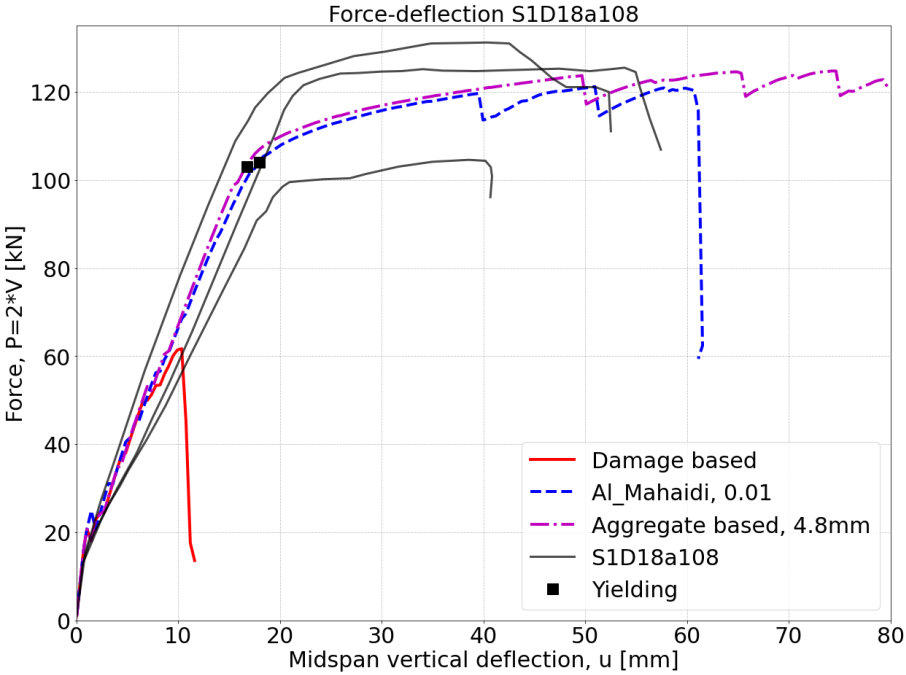


Figure 4.1 – Force-deflection plot for the experiment and varying shear retention models for beam S1D18a108

Figure 4.1 presents the force-deflection curve for lowest beam, denoted as S1D18a108, for three different shear retention models. One can also see three curves for the experiment, as three similar specimens of similar geometry and concrete quality were experimentally tested. This is also the case for the other beams, where two or three similar specimens were tested.

As can be seen in Figure 4.1, the damage based shear retention model deviates from the other two numerical models, as well as the experiment itself. The reinforcement never yielded, and the failure mode obtained by the damage based shear retention model becomes tension shear rather than the expected flexural failure. The wrongly predicted failure mode results in a capacity almost 50% lower than the experimental capacity.

The crack pattern of the damage based shear retention model shows little resemblance to the experimental one, as the development of large, coherent, horizontal cracks presents itself as the beam is loaded. In comparison, the experimental crack pattern has several localized cracks, all being relatively vertical, as the beam fails through extensive yielding of the reinforcement and concrete crushing.

A possible explanation to the capacity deviation between the damage based model and the experimental model might have cause in the formulation of the damage based shear retention model. As presented in Chapter 2.5.4 and Appendix A.3, the shear retention in the cracks descends quickly when using the damage based model. Additionally, there is no shear retention at all when a full macro crack is formed. Hence, since the S1D18a108 beam is flexural, large cracks will occur, and the use of the damage based model would thereby drastically impair the shear retention in these cracks, resulting in the wrongly predicted tension shear failure mode.

On the other hand, both the Al-Mahaidi and the aggregate based shear retention model have good correlation with the experimental results, only deviating from the experimental capacity by 0.36% and 3.32% respectively. In these cases, the failure mode was flexural, as in the experiment. The crack patterns of these models showed better resemblance to the experimental crack pattern than the damage based model did. Even though the formation and number of cracks were sufficiently represented by these models, the distance between localized cracks in the midspan was too short. In addition, the horizontal crack incline in the shear span was somewhat exaggerated in the numerical models, especially by the Al-Mahaidi model. In terms of ductility, the Al-Mahaidi was the most accurate.

As mentioned, all three shear retention models were analyzed and compared in Appendix A.3. Here, one could see that the Al-Mahaidi shear retention curve showed similarities to the damage based shear retention curve. However, an important difference between the models were the fact that the Al-Mahaidi retains a small amount of shear retention even when the cracks grow large, while the damage based, as mentioned, does not. Hence, this chapter shows that this small amount might be the difference between a correct and a wrongly predicted failure mode.

### 4.1.2 Beam S1&2D36a108

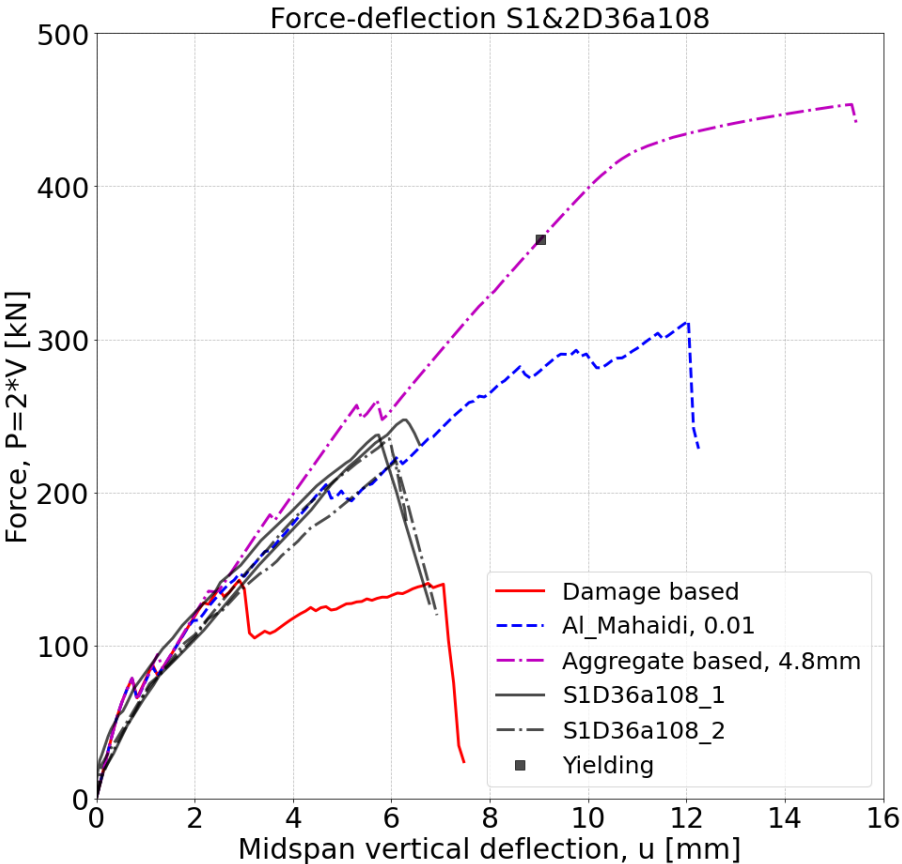


Figure 4.2 – Force-deflection plot for the experiment and varying shear retention models for beam S1&2D36a108

Note the two experiments noted as S1D36a108\_1 and S1D36a108\_2 in Figure 4.2. This refers to the experiments from series 1 and series 2 respectively. Also note that the experiments are having quite similar responses, which is the reason why separate analyses for the two experiments seemed unnecessary.

Furthermore, as seen in Figure 4.2, again, the damage based shear retention model deviates from the other two models. However, for this analysis, none of the three models were able to present a good representation of the experimental behavior.

The damage based shear retention model might suffer the same destiny as in the analysis of the S1D18a108-beam. The S1&2D36a108 beam is also relatively flexural, giving large cracks and thereby little post-crack shear resistance. The capacity is underestimated with almost 40% by the damage based model.

The other two shear retention models seem to have the opposite effect, giving too much resistance in the cracks. As the experimental failure mode was tension shear, the damage based, Al-Mahaidi and aggregate based shear retention model yielded a tension shear, compression shear and flexural failure mode respectively. The Al-Mahaidi overestimated the capacity by 32%, while the aggregate based almost doubled the experimental capacity.

In the damage based model, also the crack propagation is similar to the analysis of the S1D18a108 beam. That is, a large diagonal crack takes form and makes the beam fail in tension shear. This crack pattern does in fact not deviate a lot from the experimental crack pattern. However, it seems like the damage based model has a tendency to underestimate the experimental capacity when failing in tension shear – despite being the correct failure mode.

The Al-Mahaidi shear retention model showed quite interesting results. Initially, it follows the experimental force-deflection curve almost identically, before it loses capacity around 4-5 mm deflection. Instead of continuing to a tension shear failure, a new crack pattern starts to form directly from the loading plate to the bearing plate, giving a capacity estimation about 30% above the experimental values, and failing in compression shear.

Similar tendencies were elaborated on by de Putter (de Putter et al., 2022), where several of the numerical analyses estimated a compression shear failure rather than tension shear or flexural failure. It was stated that the position of the critical shear cracks were changed from their original position, which crosses the compressive strut, to their final position, which was under the strut. This over-rotation of crack patterns enables the possibility to have an alternative shear force transfer mechanism through the compression strut, thus, significantly increasing the load bearing capacity. As the term “over-rotation” might indicate, this spurious behavior was only reported for the rotating crack models, and not the fixed ones, in de Putter’s research. However, de Putter only utilized one type of shear retention model for the fixed crack models, namely, the damage based shear retention model. As we can see in Figure 4.2, the fixed, damage based shear retention model does not exaggerate the capacity by creating a new crack pattern.

The cause of the reestablishment of crack paths cannot be the result of over-rotation, as the crack model is fixed. As this does not happen for the damage based shear retention model, it would be logical to assume that the higher amount of shear retention in the Al-Mahaidi model is sufficient enough to cause shear stress locking in the crack, not letting the beam fail in tension shear, but compression shear. The alternative crack formation formed in the Al-Mahaidi model is presented in Figure 4.3. Figure 4.3 A) and B) is plots just before and after the capacity drop at 5 mm, while Figure 4.3 C) is the final crack pattern just after failure. The expression used in this thesis, “reestablishment of crack pattern”, then refers to a similar change in crack pattern as observed in Figure 4.3.

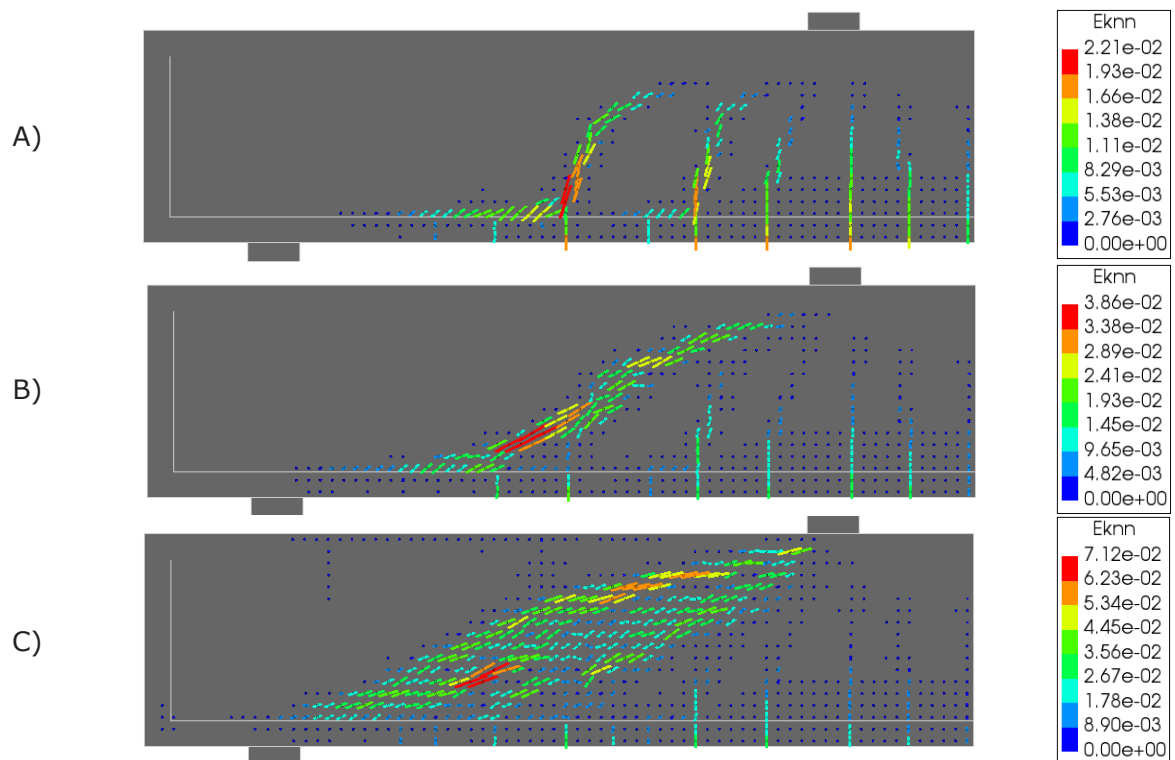


Figure 4.3 – Crack strain plot of S1&2D36a108 with the Al-Mahaidi shear retention model, establishment of an alternative crack formation

The aggregate based shear retention model also shows a capacity drop close to the experimental failure. However, in this case, the reestablishment of the crack pattern is not as obvious as in the Al-Mahaidi case. A direct, coherent, and localized crack between the loading plate and the support plate never took place in the aggregate based model, as a contrast to the Al-Mahaidi model. Also, the vertical cracks in the bending zone of the beam had a relatively large size compared to the inclined cracks in the shear zone. This is also in contrast to the Al-Mahaidi and damage based model, where the inclined crack in the shear zone clearly dominated in size. The cause may again be shear stress locking in the cracks.

In short, the following can be stated:

- The damage based shear retention model has too low shear resistance in the cracks, as it has the correct failure mode, but too low capacity.
- The Al-Mahaidi shear retention model has enough shear resistance in the cracks to create an alternative crack path which carry the shear in an alternative way through the compressive strut.
- The aggregate based shear retention model simply has too much shear resistance in the cracks, as the beam seems rather unaffected by the inclined shear cracks, and just keeps expanding the vertical flexural cracks as the loading proceeds, finally failing in a flexural failure mode.

### 4.1.3 Beam S1D72a108

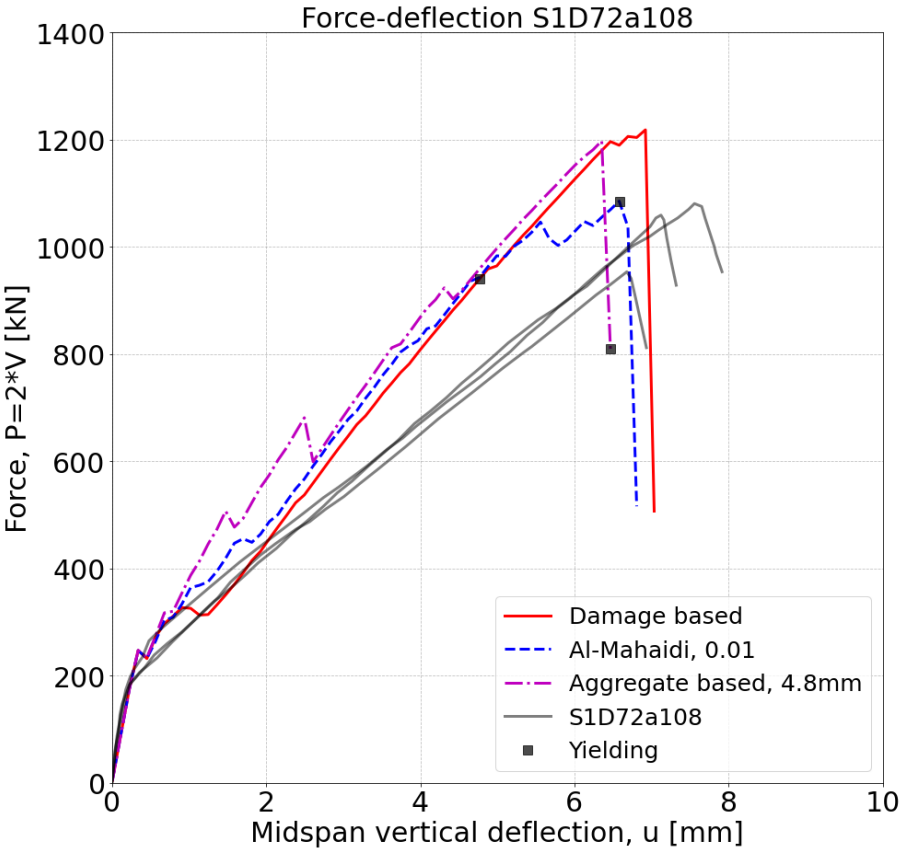


Figure 4.4 – Force-deflection plot for the experiment and varying shear retention models for beam S1D72a108

Figure 4.4 presents the numerical and experimental comparison of the S1D72a108 beam. The different shear retention models did not deviate a lot from each other, and relatively good correlation was found between the experiment and the analysis.

The damage based shear retention model did in fact show the highest capacity (unlike the previous analyses), with an overestimation of the experimental mean capacity of 18.3%. The Al-Mahaidi overestimated the capacity by 8.4%, while the aggregate based overestimated the capacity by 16.3%. All three shear retention models were evaluated to have the compression shear failure modes, despite yielding in the reinforcement. The model which experienced most yielding was the damage based model shear retention model. However, the failure mode was still classified as compression shear due to the fact that only one of the two reinforcement layers yielded, in combination with not showing tendencies to opening of flexural cracks. In addition, the general behavior of the force-deflection curve did not flatten out or change direction after yielding took place. As a final argument, the reinforcement yielding only took place locally. Local yielding is discussed in Chapter 4.3.5. The Al-Mahaidi and the aggregate based shear retention model experienced yielding in a late stage, and also only in one of the reinforcement layers. Hence, a flexural failure mode would be a less suiting classification than the compression shear failure mode.

By further analyzing Figure 4.4, one can see that the elastic phase and the first change in the force-deflection curve due to cracking is correct compared to the experimental behavior. On the other hand, all three models shows that the cracking propagation phase,

that is between the first force-deflection curve change and the capacity peak, acts too stiff compared to the experimental results.

The damage based shear retention model showed a development of too few cracks compared to the experimental crack pattern, in addition to lacking a more direct crack path from the loading plate to the support plate. The two other models were able to represent a crack pattern more similar to the experimental one. This direct crack pattern takes place in the experiment because the shear span to effective depth ratio  $a/d = 1.5$ , which is quite low, and thereby allows for a direct force transfer from the loading plate to the support plate.

Another deviation from the experiment was the formation of a vertical crack forming in the top of the beam above the support plate. This more or less took place for all three models. If we plot the in-plane principal stresses before and after this crack formation, one can see that tension stress is building up in the upper region of the beam and being released as the crack forms. This is illustrated in Figure 4.5.

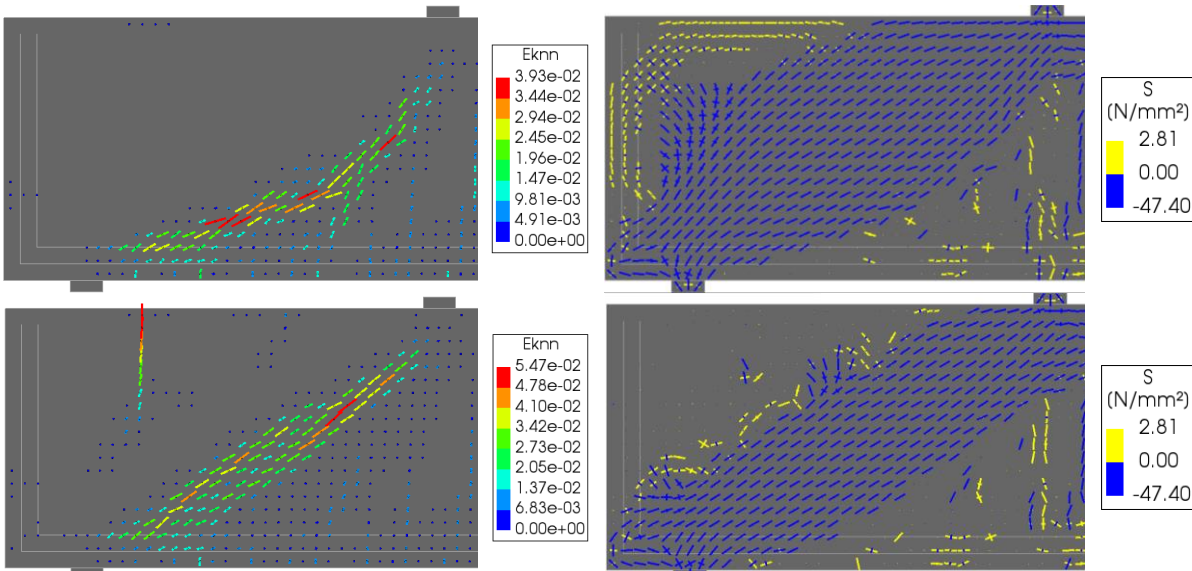


Figure 4.5 – Crack strain (left) and principal stress (right) before and after the emergence of a crack in the top part of the beam for the Al-Mahaidi shear retention model

One possible solution to the behavior observed in Figure 4.5 could be that the anchorage is experiencing too large tensile stresses in its longitudinal direction, and by the looks of it, is pulling the concrete in the upper part of the beam. The reason for the large tensile stresses in the anchorage may be the result of a loose or damaged bond between the longitudinal reinforcement and the concrete, so that tensile stresses in the longitudinal reinforcement are no longer a clean function of the moment force but are working more like a rope pulled in each end, where the ends would be the anchorage.

Alternatively, or additionally, stresses in the longitudinal reinforcement close to the anchorage must arise to satisfy equilibrium whenever inclined cracking takes place near the support, as illustrated to the right in Figure 4.38. This is also described in the Eurocode and is taken into consideration by shifting the moment diagram (Eurocode 2). Regardless of what the exact reason for this spurious crack formation might be, it was necessary to investigate whether or not it influenced the capacity of the beam. Two different approaches

were used in an attempt to try to fix the spurious cracking, which are illustrated in Figure 4.6.

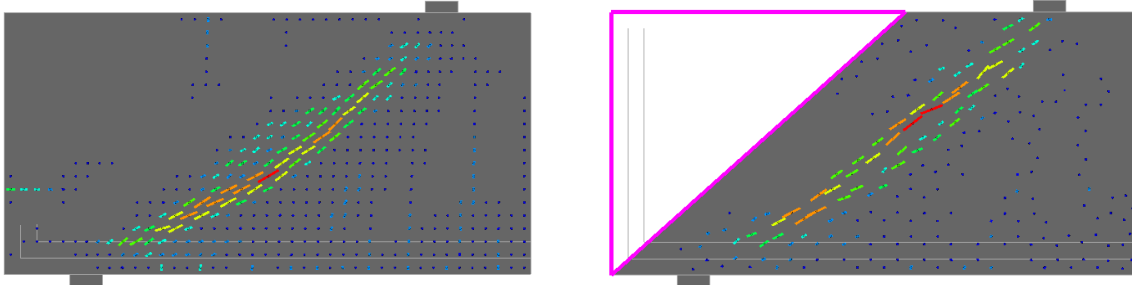


Figure 4.6 – Crack strain plots with short anchorage (left) and an isotropic linear elastic corner (right)

In the first attempt, the anchorage length was decreased, presented to the left in Figure 4.6. This was done in order to evaluate the effect of the long anchorage on the top beam cracks. The smaller anchorage resulted in a reduced top-beam crack size. However, the cracks were not eliminated, and also, another spurious crack of larger size appeared above the anchorage. Hence, despite improving the crack pattern, it was concluded that lowering the anchorage was not sufficient enough.

The next alternative considered a corner part of the beam as linear elastic. This is illustrated to the right in Figure 4.6, where elastic material properties were inserted in the white part of the beam with the pink contour. That way, cracking in this zone is entirely eliminated, which can be observed in the crack strain plot in the figure. The resulting force-deflection for this beam was plotted in Figure 4.7 and was compared to original Al-Mahaidi beam without the elastic corner.

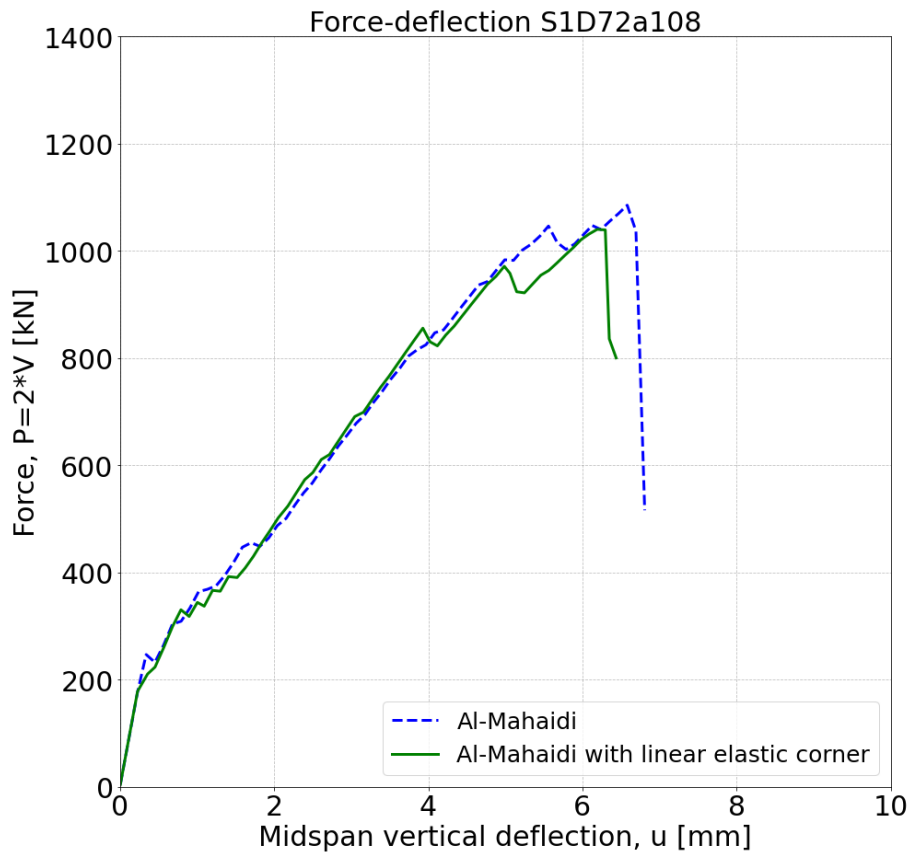


Figure 4.7 – Force-deflection plot using the Al-Mahaidi shear retention model for beam S1D72a108 with and without a linear elastic corner

As Figure 4.7 illustrates, the deviation between the two models is not large. Note that to insert the elastic material properties to the corner of the beam, an oblique separation line had to be drawn. This oblique line made it impossible to obtain the same meshing layout as the one presented in Figure 3.8. Thus, the small deviation in the force-deflection diagram might also be caused by the different meshing layouts.

Throughout the analyses in this thesis, other models and beams also exhibited the discussed top-beam cracking. However, separate analyses for each of these cases would be very time consuming and probably repetitive. Therefore, with the findings in this chapter, it is concluded that the spurious cracking in the top of the beam does not affect the behavior in such a degree that it is necessary to prevent this in each case.

### 4.1.4 Beam S2D36a72

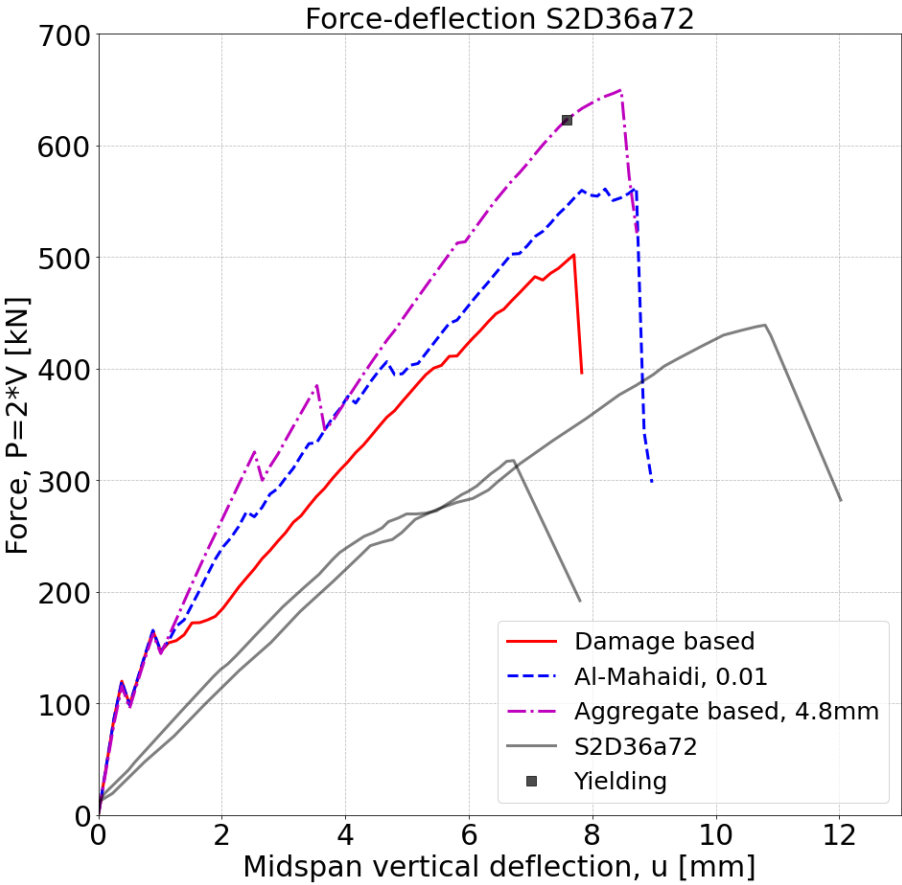


Figure 4.8 – Force-deflection plot for the experiment and varying shear retention models for beam S2D36a72

Figure 4.8 presents the numerical and experimental comparison of the S2D36a72 beam. The numerical analyses acts too stiff and are reaching much higher capacities than the one reached in the experiment. The damage based shear retention model overestimates the capacity by 32.2%, Al-Mahaidi overestimates by 48.0 % and the aggregate based by 71.1%. However, these numbers are comparisons of the numerical capacity and the *mean* experimental strength. This is of particular importance for this beam, as the S2D36a72 beam turned out to work as a transitional limit between high and low beams where the failure changed its mode (Suchorzewski et al., 2018). As can be seen in Figure 4.8, the two experimental force-deflection curves show quite different capacities. The highest capacity exceeds the lowest by 37%, which is due to a tension shear failure in one experiment, and compression shear failure in the other. As all of the failure modes in the numerical analyses were determined to be compression shear or even flexural, the comparison with the mean experimental values resulted in large overestimations.

Nevertheless, by comparing the numerical capacities only to the experiment failing in compression shear, there are still large overestimations of 14.3%, 27.9% and 47.9% for the damage based, Al-Mahaidi and aggregate based shear retention model respectively. This overestimation might still have cause in the relatively flexural nature of this beam. It is worth noting that Suchorzewski classified a compression shear failure as a tangential

crack slip of considerable size, compared to the normal crack opening. Hence, a combination of a large normal crack opening and a large tangential crack slip will also be determined as a compression shear failure. Thereby, if the experimental critical crack already exhibited a substantial normal crack opening, the resistance for tangential crack movement would decrease. As the numerical models have continuously showed incapability of properly representing a tension shear failure, the experimental compression shear failure affected by the characteristics of a tension shear failure might also be badly predicted by the numerical models.

Furthermore, as mentioned, the compression shear failure was the failure mode for the damage based and Al-Mahaidi shear retention model, while the aggregate based yielded a flexural failure. All models failed due to crushing of the concrete, but only the aggregate based model had yielding in the reinforcement. In addition, one can also see that the force-deflection curve changes behavior after yielding, and the crack pattern have vertical, flexural cracks of considerable sizes.

The damage based shear retention model formed too few cracks. The crack formation missed the outer experimental crack in which eventually caused the experimental beam to fail. Beyond this, the crack pattern was quite similar to the experimental one.

Both the Al-Mahaidi and the aggregate based shear retention model gave straight crack paths between the loading plate and the support plate. The experiment also showed a crack leading from the loading plate to the support plate, but the crack was more curved compared to the cracks in the numerical analyses.

### 4.1.5 Beam S2D36a36

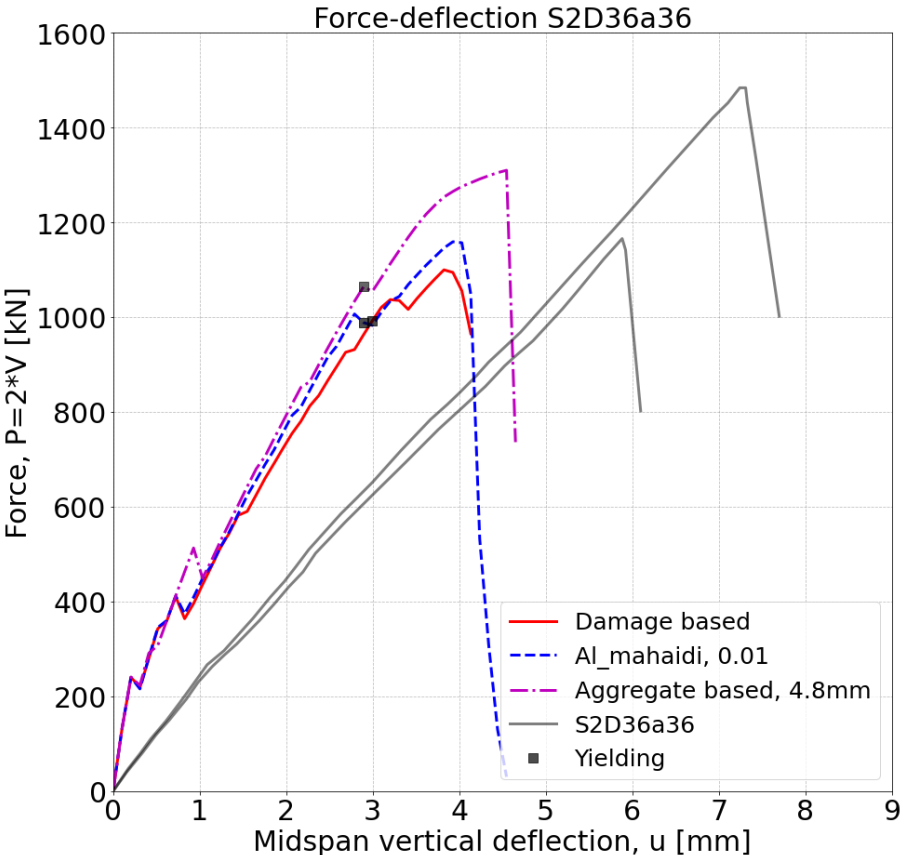


Figure 4.9 – Force-deflection plot for the experiment and varying shear retention models for beam S2D36a36

Figure 4.9 shows the numerical and experimental force-deflection curves of the S2D36a36 beam. Even though all numerical models experienced yielding of the reinforcement, a difference was observed between the aggregate based shear retention model and the other two. While the yielding of the reinforcement for the aggregate based model was widespread across a larger area in the midspan of the beam, the other two models had a local area of yielding, being restricted to only a short span at the end of the compressive strut (see example in Figure 4.37 and Chapter 4.3.5). One can also see how the global and local yielding of the reinforcement affect the force-deflection curve differently, as the aggregate based shear retention model showed a descending stiffness before failure took place, which is not as clear in the other two models. Thus, the failure mode for the aggregate based shear retention model will be classified as a flexural failure, while the other two will be classified as compression shear.

One can see, as in the S2D36a72 beam, that the initial elastic stiffness of the numerical analyses differs from the experimental elastic stiffness. It almost seems like the experiment does not yield a pre-crack phase and post-crack phase, as it is hard to detect any change in the experimental force-deflection curve. Initially, it was assumed that this could either be due to a very small pre-crack elastic range, as a very small experimental pre-crack phase was observed in Figure 4.8, or that initial cracks in the beam were present

before the experiment took place. However, calculations presented in Appendix B.3 revealed that the former argument would most likely not be the reason for the numerical and experimental deviation. The reason for the initial stiffness deviation is further discussed in Chapter 4.1.6.

The crack propagation phase also acts too stiff. This causes the numerical ductility to be too small, compared to the experimental ductility. The capacity is in this case numerically underestimated. The numerical capacity is 17.3%, 12.9% and 1.5% lower than the experimental mean capacity for the damage based, Al-Mahaidi and aggregate based shear retention model respectively.

This beam has the smallest shear span to effective depth ratio, where  $a/d = 1.0$ , which causes the experimental crack pattern to form a direct and relatively linear crack path between the loading plate and the support plate. This direct crack path is also seen in all three numerical analyses.

#### 4.1.6 Comparisons and Remarks

Table 4.1 – Summary of chapter 4.1 – The influence of varying shear retention models

Beam	Mean capacity (experiment)[kN]	Failure mode (exp)	Shear retention model	Mean capacity (DIANA)[kN]	Failure mode	Difference [%]
S1D18a108	120.74	Y	Dam.	61.70	T	-48.9
			Al-M.	121.18	Y	0.4
			Agg.	124.75	Y	3.3
S1&2D36a108	235.95	T	Dam.	142.66	T	-39.5
			Al-M.	311.94	C	32.2 (-13.0*)
			Agg.	453.46	Y	92.2 (8.9*)
S1D72a108	1029.70	C	Dam.	1218.55	C	18.3
			Al-M.	1116.14	C	8.4
			Agg.	1197.84	C	16.3
S2D36a72	379.80 (439.43/320.17)	C/T	Dam.	502.12	C	32.2 (14.3**)
			Al-M.	562.10	C	48.0 (27.9**)
			Agg.	649.88	Y	71.1 (47.9**)
S2D36a36	1330.48	C	Dam.	1100.02	C	-17.3
			Al-M.	1159.29	C	-12.9
			Agg.	1310.11	Y	-1.5

\*Manually deciding the capacity by locating the moment of crack path reestablishment

\*\*Compared only to the experimental compression shear capacity

Table 4.1 summarizes and compares the experimental and numerical failure modes and capacities for each beam in Chapter 4.1. In the table, two marks (\* and \*\*) are added. The first mark (\*) describes the numerical and experimental capacity difference if one were to compare the manually located numerical capacity at the moment of crack path reestablishment, as can be seen in Figure 4.3, with the experimental mean capacity. This

is somewhat discussed in de Putters research (de Putter et al., 2022), as they added an alternative way of determining the capacity for beams expected to fail in tension shear. In this case, the failure load was no longer taken to be the maximal sustained load in the numerical analysis, but the load at the moment where the shear crack opened and changed the crack path. As mentioned, this includes a manual interpretation of the results. As explained in the de Putters research, this only happened for the rotating crack models, which was not used in Chapter 4.1. As discussed in Chapter 4.1.2, shear stress locking in the cracks enables the reestablishment of the crack pattern, letting the analysis continue to reach a higher capacity as it yields a different failure mode than the expected tension shear failure. The second mark (\*\*) is simply included to have an isolated comparison of the numerical and experimental capacity of the same failure mode, which would be compression shear, in the S2D36a72 beam.

One insecurity in Table 4.1 is whether or not to include an improved, manual determination of the capacity for the aggregate based shear retention model in the S1&2D36a108 beam. The reason for this was touched upon in Chapter 4.1.2, as the crack path reestablishment of the aggregate based shear retention model was not as obvious as in the Al-Mahaidi case. The insecurity lies in whether the capacity is overestimated due to an alternative transfer of the shear, as is clearly seen in the Al-Mahaidi case, or if the overestimation is simply due to the fact that the aggregate based shear retention model provides too large shear resistance in the cracks. The latter is also supported by the fact that the aggregate based analysis does not fail in a compression shear failure, but in a flexural failure, containing yielding of the reinforcement in combination with crushing of the concrete. Nevertheless, the improved, manual comparison is included for the aggregate based shear retention model as the force-deflection curve shows a clear disruption very close to the moment of experimental failure before it continues and completes its path by failing in a flexural mode.

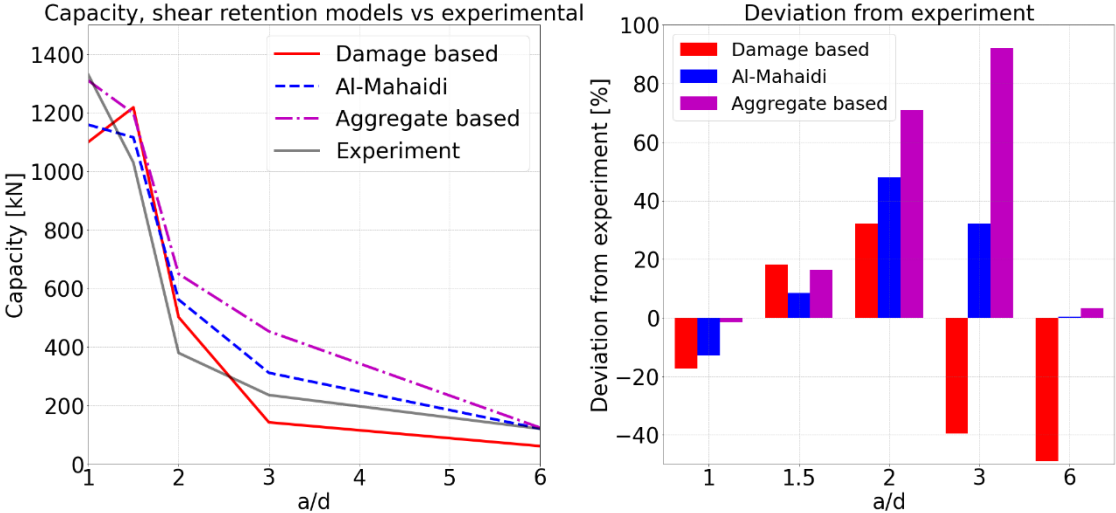


Figure 4.10 – Capacity comparison (left) and a capacity deviation diagram (right) between numerical and experimental results for the shear retention analysis

Figure 4.10 visualizes the numerical and experimental differences. The figure to the left shows how the numerical models follows the capacity of the experiment, while the right

shows the numerical capacity deviation from the experiment for every shear span to effective depth ratio. Negative percentages in the right figure means that the numerical capacity was lower than the experimental capacity, and vice versa. As illustrated, the numerical models especially struggle to give reasonable predictions of the experimental behavior for the beams with intermediate shear span to effective depth ratios. That is for  $a/d = 2.0$  and  $a/d = 3.0$ . As pointed out in Chapter 2.6, these ratios have the properties of experimentally failing in tension shear, which turned out to be difficult to numerically simulate. The only model that produced a tension shear failure was the damage based shear retention model. However, the experimental capacity was underestimated, for reasons discussed in Chapter 4.1.1 and Chapter 4.1.2. On the other hand, for very low shear span to effective depth ratios (1 and 1.5) or high ratios (6) the numerical models were for the most part (not the damage based for high ratios) able to give good predictions of the experimental capacity.

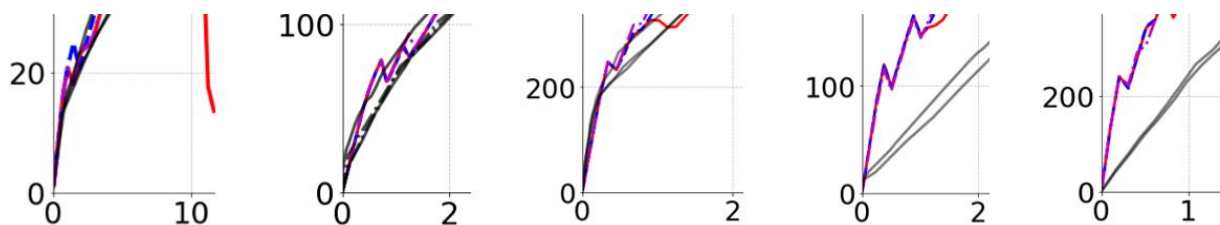


Figure 4.11 – Initial slope of the numerical and experimental force-deflection curves for beam S1D18a108, S1&2D36a108, S1D72a108, S2D36a72 and S2D36a36

Figure 4.11 shows the initial slopes of the force-deflection curves for the different beams. It is noted that the numerical force-deflection curve struggles to follow the initial experimental slope as the beams gets shorter. Some of the possible reasons for this were discussed in Chapter 4.1.5, where it was assumed to be caused either by pre-existing cracks or a very small pre-cracking phase. However, an analytical comparison provided in Appendix B.3 found that the numerical initial stiffness is more correct than the experimental initial stiffness. In addition, the deflection at crack initiation was also calculated. The results are presented in Table B.4.

The analytical calculation showed that for the beams S2D36a72 and S2D36a36, the deflection at crack initiation should be 0.21 mm and 0.11 mm respectively, while the representative numerical deflections were found to be 0.38 mm and 0.21 mm. Hence, the analytical and numerical values are in fairly good agreement. (Note that the crack initiation in the numerical context means the point where the cracks localizes. It is at this point one can see that the force-deflection curve is changing direction, and not necessarily at the point where the first cracks appear in the numerical model. An example of initial non-localized cracks which do not affect the stiffness in a particular degree is presented in Figure 4.26. By these statements one can find the numerical deflection at crack initiation in Figure 4.11, by locating the deflection at the point of the first “bump” in the numerical force-deflection curves.)

In the calculations of the deflection at crack initiation, the cracking-force was also calculated. These values were not presented in Appendix B.3, as they were not the main focus of the calculation, but they revealed to be 82.6 kN and 165 kN for beam S2D36a72

and S2D36a36 respectively. As the numerical force at cracking were 120 kN and 241 kN, it overestimates the analytical force to some degree, but undoubtedly provides a closer estimate than the experiments.

All in all, these results show that the experimental force-deflection curves for the shortest beams (S2D36a72 and S2D36a36) lack a proper pre-crack phase compared to the analytical results. Hence, the former discussed option of a very small pre-cracking phase is probably not the answer of the numerical and experimental initial deviation in the force-deflection.

The analytical calculations and numerical results then rise questions to the accuracy of the experiment itself. Thus, the author of the experiment, Dr. Jan Suchorzewski, was contacted in an attempt to clarify the issue. In the email response, Dr. Suchorzewski mentioned that the problem could be related to incorrect settings of the support, despite the fact that they were measured. Furthermore, he also mentioned that a colleague, who has also simulated the experiments, has had similar problems (Suchorzewski 2022; Marzec et al., 2019). The sensitivity to the stiffness of the loading frame is significant for the shorter beams (S2D36a72 and S2D36a36). Thereby, it is concluded that the most probable cause of the stiffness deviation between the numerical analyses and experiment seen in beam S2D36a72 and S2D36a36 in Figure 4.11 is the result of experimental errors.

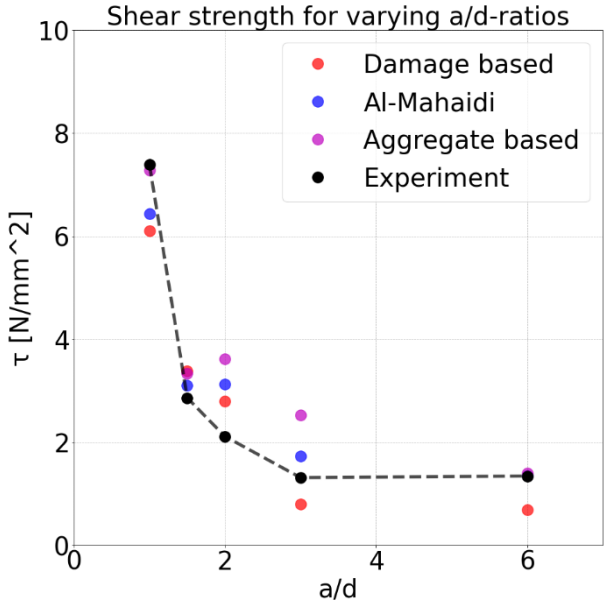


Figure 4.12 – Experimental and numerical shear strength  $\tau = \frac{P}{2td}$  ( $P = 2V$ ) for varying a/d-ratios for different shear retention models

As described in Chapter 2.7, to capture the size effect, and no other influences, one must consider structures of different sizes but geometrically similar shapes. This is not the case in the present study, as length and height of the structure was independently adjusted. This is why Figure 4.12 plot the shear strength as a function of the shear span to effective depth ratio. The differing shear strength in Figure 4.12 is especially affected by varying failure mechanisms, and in general how the loading is transferred through the beam and on to the support. In addition, the size effect, described in Chapter 2.7, will also contribute to the differing shear strength.

# 4.2 The Influence of Crack Models

Chapter 4.2.1 – Chapter 4.2.5 compare the fixed, rotating, and different rotating to fixed (RTF) crack models within one beam analysis, while Chapter 4.2.6 compare how the numerical analyses perform overall. In this chapter, the terms half, full and 5\*full RTF crack model will be used. This refers to the total normal strain threshold value in which the model shall switch from a rotating to a fixed crack model. The models are further explained in Chapter 3.3.2.

The fully fixed crack model is the same as presented and discussed in Chapter 4.1, hence, this model will not be the main focus in this chapter. Yet, the fully fixed model will be presented, and in some occasions shortly discussed, in order to get a good perspective on how the numerical behavior varies between the different crack models.

The crack strain plots for the analyses performed in this chapter are visually presented in Appendix C.2.

## 4.2.1 Beam S1D18a108

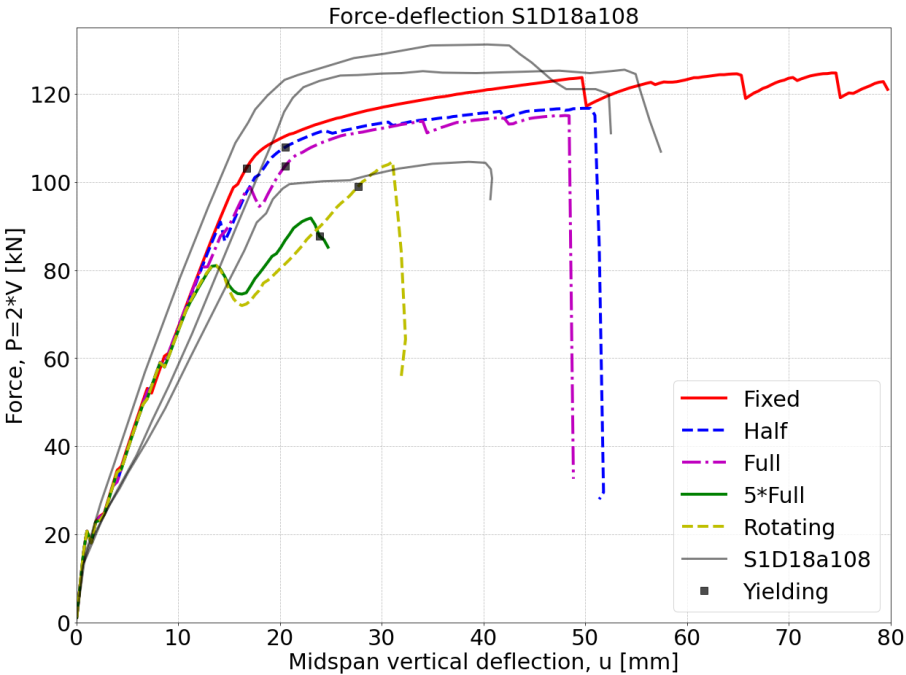


Figure 4.13 – Force-deflection plot for the experiment and varying crack models for beam S1D18a108

Figure 4.13 shows the force-deflection curve for the beam S1D18a108, for five different crack models, as explained in Chapter 3.3.2. For the most part, the RTF crack models, denoted as half, full and 5\*full in Figure 4.13, proves to give a force-deflection curve between the fully fixed and fully rotating crack model throughout the analyses in Chapter 4.2. If the threshold value is very small, then the RTF model will act more like the fixed

model, and if it is large, it will act more like the rotating model. This can also be seen in Figure 4.13.

In the half and full RTF crack models, the ductility is severely improved compared to the other numerical models. Both of these models show good resemblance to the experimental behavior, and yield the same failure mode as the experiment, namely the flexural failure mode. The capacity of the half and full RTF crack models underestimated the mean experimental capacity by 3.3 % and 4.7 % respectively. The crack pattern of the half RTF crack model are quite similar to the one of the fully fixed crack model, while the full RTF crack model have a crack pattern that looks like a mixture of the fully fixed and fully rotating crack pattern. Also, for all analyses in Chapter 4.2, the crack patterns seems to work “between” the fully fixed and fully rotating crack model, where if the threshold value is very small, then the crack pattern of the RTF model will look more like the one in the fixed model, and vice versa.

The fully rotating crack model and the 5\*full RTF crack model did not show experiment-like force-deflection behaviors. The force-deflection curves turn to early, at around 13-14 mm deflection, lose some capacity, before they increase again, and finally fail at 20-30 mm deflection. The fully rotating crack model underestimates the experimental capacity by 13.3 %, while the 5\*full RTF crack model underestimates the experimental capacity by 24.0 %. In the crack strain plots in Appendix C.2.1 it can be seen that the “bump” in the force-deflection curves in Figure 4.13 (seen in the rotating, 5\*full and slightly in the full RTF crack model) takes place in conjunction with the formation of a large coherent and inclined crack. The crack stretches from the loading plate to the support plate, as illustrated in Figure 4.14.

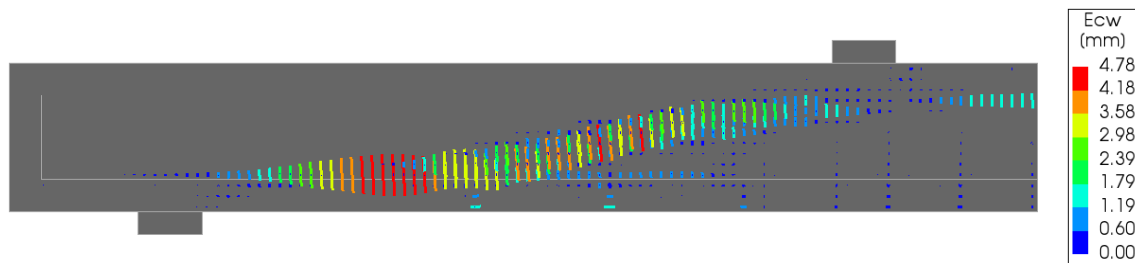


Figure 4.14 – Crack width formation after failure for the fully rotating crack model for beam S1D18a108

Note that in Figure 4.14, the crack widths are plotted. In this case, the lines are plotted orthogonal to the actual crack direction. It is also scaled by value, so the larger the crack width, the longer the lines. This illustrates the relative domination of the inclined crack. It is also observed that the cracks are parallel to the reinforcement, and not orthogonal, as one might expect for this type of flexural beam.

In Chapter 4.1.2, the topic of over-rotation of cracks was mentioned. The issues of over-rotation was faced in de Putters research, as 24 of the beams with experimentally observed flexural (bending or tension shear) failure were simulated as compression shear failure, due to the critical crack changing from its original position, which crosses the strut, to its final position being under the strut (de Putter et al., 2022). This issue is present for beam

S1D18a108, and also for the other beams in Chapter 4.2, which uses the rotating crack model.

In an attempt to understand why the over-rotation is happening, it was necessary to take a closer look at the formulation for the rotating crack model, which was presented in Chapter 2.5.2. As explained, co-axiality between the principal stress and the principal strain is enforced in the rotating crack model. With this enforcement, a shear stiffness is generated. Furthermore, in an experiment where reinforced concrete panels were exposed to large shear stresses, it was proven that the rotation of the principal stress lagged behind the rotation of the principal strain (Vecchio and Lai, 2004). Thereby, it is possible that the shear stiffness generated in the rotating crack model causes the original, "correct" critical crack to over-rotate. As the stiffness is only reduced orthogonal to the crack direction, the over-rotation of cracks will also result in an over-rotation of the stiffness reduction. This also implies that the initially damaged concrete can regain stiffness. Hence, it is possible that the process of crack over-rotation provides new stiffness to a critical crack instead of opening it, and in the same process, forms a new crack from the support plate to the loading plate, as for example illustrated in Figure 4.19 B).

Furthermore, the failure mode in the rotating crack model might look like a tension shear failure, but the concrete in the compression zone in the midspan crushes as the beam fails. Due to the small range of yielding (see Figure 4.13), it is difficult to assess whether the failure mode can indeed be classified as the flexural failure mode, or if it is compression shear. Either way, the large, diagonal crack does not match the experimental crack pattern, and the force-deflection behavior suffers from this. Despite the uncertainty, the failure mode is concluded to be flexural, as the yielding of reinforcement takes place before the final capacity. Note that this argument alone has not been reason enough to classify the beam as flexural in other analyses, but have, in those cases, also shown more characteristics similar to a compression shear failure, than in the present case.

The failure mode of the 5\*full RTF crack model is also difficult to assess. One can see that the curve reaches its maximum capacity before yielding in the reinforcement occurs, hence the conclusion of a flexural failure might be misleading. In addition, the concrete does not crush as the beam fails. Therefore, the failure mode is considered to be a tension shear failure.

## 4.2.2 Beam S1&2D36a108

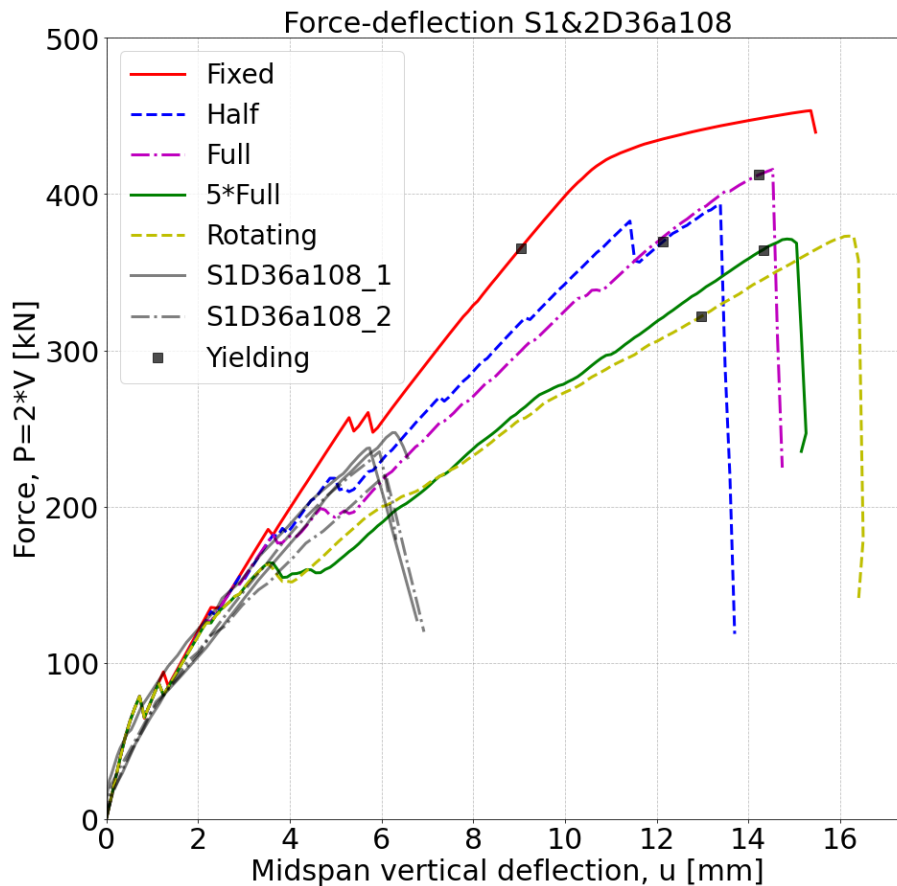
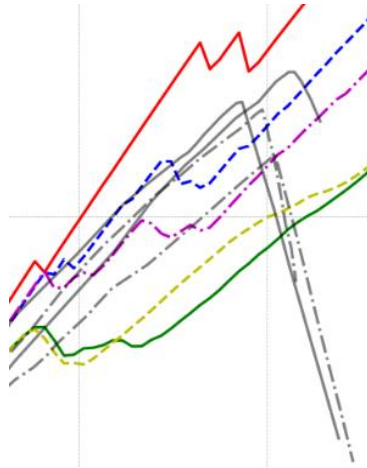


Figure 4.15 – Force-deflection plot for the experiment and varying crack models for beam S1&2D36a108

Figure 4.15 shows the force-deflection curves for the beam S1&2D36a108. As the fully fixed crack model yielded a flexural failure due to shear stress locking in the cracks, discussed in Chapter 4.1.2, and the fully rotating crack model suffers from over-rotation of the crack pattern, as discussed in Chapter 4.2.1, and failing in compression shear, all the RTF crack models also suffered wrong failure modes. Hence, every model heavily over-estimated the experimental capacity, where the numerical model which was closest to the experimental capacity had an over-estimation of 57 %, being the 5\*full RTF crack model. Every model experienced reinforcement yielding, however, only the fully fixed model is concluded to have a flexural failure. This is mainly because the yielding of the other models does not seem to affect the structural behavior in a considerable degree, as it does in the fully fixed model. In addition, only the fully fixed model had relatively large, vertical cracks in the midspan, which insinuates a flexural bending failure.

However, every model also shown the “bump” in the force-deflection curve, which can be seen in Figure 4.15 and more closely in Figure 4.16.



*Figure 4.16 – Reestablishment of crack pattern reflected in the force-deflection curve*

As discussed in Chapter 4.1.6, de Putter established an alternative, manual way of determining the numerical capacity. This can also be done for the models in this chapter, at the curve-disruptions observed in Figure 4.16. This would drastically improve the capacity for all models, from the original errors spanning from 57 % to 92 % to the improved -31 % to 9 %. However, this method is evaluated to be not sufficient enough to be included in an acceptable unified solution procedure for the beams in this thesis, as this would demand a certain experience and general practice from the user. In other words, these manually improved results will not be taken into consideration when the main research question of this thesis is answered, as presented in Chapter 1.

### 4.2.3 Beam S1D72a108

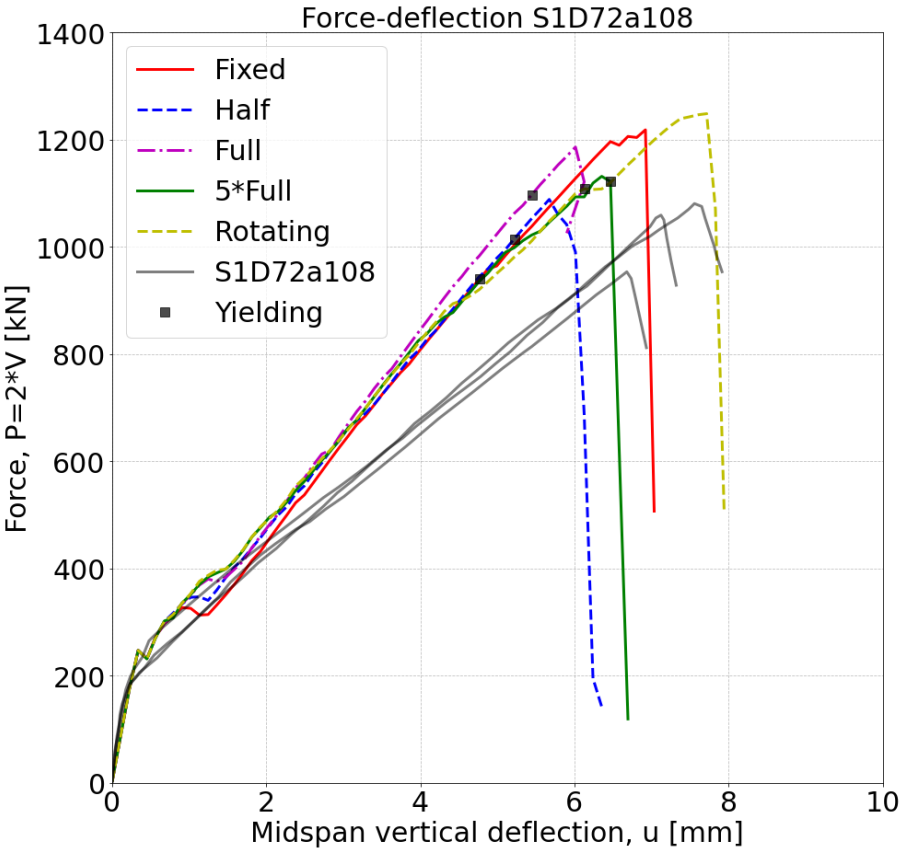


Figure 4.17 – Force-deflection plot for the experiment and varying crack models for beam S1D72a108

Figure 4.17 presents the force-deflection plots for the beam S1D72a108. Note that in this analysis, we switch the shear retention model from the aggregate based to the damage based, for reasons discussed in Chapter 3.3.2. The numerical models did not deviate a lot, and overestimated the experimental capacity by 6 % - 21 %, approximately. The formation of the critical crack in the fully fixed crack model forms along the reinforcement before it grows into the web approximately at the middle between the load plate and the support plate. On the contrary, the fully rotating crack model forms a longer critical crack expanding from the load plate to the support plate. Similar crack patterns are presented in Figure 4.19, for the rotating and fixed crack model. The three RTF models form crack patterns which could be said to be between the extremes of the fully rotating and fully fixed model. Once again, the formation of spurious cracks occurred on the top of the beam. This will not be further discussed here as it was elaborated on in Chapter 4.1.3.

In this analysis, all models were considered to fail in a compression shear, because yielding did not affect the overall structural behavior considerably, and in addition, yielding only happened locally at the end of the compressive strut, as further explained in Chapter 4.3.5. Also, in several cases, only one of the two reinforcement layers yielded.

The failure mode of the fully rotating model was somewhat difficult to determine, as one can see a slight stiffness decrease before failure. However, also this model only exhibited

local yielding, and shown a crack pattern fitting to a compression shear failure. Despite the insecurities, the fully rotating model is assigned the compression shear failure.

#### 4.2.4 Beam S2D36a72

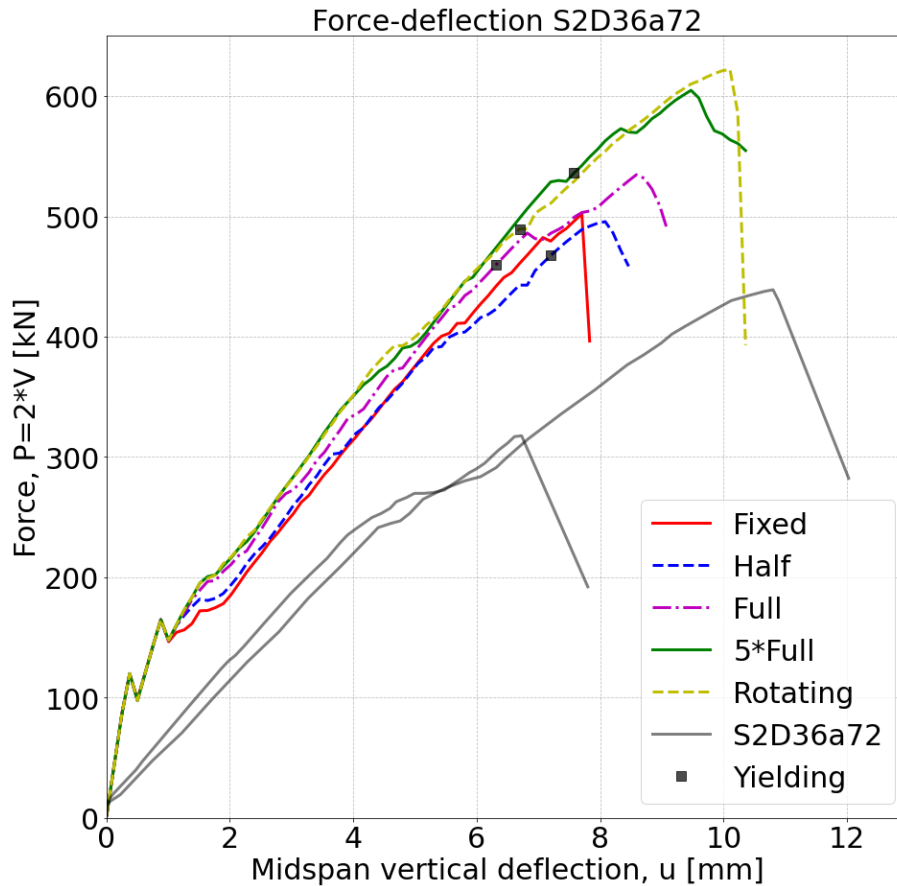


Figure 4.18 – Force-deflection plot for the experiment and varying crack models for beam S2D36a72

Figure 4.18 presents the force-deflection plots for the beam S2D36a72. The fully fixed model showed a lower capacity than the fully rotating model. This can be explained by the crack propagation, which was quite similar to the one explained in Chapter 4.2.3. This is also illustrated in Figure 4.19. Figure 4.19 A) shows the fixed crack model. The cracks form along the reinforcement, before growing relatively vertically into the web. In contrast, the rotating crack model, in Figure 4.19 B), creates a crack path which localizes underneath the compressive strut. Again, the RTF crack models act between the fully fixed and rotating model. The fully fixed, half RTF and full RTF crack model failed in compression shear, as yielding for the two latter models only occurred locally and did not seem to affect the general behavior of the structure. The fully fixed model had a larger opening of the critical crack as the beam failed, but in combination with crushing of the concrete, hence, a compression shear failure. The rotating and 5\*full RTF crack model had a failure mode more similar to a flexural failure, as the reinforcement yielded over a larger area in the midspan as well as locally underneath the compressive strut and also showed tendencies of stiffness loss.

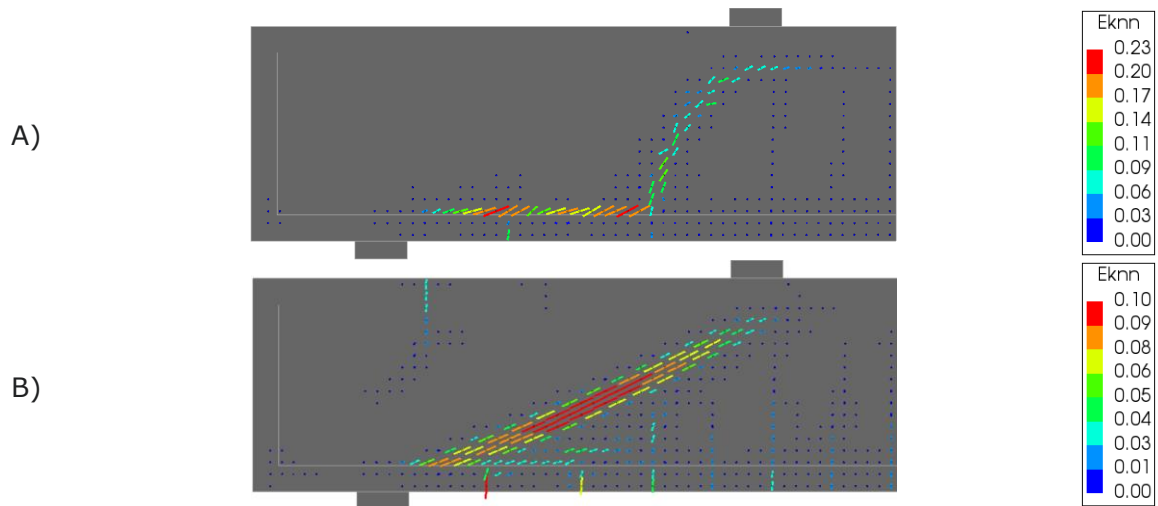


Figure 4.19 – Crack strain plots for A) fully fixed damage based model and B) fully rotating crack model just before failure for beam S2D36a72

As in Chapter 4.1.4, none of the models were able to simulate the tension shear failure, and thereby large numerical overestimations of the capacity occurred again. The numerical capacity was 31 % – 64 % higher than the mean experimental capacity, and 13 % – 42 % higher compared to only the experimental compression shear capacity.

### 4.2.5 Beam S2D36a36

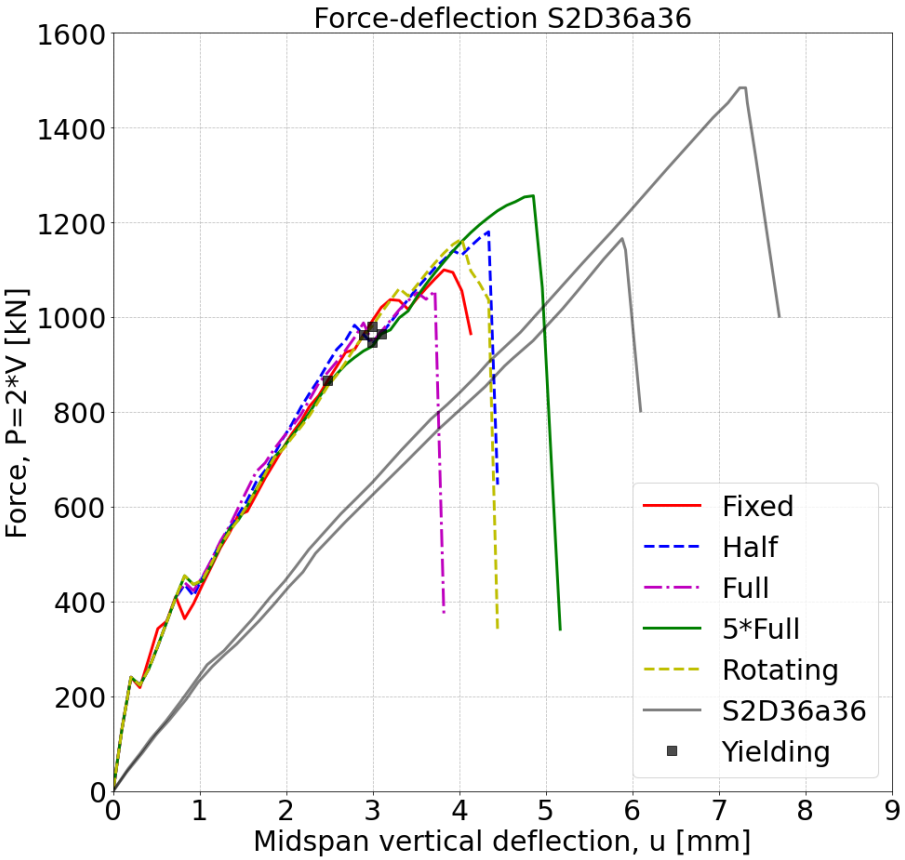


Figure 4.20 – Force-deflection plot for the experiment and varying crack models for beam S2D36a36

Figure 4.20 presents the force-deflection plots for the beam S2D36a36. As it may be difficult to see in the figure, the fully fixed crack model experience reinforcement yielding at about 2.5 mm deflection, while the other models yields at about 3 mm. In this case, the fully fixed model and the fully rotating model showed similar behaviors on the force-deflection curve, while the RTF models had both lower and higher capacities than the two non-hybrid crack models.

The failure mode in the 5\*full RTF crack model was determined to be a flexural failure. This is because extensive yielding zones occurred both locally underneath the compressive strut and in the midspan. Also, the stiffness decreases before the final failure. For the four other models, the failure mode was evaluated to be compression shear, as only local yielding (see illustrations in Chapter 4.3.5) underneath the strut took place, which did not seem to affect the overall structural behavior.

The numerical capacities ranged from 6 % - 21 % lower than the experimental capacity, which is about the same as was found in the shear retention analysis in Chapter 4.1.5.

## 4.2.6 Comparisons and Remarks

Table 4.2 – Summary of chapter 4.2 – The influence of varying crack models

Beam	Mean capacity (experiment) [kN]	Failure mode (exp)	Crack model	Mean capacity (DIANA) [kN]	Failure mode	Difference [%]
S1D18a108	120.74	Y	Fixed	124.75	Y	3.3
			Half	116.72	Y	-3.3
			Full	115.10	Y	-4.7
			5*Full	91.82	T	-24.0
			Rot	104.59	Y	-13.4
S1&2D36a108	235.95	T	Fixed	453.46	Y	92.2 (8.9*)
			Half	393.56	C	66.8 (-7.6*)
			Full	415.84	C	76.2 (-15.2*)
			5*Full	371.28	C	57.4 (-30.6*)
			Rot	373.14	C	58.1 (-31.4*)
S1D72a108	1029.70	C	Fixed	1218.55	C	18.3
			Half	1088.74	C	5.7
			Full	1186.42	C	15.2
			5*Full	1131.74	C	9.9
			Rot	1248.64	C	21.3
S2D36a72	379.80 (439.43/320.17)	C/T	Fixed	502.12	C	32.2 (14.3**)
			Half	495.65	C	30.5 (12.8**)
			Full	534.66	C	40.8 (21.7**)
			5*Full	604.81	Y	59.2 (37.6**)
			Rot	622.16	Y	63.8 (41.6**)
S2D36a36	1330.48	C	Fixed	1100.02	C	-17.3
			Half	1180.42	C	-11.3
			Full	1055.53	C	-20.7
			5*Full	1256.35	Y	-5.6
			Rot	1165.45	C	-12.4

\*Manually deciding the capacity by locating the moment of crack path reestablishment

\*\*Compared only to the experimental compression shear capacity

Table 4.2 summarizes and compares the experimental and numerical failure modes and capacities for each beam in Chapter 4.2. Also, in this table the marks \* and \*\* were added, for reasons discussed in Chapter 4.1.6. This includes the insecurity of adding the \* to the fixed model in the S1&2D36a108 beam, which was also discussed in Chapter 4.1.6.

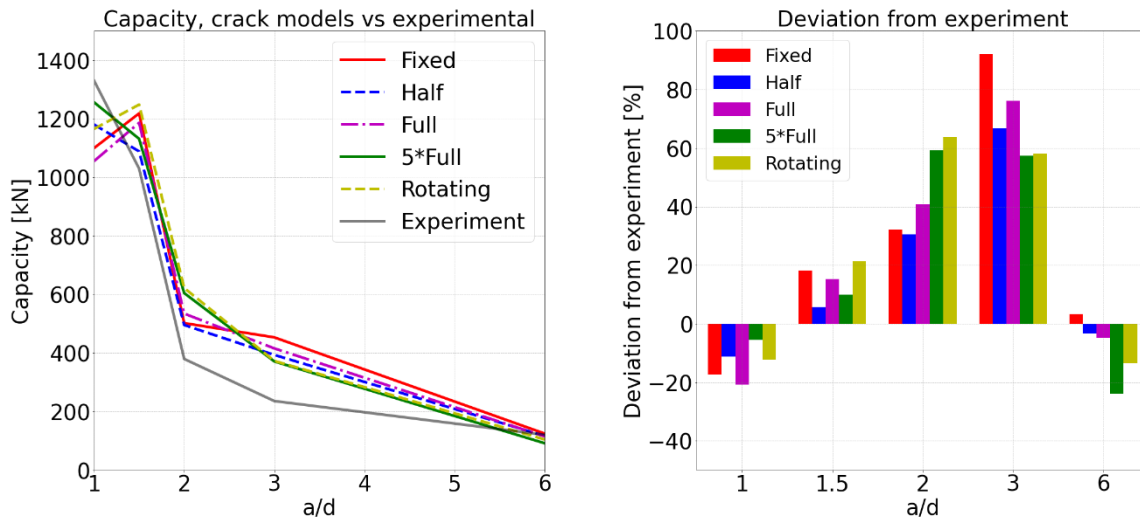


Figure 4.21 – Capacity comparison (left) and a capacity deviation diagram (right) between numerical and experimental results for the crack model analysis

Figure 4.21 visualizes the numerical and experimental differences in the crack model investigation and is further explained in Chapter 4.1.6. Note that for  $a/d = 3.0$  and  $a/d = 6.0$  the aggregate based shear retention is utilized, while the damage based shear retention model is used for the remaining beams, due to individual struggles to represent certain beams for each of the shear retention models. Reasons for this choice were also discussed in Chapter 3.3.2.

Once again, the numerical analyses struggles to represent the beams with  $a/d = 2.0$  and  $a/d = 3.0$ . The use of the rotating crack model did not lead to a correct failure mode in the S1&2D36a108 beam, hence, also the RTF crack models predicted the wrong failure mode. This causes the heavily overestimated numerical results.

Furthermore, as discussed in Chapter 4.1.4, the S2D36a72 beam acted as a transitional limit between the tension and compression shear failure mode. For this beam ( $a/d = 2.0$ ) the fully fixed damage based shear retention model presented more accurate results compared to the fully rotating model, and the RTF models mainly estimated capacities between the two extremes. The error plot to the right in Figure 4.21 compares the numerical analyses to the mean capacity of the experimental analyses. Hence, one part of the overestimation can be explained by the fact that the numerical beams, that fail in compression shear, or even in a flexural failure, are compared to a capacity value which is strongly affected by the lower tension shear capacity. However, as can be seen by the markings \*\* in Table 4.2, the numerical results still overestimate the capacity when only compared to the experimental compression shear capacity. The largest overestimations can be found in the rotating and 5\*full RTF crack model, which was concluded to exhibit a flexural failure, and not a compression shear failure, which might also contribute to the overestimation. The other three models, which failed in compression shear, overestimated the experimental compression shear capacity by 13 % - 22 % approximately. Errors in this range are not easy to explain, as it might be the result of several complex reasons in the numerical analysis. Some possible reasons were discussed in Chapter 4.1.4, where it is considered whether overestimation might be related to the transitional (between tension and compression shear failure) properties of the beam.

The initial pre-crack stiffnesses of the shorter beams are yet again wrongly predicted by the numerical models. See discussion and calculations in Chapter 4.1.6 and Appendix B.3.

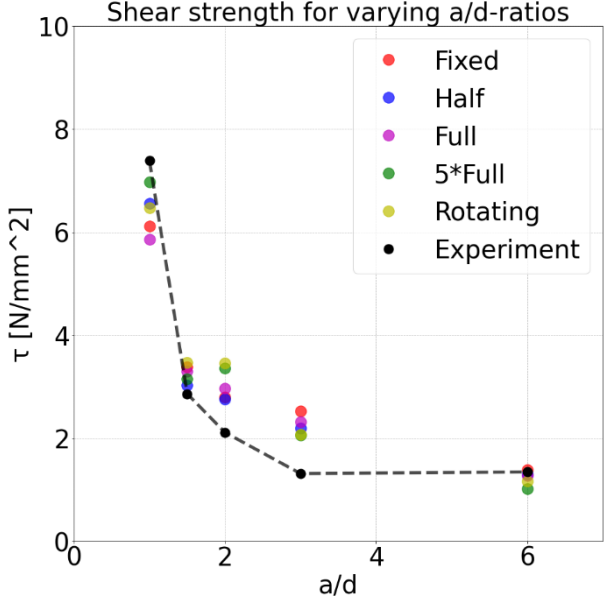


Figure 4.22 – Experimental and numerical shear strength  $\tau = \frac{P}{2td}$  ( $P = 2V$ ) for varying a/d-ratios for different crack models

Figure 4.22 illustrates the highest shear stress values reached in each crack model analysis compared to the experimental values. The x- and y- scales are discussed in Chapter 4.1.6. As also discussed in Chapter 4.1.6, the differing shear strengths are mainly affected by the different failure modes obtained in the different beams, but also by the size effect, which was discussed in Chapter 2.7. The largest numerical-experimental shear strength deviation occurs for the beams with  $a/d = 2.0$  and  $a/d = 3.0$ .

Another important observation was concerning the convergence rate of the analyses between the different crack models. Because a unified solution procedure is searched for in this thesis, a fixed equilibrium control was used throughout all analyses. However, the equilibrium control, specified in Chapter 3.2, has in general provided reliable results as quite few load steps did not converge. That is, up until the point of the present analyses, where especially the rotating crack model exhibited a large number of non-converged load steps. The results were logged and presented in Figure 4.23.

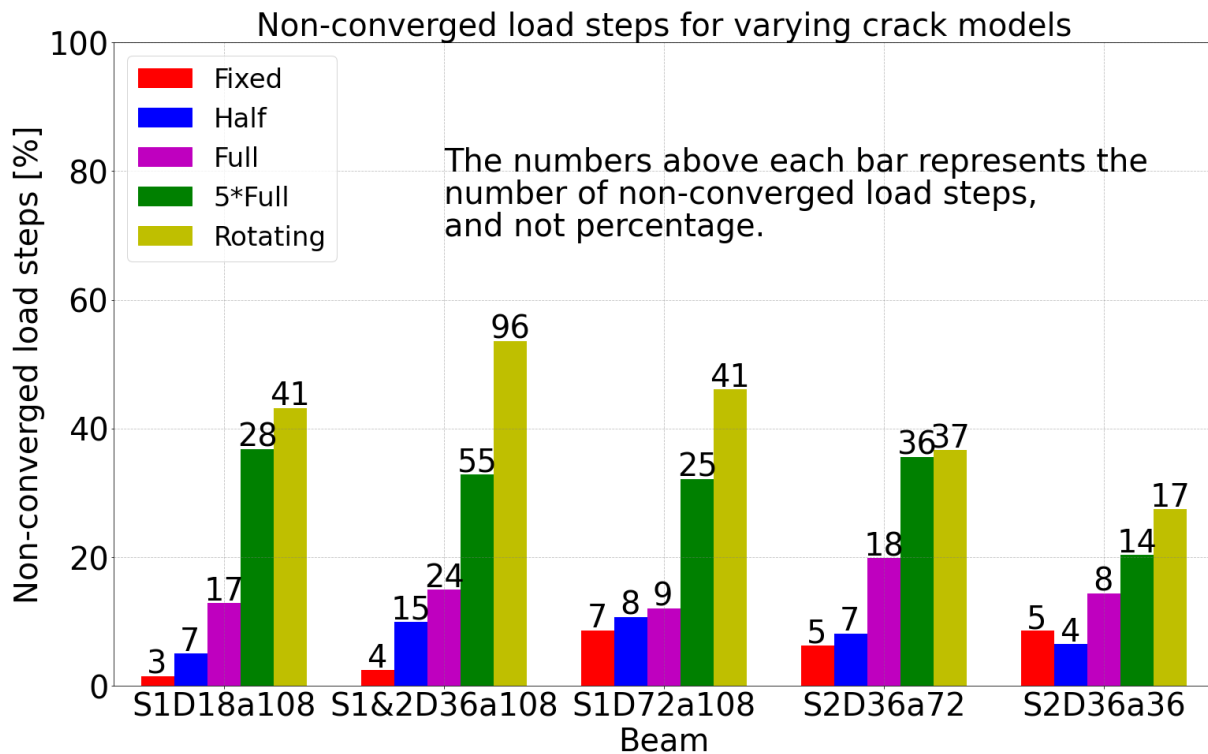


Figure 4.23 – Non-converged load steps presented as percentage (bar) and in numbers (numbers above bar) for each analysis for each beam

Figure 4.23 shows that the analyses of the fixed crack model in general contains less non-converged steps compared to the rotating crack model. The RTF crack models are decreasing the number of non-converged load steps as the threshold value (the total normal strain value that switches the crack model from the rotating to the fixed when exceeded) gets smaller. The number of non-converged load steps are plotted above the bar of its respective analysis in order to not only show the non-convergencies as a percentage, but also the exact number. The non-converged load steps seem to occur parallel to the over-rotation of cracks. As about 25 % - 55 % of the load steps in the rotating crack models are non-converged, the reliability of these analyses are considered to be low.

It is not easy to evaluate what the limit of non-converged steps is before the results should be considered to be invalid. Several factors, as how many non-converged steps takes place consecutively, the error size, and where on the force-displacement curve the non-converged load steps occurs, would be important when determining the quality of the solution. For example, de Putter evaluated the numerical capacity to be the highest capacity shown for a converged load step (de Putter et al., 2022). This means that a great number of non-converged load steps could be present in the analysis without disposing the results.

If the rotating crack model would have satisfied the conditions of being an acceptable unified solution procedure, that is, provided accurate results for all beams, it would not be a straightforward task to determine if the model would fulfill the requirements of the research question in this thesis, as a large part of the load step did not converge. However, as the results show, the rotating crack model provides less accuracy than several of the

other crack models, and thereby, there is no need to evaluate the reliability of the model any closer.

### 4.3 The Influence of Tension Stiffening

Chapter 4.3.1 – Chapter 4.3.5 compare the model with and without tension stiffening (TS) within one beam analysis, while Chapter 4.3.6 compare how the numerical analyses perform overall. The TS effect is often used for structures with very large elements. As can be seen in Figure 3.6 - Figure 3.10, the elements in the analyses in this thesis are relatively small. Thereby, the following elaborates on other reasons to why a TS model could be interesting to analyze. Furthermore, as will be seen in the following chapters, the credibility of the results produced by the present TS model is also challenged.

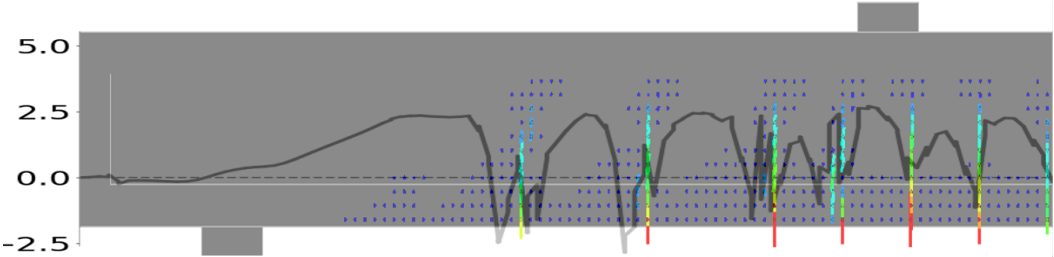


Figure 4.24 – The concrete stress (SXX) in the longitudinal direction plotted along the dashed line just above the reinforcement. This is plotted on top of the crack strain for the beam S1D18a108 with the aggregate shear retention model analyzed in chapter 4.1.1. The left scale holds the unit of measurement N/mm<sup>2</sup>. The horizontal and vertical beam aspect ratio is not correct.

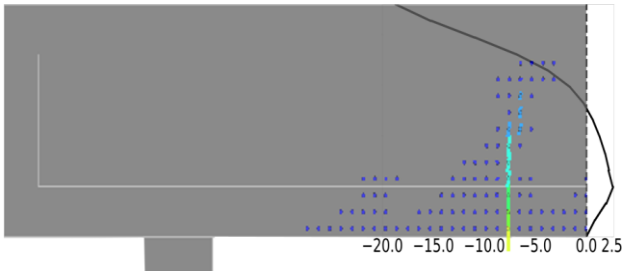


Figure 4.25 – The concrete stress (SXX) in the longitudinal direction plotted along the beam cut-off. This is plotted on top of the crack strain for the beam S1D18a108 with the aggregate shear retention model analyzed in chapter 4.1.1. The underneath scale holds the unit of measurement N/mm<sup>2</sup>. The horizontal and vertical beam aspect ratio is not correct.

Figure 4.24 and Figure 4.25 represent the concrete stress SXX plotted on top of the crack strain plot. The plot in Figure 4.24 resembles the stress plot one might expect between the cracks. There are three main reasons for the investigation of the TS effect.

The first reason is illustrated in Figure 4.25, where one can see how the longitudinal concrete stress SXX reduces to zero as it approaches the bottom of the beam. This implies that there is no concrete contribution to the stiffness at the bottom of the beam, which in an uncracked case should have been present, given that the concrete provides a larger tensile-area above the reinforcement than underneath.

The second reason has cause in the development of cracks in the smeared crack model, as this type of crack modelling often results in a too large number of cracks appearing at the same time. That is, before the cracks localize, there could arise a zone of non-localized cracks, which takes place as a larger part of the structure reaches the tensile strength at the same time, or more precisely, at the same load increment. This phenomenon is illustrated in Figure 4.26.



*Figure 4.26 – Crack strain plot before the crack localizes for the damage based shear retention model in beam S1D18a108*

Alternatively, one can study the output file, which is a file created when starting an analysis in DIANA. This file provides information about the performance of the job such as error messages and log information (DIANA TNO, 2020). This is presented in Figure 4.27.

```

STEP 10 TERMINATED, CONVERGENCE AFTER 1 ITERATION
TOTAL LOAD FACTOR: LOADING( 1) * 5.000E-01

PLASTICITY LOGGING SUMMARY
GROUP NAME      PLAST, PRV. PL, CRITIC, PLAST NEW, PRV.PL NEW, CRITIC NEW
TOTAL MODEL      0          0          0          0          0          0
CRACKING LOGGING SUMMARY
GROUP NAME      CRACK,  OPEN,  CLOSED,  ACTIVE,  INACTI,  ARISES,  RE-OPENS,  CLOSES
TOTAL MODEL      0          0          0          0          0          0          0
CUMULATIVE REACTION:
                    FORCE X      FORCE Y      MOMENT Z
                    0.18190D-11  -0.97316D-10  0.00000D+00

STEP 11 TERMINATED, CONVERGENCE AFTER 1 ITERATION
TOTAL LOAD FACTOR: LOADING( 1) * 5.500E-01

PLASTICITY LOGGING SUMMARY
GROUP NAME      PLAST, PRV. PL, CRITIC, PLAST NEW, PRV.PL NEW, CRITIC NEW
TOTAL MODEL      0          0          0          0          0          0
CRACKING LOGGING SUMMARY
GROUP NAME      CRACK,  OPEN,  CLOSED,  ACTIVE,  INACTI,  ARISES,  RE-OPENS,  CLOSES
TOTAL MODEL      31          31          0          31          0          31          0
CUMULATIVE REACTION:
                    FORCE X      FORCE Y      MOMENT Z
                    0.81250D+01  -0.34561D-09  0.00000D+00

```

Figure 4.27 – Output file logging for step 10 and 11 in the damage based shear retention model in beam S1D18a108

The yellow-marked values in Figure 4.27 show how the number of cracks increase too fast from one step to another. This fast increase of cracks seems inevitable when using the smeared total-strain based crack model. However, the size of these cracks are very small, and thereby the damage inflicted by each individual crack is also small. Despite this, the collective damage induced by these cracks could reduce the overall beam stiffness. The reason for this is that the stiffness that was lost as a cause of the unrealistic crack pattern seen in Figure 4.26 is never retrieved. Hence, the procedure would be as follows: unlocalized cracks arise as seen in Figure 4.26, then cracks localize and release the stress in the surrounding concrete which would close and unload many of the unlocalized cracks, and finally, as the structure is further loaded, the stress between the cracks will build up again as seen in Figure 4.24. In the latter step, the elements would be in a reloading phase, and can thereby not reach the resistance provided by completely undamaged concrete. The reloading phase is further explained and illustrated in Chapter 2.3.4 and Appendix A.1. Thus, the general thought behind inserting a TS effect in the zone which is most exposed for the unlocalized cracking is that the TS model would work as a counterweight to the collective damage induced by the unlocalized cracks.

The third and final reason regards the numerical representation of the complex biaxial stress state in the beams. As seen in Chapter 4.1, the failure of the beams varies greatly with the different shear retention models. This is the result of the different shear resistance the models provide in the cracks, which are dependent on the crack size. Furthermore, the crack size depend on the tension softening model. Hence, by using a different softening model in a restricted area of the beam with the damage based shear retention model could help stabilize the analysis, as the damage based model has given very conservative results for the more flexural beams. It is important to recognize that this argument is not directly linked to the physical aspect of TS, but rather to the attempt of “repairing” or improving a model based on what is discovered in the previous analyses.

Furthermore, as mentioned, only the fixed, damage based model are utilized in this chapter. The model will be presented with and without TS to perceive the relative effect of TS in a clear manner.

### 4.3.1 Beam S1D18a108

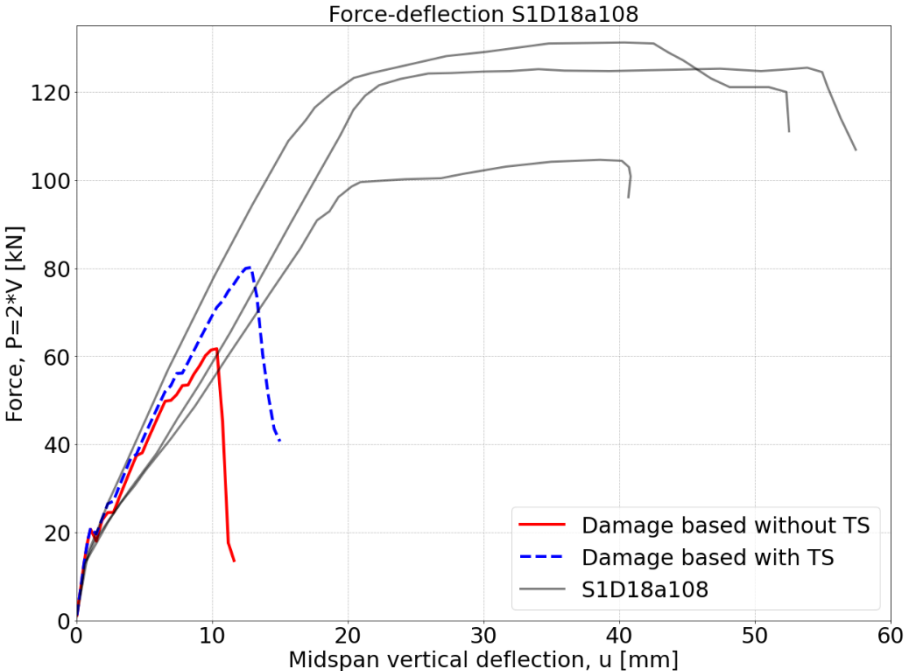


Figure 4.28 – Force-deflection plot for the experiment and numerical models with and without tension stiffening for beam S1D18a108

As Figure 4.28 presents, the TS effect does have a positive influence on the numerical behavior, as the capacity error is reduced from -49 % to -34 %. However, the TS effect does not solve the issue with the damage based shear retention model for this beam, as it still yields the wrong failure mode, namely the tension shear. It is concluded to be a tension shear failure due to the fact that the reinforcement never yields, the concrete never crushes, and the critical crack opens as the failure takes place.

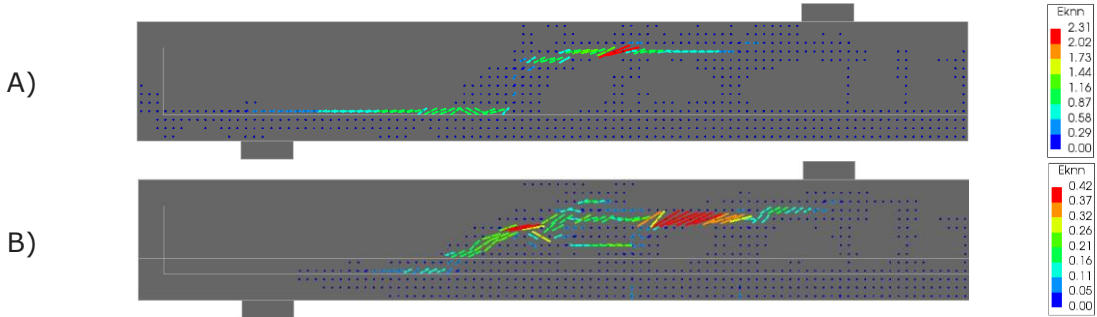


Figure 4.29 – The crack strain pattern A) without and B) with tension stiffening after failure for beam S1D18a108

As Figure 4.29 shows, the size of the critical crack is restrained in the TS zone. This causes the critical crack to grow larger in the upper part of the beam, compared to the non-TS model. Also, as can be seen on the scales to the right in the figure, the crack is smaller for the model with TS. If one were to take a look at Appendix C.3.1, the crack strain pattern for the TS model just before failure has a better resemblance to the experimental crack pattern than the model without TS.

### 4.3.2 Beam S1&2D36a108

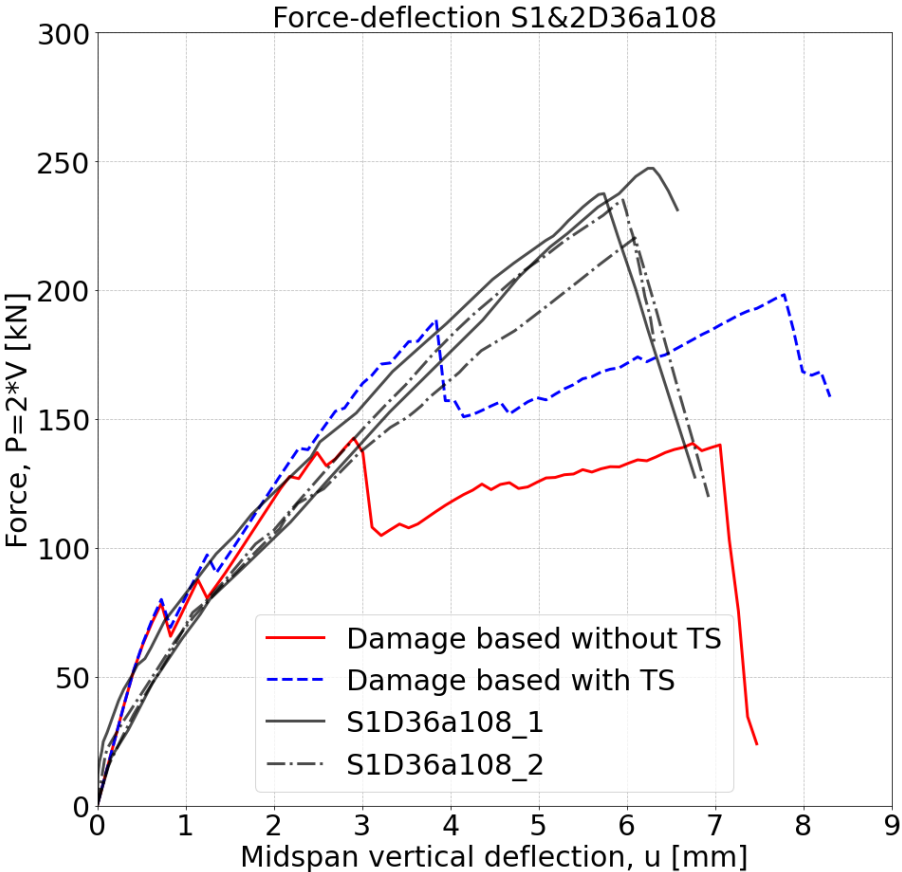


Figure 4.30 – Force-deflection plot for the experiment and numerical models with and without tension stiffening for beam S1&2D36a108

Figure 4.30 compares the experimental and numerical force-deflection behavior with and without TS. The shape of the numerical curves looks quite similar, but the TS effect results in a higher capacity, reducing the capacity error from -40 % to -16 %. One can again conclude with the numerical models failing in tension shear, for the same reasons stated in in the previous chapter. The crack strain pattern after failure with and without TS is presented in Figure 4.31.

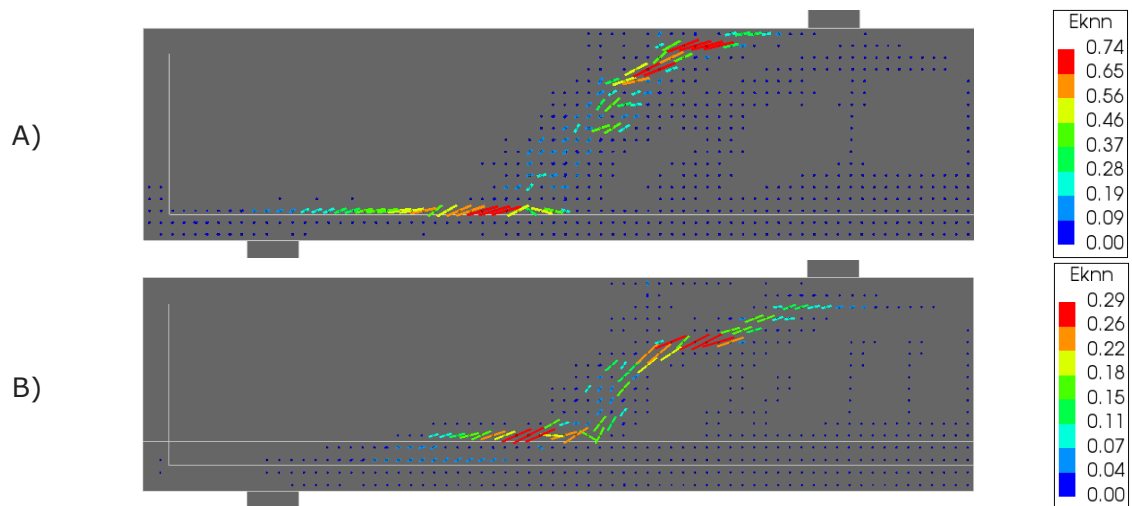


Figure 4.31 – The crack strain pattern A) without and B) with tension stiffening after failure for beam S1&2D36a108

The crack patterns in Figure 4.31 are differed by the evolvement of the critical crack in the lower part of the beam. As the model without TS creates a localized crack along the reinforcement bars, the TS model localizes the crack just above the TS zone. Also, the crack width is smaller for the TS model compared to the non-TS model.

### 4.3.3 Beam S1D72a108

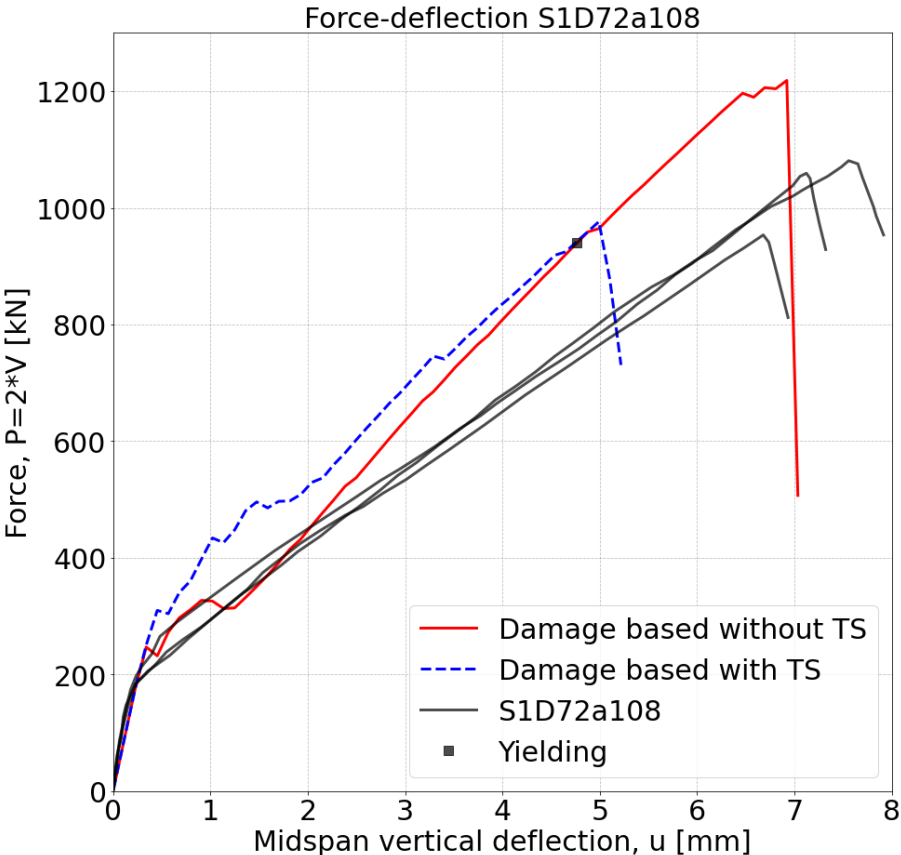


Figure 4.32 – Force-deflection plot for the experiment and numerical models with and without tension stiffening for beam S1D72a108

As it is difficult to see, the reinforcement yielding in Figure 4.32 applies to the model without TS. Yielding does not take place for the TS model. The capacity accuracy changes from 18 % overestimation in the non-TS model, to -5 % in the TS model compared to the mean experimental capacity. However, the accuracy of the ductility is better for the non-TS model. The crack strain pattern after failure in the TS model is more similar to the experimental crack pattern than the non-TS crack strain pattern. This is illustrated in Figure 4.33 below. The figure shows that the non-TS model exhibit a crack opening just to the right of the support, in addition to having a quite large crack in the top of the beam, above the support. On the other hand, for the TS model the main crack opening happens along a crack that gives a better resemblance to the experimental crack pattern. Also, the TS model had lower crack width than the non-TS model.

The non-TS model yielded a compression shear failure, for reasons discussed in Chapter 4.1.3. This is also the case for the TS model, as the reinforcement did not yield, in addition to the presence of concrete crushing.

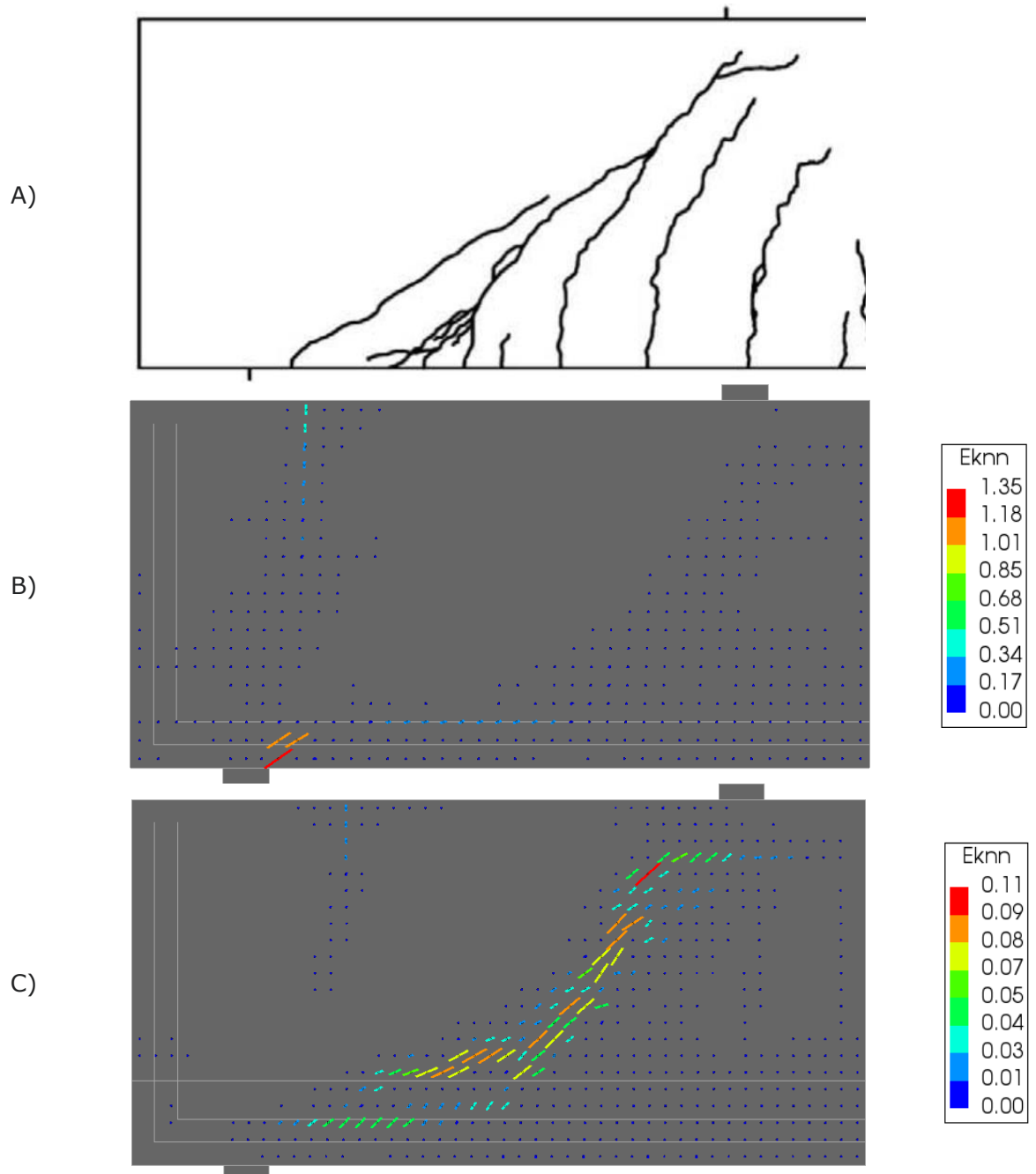


Figure 4.33 – The crack strain pattern for the A) experimental, B) without, and C) with tension stiffening after failure for beam S1D72a108

### 4.3.4 Beam S2D36a72

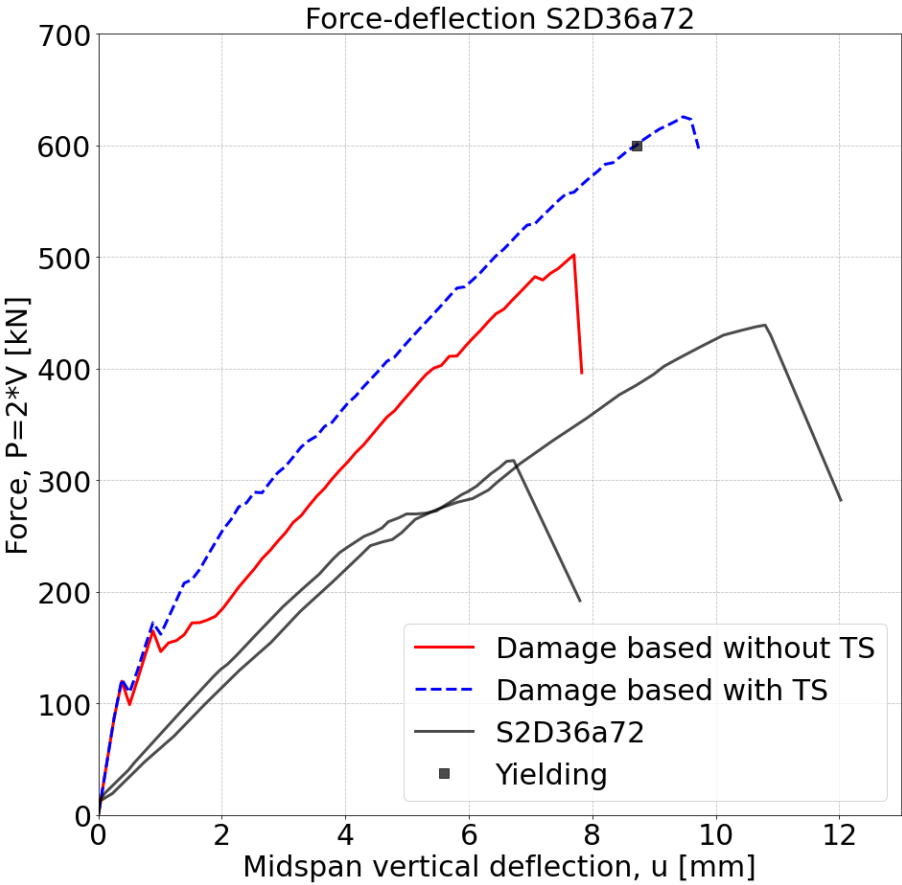


Figure 4.34 – Force-deflection plot for the experiment and numerical models with and without tension stiffening for beam S2D36a72

The capacity accuracy changes from 32 % overestimation in the non-TS model, to 65 % in the TS model compared to the mean experimental capacity. In this analysis, the TS model experienced yielding, in contrast to the non-TS model. Despite this fact, both models were assessed to fail in a compression shear failure. The non-TS model failure is discussed in Chapter 4.1.4. The reason for the failure mode classification in the TS model is that the reinforcement yielding happens locally (see Figure 4.37) and the force-deflection behavior does not seem to be particularly affected by the yielding. It is worth mentioning that this was a close call, as the failure showed properties of a flexural failure as well.

Another observation is that for the TS model, cracks grew large in the TS zone, in contrary to what have been seen for the previous analyses in Chapter 4.3, where cracks have tended to remain relatively small within the TS zone. The crack strain pattern is presented in Figure 4.35. One possible explanation could be that the beam in the present analysis is shorter than the beams in the previous analyses (Chapter 4.3.1– Chapter 4.3.3), and thereby a smaller moment force will develop as the loading is applied. This would result in a shorter cross sectional tension zone. Hence, if a large part of the tension zone is located within the TS zone, the threshold for crack localization might be lower here than just outside the TS zone.

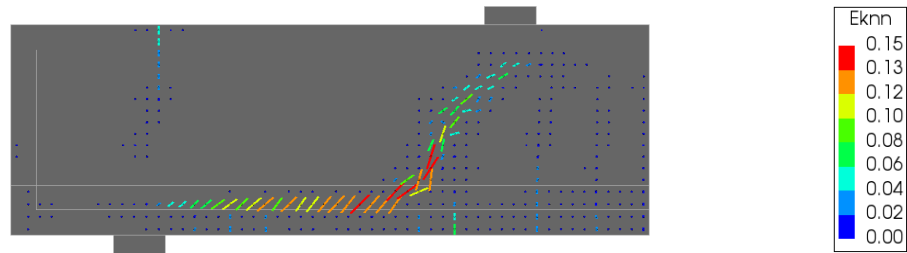


Figure 4.35 – The crack strain pattern with tension stiffening after failure for beam S1D72a108, where large cracks develop in the tension stiffening zone

As the crack pattern in Figure 4.35 was rather similar for both the model with and without TS, the question rises to what the reason for the increasing capacity in the TS model might be. The crack patterns, which can be further analyzed in Appendix C.3.4, show that the crack strain, and thereby the crack width, is smaller for the TS model compared to the non-TS model, both before and after failure. The smaller crack width is the result of a slower decrease of stiffness after cracking for the TS model compared to the non-TS model. The relatively small crack width imposed by the TS model may then be the main factor for the differing capacity between the two numerical models.

#### 4.3.5 Beam S2D36a36

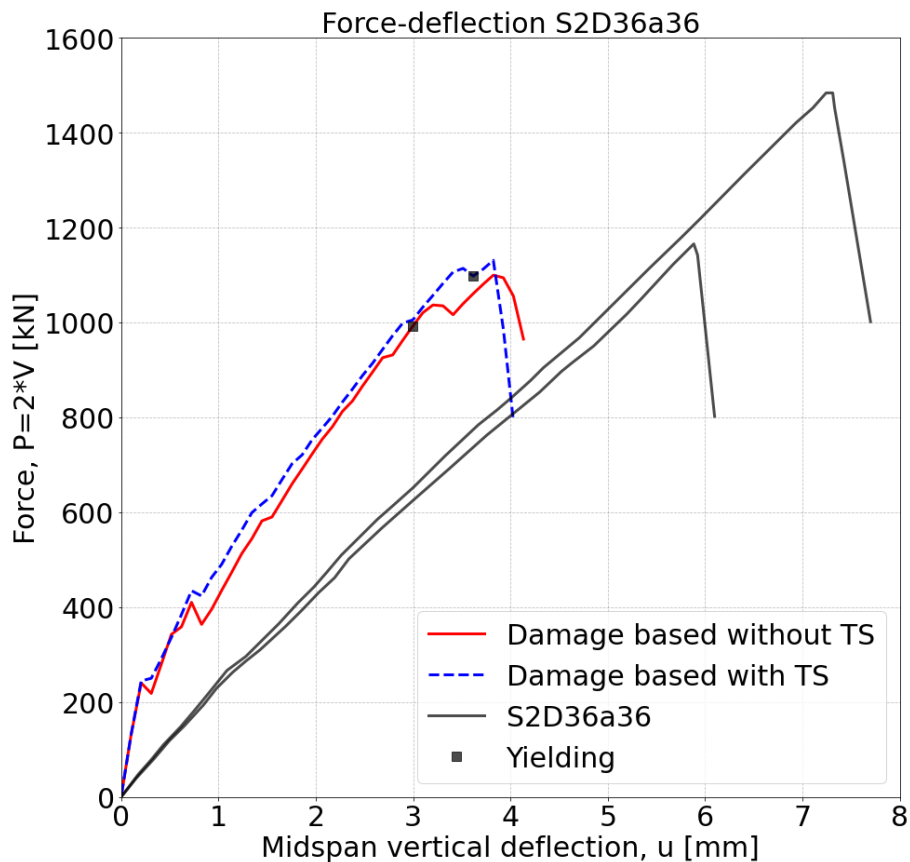


Figure 4.36 – Force-deflection plot for the experiment and numerical models with and without tension stiffening for beam S2D36a36

The difference in the TS model and the non-TS model are nearly inseparable for the S2D36a36 beam. The numerical capacity is, compared to the mean experimental capacity, -17 % for the non-TS model and -15 % for the TS model. Chapter 4.1.5 explains why the non-TS model is classified as a compression shear failure. The same arguments goes for the TS model, as this is also concluded to fail in compression shear. That is, the yielding of reinforcement takes place locally at the end of the compression strut. In addition, the force-deflection curve does not seem affected by the yielding, as it happens late, just before failure takes place. The local yielding is illustrated in Figure 4.37.

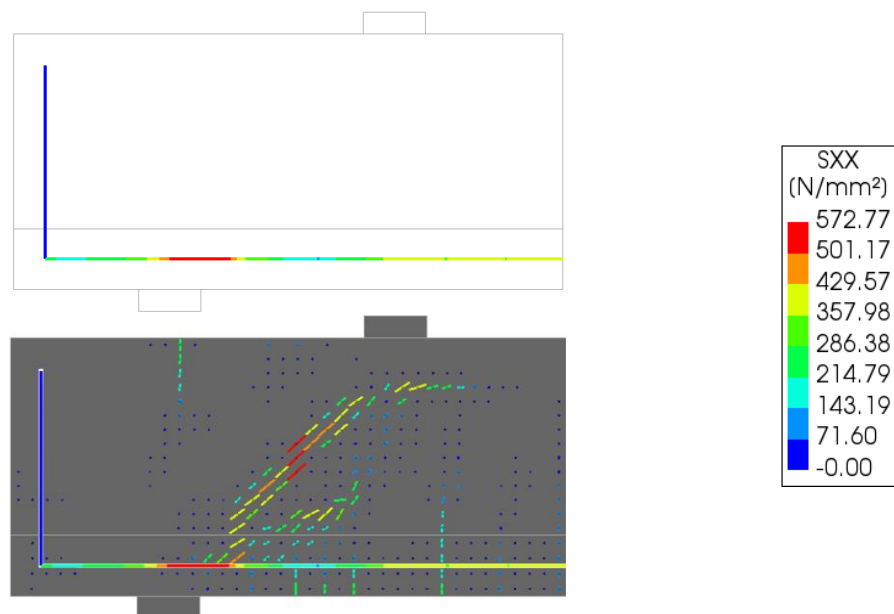


Figure 4.37 – The reinforcement stress plot SXX with local yielding plotted alone (upper figure) and together with the respective crack strain plot (lower figure). The legend to the right only represents the reinforcement stress SXX.

Note that yield strength of the reinforcement is  $f_y = 560 \text{ N/mm}^2$ . As Figure 4.37 illustrates, the yielding only takes place above the support plate, being at the end of the compressive strut, where the cracks have localized. The local yielding might be the result of the Poisson's effect induced by the large compressive forces in the compressive strut. The compressive forces will give rise to an orthogonal expansion, which could cause large tensile stresses in the longitudinal reinforcement and give a reinforcement stress plot as seen Figure 4.37. Alternatively, the local yielding could be the result of the equilibrium conditions that arise when an inclined crack takes place close to the support, as discussed in Chapter 4.1.3. Both reasons are visually illustrated in a simplified manner in Figure 4.38.

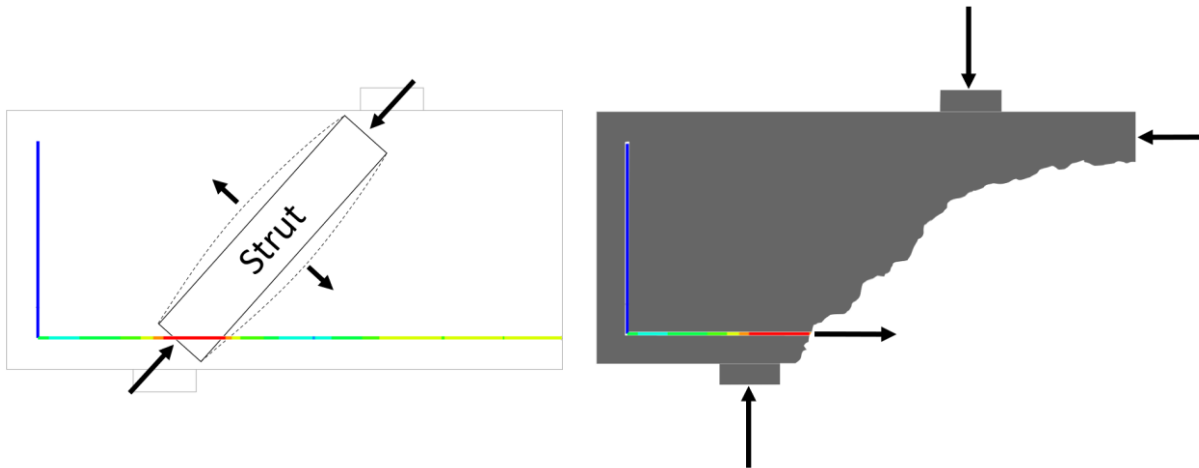


Figure 4.38 – Poisson's effect of compressive strut (left) where the arrows illustrate the strain directions and a free body diagram of the end support region cut out at an inclined crack (right) where the arrows illustrate the forces

When the reinforcement yielded as presented in Figure 4.38, the analysis has not been classified with a flexural failure.

#### 4.3.6 Comparisons and Remarks

Table 4.3 – Summary of chapter 4.3 – The influence of tension stiffening

Beam	Mean capacity (experiment)[kN]	Failure mode (exp)	Tension stiff.	Mean capacity (DIANA)[kN]	Failure mode (DIA)	Difference [%]
S1D18a108	120.74	Y	No	61.70	T	-48.9
			Yes	80.15	T	-33.6
S1D36a108	235.95	T	No	142.66	T	-39.5
			Yes	198.30	T	-16.0
S1D72a108	1029.95	C	No	1218.55	C	18.3
			Yes	976.43	C	-5.2
S2D36a72	379.80 (439.43/320.17)	C/T	No	502.12	C	32.2 (14.3**)
			Yes	625.71	C	64.7 (42.4**)
S2D36a36	1330.48	C	No	1100.01	C	-17.3
			Yes	1131.37	C	-15.0

\*\*Compared only to the experimental compression shear capacity

Table 4.3 summarizes and compares the experimental and numerical failure modes and capacities for each beam in the Chapter 4.3. Also, the mark \*\* is explained in Chapter 4.1.6.

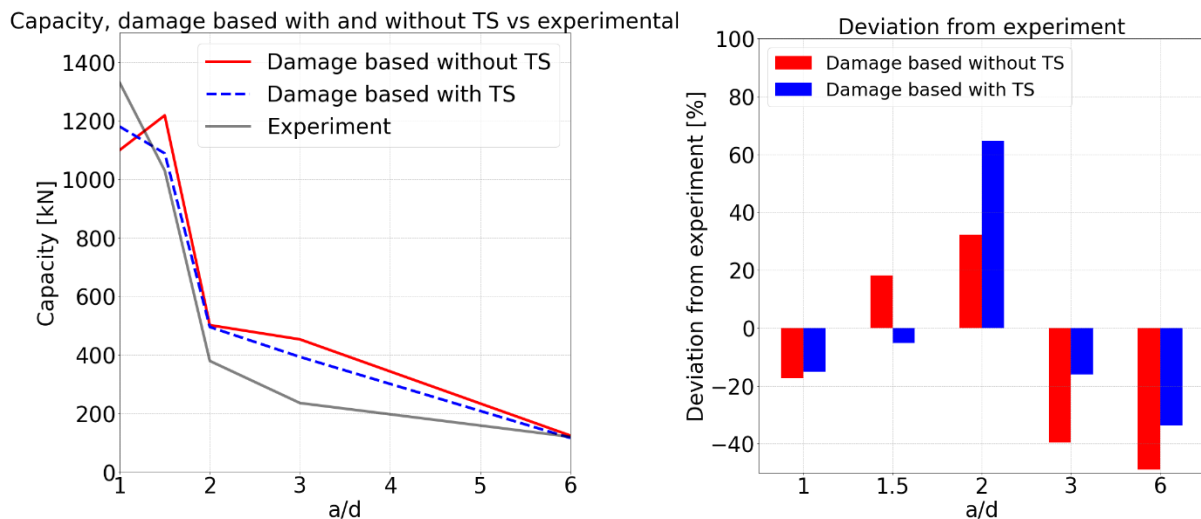


Figure 4.39 – Capacity comparison (left) and a capacity deviation diagram (right) between the numerical and experimental results for the tension stiffening analysis

Figure 4.39 visualizes the numerical and experimental differences in the TS analyses and the figure is also further explained in Chapter 4.1.6. The use of the TS effect did not seem to affect the failure modes of the original fixed, damage based shear retention model. However, the TS model improved the capacity error compared to the experimental capacities for all beams but the beam S2D36a72. That is, the beam with  $a/d = 2.0$ , which is discussed in Chapter 4.3.4. The fact that the TS effect did not only increase the capacity, but also decreased the capacity compared to the non-TS model is quite interesting, as the model then show ability to adjust the capacity error regardless of the initial error being too high or too low. Unfortunately, the TS model increased the originally overestimated capacity in the beam S2D36a72, which gave a pattern of increasing the capacity to the more flexural beams. Thus, it cannot be concluded that the TS model necessarily would improve the numerical results.

It is important to remember that the TS effect is the concrete contribution to the stiffness of the beam tie as the reinforcement is stretched in its longitudinal direction. Due to factors as the beams failing in shear with non-vertical cracks combined with the fact that the imposed TS effect is isotropic, and not orthotropic to the longitudinal reinforcement direction, it is difficult to evaluate whether the improved results are due to a more realistic numerical model, or if it is simply caused by coincidental and unintended effects. An example of the latter could be when a non-vertical crack evolves within the TS zone. In this case, the crack stiffness would have the same properties as the one in a vertical crack, which is not realistic.

On the other hand, one could discuss whether or not the crack evolution for the numerical, fixed, damage based model is realistic and similar to the actual experiment. Figure 4.40 compares the numerical crack strain pattern for the damage based model with the experimental crack pattern at failure.

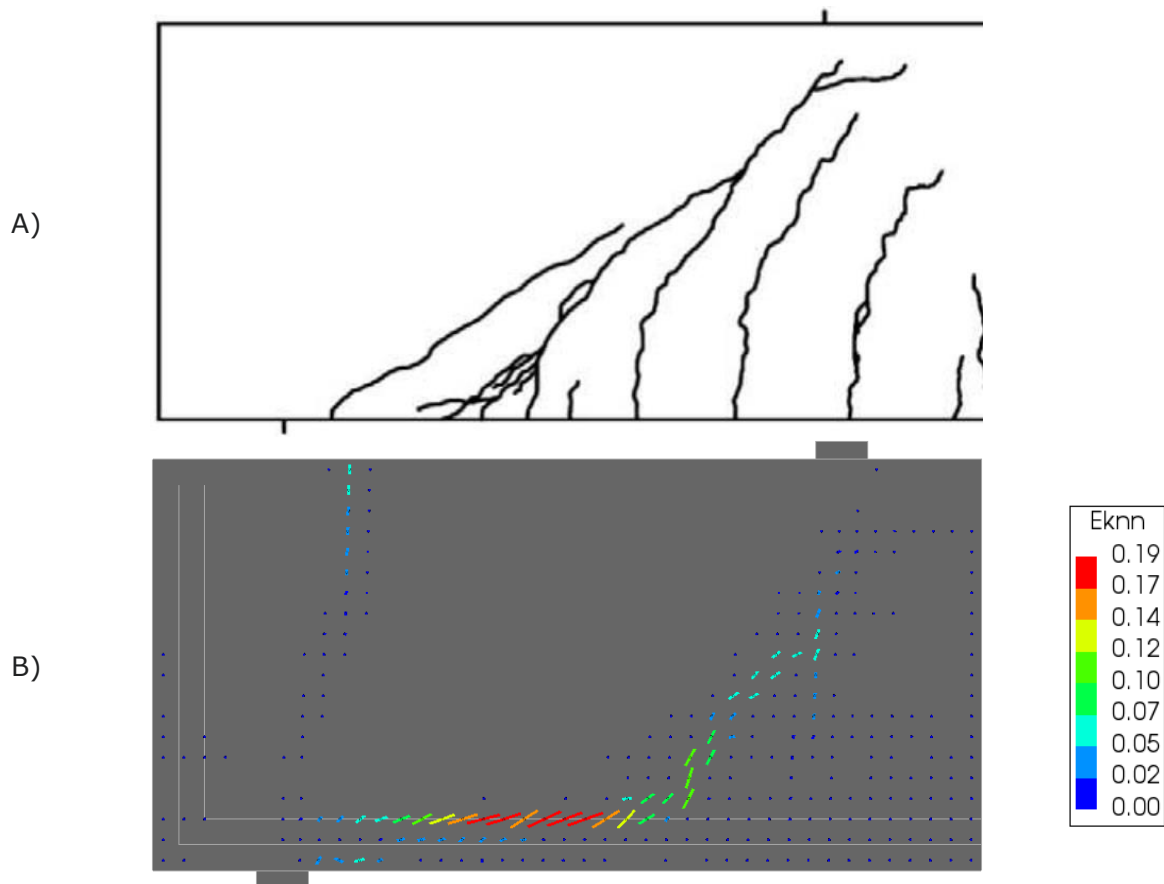


Figure 4.40 – Crack pattern comparison at failure of the fixed, damage based shear retention model without tension stiffening and the experiment

As seen in the figure, a continuous crack has developed along the reinforcement. This crack development does not properly reflect the experimental crack pattern. By the influence of a TS zone covering the reinforcement, a more realistic crack opening takes place as the beam fails, which is presented in Figure 4.33 in Chapter 4.3.3. However, this is just the case for one analysis of one beam, and the TS effect could just as easily affect realistic crack evolutions wrongly. Hence, stating that the TS effect would always improve spurious crack patterns along the reinforcement would be rather optimistic, and most likely wrong.

Also note that the TS effect indirectly affects the shear retention in the cracks. As the resistance of the normal crack opening increases, resulting in a smaller crack width, the shear retention would also be increased. Hence, the shear retention model will also be of great importance when utilizing the TS model. In this case, the damage based formulation is used. That includes rapidly reducing the shear crack resistance to zero as the crack is opened. With smaller crack widths the shear resistance of the crack could be significantly larger when using damage based formulation. On the other hand, if the Al-Mahaidi shear retention was used, an instant decrease of shear retention by 60% would be applied at the moment a crack initiated, and the effect would maybe have been smaller. The aggregate based has a linear formulation, hence smaller deviations in the crack opening would probably affect this model even less than the other two shear retention models.

Furthermore, larger TS zone would probably improve the results of the two most flexural beams, that is beam S1D18a108 and beam S1&2D36a108. However, as discussed, the

isotropic TS effect would wrongly affect inclined cracks. This is also the main reason for choosing the EC2 TS zones calculated and presented in Appendix B.2, as this zone was smaller than the alternative Maekawa TS zones.

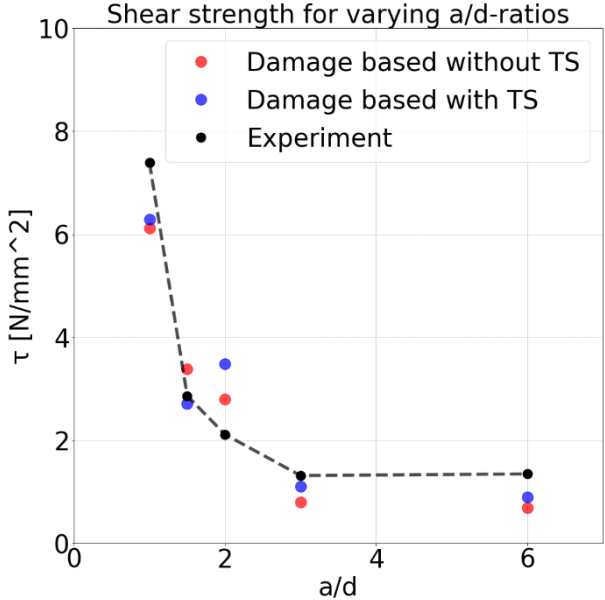


Figure 4.41 – Experimental and numerical shear strength  $\tau = \frac{P}{2} \frac{1}{td}$  ( $P = 2V$ ) for varying a/d-ratios for the damage based model with and without tension stiffening

Figure 4.41 illustrates the shear stress values reached in the TS analyses compared to the experimental values, where x- and y- scales are discussed in Chapter 4.1.6. As also discussed in Chapter 4.1.6, the differing shear strengths are mainly affected by the different failure modes obtained in the different beams, and by the size effect discussed in Chapter 2.7.

## 5 Conclusion

The main objective of this thesis was to evaluate if it was possible to obtain good numerical results for a variety of beam geometries with one unified solution procedure. The solution procedure was further limited within the scope of a local, smeared, total-strain based crack approach. With the parameter variations and general modelling choices made in this thesis, the results have been less successful than the results in the non-local solution procedure discussed in Chapter 3. Good results were obtained in individual cases, but none of the models were able to properly simulate all five beams.

The first investigation, presented in Chapter 4.1, considered the influence of varying shear retention models. The results of the models deviated greatly from each other. In the most extreme example, which was achieved for the S1&2D36a108 beam, the aggregate based shear retention model overestimated the capacity with about 90% while the damage based shear retention model underestimated the capacity by 40%. This large deviation is the result of the damage based shear retention model's tendency to underestimate the capacity of flexural beams, while the aggregate based shear retention model has a tendency to exhibit crack shear locking. The former problem is due to the conservative nature of the damage based shear retention formulation, and vice versa for the aggregate based. The damage based formulation has a very rapid decrease of shear retention as the crack width gets larger. Hence, when this model is used in flexural beams that exhibit large cracks, the capacity is underestimated. However, this model was the only model that was able to properly represent a tension shear failure, even though the capacity in this case also was underestimated. On the other hand, the aggregate based shear retention model has an unconservative formulation, which resulted in large capacity overestimations for some of the beams. The aggregate based shear retention model gave the beams too much crack shear stiffness as the crack opened and did in some cases wrongly predict the failure mode to be flexural, rather than the expected compression shear. Furthermore, in most cases the Al-Mahaidi shear retention model provided a result between the damage based and aggregate based shear retention models. This model can in fact also be concluded to be the most stable model in terms of estimating the capacity, as it did not fail too soon in the flexural beams, such as the damage based, but neither overestimate the capacity in the same degree as the aggregate based. The downside of using this model is that it had a strong tendency of reestablishing the crack pattern in a direct path between the loading plate and the support plate, despite this not being the case in the experimental crack pattern. This model is also the only one of the three shear retention models that was not recommended in the guidelines for NLFEA of concrete structures (Hendriks and Roosen, 2019). This is probably due to the need for a lower bound value, which lack physical meaning. By evaluating the crack patterns, one can in summary conclude that the damage based has a very low tendency of reestablishing an alternative crack pattern as it rather seems to fail when the critical crack is opened, the Al-Mahaidi, as mentioned, has a high tendency of reestablishing an alternative crack pattern, while the aggregate based does not necessarily reestablish a false crack pattern, but gives too much resistance in the existing cracks.

The second investigation, presented in Chapter 4.2, considered the influence of varying crack models. More specifically, a fully fixed crack model, a fully rotating crack model, and three variations of the threshold value in the rotating to fixed crack model. The results were not too surprising, as the hybrid crack model in most cases estimated a capacity between the one estimated by the fully fixed and the fully rotating crack model. Thus, as

both the rotating and the fixed crack model yielded different types of spurious behaviors, the rotating to fixed crack model also suffered from these faults. The faults of the fixed crack model were mentioned in the section above, while the rotating crack model tended to suffer from over-rotation of the cracks. There was a direct and clear correlation between this over-rotation and the amount of non-converged load steps. The latter was presented in Figure 4.23. The figure shows a consistently increasing number of non-converged load steps as the crack models moved from the fixed to the rotating one. Hence, when using the hybrid model with a crack strain threshold value responding to a 5\*fully developed crack, the number of non-converged load steps was relatively large. Moving on to a threshold value responding to 1\*fully developed crack, the number of non-converged load steps improved significantly. Furthermore, using the rotating to fixed crack model with a threshold value responding to a half full crack opening provided the least amount of non-converged load steps compared to the other hybrid models. This model also showed quite promising capacity results, as it often tended towards the experimental capacity compared to the other crack models.

The final investigation considered tension stiffening. The tension stiffening was applied to the structure by using an alternative tension softening diagram, which provided more resistance compared to the "normal" tension softening diagram as the crack got larger. This stiffening curve was then inserted to a limited area on the beam, calculated with formulations from the Eurocode. The effect of tension stiffening did provide more accurate capacities in all beams but one. Thereby, the effect of tension stiffening was mostly positive. However, as discussed in Chapter 4.3.6, it is difficult to assess whether the improved results are indeed the cause of the intended effect or if it is a spurious effect caused by the isotropic formulation in the tension stiffening zone. However, as the numerical capacity estimation of one of the beams aggravated with the use of tension stiffening, it could yet not be concluded that the tension stiffening effect consistently improved the results for every beam geometry. Furthermore, the crack pattern was in some cases also improved by utilizing the tension stiffening effect, which is exemplified in Figure 4.33. The larger post crack tensile resistance gave the crack pattern a more logical appearance, seen in the light of the experimental crack pattern.

Furthermore, when all analyses in this thesis were taken into consideration, some patterns emerged. First of all, the general tendency of creating a direct crack path between the support and loading plate was high. It seems that the smeared total-strain based crack formulation struggles to represent a tension shear failure mode. When the beams in reality fail due to a large opening of a critical diagonal crack, the numerical models rather change their crack pattern and create a direct force transmission path, going straight from the load plate to the support plate, making the beam fail in compression shear instead. Hence, one should be especially aware when this type of behavior is seen in the numerical model and give a proper evaluation of which failure mode is more realistic for the relevant structure and load situation.

Another pattern seen is probably connected to the statements in the above section. That is how the numerical model is working within sufficient accuracy for the very low shear span to effective depth ratios,  $a/d = 1.0$  and  $a/d = 1.5$ , and relatively high shear span to effective depth ratios, with  $a/d = 6.0$ , while for the intermediate ratios, with  $a/d = 2.0$  and  $a/d = 3$ , the numerical models are struggling significantly more. In fact, the average absolute percent value of the error of all analyses, that is the three shear retention models, four crack models (excluding the fully fixed as this is the same as in the shear retention analyses), and the one tension stiffening model, we get 10%, 10%, 51%, 59% and 16% error for  $a/d = 1, 1.5, 2, 3$  and 6, respectively. Hence, there is an obvious jump in error for the intermediate shear span to effective depth ratios. However, note that some of the

errors are due to reasons which could have been avoided. For example, the damage based shear retention model obviously failed to represent the most flexural beam, with  $a/d = 6.0$ , as the beam failed in tension shear rather than in a flexural failure. Furthermore, almost every beam exhibited an alternative crack pattern instead of failing in tension shear for  $a/d = 3.0$ , where the capacity could have been manually decided as discussed in Chapter 4.1.6. By a manual interpretation, the error could have been reduced from 59% to 20%. Also, it is worth mentioning the error for the  $a/d = 2.0$  beam could have been improved by comparing the numerical results to the experimental beam which yielded the same failure mode. That is because all the numerical models failed in compression shear, and the experimental comparable capacity was the mean value of two experimental beams, where one failed in compression shear and the other in tension shear. However, this is less appropriate as this beam could just as well have failed in tension shear as compression shear in a real situation. The other notation about the beam with  $a/d = 2.0$  is that even when the numerical capacities are compared to the experimental compression shear capacity it is still quite overestimated. This might be the result of the beam having relatively large crack widths, as it is a transitional beam between compression and tension shear failure, which could affect the experimental capacity to be lower, which was discussed further in Chapter 4.1.4.

## 6 Suggestions for Further Research

In this thesis research has been done to find a unified solution procedure which was able to represent a diversity of beam geometries. As this was not satisfactorily achieved, the search for such a solution procedure continues. Thereby, some suggestions for further research will be presented in this chapter.

When several numerical models shall be investigated within a limited amount of time, the analyst has to balance on a line between computational time and realistic numerical representations. In this thesis, a 2D-representation with symmetry boundary conditions was chosen in order to make it possible to investigate a great number of modelling procedures. Hence, a next step is to extend the analyses to a full size 3D model to achieve a more accurate numerical representation. This way, effects as tension stiffening (more accurate TS zones) and confinement would be more realistic.

Furthermore, it was proved that the influence of shear retention was highly important to the numerical capacities and behaviors in general. Three shear retention models were investigated in this thesis, namely the damage based, Al-Mahaidi and aggregate based shear retention model. However, these models have the setback of not representing shear dilatancy, which could be of great importance in the simulation of RC beams. DIANA does in fact have some models that also include this, for example the Maekawa contact density model, which could be interesting to investigate further.

A limited number of material parameter changes and combinations were investigated in this thesis, simply due to the lack of time. Hence other important factors, as for example variabilities of the tensile strength might be investigated. In this thesis, the tensile strength was extracted directly from a splitting tensile test performed by Suchorzewski, with the same concrete mixture as the one in the experimental beams. However, Maekawa claims that structural tensile strength tend to be smaller than material values obtained in splitting tensile tests due to shrinkage, residual stresses, and other effects (Maekawa et al., 2003). Hence, an investigation of different values of the tensile strength might result in better numerical capacity estimations and even change the failure modes. Another material tweak could be to reduce the Young's modulus. This was also taken directly from the experimental tests performed by Suchorzewski. However, the guidelines for NLFEA of concrete structures recommends reducing this by 15 % to account for initial cracking due to creep, shrinkage, and such (Hendriks and Roosen, 2019). In general, parameter changes and uniaxial and biaxial models beyond what is investigated in this thesis could be of great importance to the numerical model and is thereby worth investigating further. Finally, an entirely different fracture model could also be worth investigating, as this thesis was limited to only the smeared, total-strain based crack model.

Furthermore, this thesis did not evaluate the effect of different kinematic approaches, nor equilibrium controls. The effect of varying mesh densities as well as the properties assigned to the nonlinear incremental-iterative procedure could be of great importance for the outcome of the analyses. Hence, it is recommended that this also is looked into.

A final suggestion is to further investigate the non-local approach, addressed in Chapter 3. The model showed good estimations for the beams presented in this thesis, and it would be interesting to see the same model being used on different types of structures and loading situations.

# Bibliography

- Bažant, Z.P. (1984). Size effect in Blunt Fracture: Concrete, Rock, Metal. *Journal of engineering Mechanics*, 110(4), pp 518-535. Available at: <https://ascelibrary.org/doi/abs/10.1061/%28ASCE%290733-9399%281984%29110%3A4%28518%29> [Accessed 24. Mars 2022]
- Bažant, Z.P. (1986). Mechanics of distributed cracking. *Appl. Mech.*, 39(5), pp. 675-705.
- Bažant, Z.P. (2000). Size effect. *International Journal of Solids and structures*, 37(1), pp. 69-80.
- Bažant, Z.P and Becq-Giraudon, E. (2002). Statistical prediction of fracture parameters of concrete and implications for choice of testing standard. *Cement and Concrete Research*, 32(4), pp. 529-556. Available at: <https://www.sciencedirect.com/science/article/pii/S0008884601007232> [Accessed 29. Mars 2022]
- Brisotto, D.de S., Bittencourt, E., Bessa, V.M.R.d'A.(2012). Simulation bond failure in reinforced concrete by a plasticity model. *Computers & Structures*, 106-107, pp. 81-90. Available at: [https://www.academia.edu/68617996/Simulating\\_bond\\_failure\\_in\\_reinforced\\_concrete\\_by\\_a\\_plasticity\\_model](https://www.academia.edu/68617996/Simulating_bond_failure_in_reinforced_concrete_by_a_plasticity_model) [Accessed 8.Mar. 2022]
- Carpinteri, A. (1989). Decrease of apparent tensile and bending strength with specimen size: Two different explanations based on fracture mechanics. *International Journal of Solids and Structures*, 25(4), pp. 407-429. Available at: <https://www.semanticscholar.org/paper/Decrease-of-apparent-tensile-and-bending-strength-Carpinteri/bb46cc5d4606e5aebbee07b122b52a20bbc9bcb2> [Accessed 24. Mars 2022]
- Chen, H.H. and Su, R.K.L.(2013). Tension softening of curves of plain concrete, *Construction and Building MATERIALS*, 44, pp. 440-451. Available at: <https://www.sciencedirect.com/science/article/abs/pii/S095006181300250X> [Accessed 20.Feb. 2022]
- Cook, R.D., Malkus, D.S., Plesha, M.E. and Witt, R.J (2001) *Concepts and applications of finite element analysis*. 4th ed.
- Cornelissen, H. a., Hordijk, D.A. and Reinhardt, H.W. (1986). Experimental determination of crack softening characteristics of normalweight and lightweight concrete. *HERON*, 31(2). Available at: <https://repository.tudelft.nl/islandora/object/uuid%3A08c29b39-5c60-4ab6-b9d5-643d11007f7c> [Accessed 18. Mars 2022]
- Deaton, B.J. (2013). Nonlinear Finite Element Analysis of Reinforced Concrete Exterior Beam-Column Joints with Non Seismic Detailing. PhD thesis. Georgia Institute of Technology.
- De Putter, A., Hendriks, M.A.N., Rots, J.G, Yang, Y., Engen, M., van den Bos., Ab A. (2022). Quantification of the resistance modeling uncertainty of 19 alternative 2D

nonlinear finite element approaches benchmarked against 101 experiments on reinforced concrete beams. *Structural Concrete*.

DIANA TNO (2012). User's manual, release 9.4.4.

DIANA TNO (2020). User's manual, release 10.4.

Engen, M.(2017) *Aspects of design of reinforced concrete structures using nonlinear finite element analysis*. PhD thesis. Norwegian University of Science and Technology. Available at: <https://ntnuopen.ntnu.no/ntnu-xmlui/handle/11250/2459524>

Feenstra, P.H.,(1993) *Computational Aspects of Biaxial Stress in Plain and Reinforced Concrete*. PhD thesis, Delft University of Technology.

*fib* Model Code for Concrete Structures 2010. International Federation for Structural Concrete (fib).

Hauke, B. and Maekawa, K. (1999). Three-dimensional modelling of reinforced concrete with multi-directional cracking.

Hendriks, M. A. N. and Roosen, M. A.(2019) *Guidelines for nonlinear Finite Element Analysis of Concrete Structures*, Rijkswaterstaat Centre for Infrastructure, Report RTD:1016-1:2019

Hendriks, M.A.N., de Boer A., Belletti B.(2017) *Guidelines for Nonlinear Finite Element Analysis of Concrete structures*, Rijkswaterstaat Centre for Infrastructure, Report RTD:1016-1:2017.

Hordijk, D.A. (1991). Local approach to fatigue of concrete. PhD thesis. Delft University of Technology. Available at:

<https://repository.tudelft.nl/islandora/object/uuid%3Afa87147b-8201-47ed-83d7-b812b09c5fbb> [Accessed 18. Mars 2022]

Hsieh, S.S., Ting, E.C and Chen, W.F. (1982). A plastic-fracture model for concrete. *International Journal of Solids and Structures*, 18(3), pp.181-197. Available at: <https://www.sciencedirect.com/science/article/pii/0020768382900014> [Accessed 18. Mars 2022]

Kotsovos, M.D. and Pavlović, M.N. (1995) *Structural concrete: Finite-element analysis for limit-state design*.

Kumari, R. (2015). Review Paper Based On the Relation between the Strength of Concrete Cubes and Cylinders. *Journal of Engineering Research and Applications*, 5(8), pp. 52-54.

Lafta, Y.J and Ye, K. (2016). Specification of Deep Beams Affect the Shear Capacity. *Civil and environmental research*. 8(2), pp. 56-68. Available at:

[https://www.researchgate.net/publication/313877264\\_Specification\\_of\\_Deep\\_Beams\\_Affect\\_the\\_Shear\\_Strength\\_Capacity](https://www.researchgate.net/publication/313877264_Specification_of_Deep_Beams_Affect_the_Shear_Strength_Capacity) [Accessed 22. Mars 2022]

Maekawa, K., Pimanmas, A., and Okamura, H.(2003). *Nonlinear Mechanics of Reinforced Concrete*.

Marzec, I., Tejchmann, J. and Mróz, Z. (2019). Numerical analysis of size effect in RC beams scaled along height or length using elasto-plastic-damage model enhanced by non-local softening. *Finite Elements in Analysis and Design*. 157, pp. 1-20. Available at:

<https://www.sciencedirect.com/science/article/pii/S0168874X18303895?via%3Dihub>  
[Accessed 31. Mars 2022]

Nakamura, H. and Higai, T. (2001). Compressive Fracture Energy and Fracture Zone Length of Concrete. Available at:  
[https://www.researchgate.net/publication/284702663\\_Compressive\\_Fracture\\_Energy\\_and\\_Fracture\\_Zone\\_Length\\_of\\_Concrete](https://www.researchgate.net/publication/284702663_Compressive_Fracture_Energy_and_Fracture_Zone_Length_of_Concrete) [Accessed 29. Mars 2022]

Reinhardt, H.W., Cornelissen, H.A.W, Hordijk, D.A. (1986) TENSILE TESTS AND FAILURE ANALYSIS OF CONCRETE, *Journal of Structural Engineering*, 112(11), Available from:  
<https://ascelibrary.org/doi/10.1061/%28ASCE%290733-9445%281986%29112%3A11%282462%29>

Rots, J.G and Blaauwendraad, J. (1989). Crack Models for Concrete, Discrete or smeared? Fixed, Multi-Directional or Rotating? *HERON*, 34(1). Available at:  
<https://repository.tudelft.nl/islandora/object/uuid%3A0a401939-2938-4f9d-a395-b6a6652b2cd9> [Accessed 21. Mars 2022]

Selby, R.G. and Vecchio, F.J. (1997). A constitutive model for analysis of reinforced concrete solids. *Canadian Journal of Civil Engineering*, 24, pp. 460-470. Available at:  
<https://tspace.library.utoronto.ca/handle/1807/10030> [Accessed 18. Mars 2022]

Standard Norge. NS-EN 1992-1-1:2004 + NA: 2008. Eurocode 2: Design of concrete structures – Part 1-1: General rules and rules for buildings.

Suchorzewski, J. (2022). E-mail to Trygve Løvli, 10. May.

Suchorzewski, J., Korol, E., Tejchman, J., Mróz, Z. (2018). Experimental study of shear strength and failure mechanisms in RC beams scaled along height or length. *Engineering Structures*, 157, pp. 203-223

Suchorzewski, J., Marzec, I., Tejchman, J. and Korol, E. (2018). Investigation on strength and fracture in RC beams scaled along height or length. *Computational modelling of concrete structures*. Available at:  
<https://www.taylorfrancis.com/chapters/oa-edit/10.1201/9781315182964-78/investigations-strength-fracture-rc-beams-scaled-along-height-length-suchorzewski-marzec-tejchman-korol> [Accessed 31. Mars 2022]

Sørensen, S.I. (2010). *Betongkonstruksjoner*, volume 2.

Ulfkjær, J.P.(1992) *Fracture Mechanics of Concrete*. PhD thesis. Aalborg University.

Van Mier, J.G.M., Shah, S.P., Arnaud, M., Balayssac, J.P., Bascoul, A., Choi, S., Dasenbrok, D., Ferrara, G., French, C., Gobbi, M.E., Karihaloo, B.L., Koing, G., Kostovos, M.D., Labuz, J., Lange-Kornbak, D., Markeset, G., Pavlovic, M.N., Smirsch, G., Thienel, K-C. and Turtsinze, A. (1997). Strain-softening of concrete in uniaxial compression. *Materials and Structures*, 30(4), pp. 195-209

Vecchio, F.J. (2001) Non-linear finite element analysis of reinforced concrete: at the crossroads? *Structural concrete*, 2(4), pp. 201-212

Vecchio, F.J. and Collins, M.P. (1993). Compression Response of Cracked Reinforced Concrete. *Journal of Structural Engineering*. 121(7), pp. 3590-3610

Vecchio, F. J. and Lai, D. (2004). Crack shear slip in reinforced concrete elements. *Journal of advanced concrete technology*. 2(3), pp 289-300. Available at:  
[https://www.jstage.jst.go.jp/article/jact/2/3/2\\_3\\_289/article](https://www.jstage.jst.go.jp/article/jact/2/3/2_3_289/article) [Accessed 20. April 2022]

Vonk, T.A. (1992). *Softening of concrete loaded in compression*. PhD thesis. Eindhoven University of Technology. Available at: <https://doi.org/10.6100/IR375705> [Accessed 24.Feb. 2022]

Zararis, P.D. (2003). Shear Compression Failure in Reinforced Concrete Deep Beams. *Journal of Structural Engineering*, 129(4), pp. 544-553. Available at: <https://ascelibrary.org/doi/abs/10.1061/%28ASCE%290733-9445%282003%29129%3A4%28544%29> [Accessed 22. Mars 2022]

Øverli, J. A. (2016). *Formulas TKT4175 concrete structures 1*.

# Appendix A

## Validation Tests

DIANA offers a great variety of possibilities on how to model your material. To validate and understand the behavior of different material behaviors, and also combination of different behaviors, a small series of simple element tests were performed. The loading was always inflicted in the form of prescribed deformation, and the tests were performed on a four-node quadrilateral isoparametric plane stress element with size  $h=100$  mm.

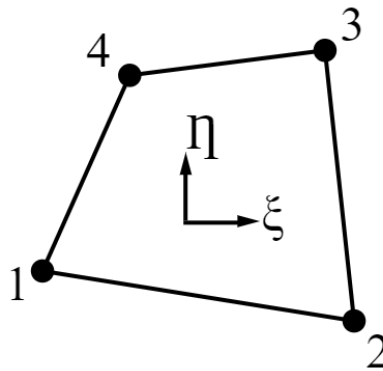


Figure A.1 – Four-noded isoparametric plane stress element (DIANA TNO, 2020)

### A.1 Compression and Tensile Behavior

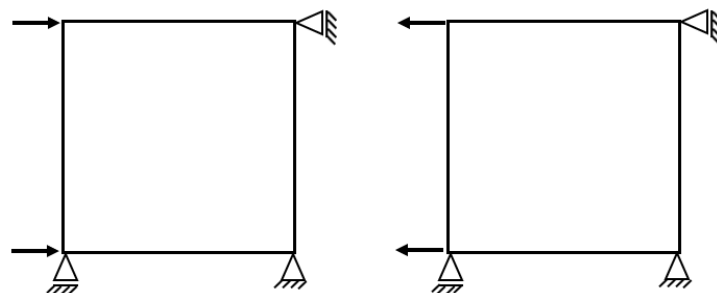


Figure A.2 – Model setup for compression and tension validation test

The motivation for these tests were to validate the compression and tensile responses. A parabolic compression model, and the Hordijk tensile model, were used. The secant unloading and reloading was also illustrated.

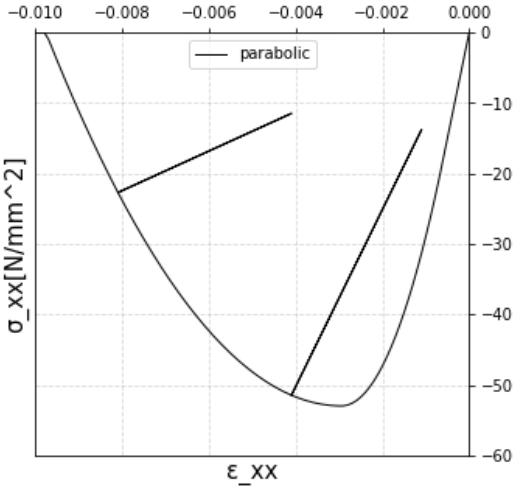


Figure A.3 – Parabolic compression response with secant unloading and reloading

Figure A.3 is the plotted response of the compression behavior with unloading and reloading. The compressive strength were set to 53 N/mm<sup>2</sup>, the compressive fracture energy was set to 24.1 N/mm, the Young’s modulus was 30 000 N/mm<sup>2</sup> in this validation test. Using the formulas for the parabolic compression curve given in Chapter 2.3.2, we obtain the strain values as:

$$\alpha_c/3 = -\frac{1}{3} \frac{f_c}{E} = -0.0006; \alpha_c = -\frac{5}{3} \frac{f_c}{E} = -0.0029; \alpha_u = \min\left(\alpha_c - \frac{3}{2} \frac{G_c}{h f_c}, 2.5\alpha_c\right) = -0.0098$$

which reflects the linear, peak, and ultimate strain limits respectively. These values fits the measured properties in the parabolic compression curve.

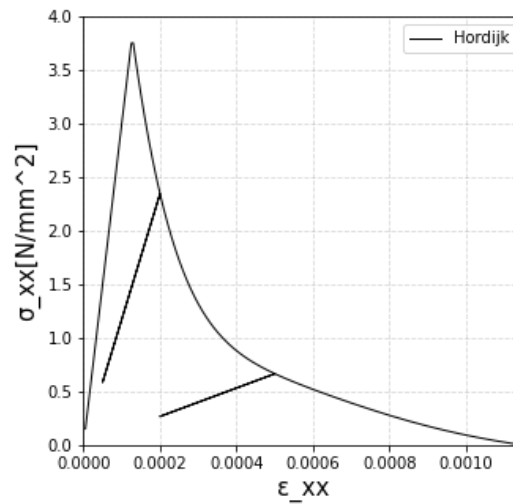


Figure A.4 – Hordijk tensile response with secant unloading and reloading

Figure A.4 is the plotted response of the Hordijk tensile behavior with secant unloading and reloading. The tensile strength was set to 3.82 N/mm<sup>2</sup>, the fracture energy as 0.1 N/mm<sup>2</sup> and the Young's modulus is still 30 000 N/mm<sup>2</sup>. Using the formulas for the Hordijk compression curve given in Chapter 2.3.1, we obtain the strain values as:

$$\varepsilon_{nn,peak} = \frac{f_t}{E} = 0.00013; \varepsilon_{nn,ult}^{cr} = 5.136 \frac{G_f^I}{hf_t} = 0.00134$$

which reflects the peak and ultimate strain. One can see a small deviation in the measured ultimate strain and the analytical ultimate strain, as the measured seems to reach 0.0012. However, a strain error of 0.0001 is concluded to be in the acceptable range, as minor inaccuracies might take place in the transition between numerical and analytical calculations. In general, the curve acts as expected.

## A.2 Compressive Reduction due to Lateral Cracking

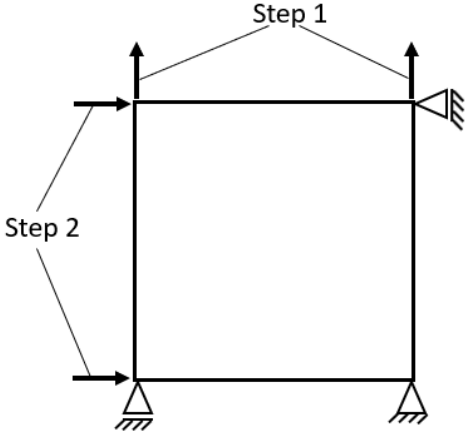


Figure A.5 – Model setup for validation of compressive reduction due to lateral cracking

The motivation for this validation test was to illustrate and understand how the compressive strength is reduced due to damage in the lateral direction. The theory background is provided in Chapter 2.3.2. Figure A.5 shows the loading procedure. First, a tensile strain was applied with a certain strain amount, denoted as “Step 1” in Figure A.5. Then, a compression force was applied. In this test, the Poisson’s ratio were not included ( $\nu = 0$ ) to avoid unwanted lateral effects. To validate the reduction a series of such loading procedures were carried through with different values of the tensile strain. Again, the compression strength was 53 N/mm<sup>2</sup>.

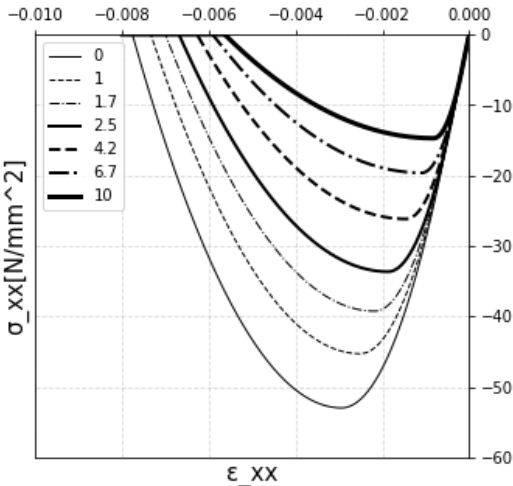


Figure A.6 – Compressive behaviors for different lateral strain values

The legend, ranging from 0 to 10, represents the lateral damage to compressive strain ratio,  $-\frac{\alpha_{lat}}{\epsilon_0}$ , where  $\alpha_{lat} = \sqrt{\alpha_{l,1}^2 + \alpha_{t,1}^2}$  and  $\epsilon_0 = -\frac{f_c}{E}$ . For example, ratio 2.5 means that a tensile strain value of  $\alpha_{lat} = 2.5\epsilon_0 = 0.0044$  was applied before initiating the compression force. Also note that the peak strain in Figure A.6 moves to the right, as more lateral damage is applied. This is not because of the strain factor, as discussed in Chapter 2.3.2, but is the result of the strain in the parabolic curve being dependent on the compressive strength.

By collecting and calculating the reduced capacity of the strength in Figure A.6, a plot against the analytical eq. (2.26) in Chapter 2.3.2 was shown to see the correlation.

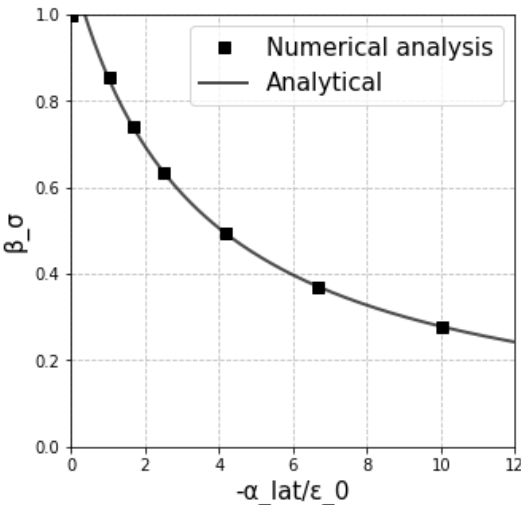


Figure A.7 – Analytical vs. numerical plots of the lateral reduction of compressive strength

As seen in Figure A.7, the numerical validation test shows good correlation with the analytical results. Note that it is possible to insert a lower bound limit in DIANA, which is recommended to be 40% (Hendriks and Roosen, 2019), and is also used in the analyses in this thesis. As seen in Figure A.7, no lower bound value was inserted in this specific validation test.

### A.3 Shear Retention

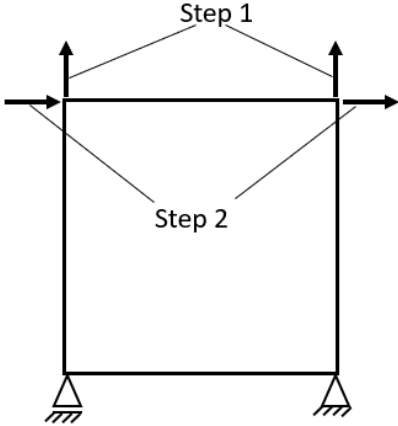


Figure A.8 – Model setup for shear retention tests

The motivation for this type of test is to investigate the differences in the three different shear retention models that were analyzed in this thesis. This is done in a similar manner as before, with different values of tensile strain in step 1, however, now the next step, step 2, results in a constant shear force. The shear retention models, presented in Chapter 2.5.4, are dependent on the tensile behavior, which in this case was the Hordijk softening curve, presented in Chapter 2.3.1.

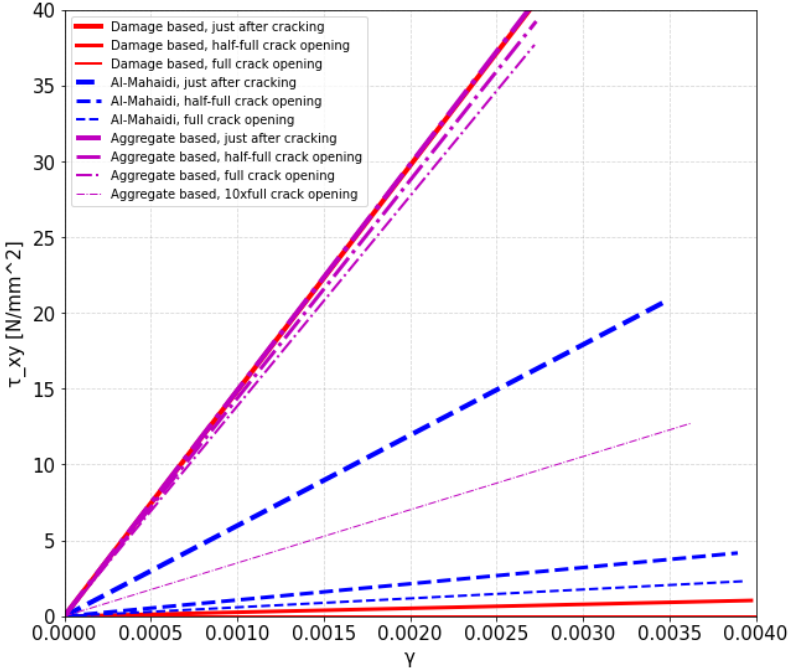


Figure A.9 – A comparison of shear retention models for different tensile strain values for the damage based, Al-Mahaidi and aggregate based shear retention model

In the legend in Figure A.9, the description of each curve is provided. The basic procedure was to evaluate the stiffness of each shear retention model for different values of the tensile strain. The three shear retention models investigated was the damage based, the Al-Mahaidi with a lower bound value of 0.01 and the aggregate based with a mean aggregate size of 4.8 mm. These models were also used in one of the studies in this thesis. Also, three tensile strains were used to illustrate the decrease in shear stiffness, which were equivalent to: right after initiation of crack, half-full crack opening, and fully opened crack. As can be seen in Figure A.9, the initial stiffness right after cracking was equivalent to  $15\,000\text{ N/mm}^2$ , which fits the inserted values of  $E = 30000$  and  $\nu = 0$  when calculated according to eq. (2.55). The damage based shear retention had, not surprisingly, the fastest decrease as the crack strain increased. However, the Al-Mahaidi shear retention model had the most conservative just-after-cracking stiffness, as this curve immediately reduces the stiffness by 60%. Still, the Al-Mahaidi curve had a slower decrease in shear stiffness than the damage based shear retention model as the crack strain got larger. Finally, the aggregate based shear retention model showed the least conservative results. An extra parameter check was performed for the aggregate based model, where the tensile strain was equivalent to 10 times a fully opened crack. Even for this strain, it showed relatively large shear stiffness. This is not surprising as this model is based on a linear decrease, reaching zero when the crack width is equivalent to half the mean aggregate size. Another way of illustrating the shear retention of the different models is by plotting the reduction factor as a function of the normal crack strain, see Figure A.10.

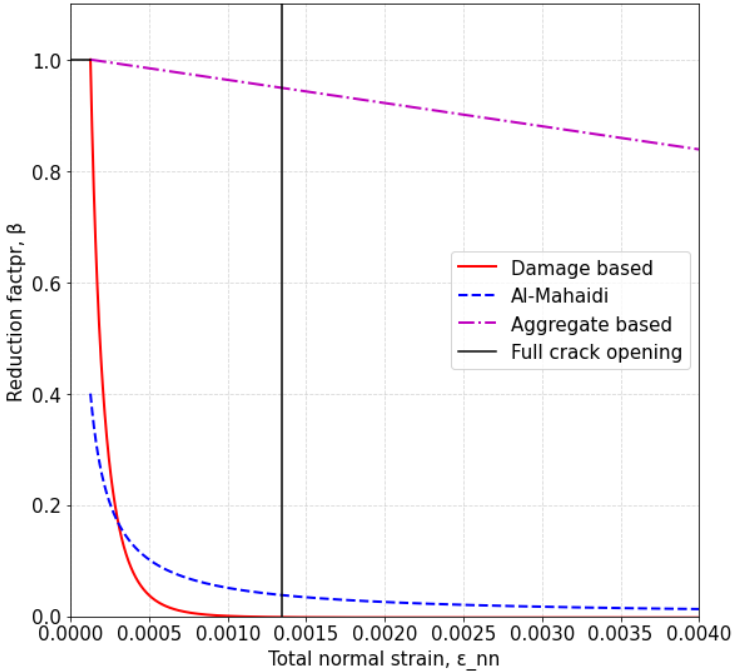


Figure A.10 – Reduction factor  $\beta$  as a function of the total normal strain  $\epsilon_{nn}$  for the damage based, Al-Mahaidi, and aggregate based shear retention model

The plots in Figure A.10 were made by plotting eq. (2.55) – (2.57). Note that there is a difference between the total normal strain and the crack normal strain, and thereby, this

had to be taken into account when plotting the shear retention models. Also note that the damage based model, that is eq. (2.55), is not a function which represents the reduction factor  $\beta$  directly, but rather the total crack shear stiffness. Hence, for the damage based shear retention model, one must find the secant stiffness in the Hordijk tension softening curve divided by the undamaged stiffness, to achieve the plot in Figure A.10. Then, if we set the Poisson's ratio  $\nu = 0$ , the equation becomes:

$$\beta_{damage\_based} = \frac{G^{cr}}{G} = \frac{E^{cr}/2}{E/2} = \frac{E^{cr}}{E} = \frac{\sigma_{nn}^{cr}(\epsilon_{nn}^{cr})_{Hordijk}/\epsilon_{nn}}{E} \tag{A.1}$$

Eq. (A.1) applies shows how the reduction factor  $\beta$  might be plotted for the Hordijk tensile curve. In the equation,  $\sigma_{nn}^{cr}(\epsilon_{nn}^{cr})_{Hordijk}$  is equivalent to eq. (2.10),  $\epsilon_{nn}$  is the total normal strain, and  $E$  is the undamaged Young's modulus.

This simple validation test illustrate the deviation between the shear retention models. It also shows that the aggregate based shear retention model is the most unconservative model, and that the Al-Mahaidi and damage based model are more conservative. Which of the latter models that are the most conservative depends on the crack widths in the given case. Also note that there is no lower bound value in the damage and aggregate based shear retention models, in contrast to the Al-Mahaidi model.

### A.4 Confinement

Another important aspect of the biaxial behavior of concrete is the effect of lateral confinement. This effect increases the compressive strength as a result of increasing isotropic stress. How DIANA implement this effect is described in Chapter 2.3.2.

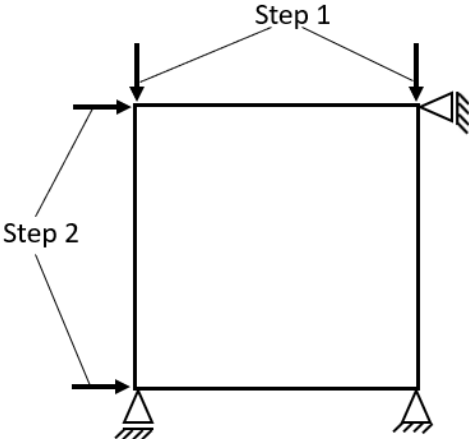


Figure A.11 – Model setup for confinement test

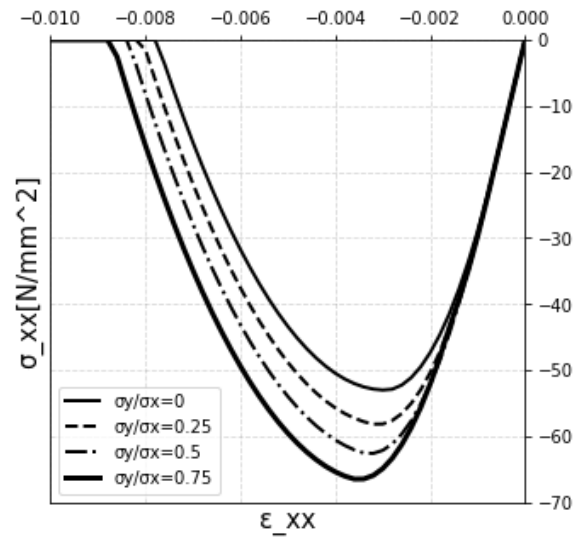


Figure A.12 – Compressive behaviors for different ratios of confinements

As can be seen in Figure A.12, an increasing strength and ductility occurs for increasing lateral confinement. One can see that the initial compression strength value at 53 N/mm<sup>2</sup> reaches about 66 N/mm<sup>2</sup> for a confinement ratio of 75 %. This is an increase of about 25%.

# Appendix B

## Modelling Calculations

### B.1 Calculation of Threshold Strain Value in the Rotating to Fixed Crack Model

The calculation of threshold values are done with respect to the crack strain in eq. (2.13). Since the equation is based on crack strain, and the threshold values are applied as total strain, one must add the pre-crack strain to get the exact value threshold value,  $\epsilon_f$ :

$$\epsilon_f = \frac{f_t}{E} + 5.136 \frac{G_f^I}{hf_t} x \tag{B.1}$$

The  $x$  represents the multiplying factor to obtain different total strain values reflecting the crack size and would for example be 1 for a fully opened crack. The values used in the equation and the corresponding result are presented in Table B.1.

*Table B.1 – Calculation of threshold strain value in the rotating to fixed crack model*

<b>Calculation of threshold strain value in the rotating to fixed crack model</b>							
	$E$ N/mm <sup>2</sup>	$f_t$ N/m m <sup>2</sup>	$G_f^I$ N/m m	$h$ mm	Half	Full	5xFull
S1D18a108	33100	2.81	0.093	16	0.0054	0.0107	0.0532
S1&2D36a108	33100	2.81	0.093	23	0.0038	0.0075	0.0370
S1D72a108	33100	2.81	0.093	40	0.0022	0.0043	0.0213
S2D36a72	35300	3.61	0.095	23	0.0030	0.0060	0.0295
S2D36a36	35300	3.61	0.095	23	0.0030	0.0060	0.0295

## B.2 Calculation of Tension Stiffening Zone

Eq. (2.38) from Chapter 2.4.3 gives:

$$h_{stiffening} = \frac{\pi f_y d_b (t_c - d_b) n}{22 f_t b} \quad (\text{B.2})$$

which is the Maekawa formulation (Maekawa et al., 2003). The Eurocode (Eurocode 2), with the national annex gives, as can be seen in eq. (2.39) and eq. (2.40) from Chapter 2.4.3:

$$h_{stiffening} = \min\{2.5(h - d); (h - x)/3; h/2\} \geq h - d + 1.5d_b \quad (\text{B.3})$$

See symbol descriptions in Chapter 2.4.3. As can be seen in eq. (B.3), the compression zone is a part of the expression. To calculate the compression zone, a service limit state cracked cross section with no residual concrete tensile stress is assumed, with the following expression:

$$x = \alpha d = \left( \sqrt{(\eta\rho)^2 + 2\eta\rho} - \eta\rho \right) d \quad (\text{B.4})$$

where  $\eta = E_s/E_{cm}$  and  $\rho = A_s/bd'$ , where  $E_s$  is the steels Young's modulus,  $E_{cm}$  is the concrete Young's modulus,  $A_s$  is the area of the reinforcement,  $b$  is the concrete width and  $d$  is the effective height. This model assumes linear elasticity following Hooke's law, and Navier/Bernoulli's hypothesis about plane strain sections remain plain (Sørensen, 2010). This is not the case in the nonlinear analyses performed in this thesis. However, eq. (B.4) is assumed to provide an approximation which is sufficient enough in the current case. Table B.2 presents the tension stiffening zones calculated according to Maekawa and Eurocode procedures.

Table B.2 – Calculation of tension stiffening zone

Calculation of tension stiffening zone												
	$f_y$ N/mm <sup>2</sup>	$f_t$ N/mm <sup>2</sup>	$d$ mm	$d_b$ mm	$t_c$ mm	$n$ /layer	$b$ mm	$h$ mm	$x$	Maekawa mm	Maekawa* mm	EC
S1D18a108	560	2.81	180	20	40	2	250	230	61	91	91	80
S1&2D36a108	560	2.81	360	20	40	4	250	410	122	182	141	96
S1D72a108 Lower layer	560	2.81	720	20	40	4	250	795	244	182	419	184
S1D72a108 Upper layer	560	2.81	720	20	90	4	250	795	244	637		
S2D36a72	560	3.61	360	20	40	4	250	410	119	142	121	97
S2D36a36	560	3.61	360	20	40	4	250	410	119	142	121	97

\*Actual tension stiffening height with geometrical boundaries, several layers and overlapping taken into account.

Note that eq. (B.3) from the Eurocode provides the actual height of the whole tension stiffening (TS) zone, while eq. (B.2) from Maekawa provides the height for each reinforcement layer, where the height is to be extracted equally from the center of the reinforcement layer. Hence, "Maekawa\*" in Table B.2 presents the actual resulting height on the beams. The actual heights of the TS zones in the Maekawa formulation then becomes: 91 mm, 141 mm, 419 mm, 121 mm and 121 mm for S1D18a108, S1&2D36a108, S1D72a108, S2D36a72 and S2D36a36 respectively. Using these values, the Maekawa/Eurocode ratio becomes 1.14, 1.47, 2.28, 1.25 and 1.25. The largest deviation happens for the S1D72a108, due to the extra layer giving the Maekawa model a very large stress expansion area, as can be seen in Table B.2 for the S1D72a108 upper layer. Due to the fact that the total-strain based crack model only allows for isotropic material modelling of the TS effect, the large expansion of the TS zone in S1D72a108 may give horizontally inclined cracks in the shear zone post-crack stiffness beyond realistic measures. Thus, the more conservative Eurocode TS height is used instead.

### B.3 Calculation of Analytical Initial Stiffness and Crack Initiation Values

Initially, the cross section should be considered uncracked. Hence, the concrete contributes both in compression and tension. This is illustrated in Figure B.1.

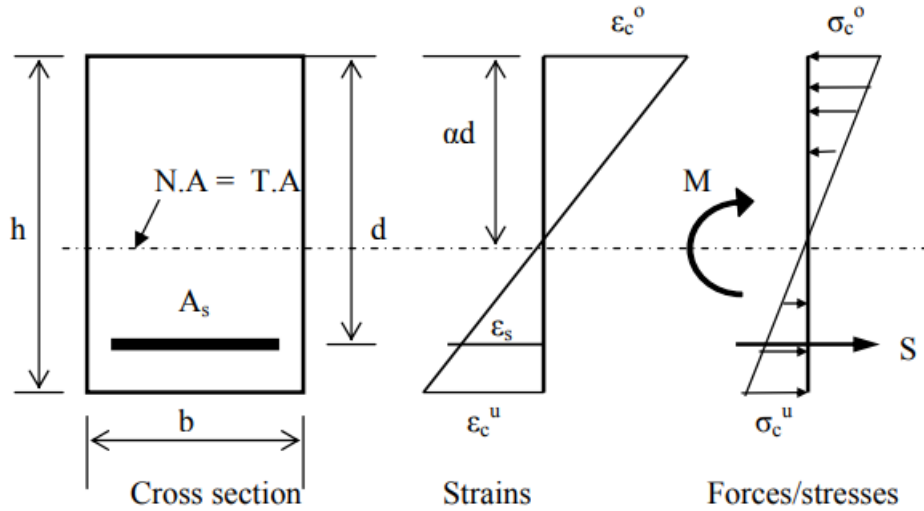


Figure B.1 – Uncracked cross section (Øverli, 2016)

The compression zone depth can then be expressed as:

$$\alpha d = \frac{A_c 0.5h + \eta A_s d}{A_c + \eta A_s} \quad (\text{B.5})$$

with  $A_c$  as the area of the concrete cross section,  $h$  as the concrete height,  $A_s$  as the total reinforcement area,  $d$  as the effective height, and finally  $\eta = E_s/E_{cm}$ , which is the Young's modulus of reinforcement over the Young's modulus of the concrete ratio. Furthermore, the concrete and reinforcement contribution of the second moment of inertia is respectively noted as:

$$I_{c1} = \frac{bh^3}{12} + bh \left( \alpha d - \frac{h}{2} \right)^2 ; I_{s1} = A_s (d - \alpha d)^2 \quad (\text{B.6})$$

where  $b$  is the cross sectional width. The flexural stiffness of the uncracked cross section can now be expressed as:

$$(EI)_1 = E_{cm} I_{c1} + E_s I_{s1} \quad (\text{B.7})$$

Eq. (B.7) is from now marked as the analytical flexural stiffness. To compare this to the numerical and experimental initial stiffnesses, the unit load method was used in combination with simplified integration.

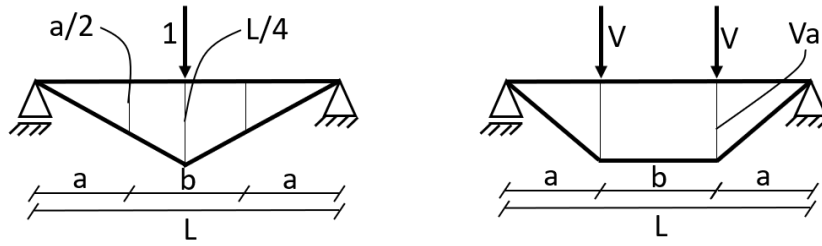


Figure B.2 – Moment diagrams of the unit load and the external loading

Figure B.2 shows the moment diagrams of the unit load, applied at the midspan, and the external loading. By integrating the product of the moment diagrams showed in Figure B.2, we find that the measured flexural stiffness of the numerical and experimental force-deflection curves can be expressed as:

$$(\mathbf{EI})_{measured} = \begin{bmatrix} (EI)_{measured\_S1D18a108} \\ (EI)_{measured\_S1\&2D36a108} \\ (EI)_{measured\_S1D72a108} \\ (EI)_{measured\_S2D36a72} \\ (EI)_{measured\_S2D36a36} \end{bmatrix} = \begin{bmatrix} \frac{1}{\delta} \frac{59}{1500} VL^3 \\ \frac{1}{\delta} \frac{59}{1500} VL^3 \\ \frac{1}{\delta} \frac{59}{1500} VL^3 \\ \frac{1}{\delta} \frac{299}{7986} VL^3 \\ \frac{1}{\delta} \frac{131}{4116} VL^3 \end{bmatrix} \quad (\text{B.8})$$

where  $\delta$  is the measured deflection,  $V = P/2$  is the measured load at the respective deflection, and  $L$  is the respective length. Note that in eq. (B.8) the deflection,  $\delta$ , and the load,  $V = P/2$ , are values drawn directly from the numerical and experimental force-deflection diagrams for the respective beam. Also note that  $L$  is varying for the geometrically different beams, that is the distance between the middle of the support plates. Hence, for beam S1D18a108, S1&2D36a108 and S1D72a108  $L = 2700mm$ , while for beam S2D36a72  $L = 1980mm$ , and finally for beam S2D36a36  $L = 1260mm$ . The lengths  $a$  and  $b$  in Figure B.2 do not show in eq. (B.8) because they were converted into different fractions of the total length,  $L$ . Without further ado, the analytical stiffness in eq. (B.7), and the numerical and experimental measured stiffness of the beams are compared in Table B.3. The results show that the initial stiffness of the beams only scaled in height (Figure 3.1 – Figure 3.3) shows good correlation between the analytical and measured values. For the shorter beams (Figure 3.4 and Figure 3.5) both the numerical and experimental measurements struggles to fit the analytical. However, the numerical model shows much better resemblance to the analytical measurements compared to the experimental. Note that for the beam S2D36a72, Figure 4.8 shows a very small range of where the experimental and numerical initial stiffnesses collide, but, for the sake of comparison, the experimental measurements were taken from values beyond this small range. Hence, if the very small initial experimental stiffness was measured, the obtained values would reflect the numerical values, with an “error” of 14% as seen in Table B.3.

Table B.3 – Analytical, numerical, and experimental initial stiffness

<b>Analytical, numerical, and experimental initial stiffness</b>					
	$(EI)_{analytical}$ Nmm <sup>2</sup>	$(EI)_{numerical}$ Nmm <sup>2</sup>	Numerical difference %	$(EI)_{experimental}$ Nmm <sup>2</sup>	Experimental difference %
S1D18a108	8.9e12	8.0e12	-10	8.0e12	-10
S1&2D36a108	53.3e12	49.8e12	-7	49.8e12	-7
S1D72a108	396.2e12	368.0e12	-7	368.0e12	-7
S2D36a72	56.5e12	48.7e12	-14	9.6e12	-83
S2D36a36	56.5e12	41.0e12	-27	7.6e12	-87

If Figure 4.11 in Chapter 4.1.6 is carefully investigated, one can see a very slight direction change in the force-deflection curve for the beam S2D36a36 (furthest to the right in the figure) at about 1 mm deflection. The stiffness alteration in a pre- and post-crack cross section would in a normal case certainly be more affected than the one observed in Figure 4.11. However, as a final check, the analytical deflection at the point of crack initiation was investigated and presented in the following sections. The cracking moment is calculated as:

$$M_{cr} = \frac{I_{c1} + \eta I_{s1}}{h - \alpha d} f_{ctm} \quad (B.9)$$

where  $I_{c1}$  and  $I_{s1}$  is calculated as in eq. (B.6),  $\alpha d$  as in eq. (B.5), and  $f_{ctm}$  was set to be the same as  $f_t$  in Table B.2. Furthermore, the cracking moment was converted to a cracking force by:

$$V_{cr} = \frac{M_{cr}}{a} \quad (B.10)$$

where  $M_{cr}$  is calculated in eq. (B.9), and  $a$  is the shear span which is illustrated in Figure B.2 and the specific values are presented in Figure 3.1 – Figure 3.5. Finally, if  $V = V_{cr}$  and  $(EI)_{measured} = (EI)_{analytical}$  (where  $(EI)_{analytical}$  is presented in Table B.3) in eq. (B.8), and we rearrange the equation to be solved for the deflection rather than the bending stiffness, we can obtain the analytical deflection values for when cracking should initiate. These values are presented in Table B.4. The values are ranging from 0.11 mm – 0.52 mm. For beam S2D36a36 the deflection was calculated to be 0.11 mm. Thus, the direction change at 1 mm in the force-deflection curve for beam S2D36a36 is probably not caused by the crack initiation.

Table B.4 – Deflection at crack initiation

<b>Deflection at crack initiation</b>	
	Deflection mm
S1D18a108	0.52
S1&2D36a108	0.32
S1D72a108	0.16
S2D36a72	0.21
S2D36a36	0.11

# Appendix C

## Crack Strain Patterns

This chapter shows the crack strain plots of different models and beams at critical changes in the force-deflection curve. To exemplify: The crack plots A) and B) in Figure C.7 are not marked by the respective letters in Figure C.6. However, A) equals the first mark on the force-deflection curve, B) is the second, and so on. This applies to all such illustrations in this thesis. Also, note that the crack strain plots are scaled by value. This is done to show more clearly where relatively large and small crack strains occur. In each of the crack strain chapters, for example in Appendix C.1.1, a systematic presentation is given as follows:

- Crack plot extractions marked as X'es on the respective force-deflection curve. The number of crack plots is not fixed as the number of critical changes in the crack pattern varies between the models and beams.
- The crack plots for the different models with the respective crack strain values.

In many cases the behavior of the numerical beam is very dependent on how the crack pattern evolves as the loading is inflicted. Deviation between the force-deflection curve in the analysis and the experiment often has a relation to deviation in respective crack patterns. Hence, the numerical crack evolution and the experimental crack pattern is presented. In the following chapters, the experimental force-deflection curves are not presented, as the main purpose of the force-deflection diagrams in this chapter is to present where the crack plots were extracted, and not to compare the numerical and experimental force-deflection curves. Such comparisons is presented in Chapter 4. The experimental crack patterns are shown in Figure C.1 – Figure C.5.

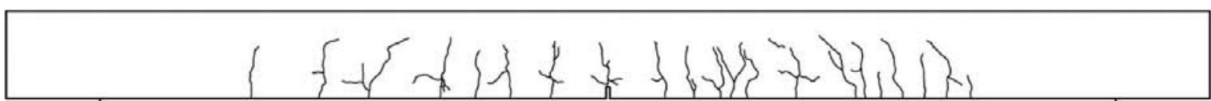


Figure C.1 – Crack pattern at failure for beam S1D18a108 (Suchorzewski et al., 2018)

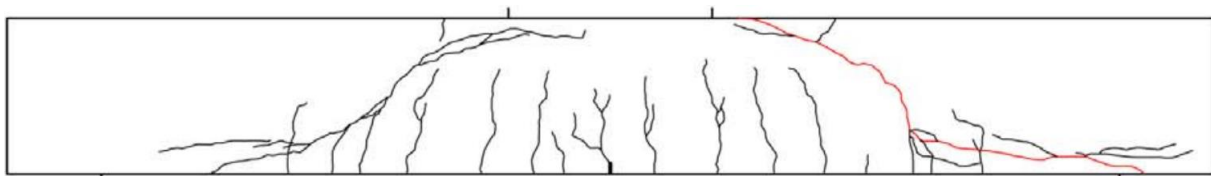


Figure C.2 – Crack pattern at failure for beam S1&2D36a108 (Suchorzewski et al., 2018)  
(critical crack is marked in red)

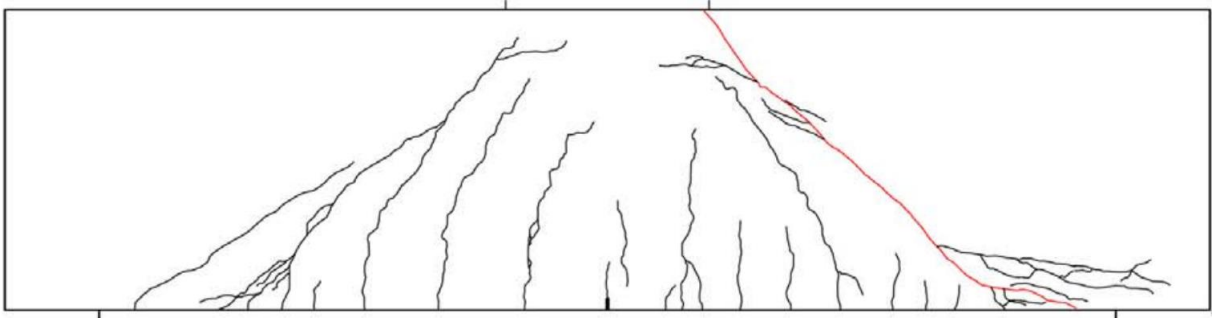


Figure C.3 – Crack pattern at failure for beam S1D72a108 (Suchorzewski et al., 2018)  
(critical crack is marked in red)

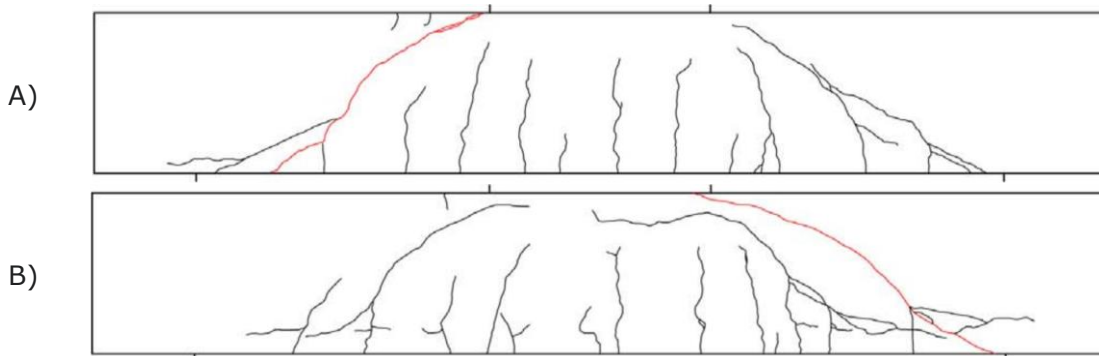


Figure C.4 – Crack pattern at failure for beam S2D36a72 (Suchorzewski et al., 2018),  
where A) failed in tension shear and B) failed in compression shear. (critical crack is  
marked in red)

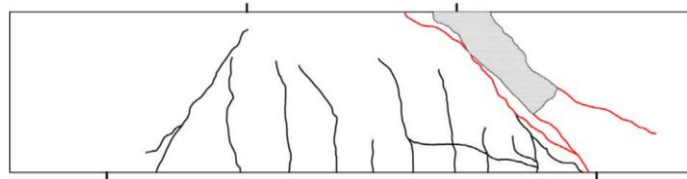


Figure C.5 – Crack pattern at failure for beam S2D36a36 (Suchorzewski et al., 2018)  
(critical crack is marked in red)

# C.1 Crack Strain Patterns of the Shear Retention Analyses

In this chapter, the crack strain patterns for different shear retention analyses are presented. This includes the damage based, Al-Mahaidi and aggregate based shear retention model for each of the five beam geometries.

## C.1.1 Crack Strain Patterns of Beam S1D18a108

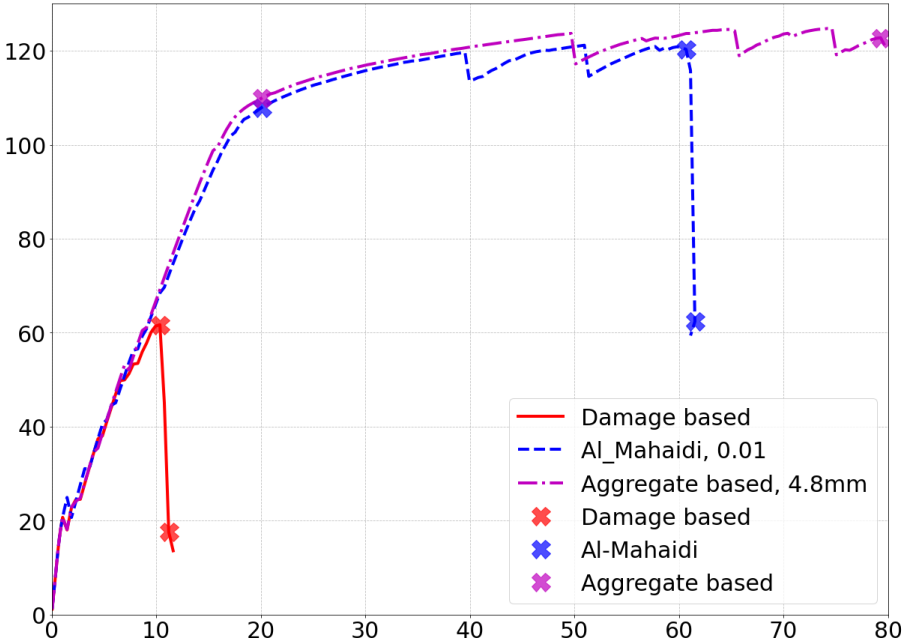


Figure C.6 – Crack plot specification for shear retention models for beam S1D18a108

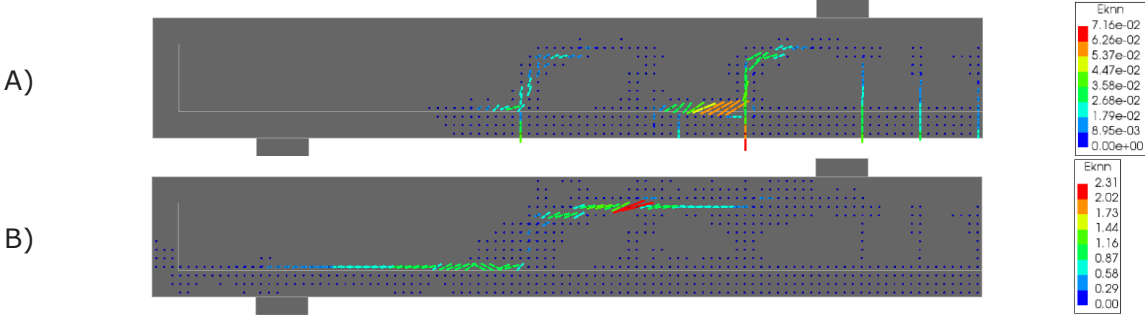


Figure C.7 – Crack strain plots beam S1D18a108, damage based

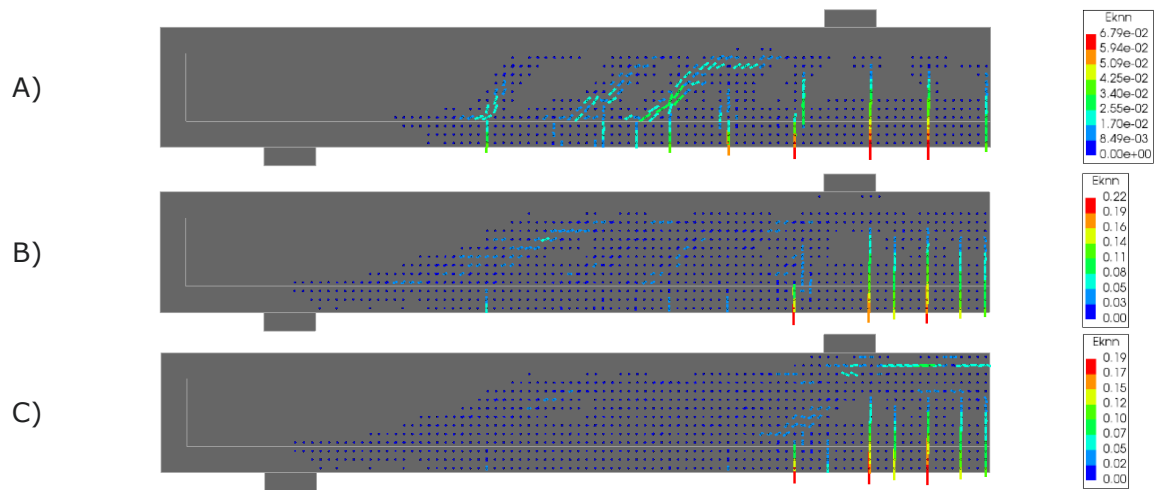


Figure C.8 – Crack strain plots beam S1D18a108, Al-Mahaidi

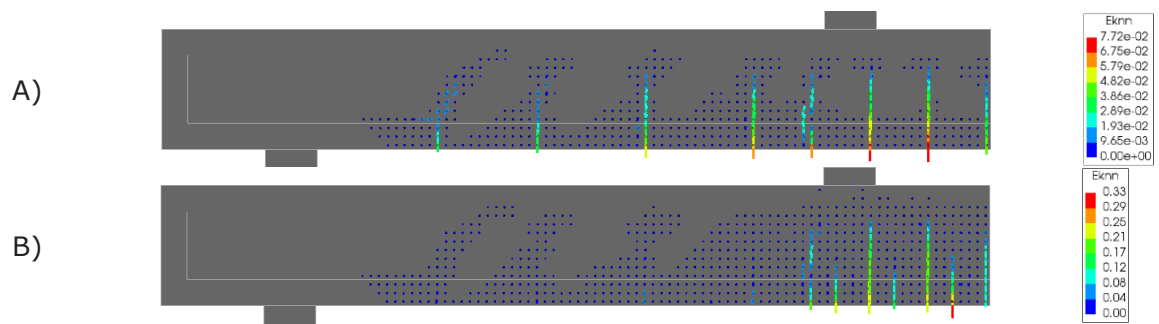


Figure C.9 – Crack strain plots beam S1D18a108, aggregate based

### C.1.2 Crack Strain Patterns of Beam S1&2D36a108

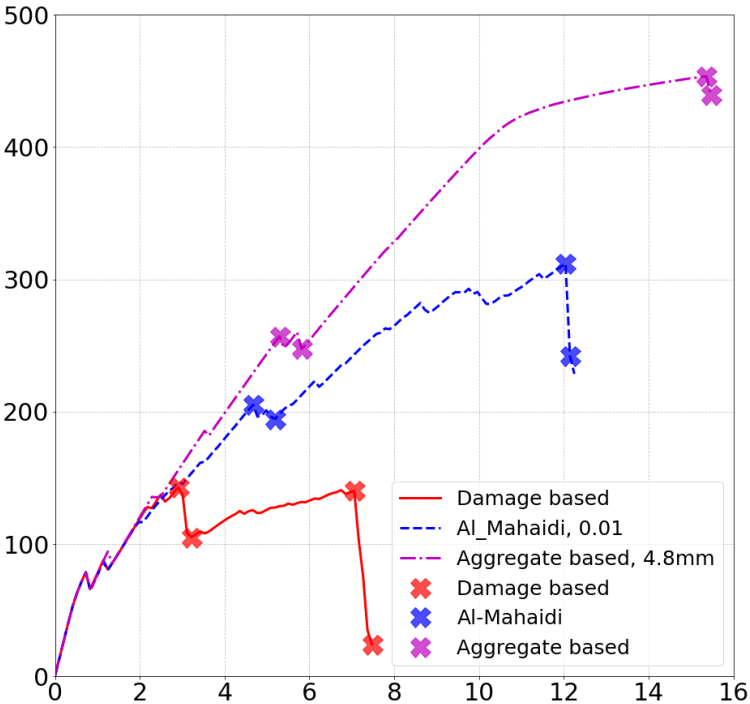


Figure C.10 – Crack plot specification for shear retention models for beam S1&2D36a108

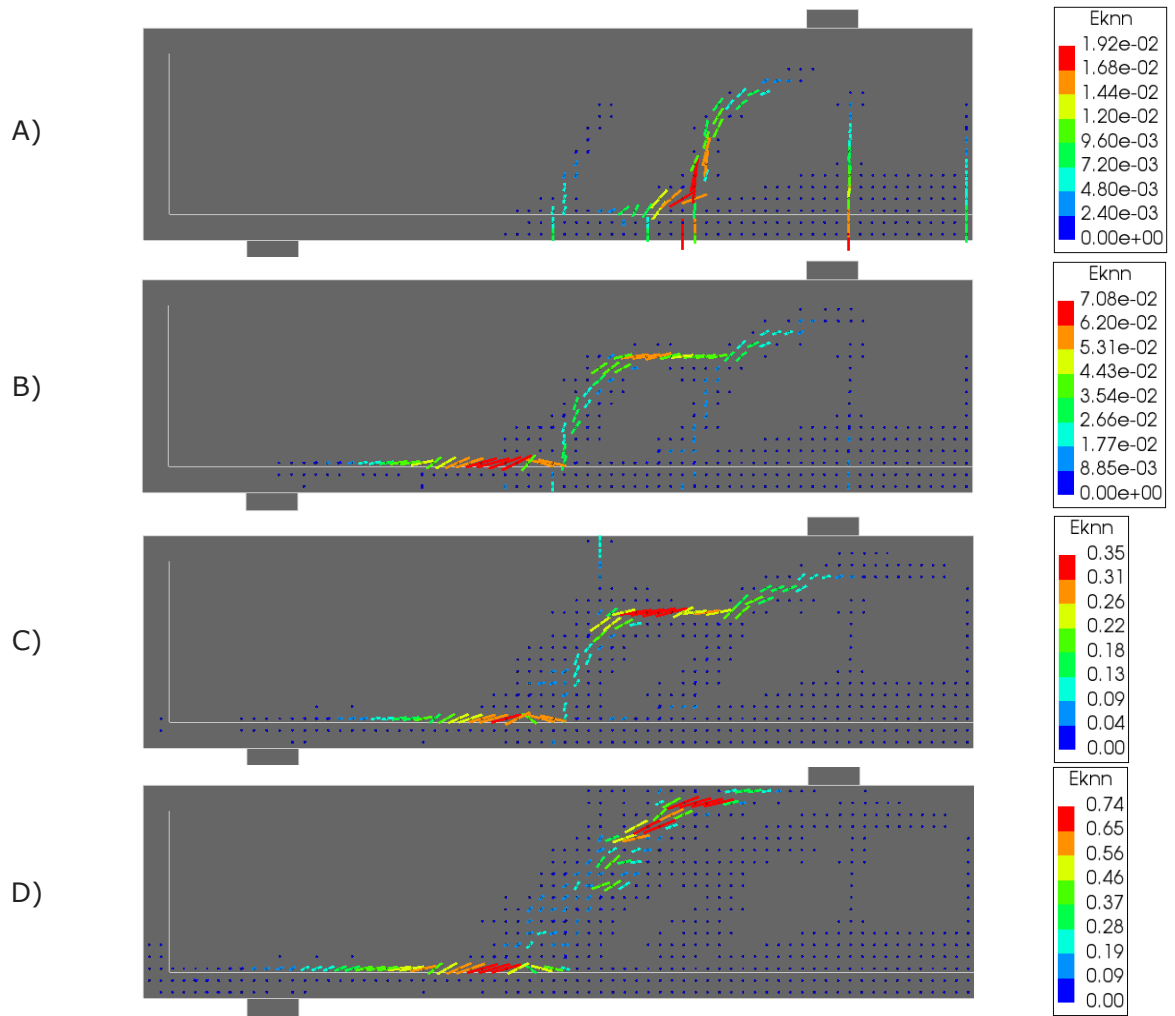


Figure C.11 – Crack strain plots beam S1&2D36a108, damage based

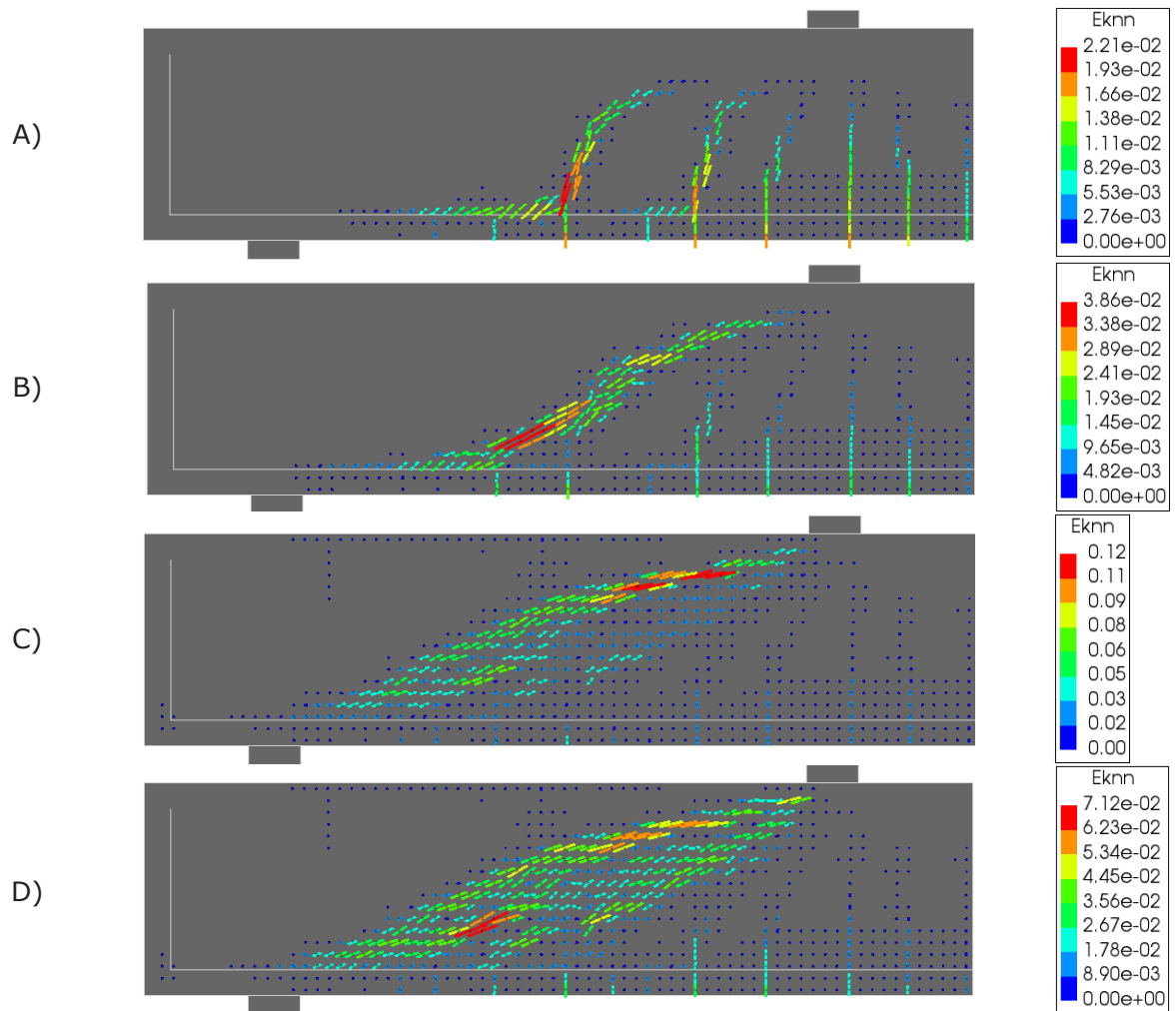


Figure C.12 – Crack strain plots beam S1&2D36a108, Al-Mahaidi

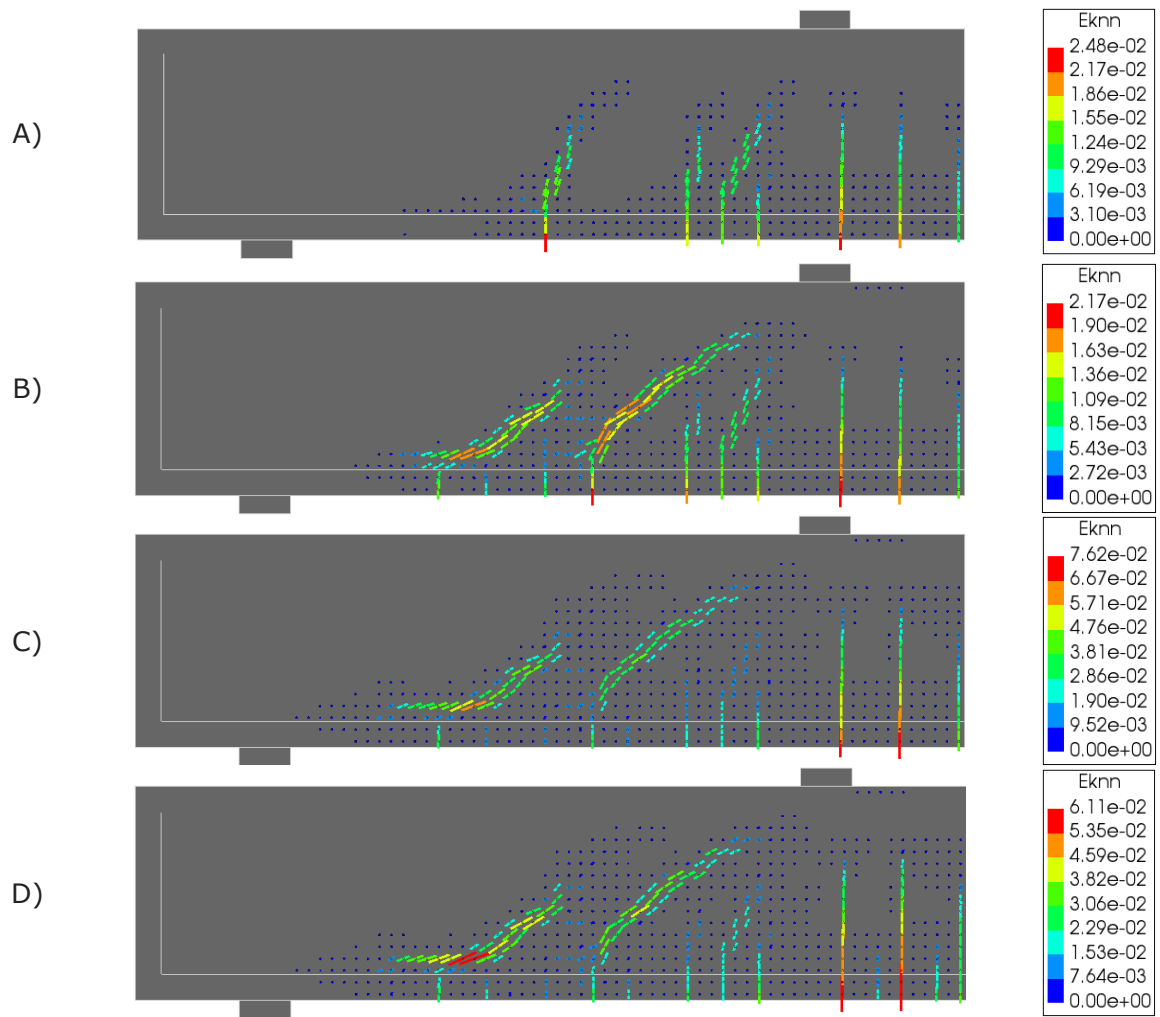


Figure C.13 – Crack strain plots beam S1&2D36a108, aggregate based

### C.1.3 Crack Strain Patterns of Beam S1D72a108

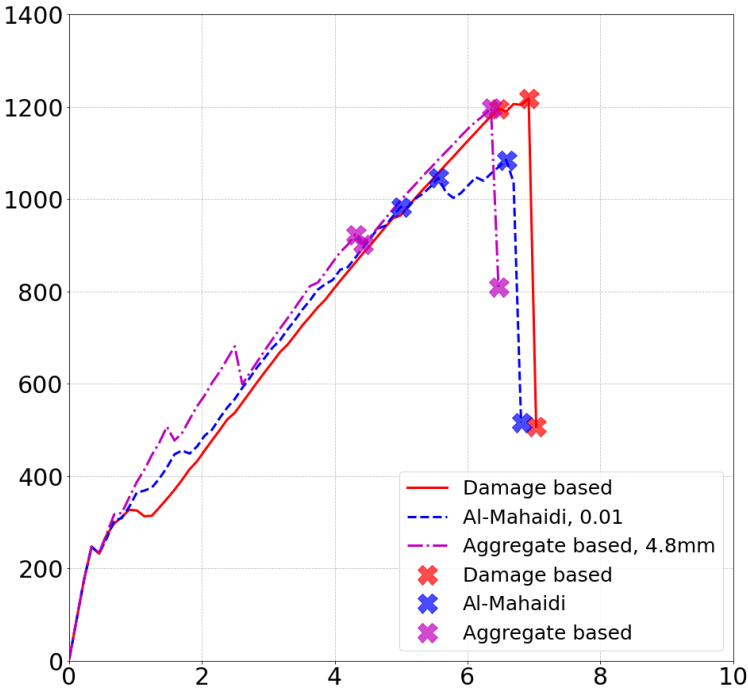


Figure C.14 – Crack strain plot specification for shear retention models for beam S1D72a108

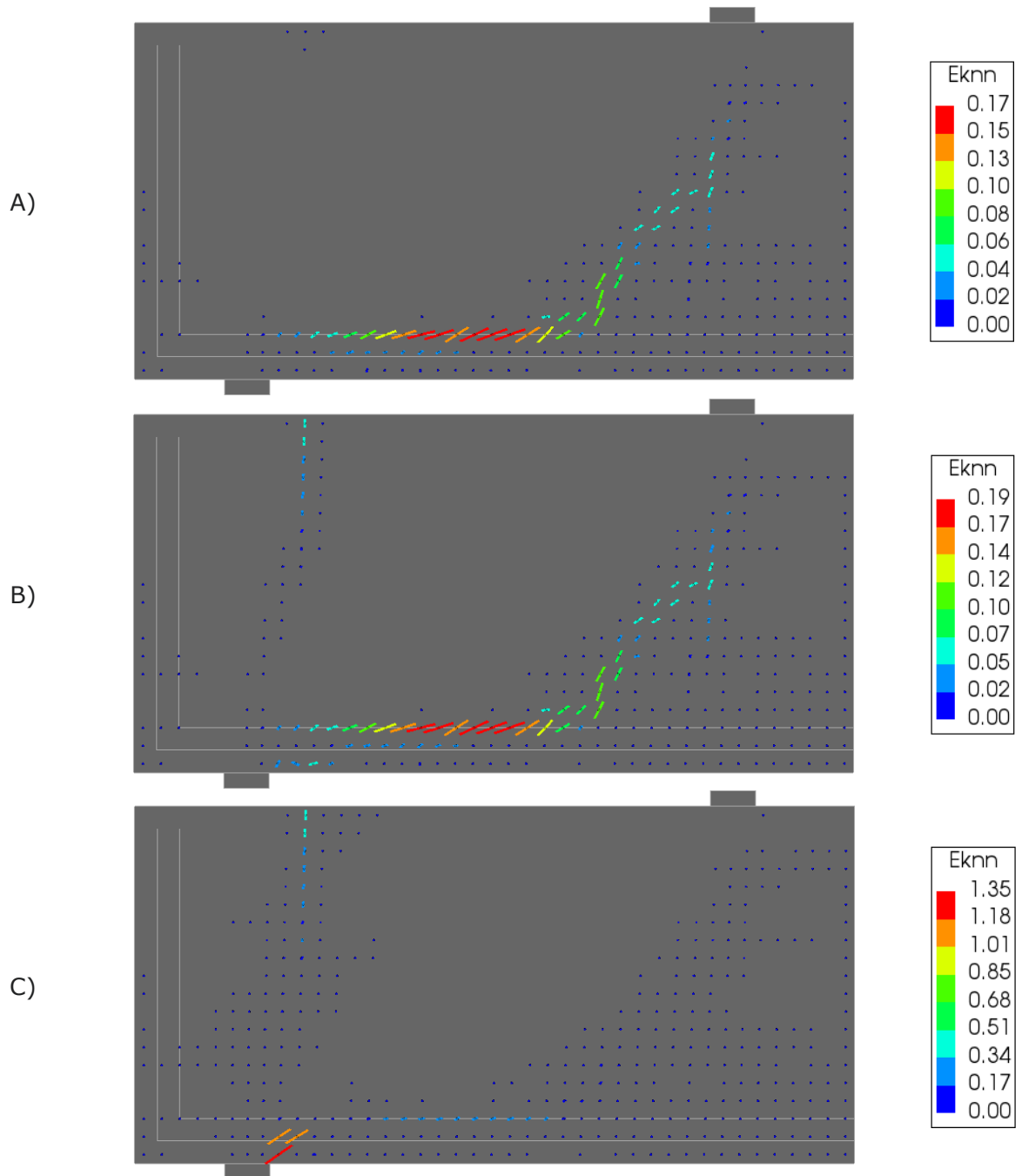


Figure C.15 – Crack strain plots beam S1D72a108, damage based

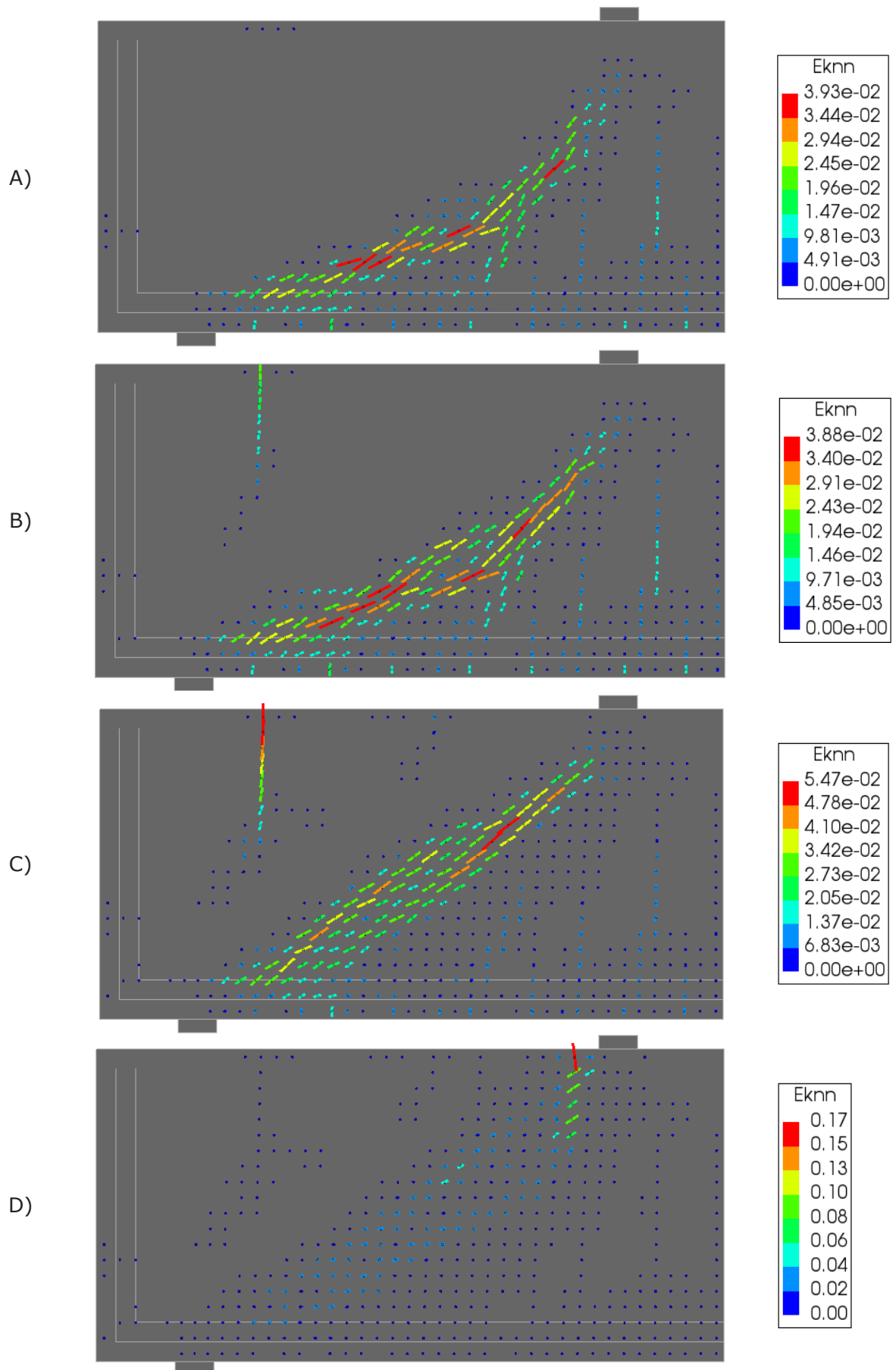


Figure C.16 – Crack strain plots beam S1D72a108, Al-Mahaidi

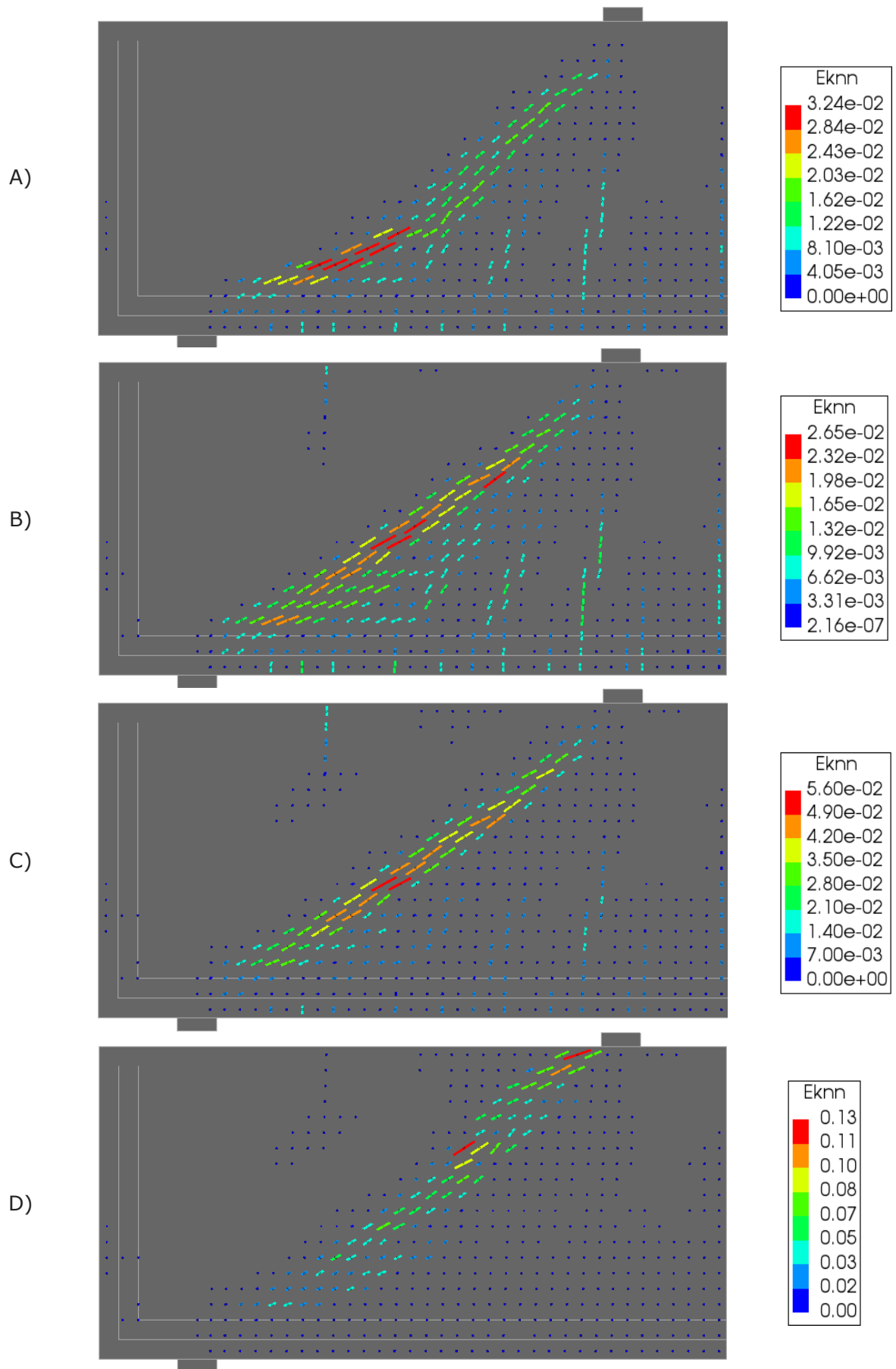


Figure C.17 – Crack strain plots beam S1D72a108, aggregate based

### C.1.4 Crack Strain Patterns of Beam S2D36a72

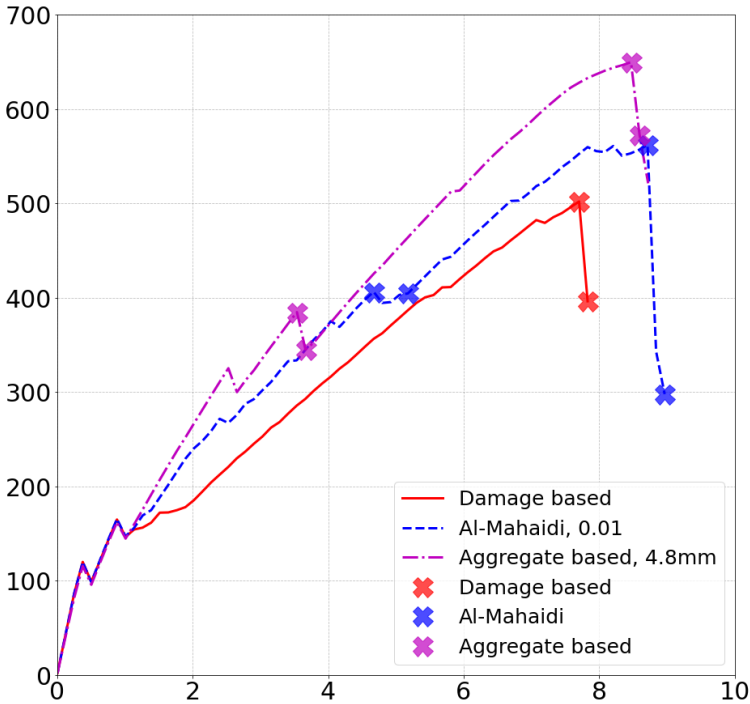


Figure C.18 – Crack plot specification for shear retention models for beam S2D36a72

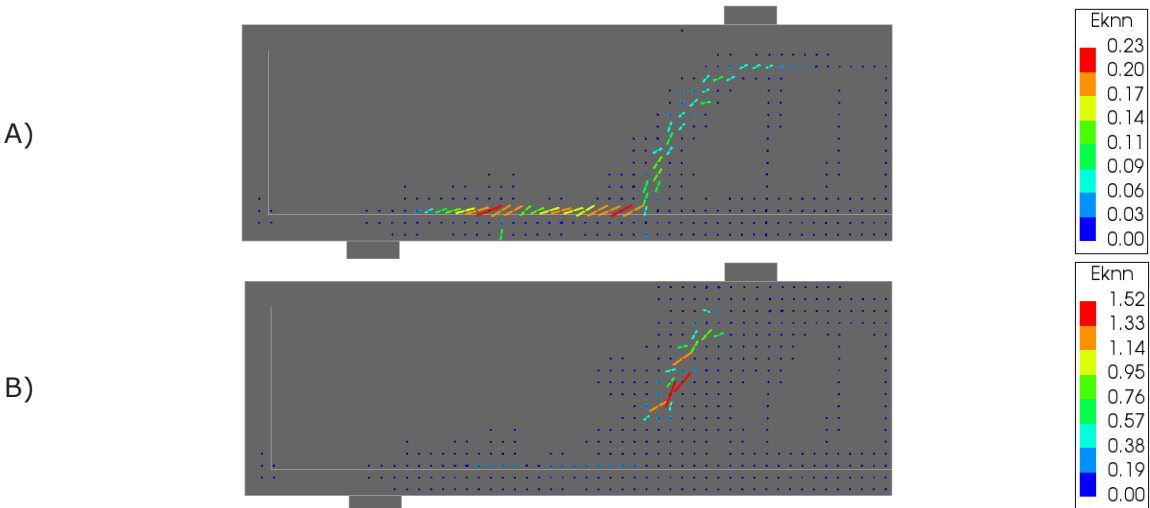


Figure C.19 – Crack strain plots beam S2D36a72, damage based

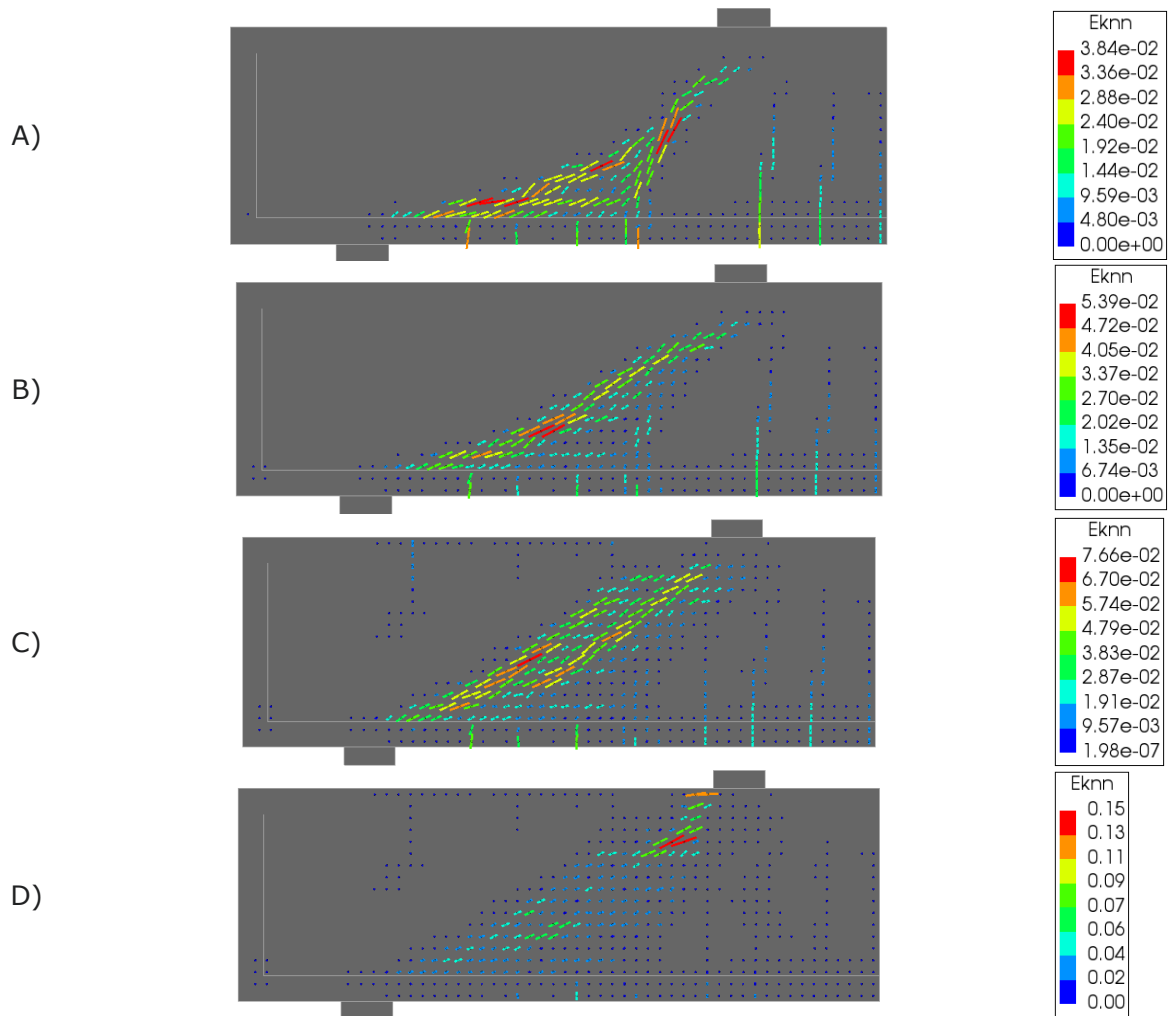


Figure C.20 – Crack strain plots beam S2D36a72, Al-Mahaidi

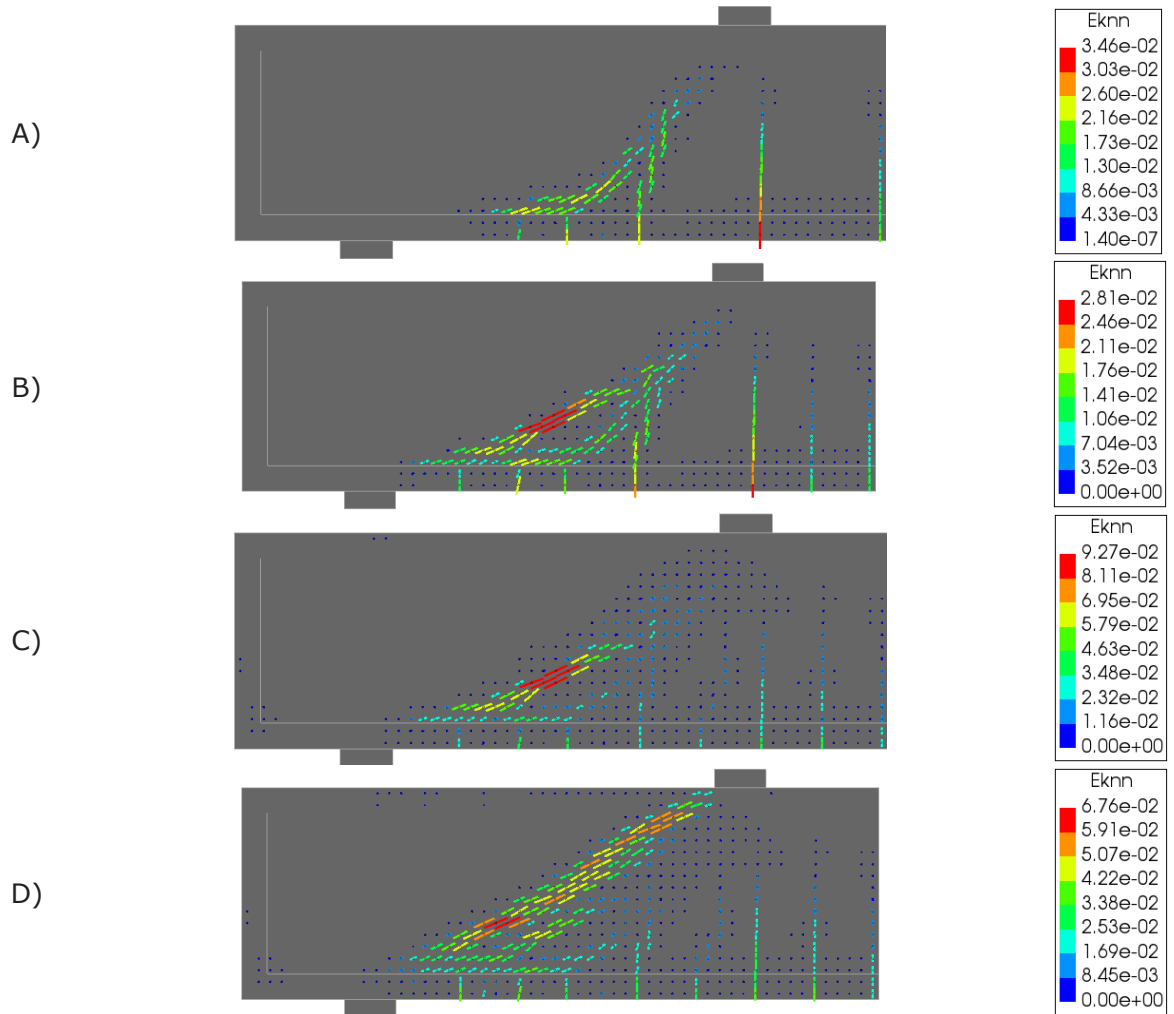


Figure C.21 – Crack strain plots beam S2D36a72, aggregate based

### C.1.5 Crack Strain Patterns of Beam S2D36a36

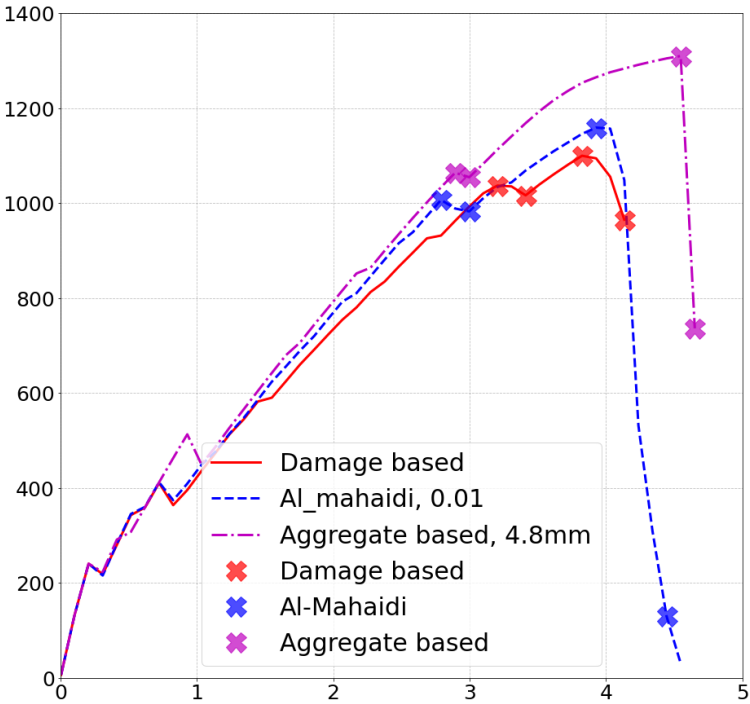


Figure C.22 – Crack plot specification for shear retention models for beam S2D36a36

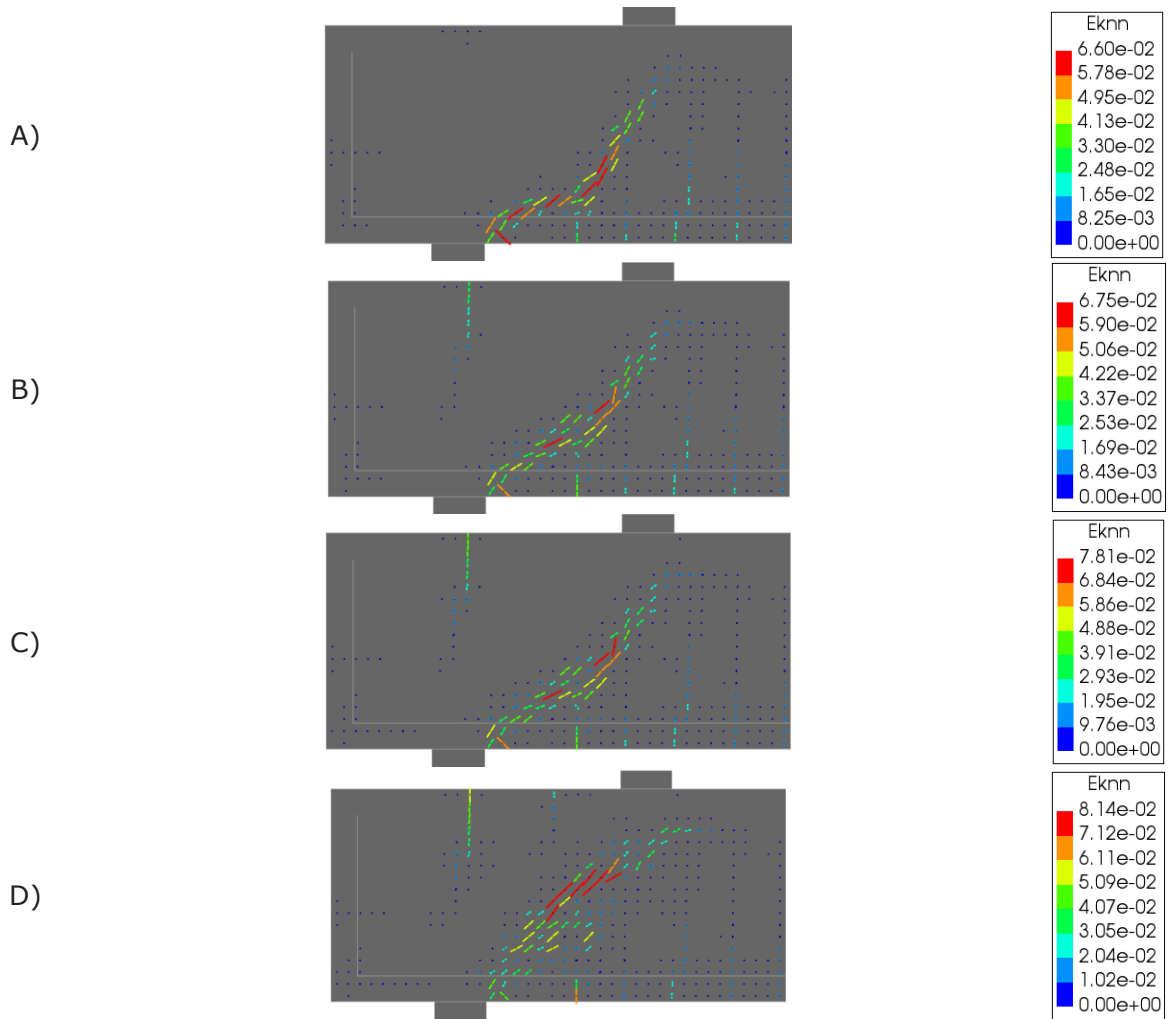


Figure C.23 – Crack strain plots beam S2D36a36, damage based

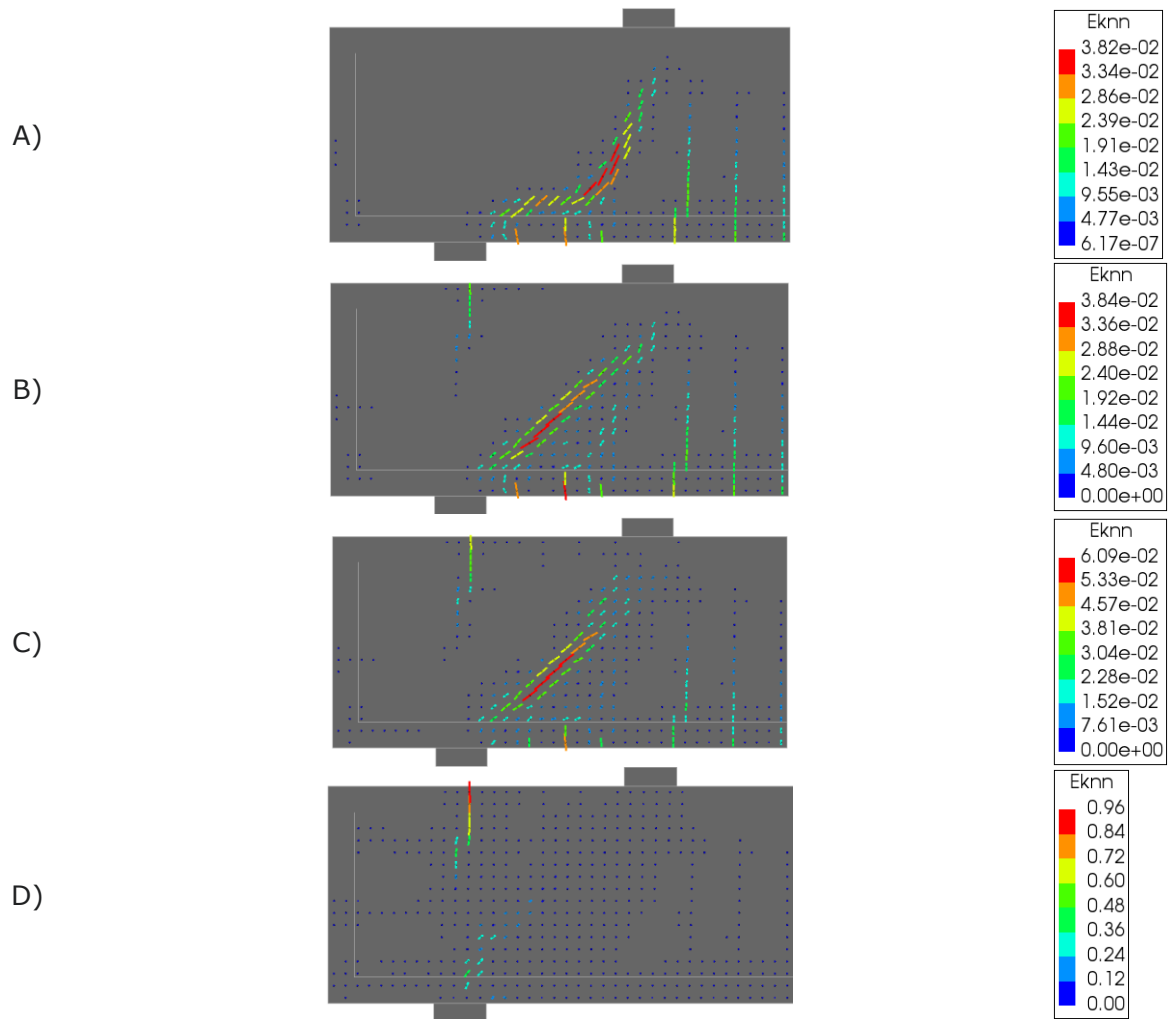


Figure C.24 – Crack strain plots beam S2D36a36, Al-Mahaidi

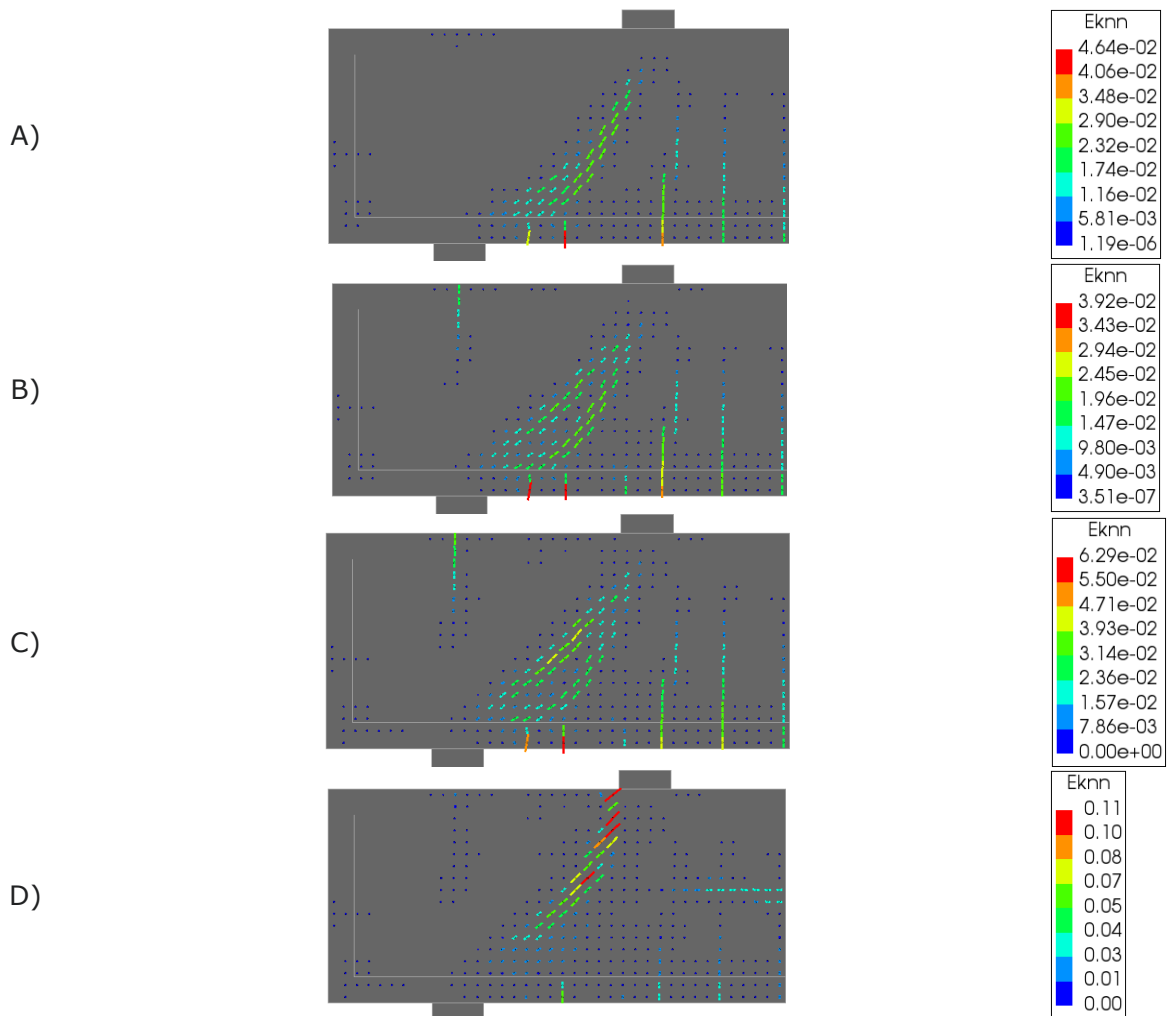


Figure C.25 – Crack strain plots beam S2D36a36, aggregate based

## C.2 Crack Strain Patterns of the Crack Model Analyses

In this chapter, the crack strain patterns for different crack model analyses is presented. This includes a fully fixed crack model, a rotating to fixed crack model with threshold values reflecting a half full developed crack, a fully developed crack and a 5 times fully developed crack, and finally a fully rotating crack model for each of the five beam geometries. The fully fixed crack plots can also be found in some of the plots in Appendix C.1. They were plotted in this chapter in order to easily see the crack development as the crack models span from fully fixed, through the rotating to fixed crack models, to the fully rotating crack model.

### C.2.1 Crack Strain Patterns of Beam S1D18a108

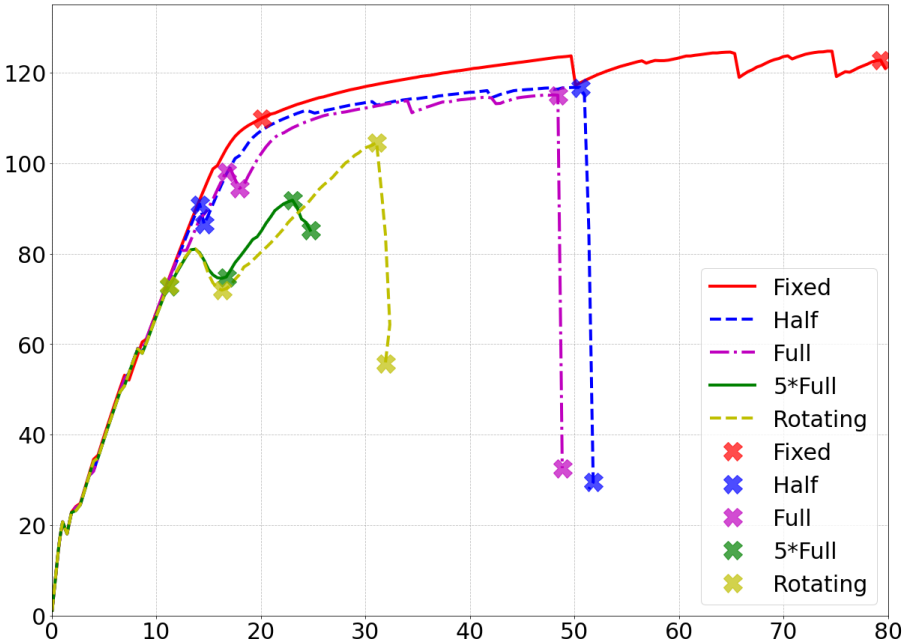


Figure C.26 – Crack plot specification for crack models for beam S1D18a108

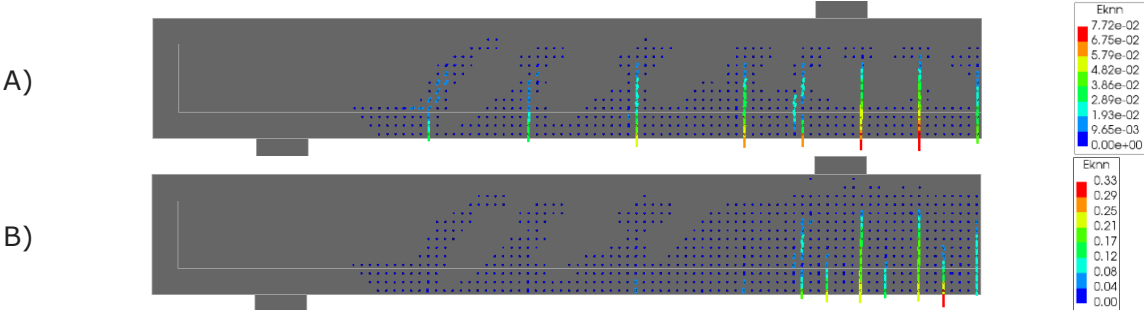


Figure C.27 – Crack strain plots beam S1D18a108, fully fixed

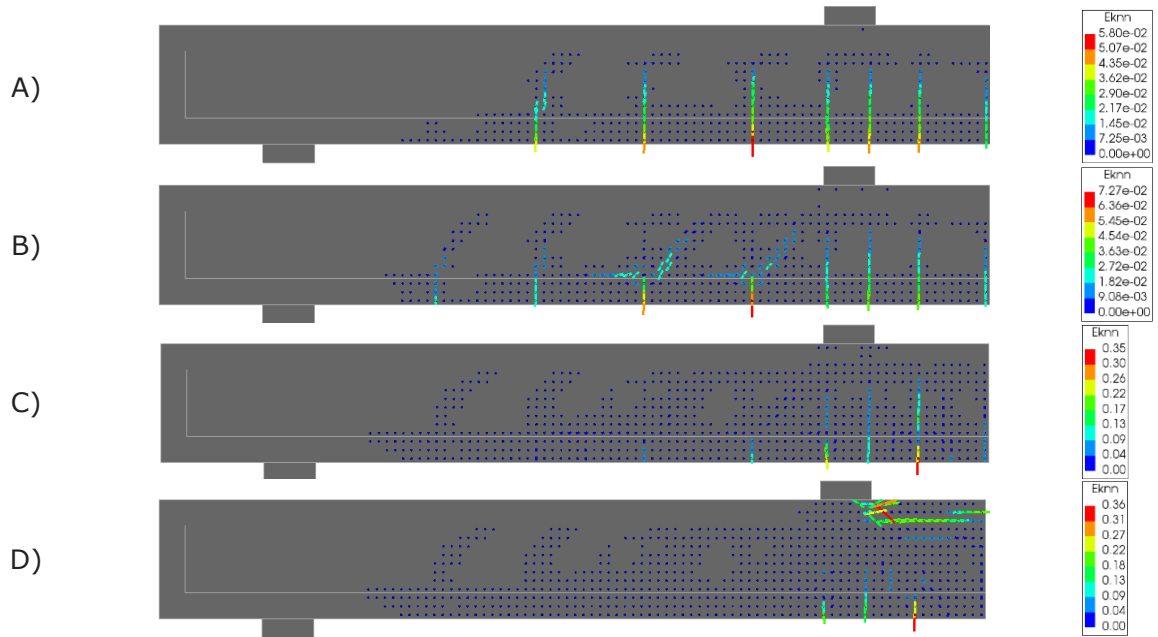


Figure C.28 – Crack strain plots beam S1D18a108, rotating to fixed – threshold at half full crack

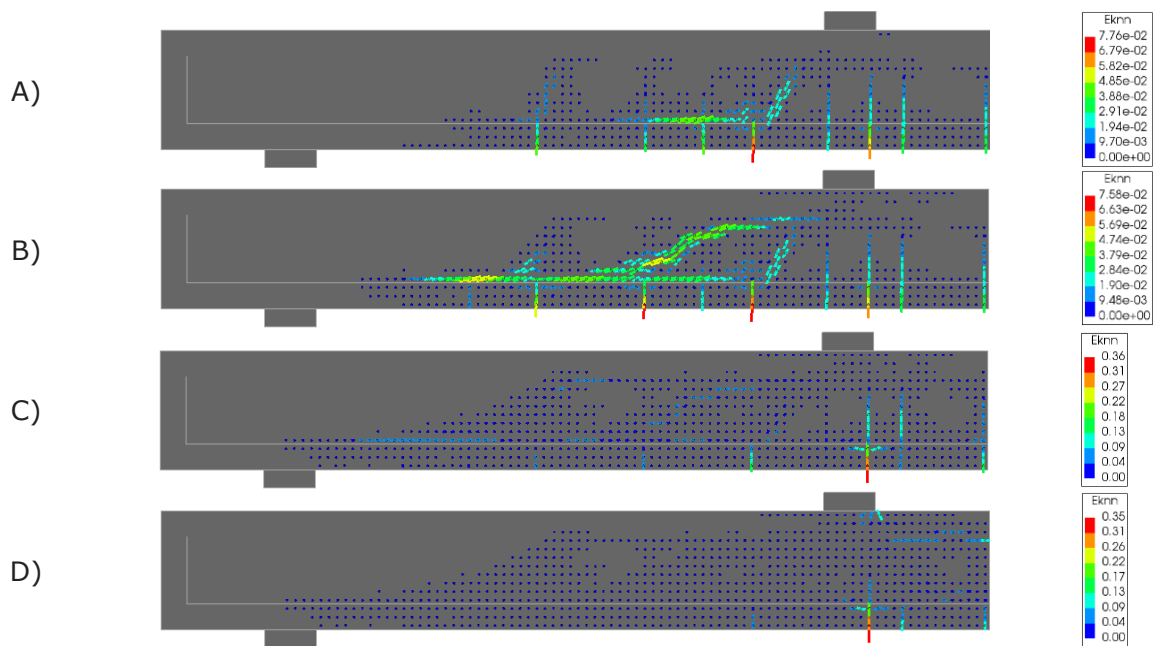


Figure C.29 – Crack strain plots beam S1D18a108, rotating to fixed – threshold at fully developed crack

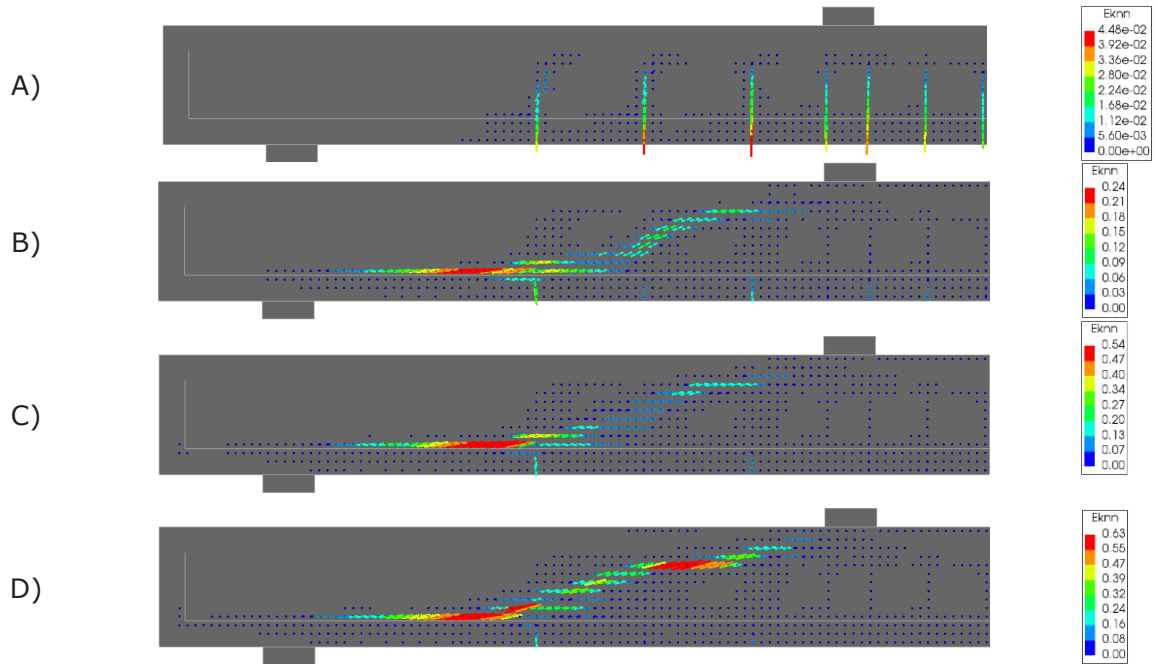


Figure C.30 – Crack strain plots beam S1D18a108, rotating to fixed – threshold at 5\*fully developed crack

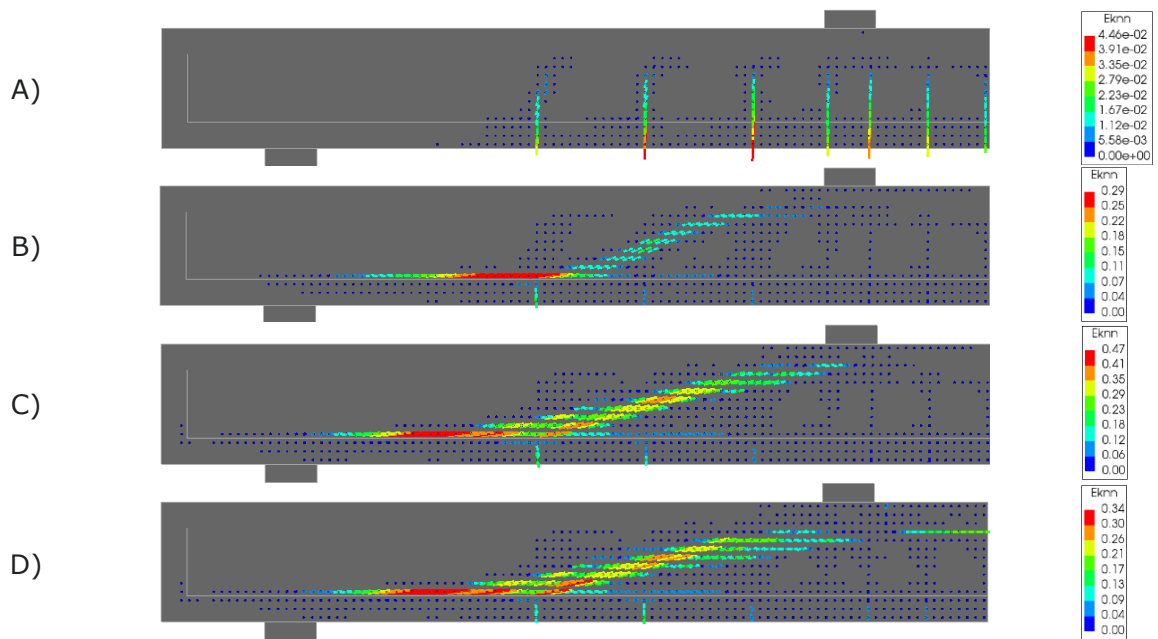


Figure C.31 – Crack strain plots beam S1D18a108, fully rotating

### C.2.2 Crack Strain Patterns of Beam S1&2D36a108

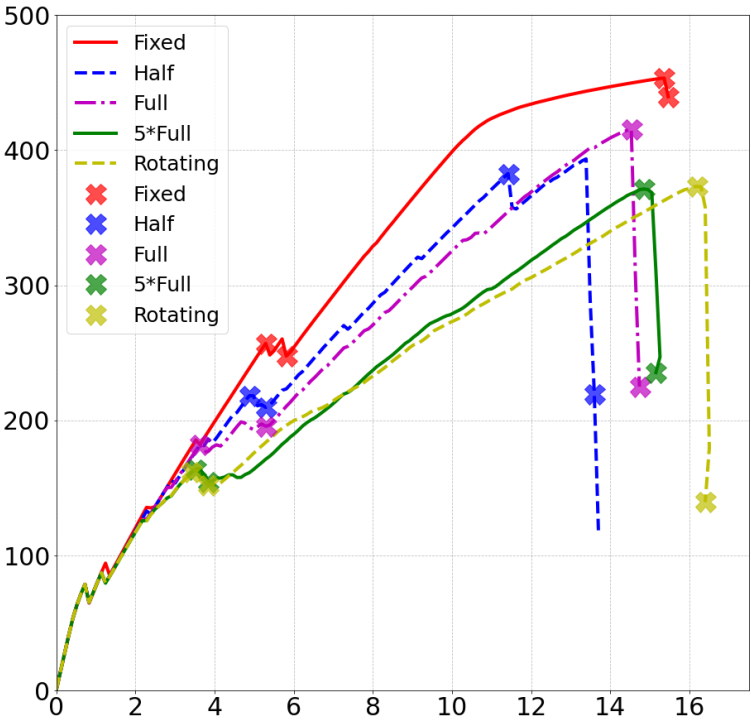


Figure C.32 – Crack strain plot specification for crack models for beam S1&2D36a108

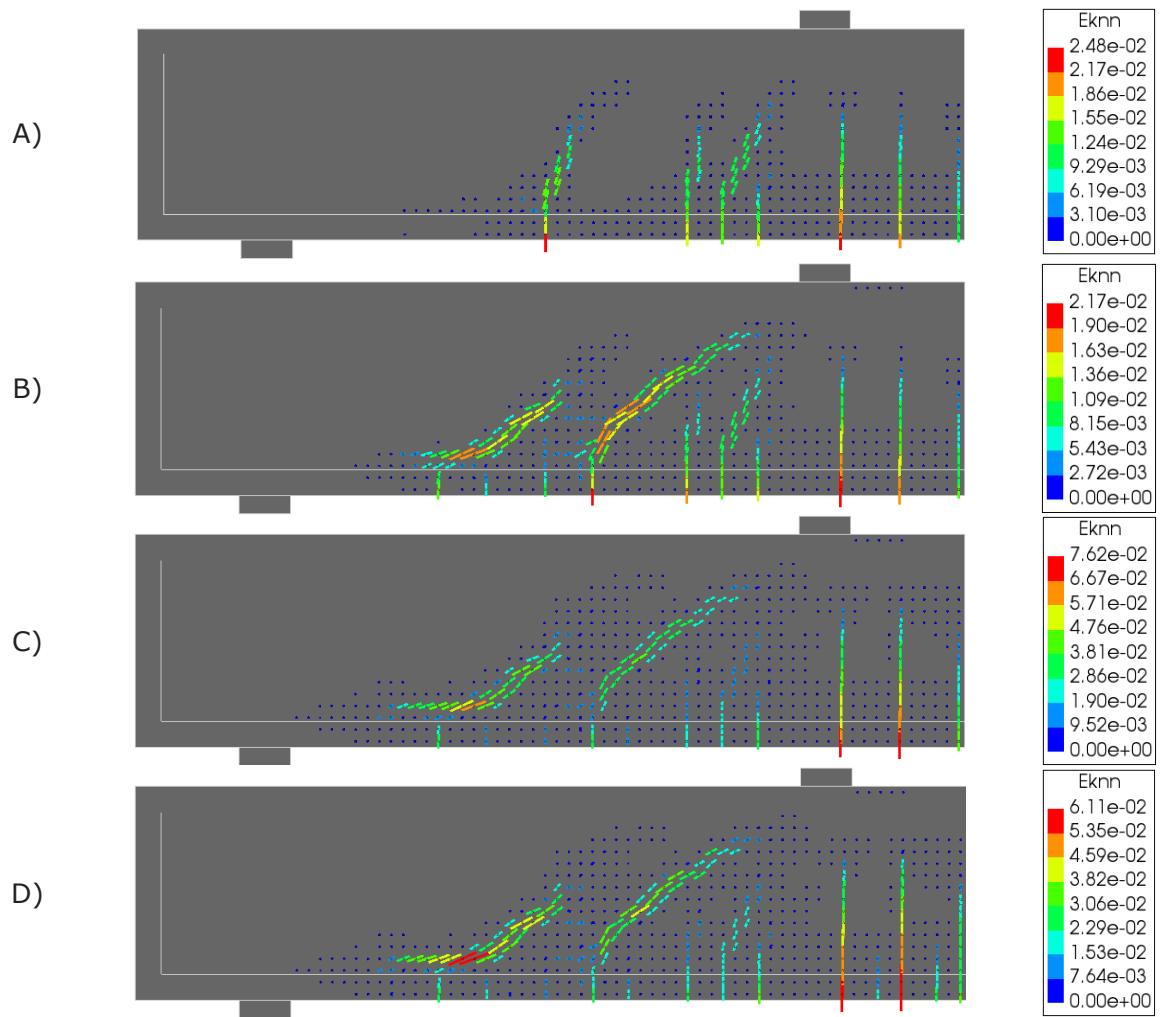


Figure C.33 – Crack strain plots beam S1&2D36a108, fully fixed

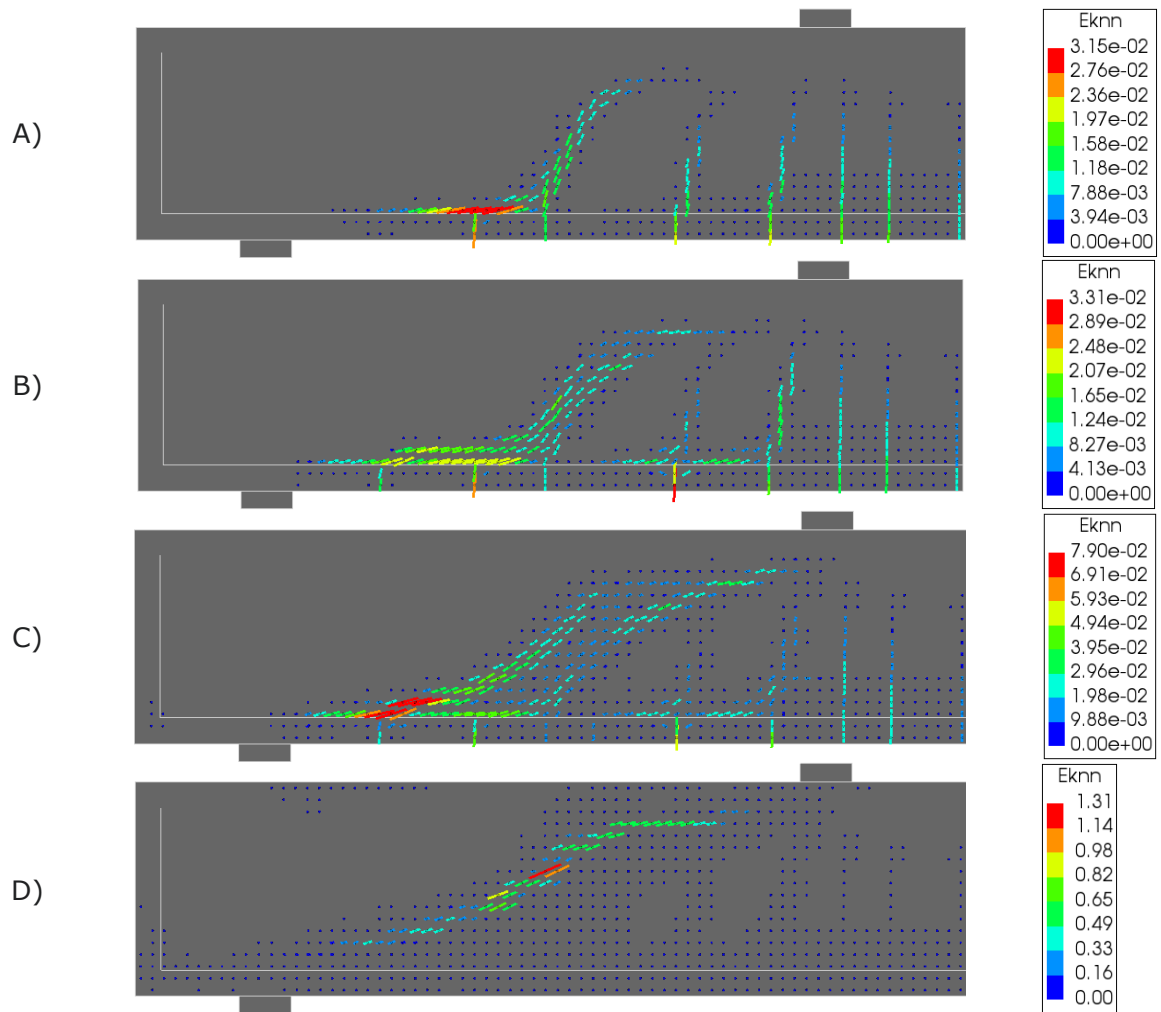


Figure C.34 – Crack strain plots beam S1&2D36a108, rotating to fixed – threshold at half full crack

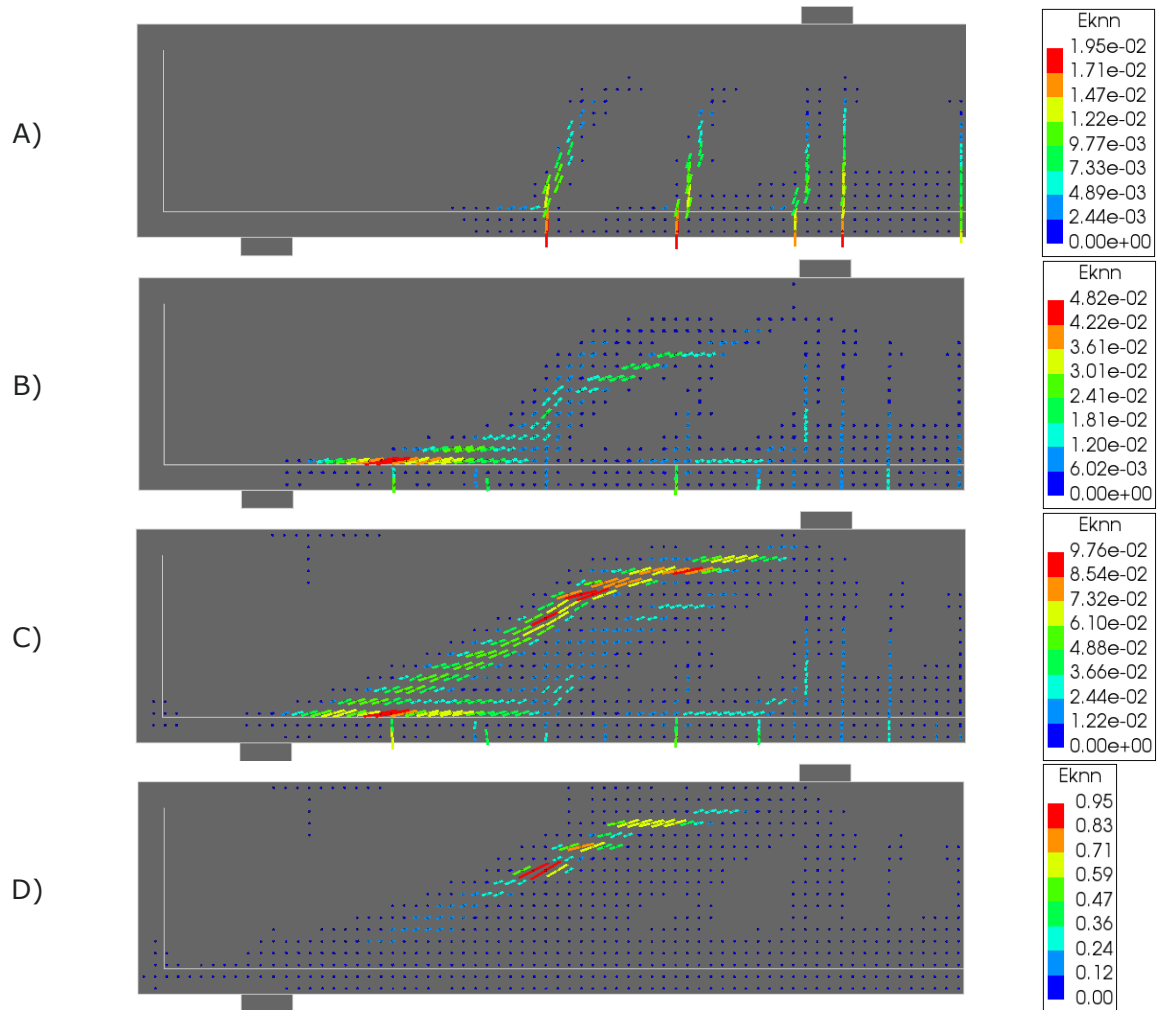


Figure C.35 – Crack strain plots beam S1&2D36a108, rotating to fixed – threshold at fully developed crack

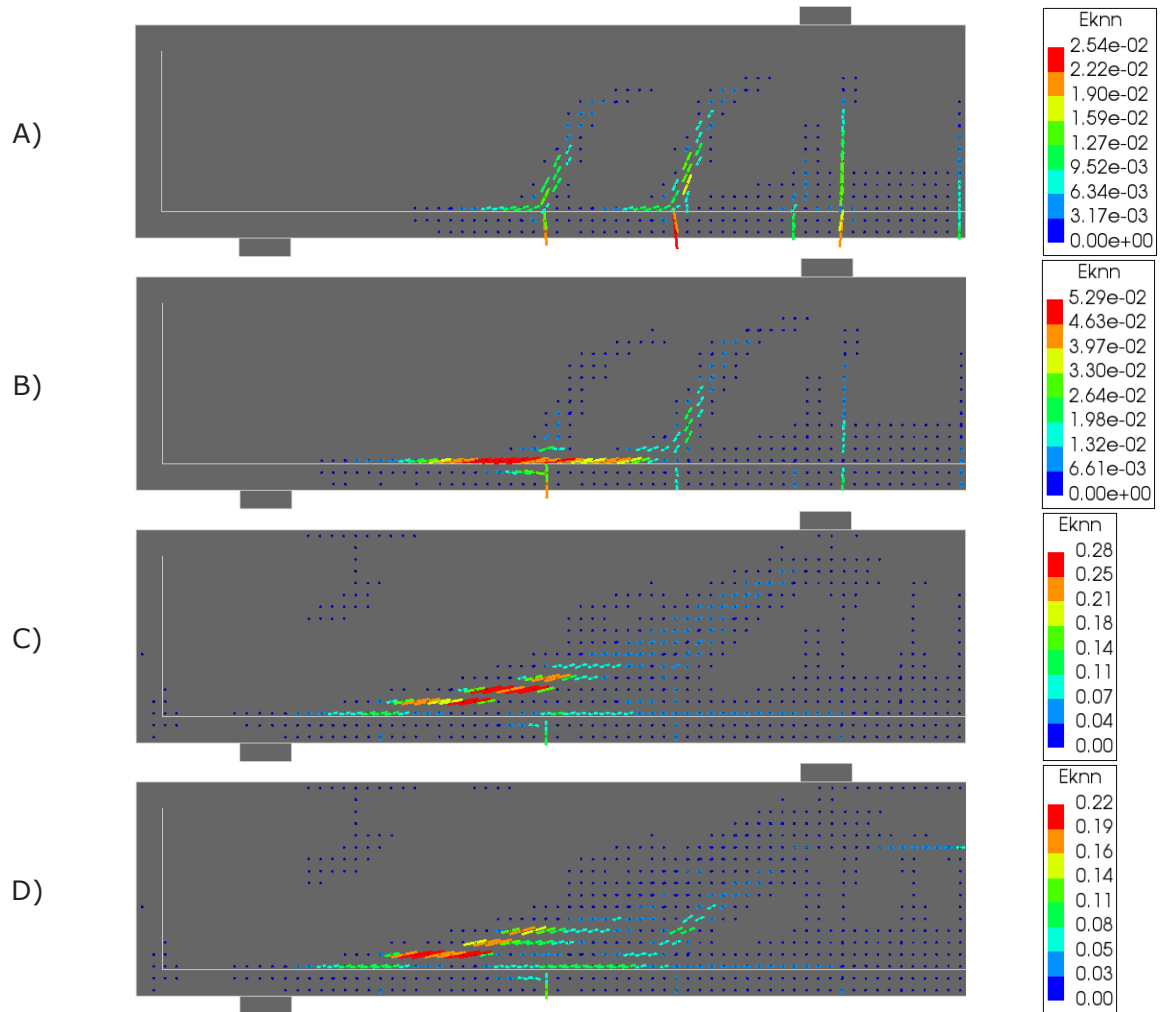


Figure C.36 – Crack strain plots beam S1&2D36a108, rotating to fixed – threshold at 5\*fully developed crack

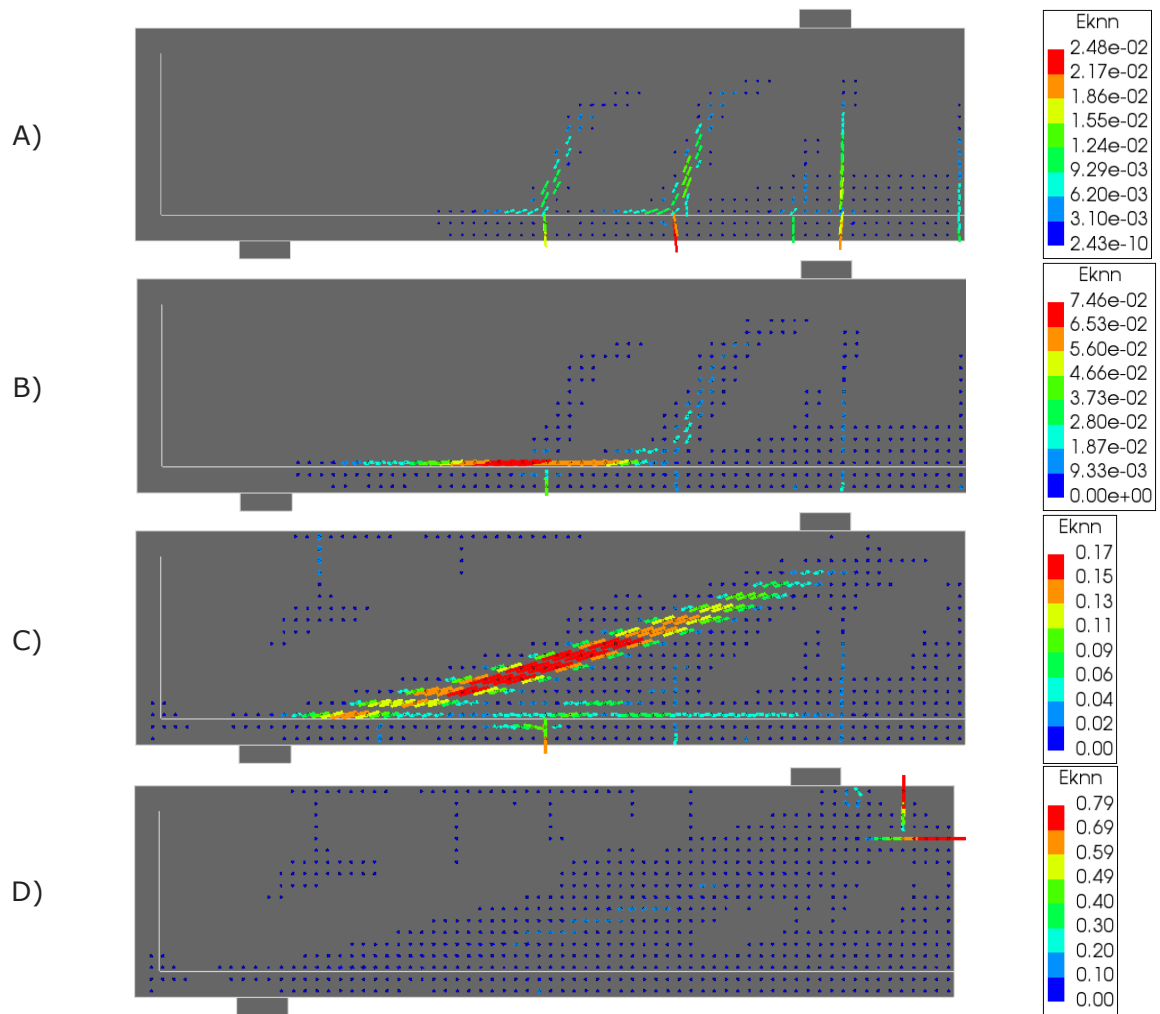


Figure C.37 – Crack strain plots beam S1&2D36a108, fully rotating

### C.2.3 Crack Strain Patterns of Beam S1D72a108

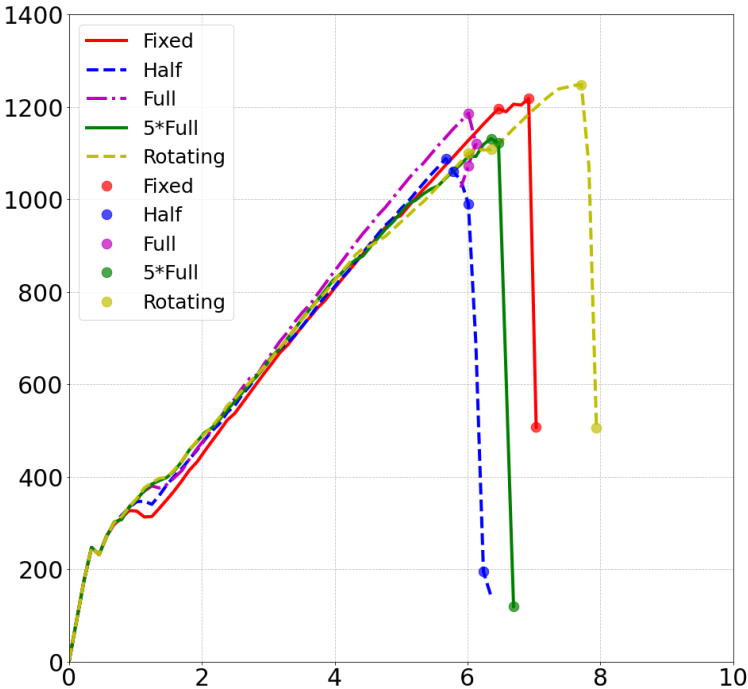


Figure C.38 – Crack strain plot specification for crack models for beam S1D72a108 (the crack plot extractions are marked as dots for better visibility)

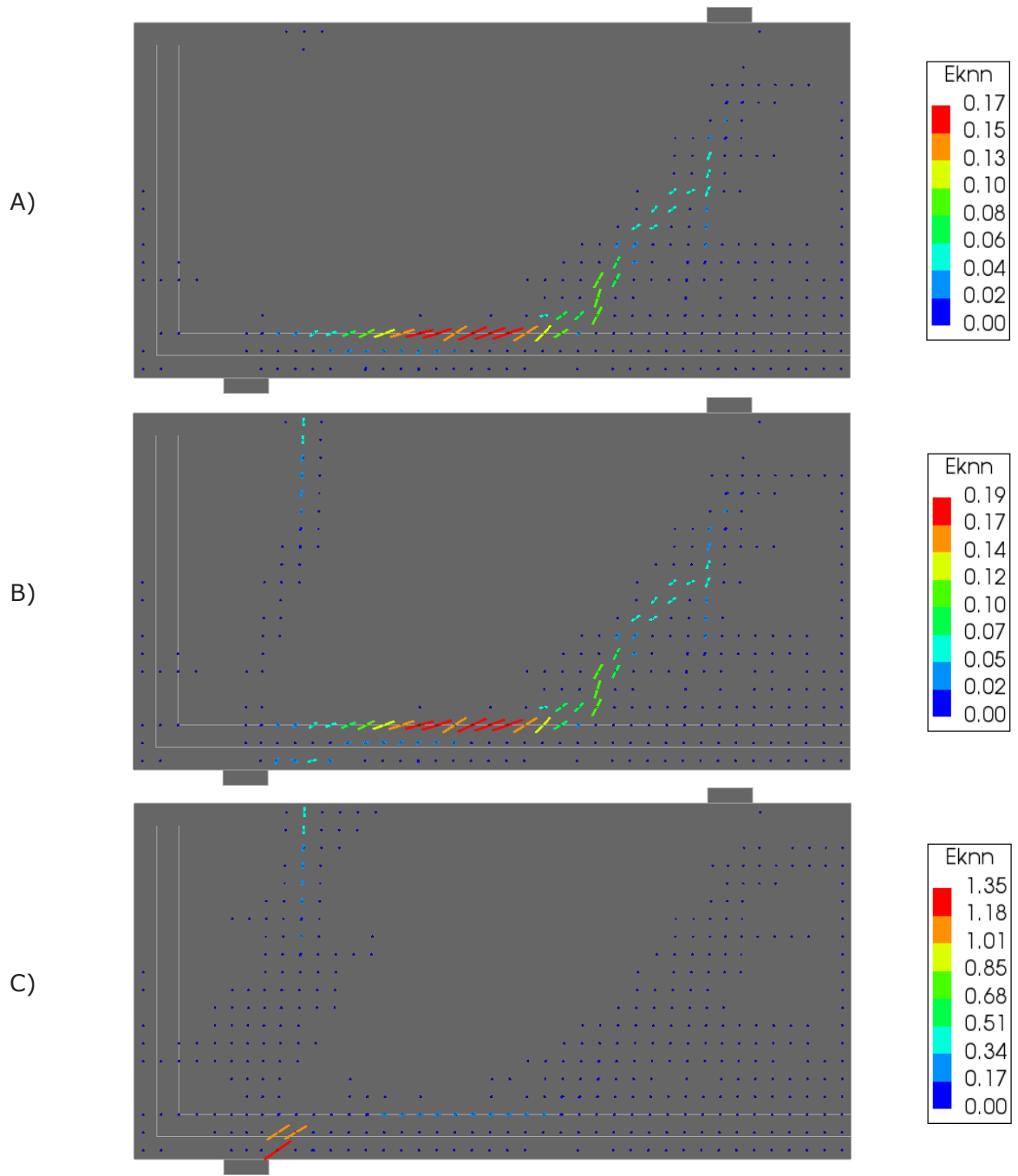


Figure C.39 – Crack strain plots beam S1D72a108, fully fixed

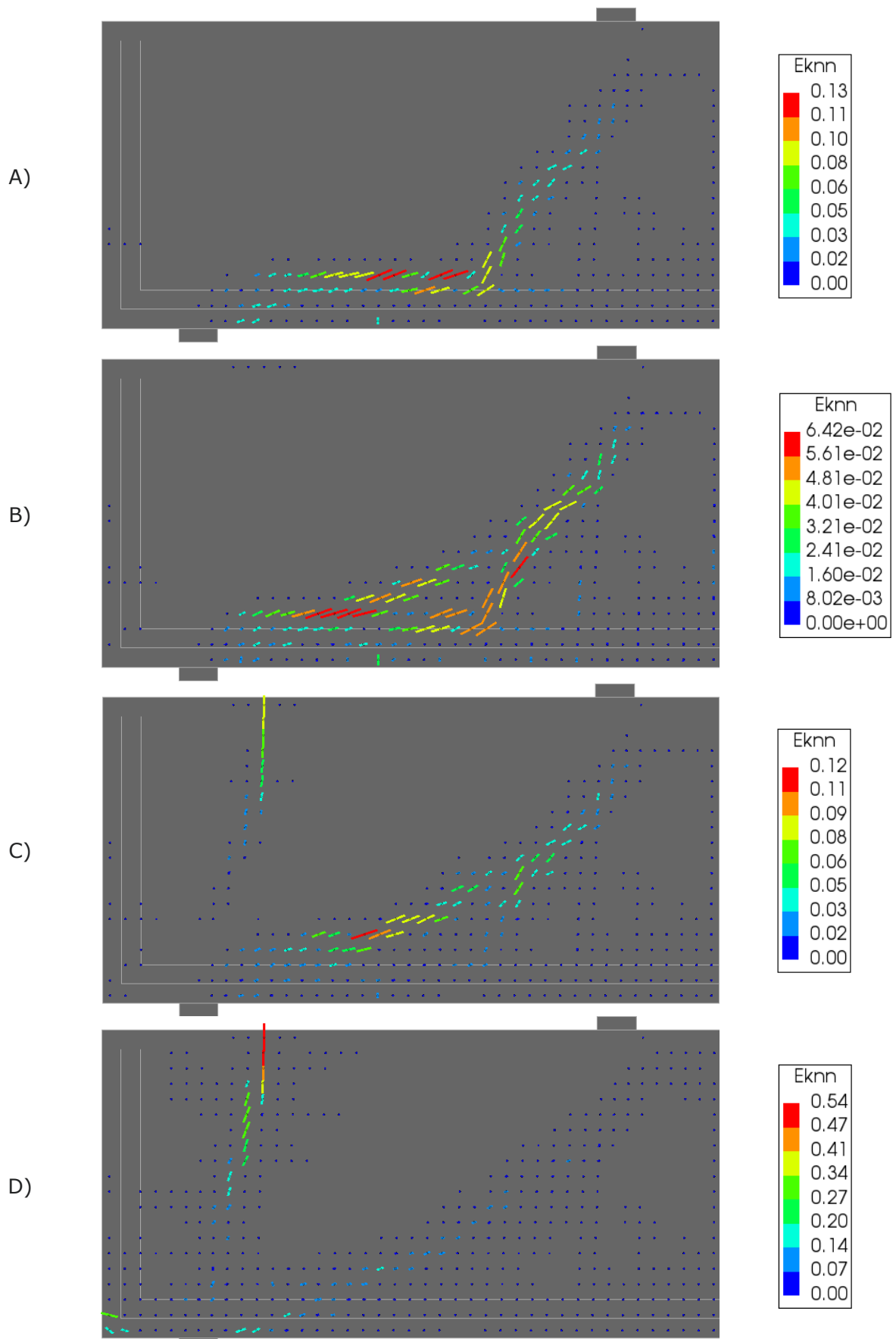


Figure C. 40 – Crack strain plots beam S1D72a108, rotating to fixed – threshold at half full crack

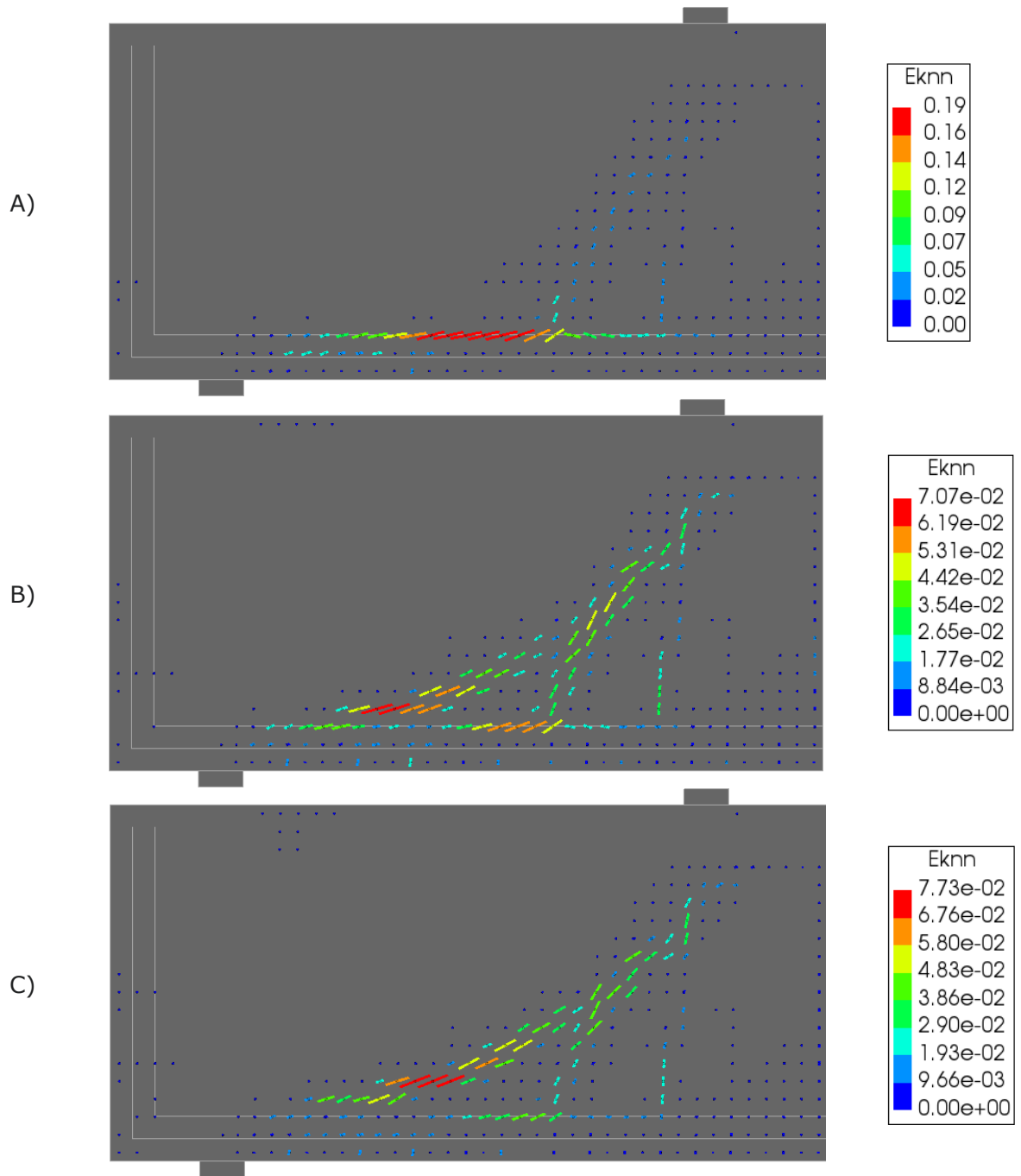


Figure C.41 – Crack strain plots beam S1D72a108, rotating to fixed – threshold at fully developed crack

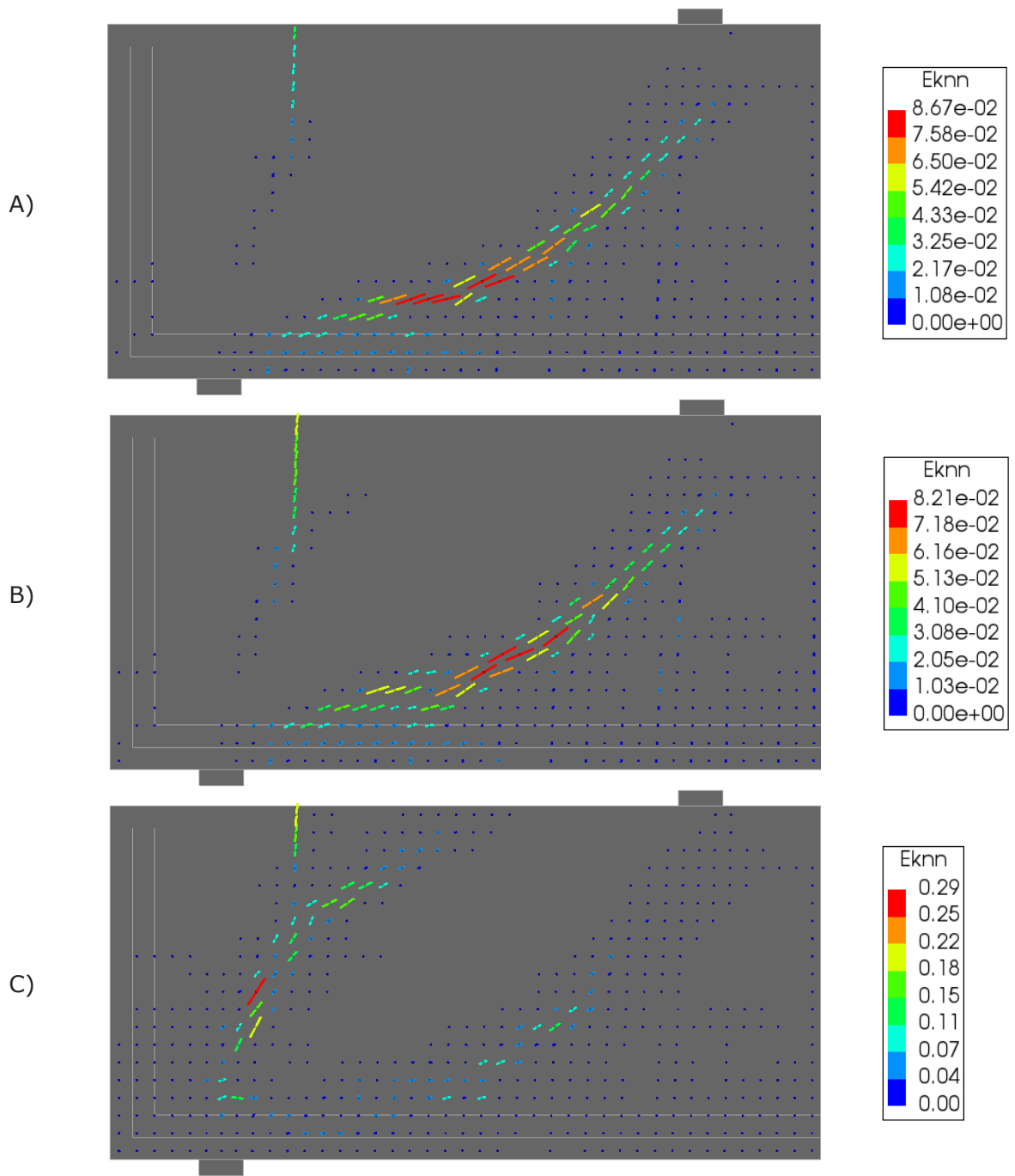


Figure C.42 – Crack strain plots beam S1D72a108, rotating to fixed – threshold at 5\*fully developed crack

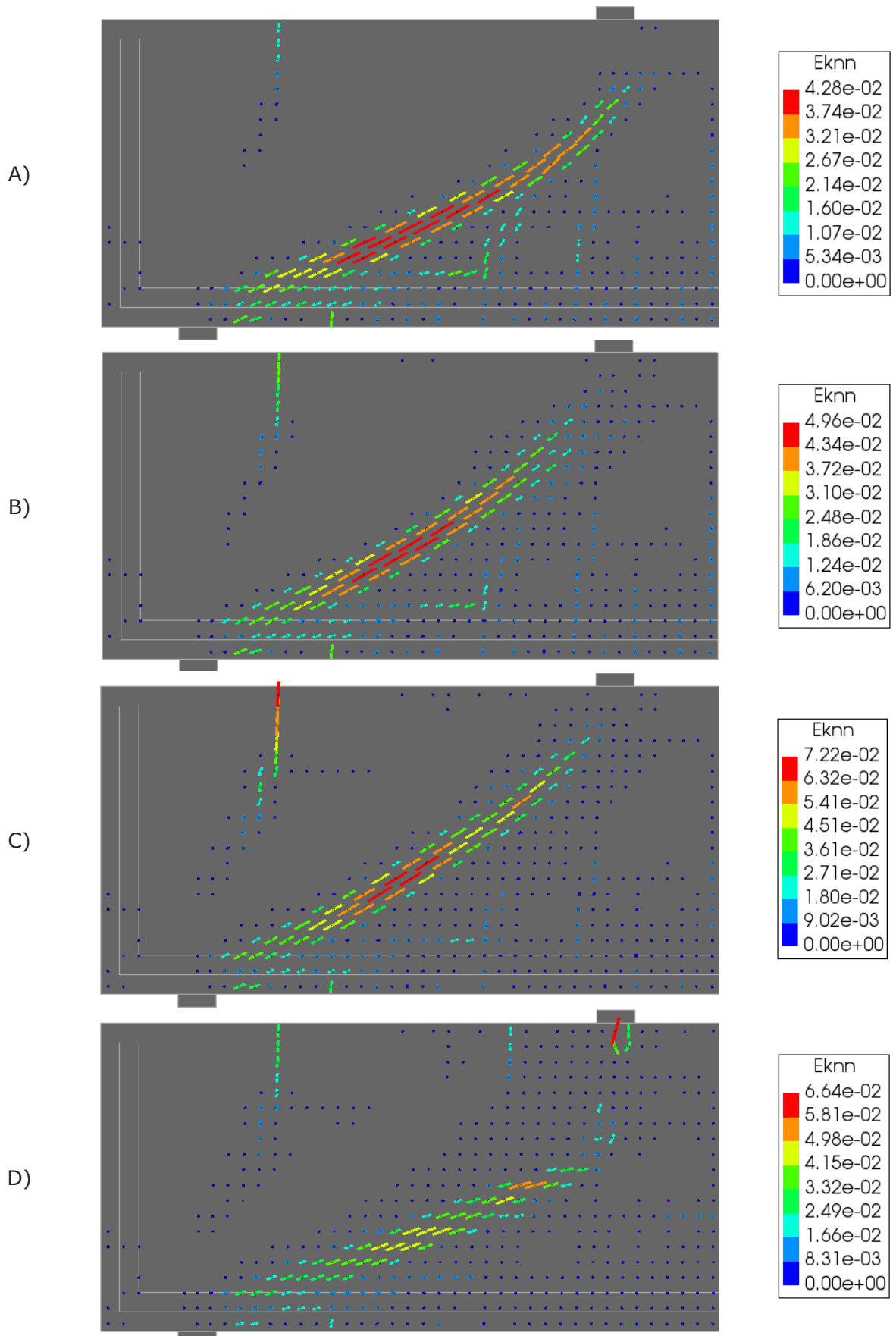


Figure C.43 – Crack strain plots beam S1D72a108, fully rotating

### C.2.4 Crack Strain Patterns of Beam S2D36a72

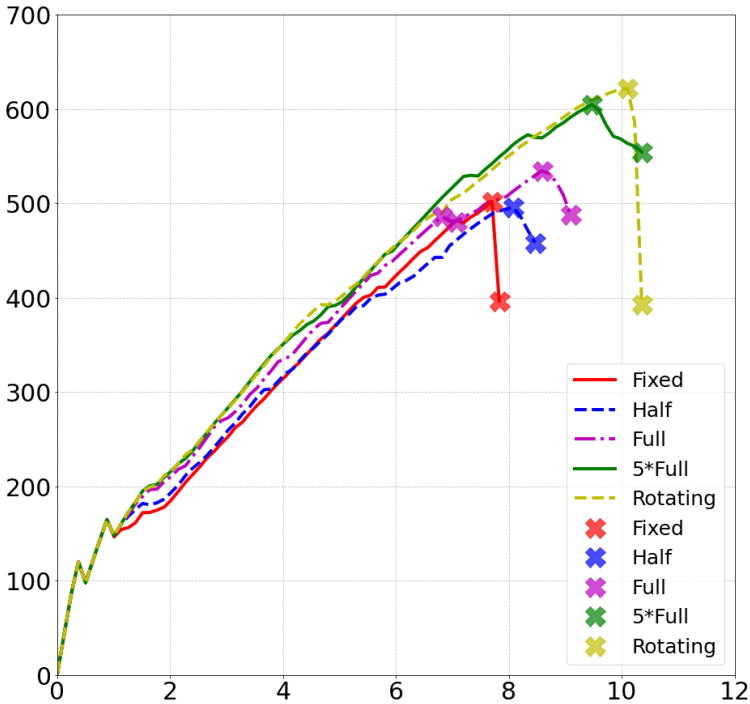


Figure C.44 – Crack plot specification for crack models for beam S2D36a72

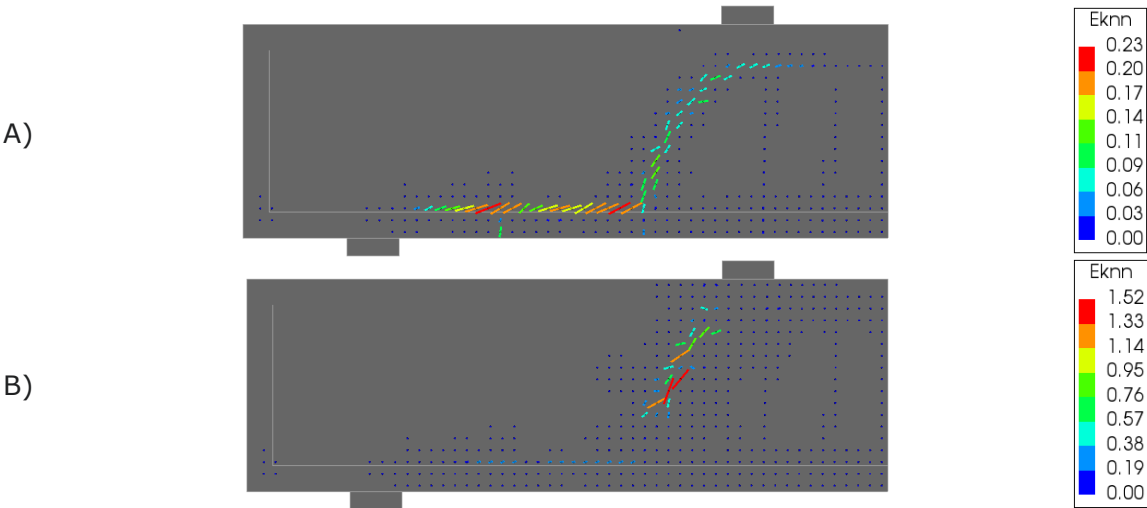


Figure C.45 – Crack strain plots beam S2D36a72, fully fixed

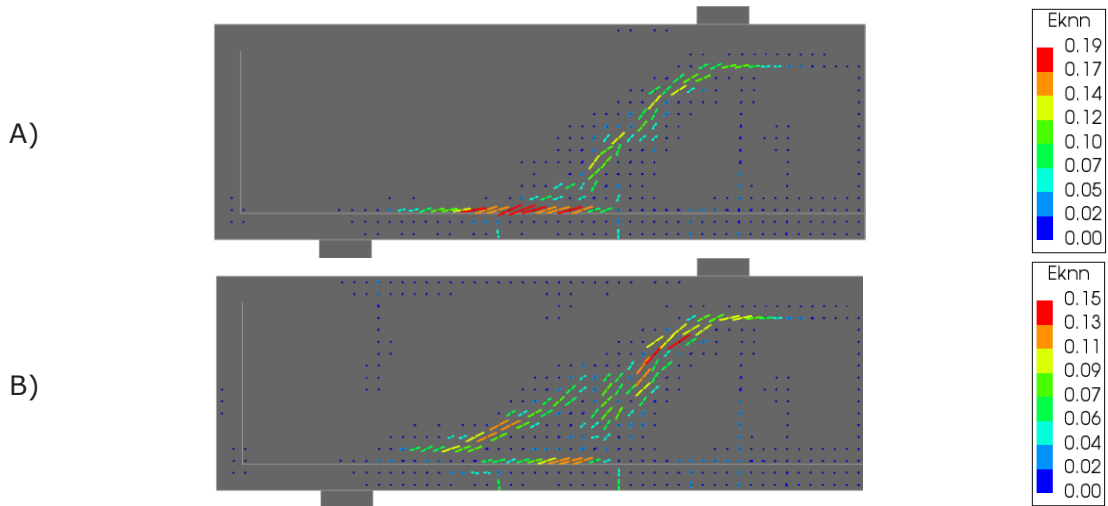


Figure C.46 – Crack strain plots beam S2D36a72, rotating to fixed – threshold at half full crack

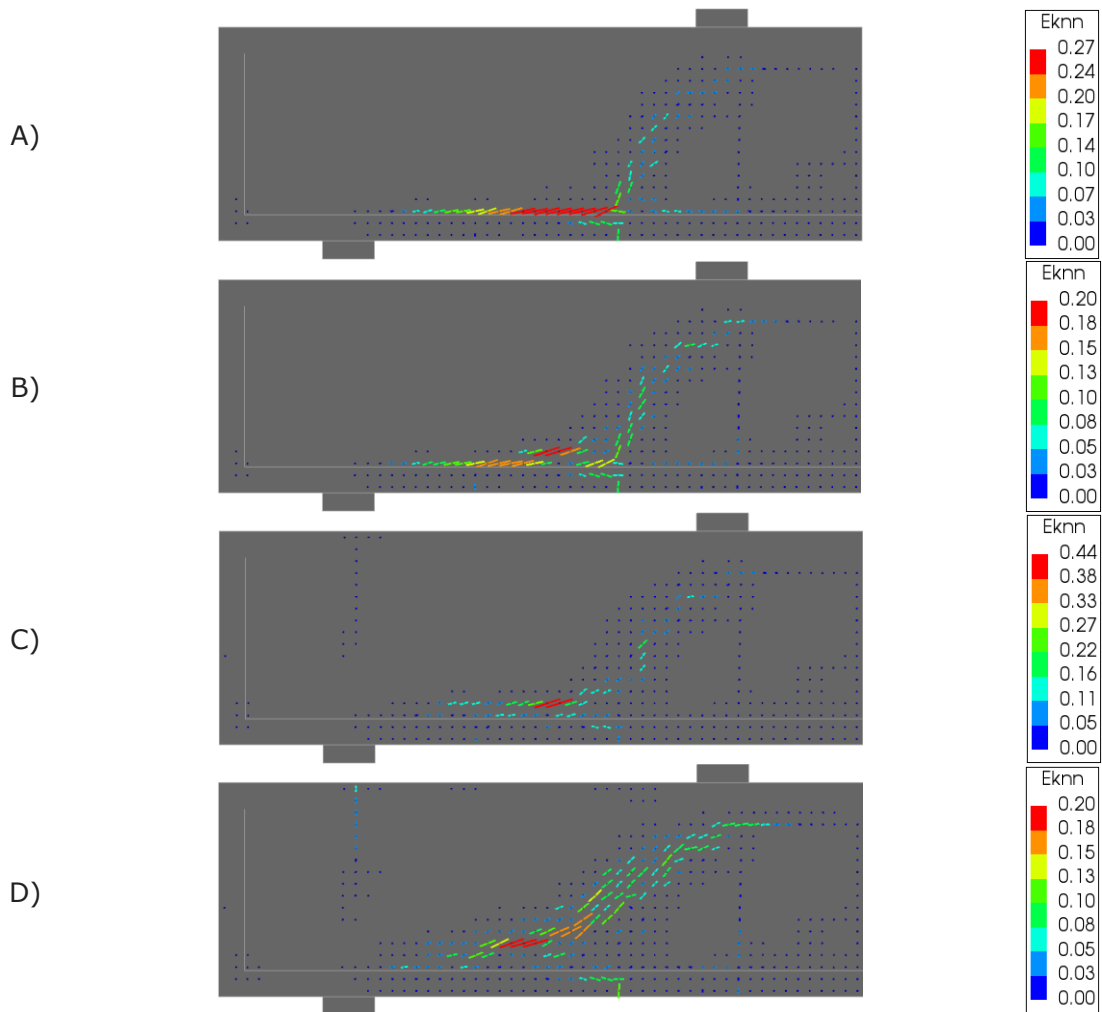


Figure C.47 – Crack strain plots beam S2D36a72, rotating to fixed – threshold at fully developed crack

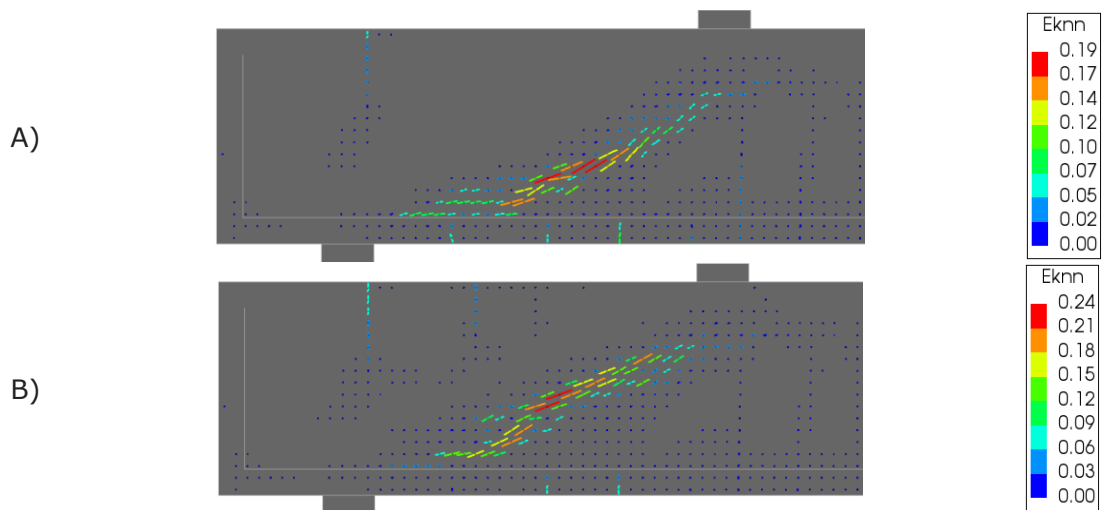


Figure C.48 – Crack plots strain beam S2D36a72, rotating to fixed – threshold at 5\*fully developed crack

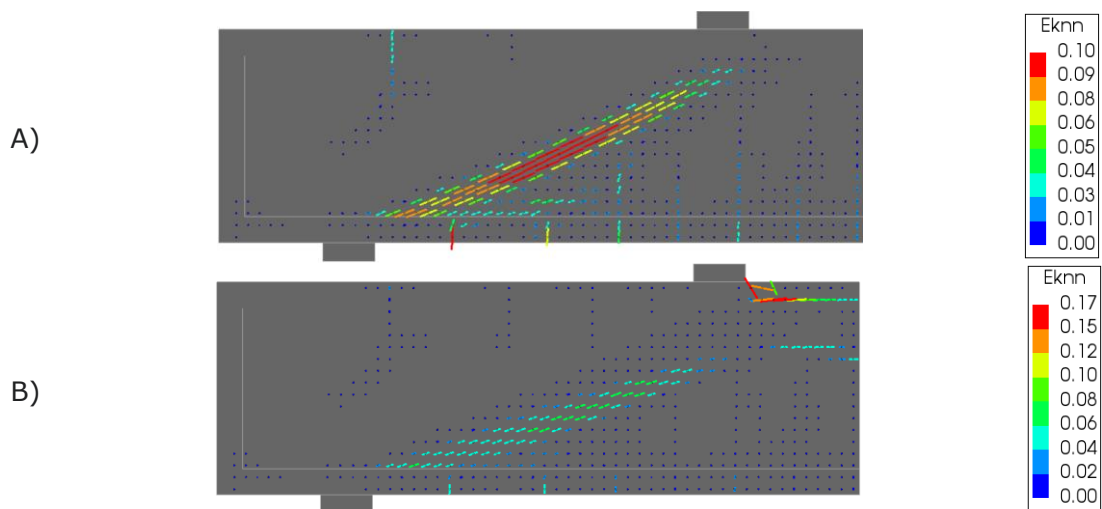


Figure C.49 – Crack strain plots beam S2D36a72, fully rotating

### C.2.5 Crack Strain Patterns of Beam S2D36a36

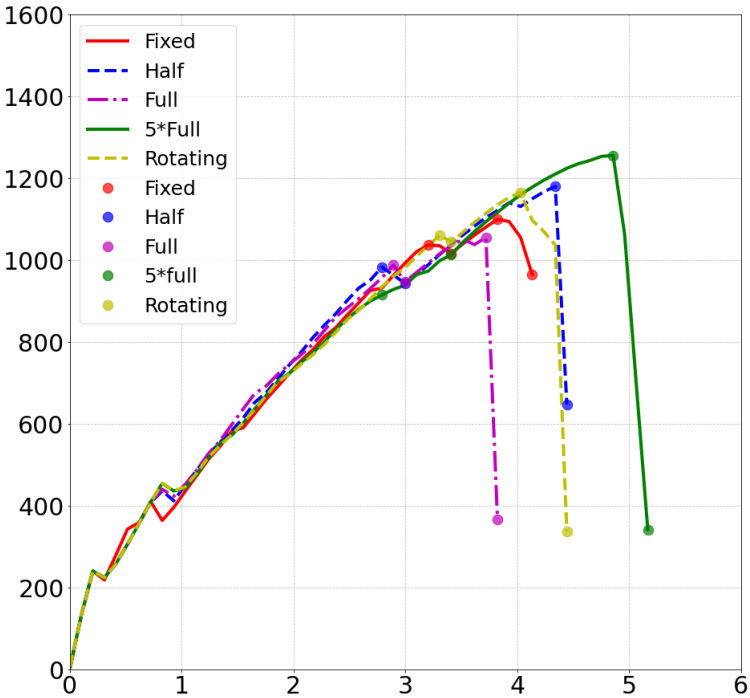


Figure C.50 – Crack strain plot specification for crack models for beam S2D36a36 (the crack plot extractions are marked as dots for better visibility)

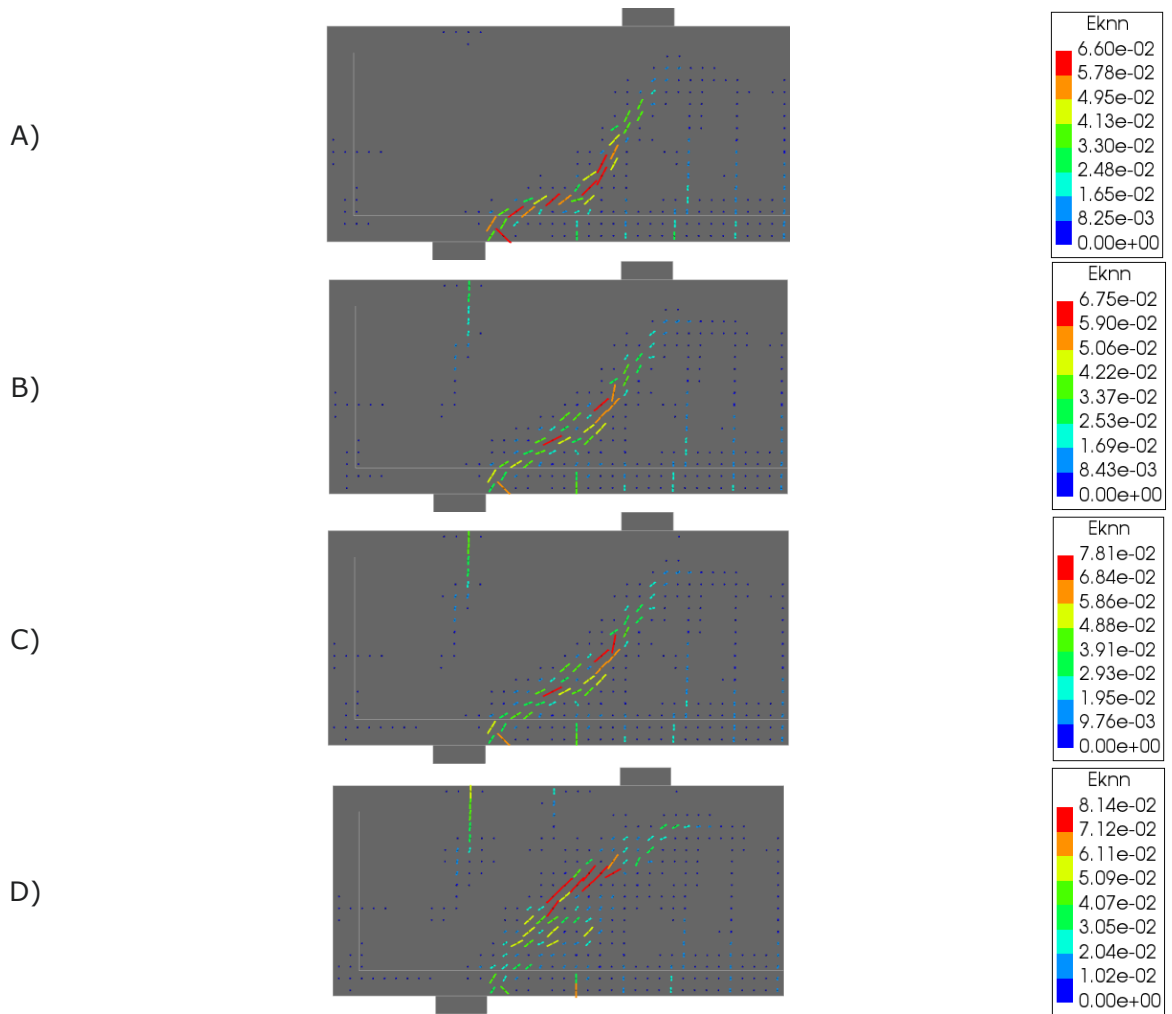


Figure C.51 – Crack strain plots beam S2D36a36, fully fixed

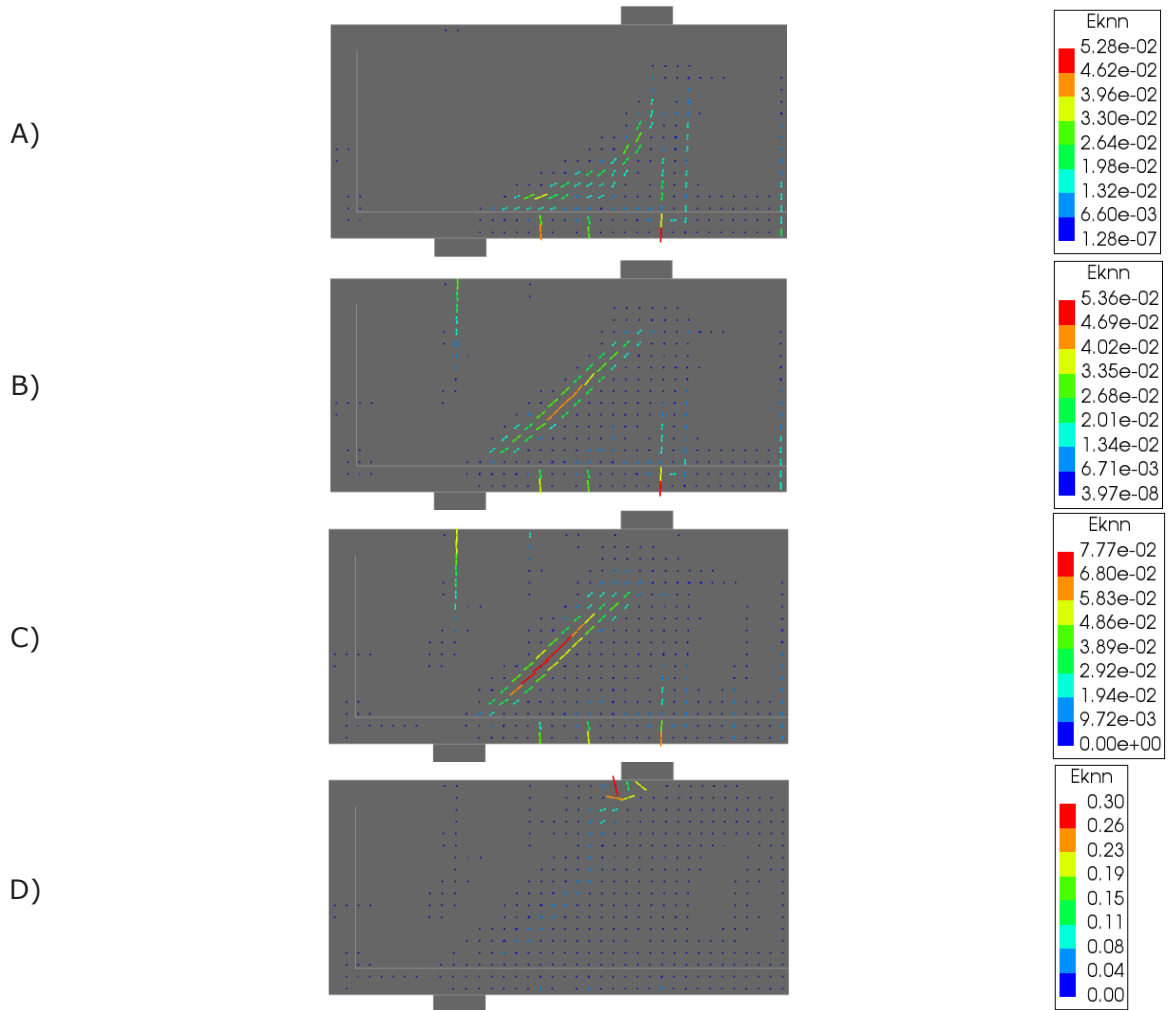


Figure C.52 – Crack strain plots beam S2D36a36, rotating to fixed – threshold at half full crack

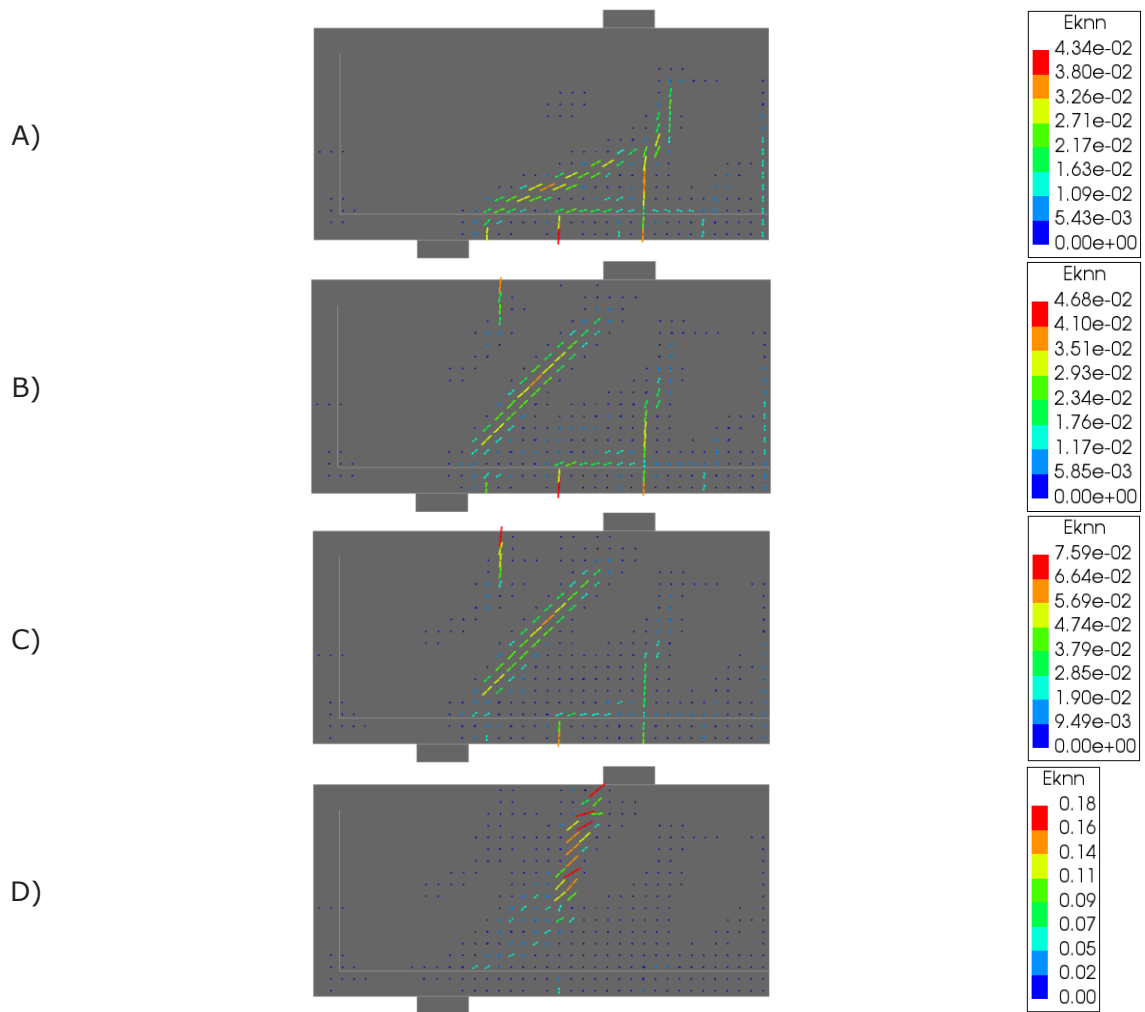


Figure C.53 – Crack strain plots beam S2D36a36, rotating to fixed – threshold at fully developed crack

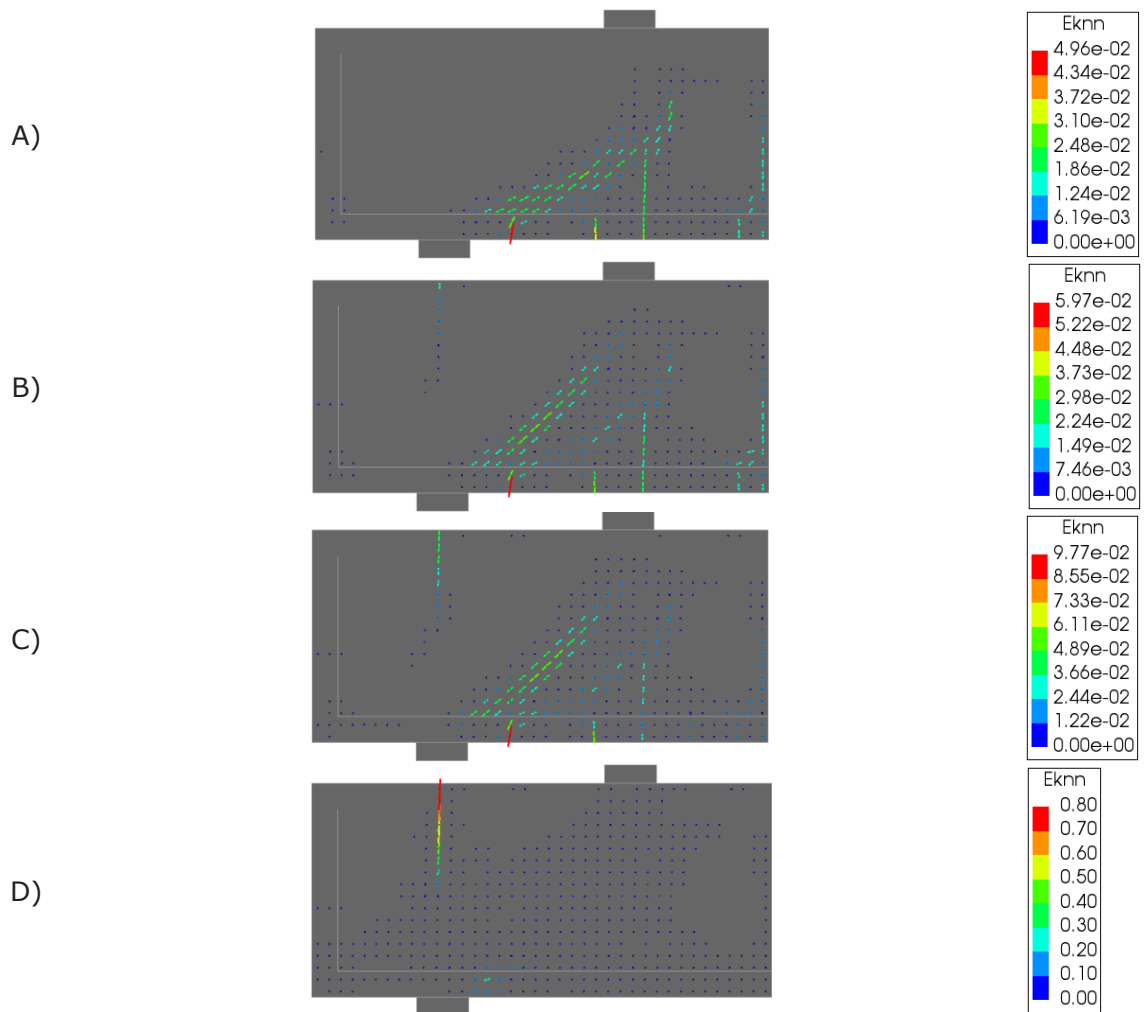


Figure C.54 – Crack strain plots beam S2D36a36, rotating to fixed – threshold at 5\*fully developed crack

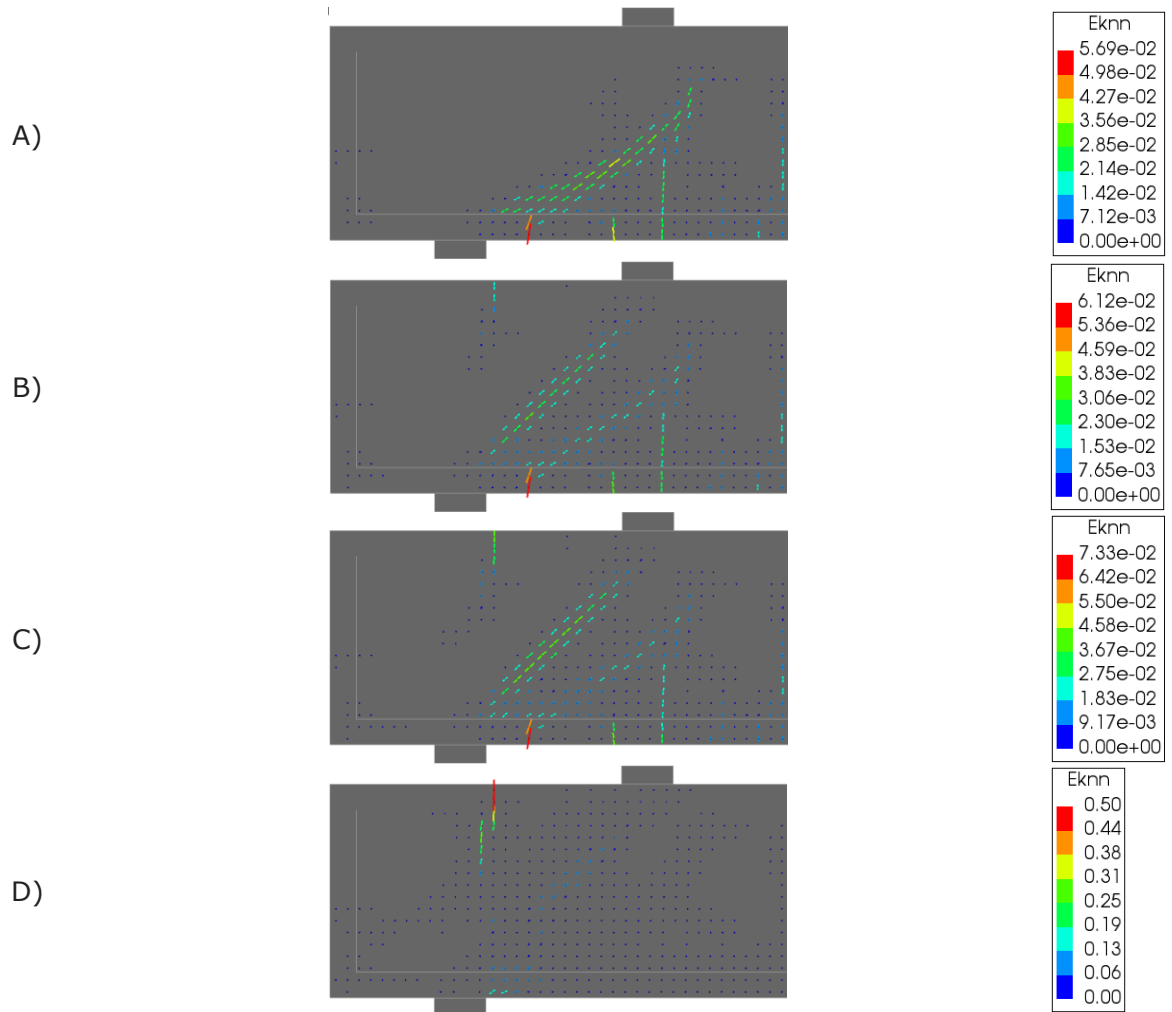


Figure C.55 – Crack strain plots beam S2D36a36, fully rotating

# C.3 Crack Strain Patterns of the Tension Stiffening Analyses

In this chapter, the crack strain patterns were plotted for a fixed crack model with damaged based shear retention with tension stiffening (TS). For the sake of comparison, the model without TS was also plotted, which is the same can be seen in Appendix C.1 for the damage based shear retention model. The extra white line, as for example can be seen in Figure C.58, marks the TS zone. That is, a TS curve is used in the post-crack phase underneath this line, instead of the Hordijk tension softening model.

## C.3.1 Crack Strain Patterns of Beam S1D18a108

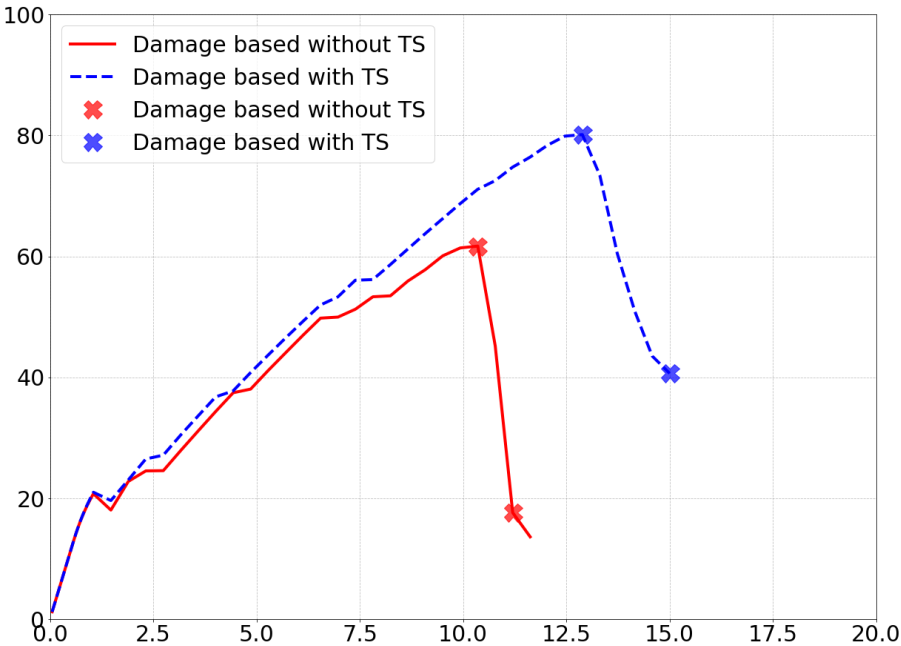


Figure C.56 – Crack plot specification with and without tension stiffening for beam S1D18a108

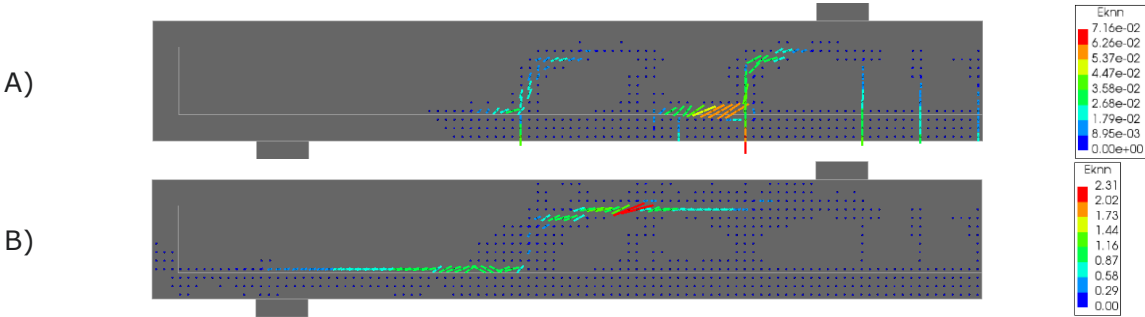


Figure C.57 – Crack strain plots for beam S1D18a108, damage based without tension stiffening

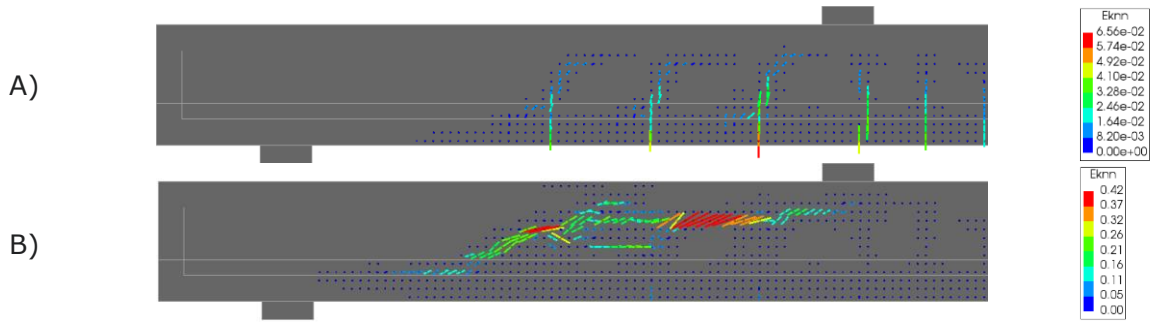


Figure C.58 – Crack strain plots for beam S1D18a108, damage based with tension stiffening

### C.3.2 Crack Strain Patterns of Beam S1&2D36a108

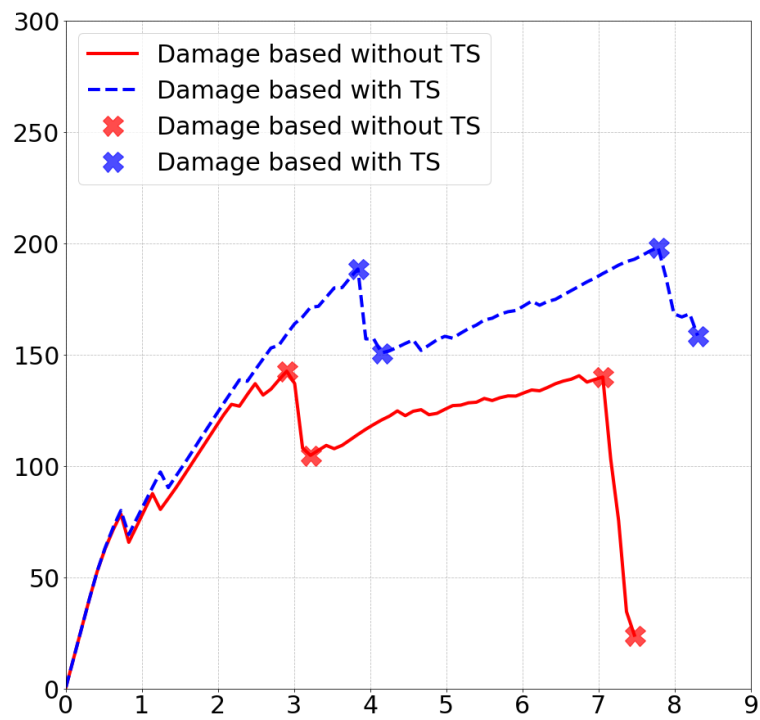


Figure C.59 – Crack plot specification with and without tension stiffening for beam S1&2D36a108

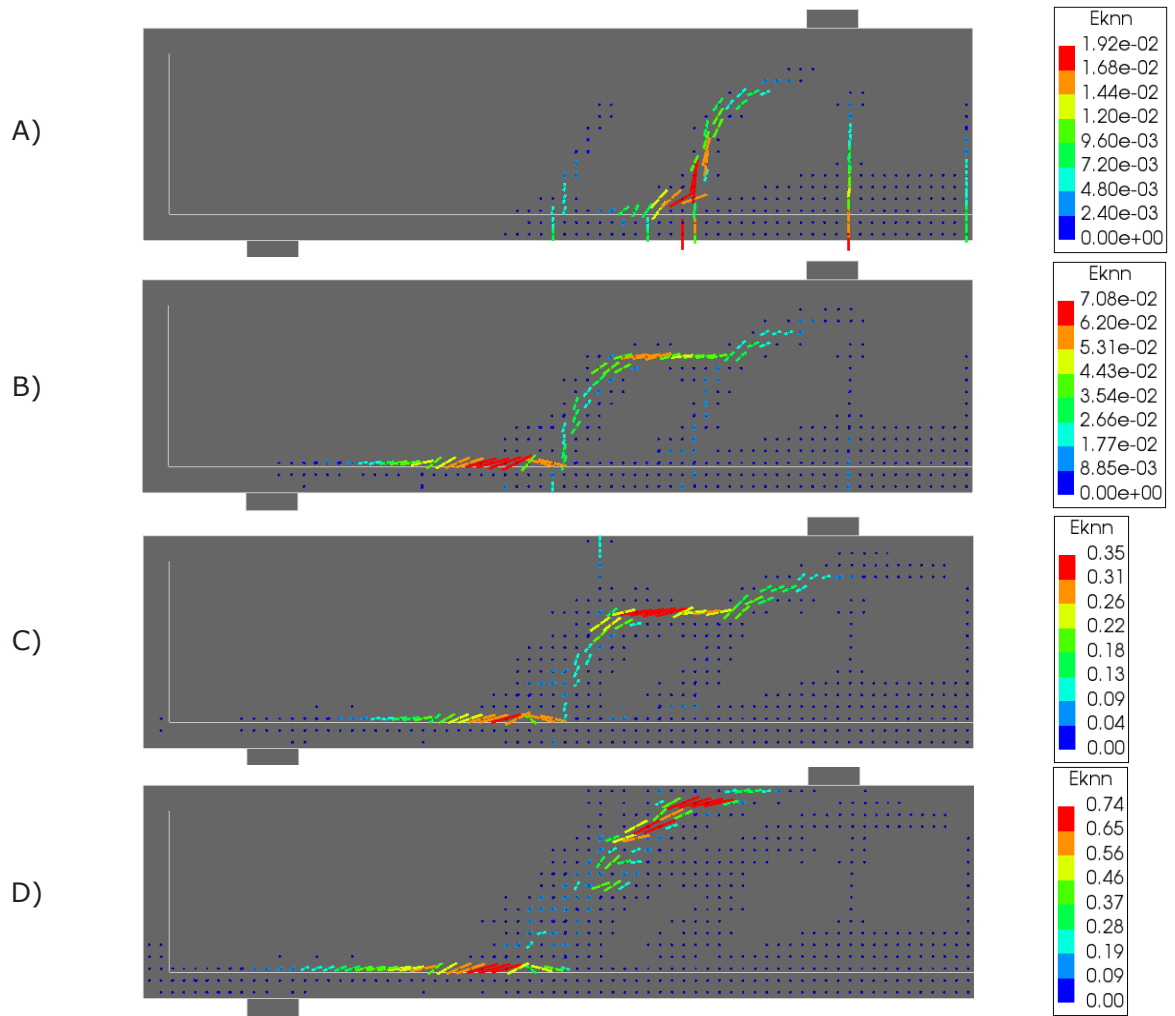


Figure C.60 – Crack strain plots for beam S1&2D36a108, damage based without tension stiffening

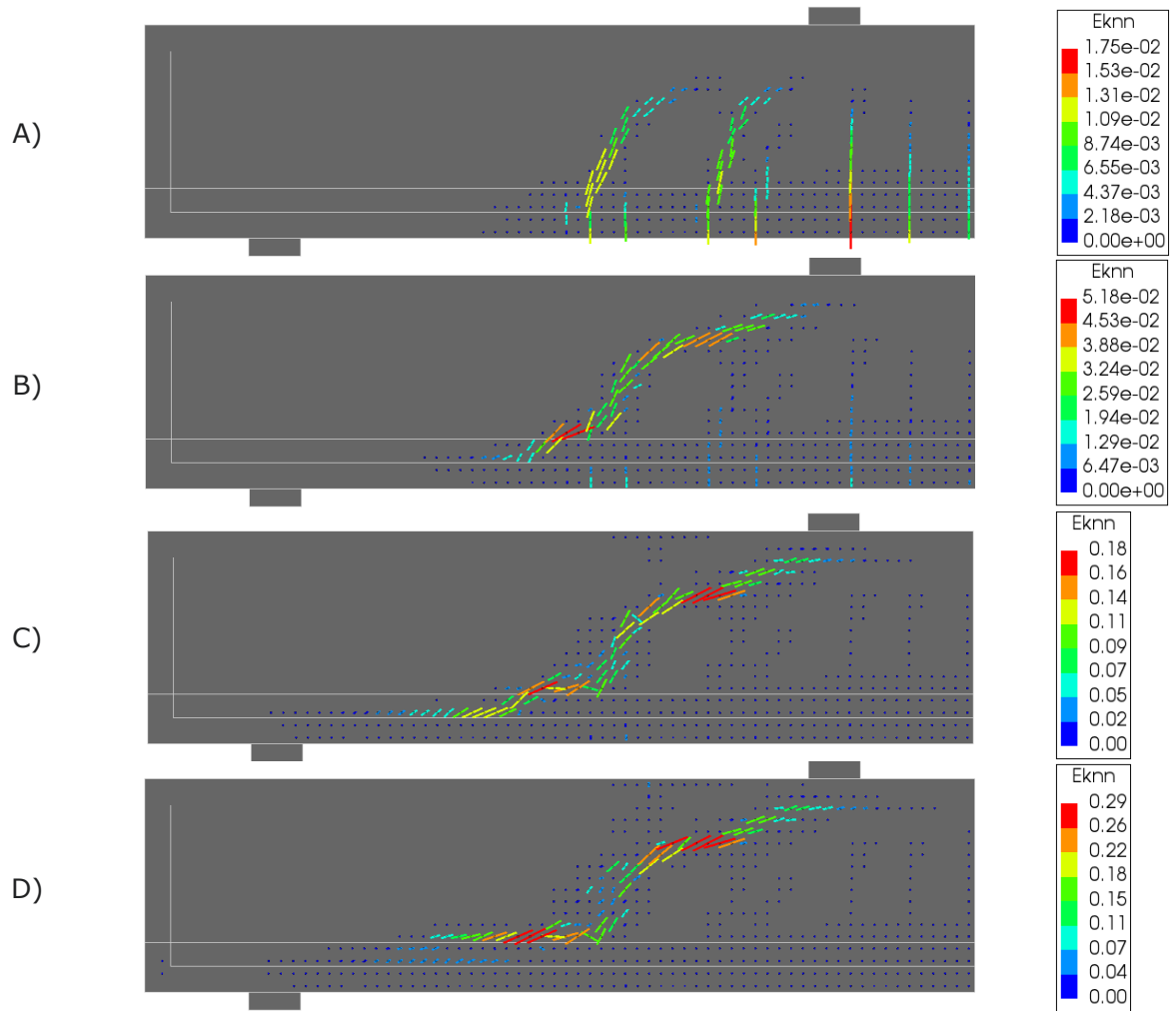


Figure C.61 – Crack strain plots for beam S1&2D36a108, damage based with tension stiffening

### C.3.3 Crack Strain Patterns of Beam S1D72a108

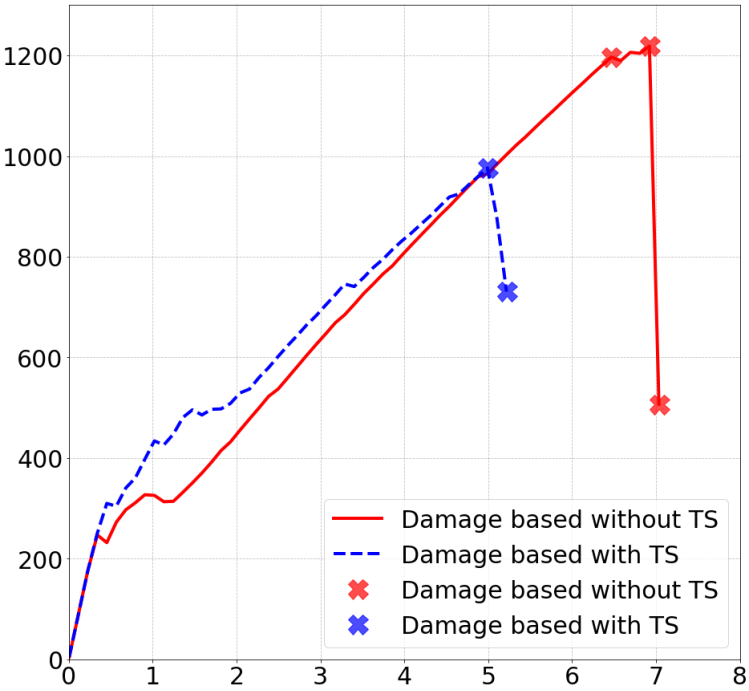


Figure C.62 – Crack plot specification with and without tension stiffening for beam S1D72a108

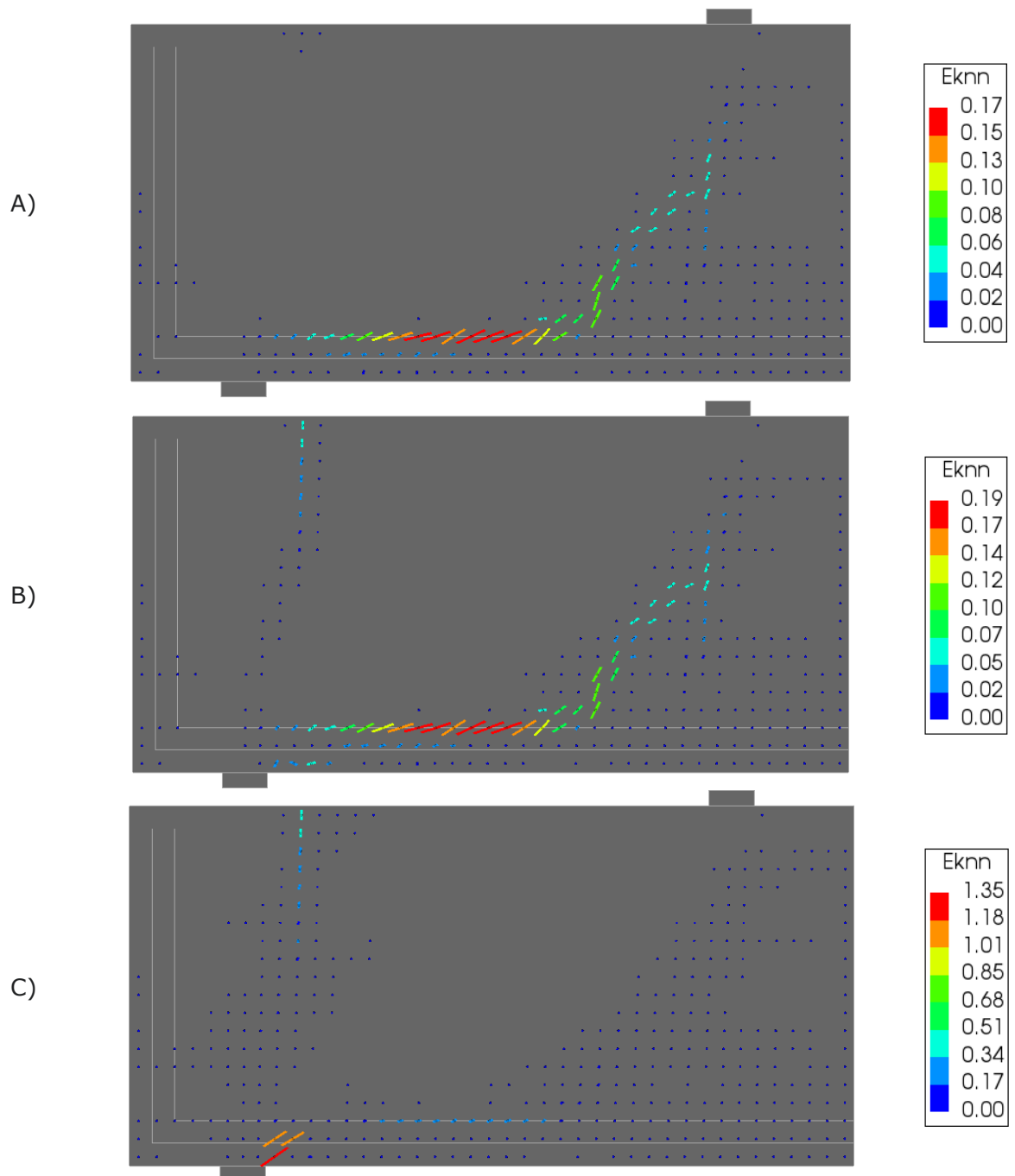


Figure C.63 – Crack strain plots for beam S1D72a108, damage based without tension stiffening

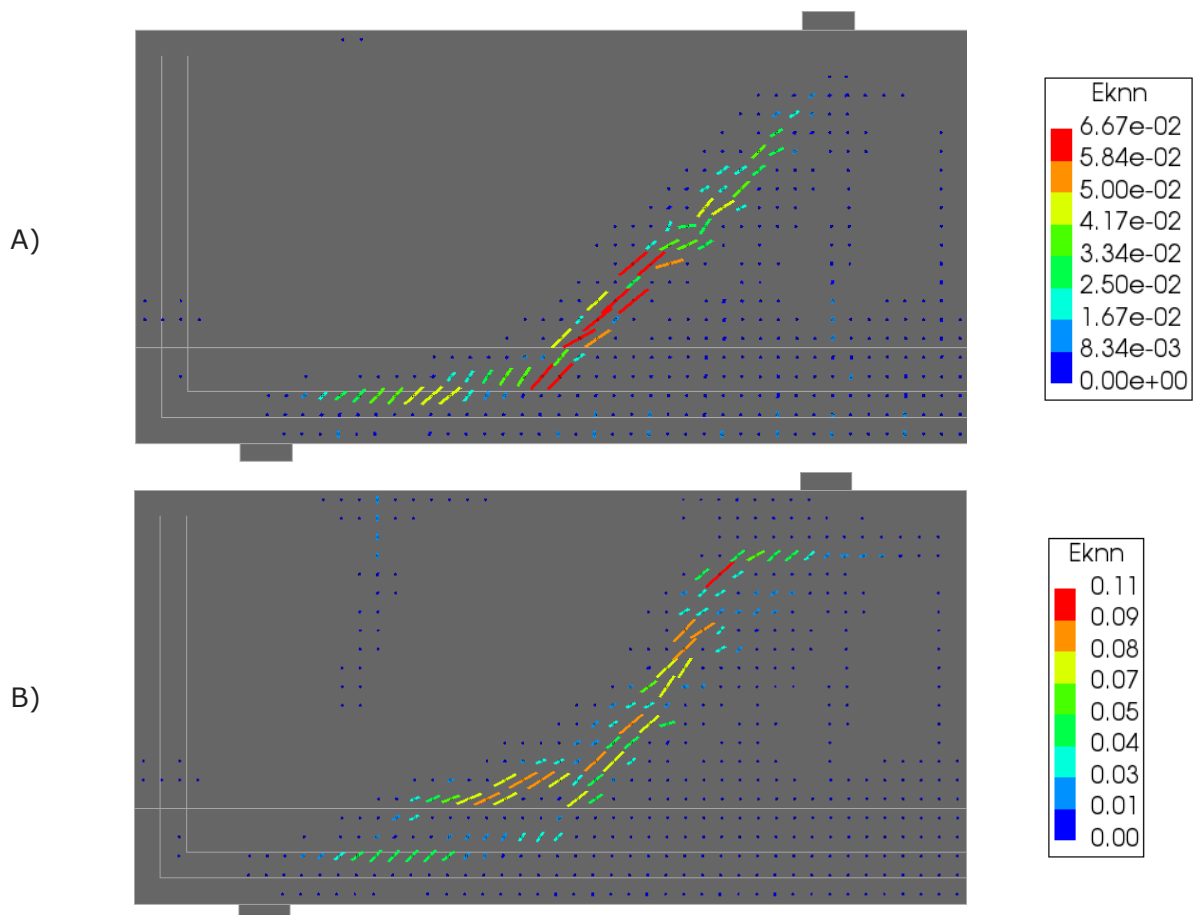


Figure C.64 – Crack strain plots for beam S1D72a108, damage based with tension stiffening

### C.3.4 Crack Strain Patterns of Beam S2D36a72

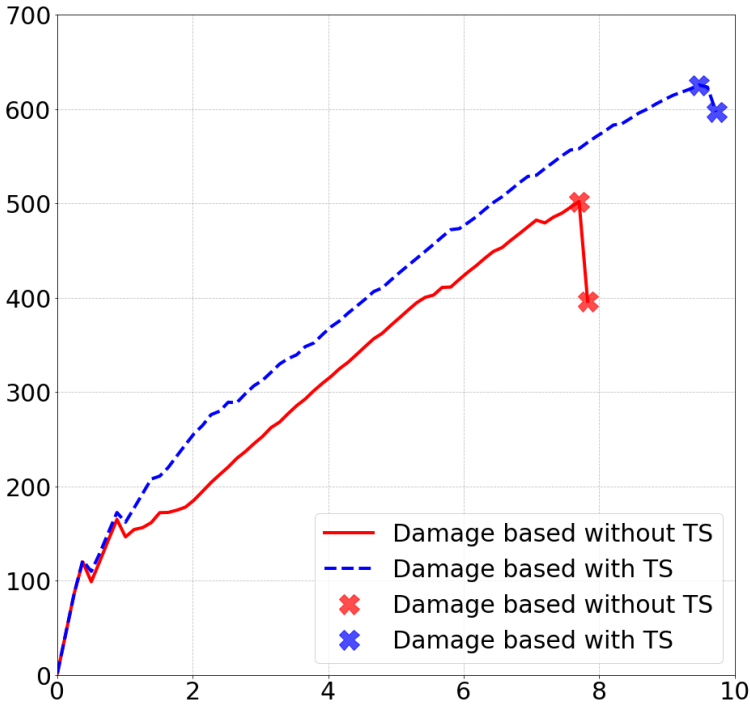


Figure C.65 – Crack plot specification with and without tension stiffening for beam S2D36a72

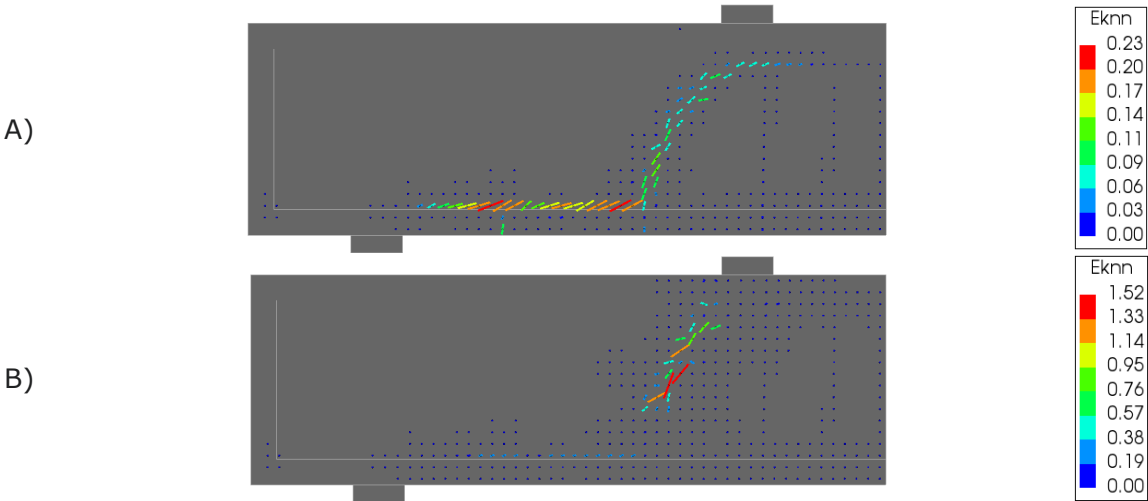


Figure C.66 – Crack strain plots for beam S2D36a72, damage based without tension stiffening

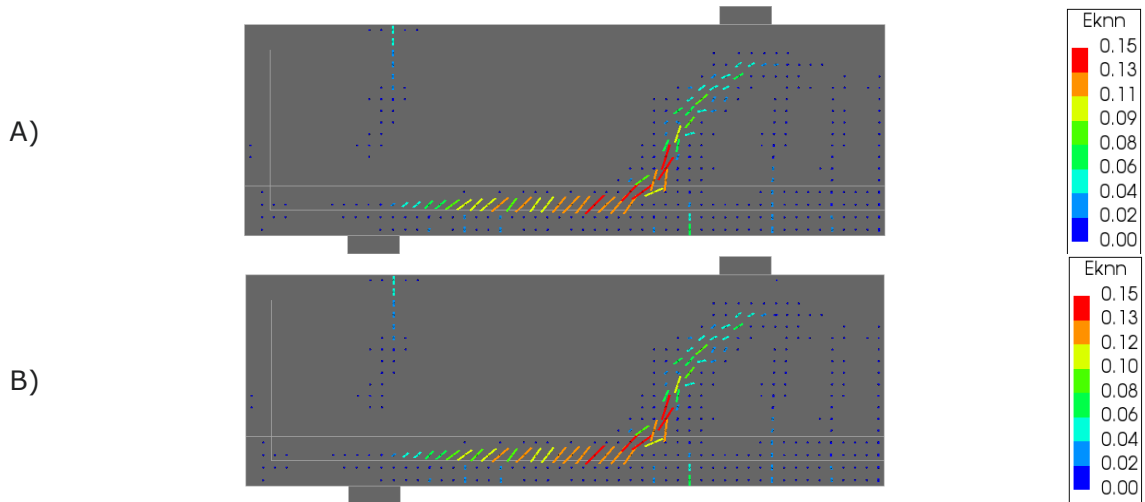


Figure C.67 – Crack strain plots for beam S2D36a72, damage based with tension stiffening (The figures are not the same, even though they are very similar)

### C.3.5 Crack Strain Patterns of Beam S2D36a36

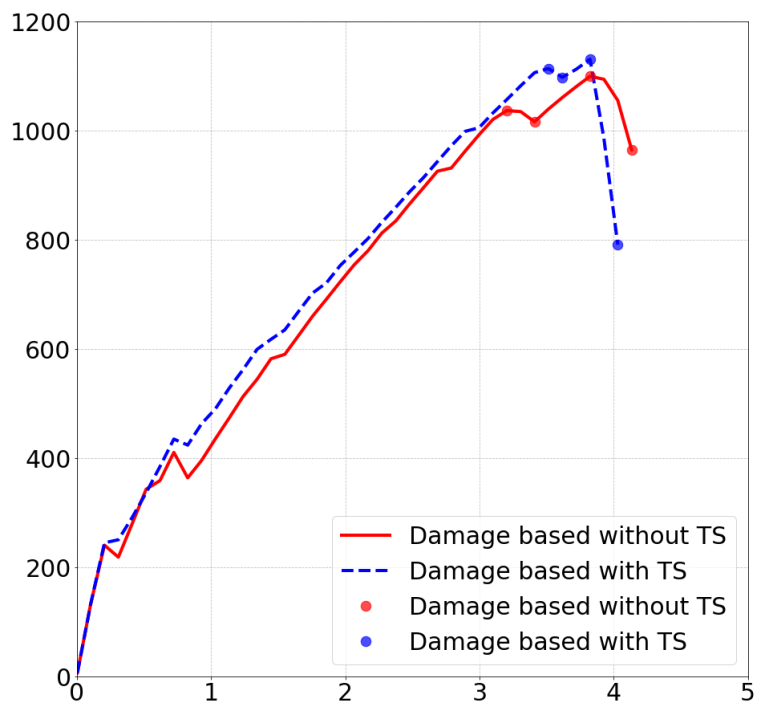


Figure C.68 – Crack plot specification with and without tension stiffening for beam S2D36a36

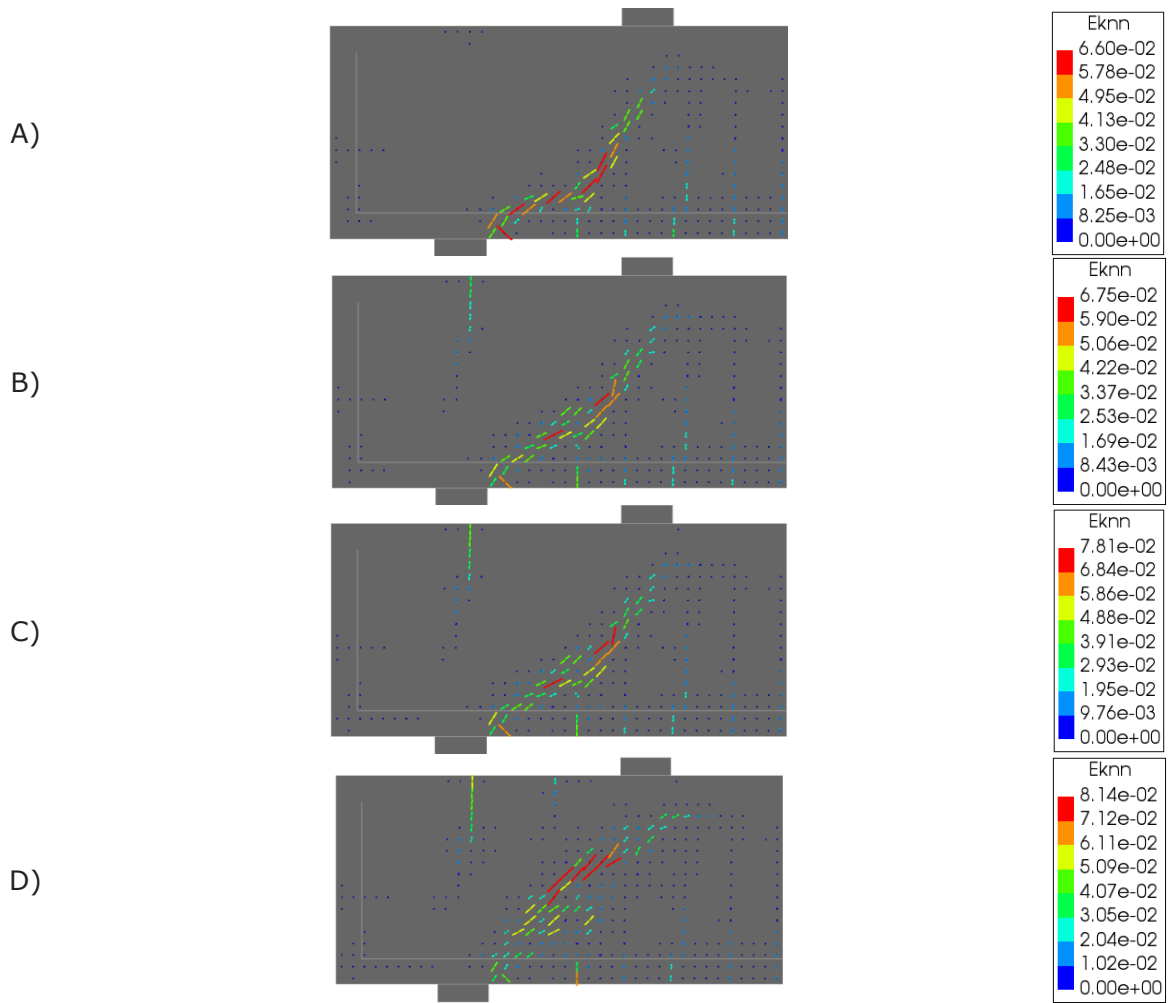


Figure C.69 – Crack strain plots for beam S2D36a36, damage based without tension stiffening

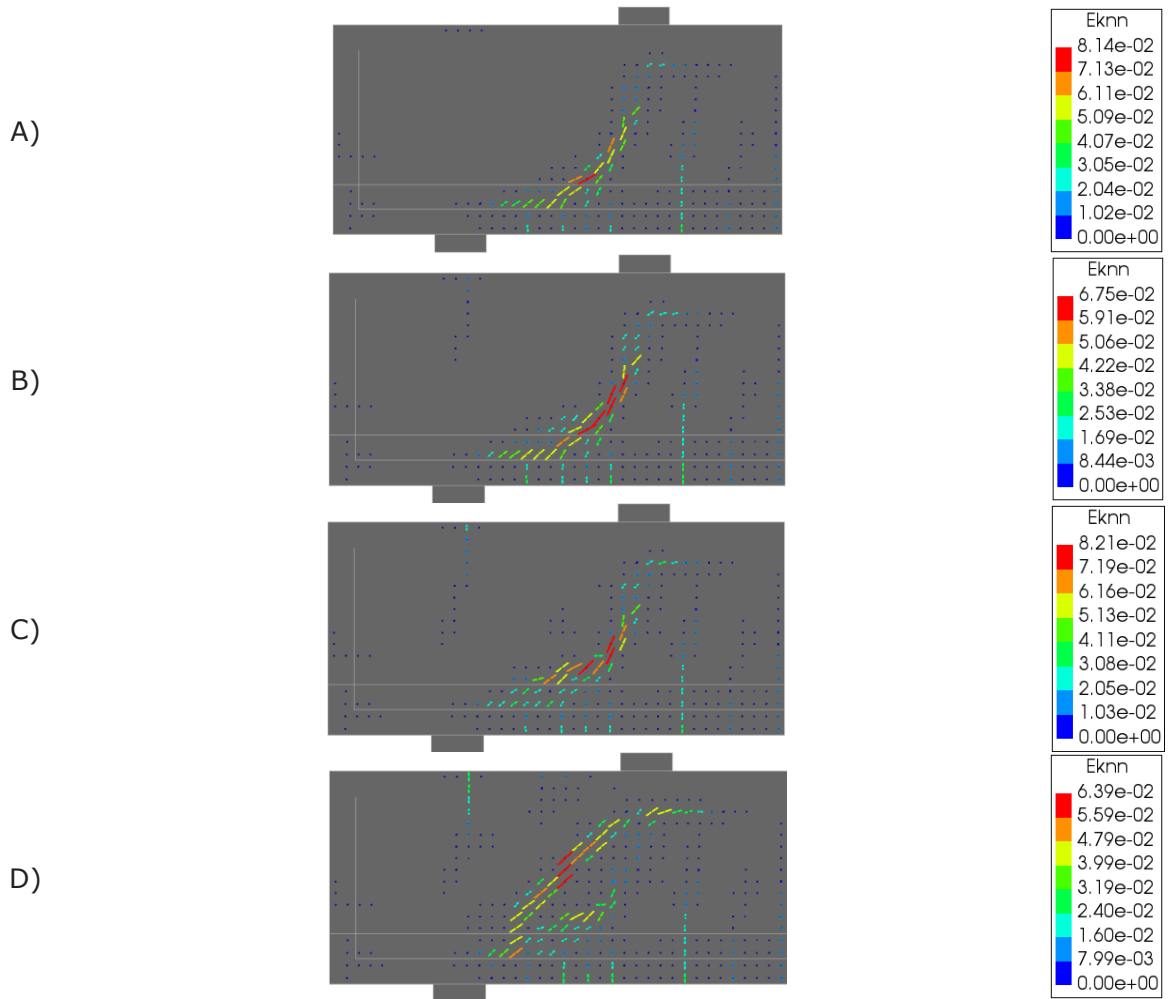


Figure C.70 – Crack strain plots for beam S2D36a36, damage based with tension stiffening

